# EXOTHERMIC CATALYTIC DECOMPOSITION OF ENERGETIC IONIC LIQUIDS ON IRIDIUM BASED CATALYSTS

A DISSERTATION SUBMITTED TO
THE GRADUATE SCHOOL OF ENGINEERING AND SCIENCE
OF BILKENT UNIVERSITY
IN PARTIAL FULFILLMENT OF THE REQUIREMENTS FOR
THE DEGREE OF
DOCTOR OF PHILOSOPHY
IN
CHEMISTRY

By
Merve Kurt
January 2022

EXOTHERMIC CATALYTIC DECOMPOSITION OF ENERGETIC IONIC LIQUIDS ON IRIDIUM BASED CATALYSTS

By Merve Kurt

January 2022

We certify that we have read this thesis and that in our opinion it is fully adequate, in scope and in quality, as a dissertation for the degree of Doctor of Philosophy.

Emrah Özensoy (Advisor)

Ömer Dağ

Ahmet Erhan Aksoylu

Ahmet Kerim Avcı

Ferdi Karadaş

Approved for the Graduate School of Engineering and Science:

Ezhan Karaşan

Director of the Graduate School

# ABSTRACT

## EXOTHERMIC CATALYTIC DECOMPOSITION OF ENERGETIC IONIC LIQUIDS ON IRIDIUM BASED CATALYSTS

Merve Kurt
Ph.D. in Chemistry
Advisor: Emrah Ozensoy
January 2022

Hydrazine ($N_2H_4$) is the most commonly used propellant for in-orbit spacecraft propulsion. However, utilization of hydrazine in space missions has challenges associated with health, environment and safety risks. Energetic ionic liquids (EILs) such as ammonium dinitramide (ADN) present themselves as environmentally friendly alternative fuels to hydrazine. EILs can be decomposed efficiently and safely in the presence of a heterogenous catalyst. In this context, monometallic catalysts containing Ir and $Al_2O_3$ were synthesized using both wetness impregnation and incipient to wetness impregnation methods, and the structural properties of these catalysts were investigated. Furthermore, the effects of the $Al_2O_3$ support material on Ir dispersion and catalytic performance of anaerobic ADN decomposition were studied. In order to improve the Ir active site dispersion on the $Al_2O_3$ support material, promoters such as La and Ce were added to the catalyst systems and different pretreatment conditions were applied to the synthesized catalysts. Furthermore, $LaMnO_3$ (perovskite) promoted alumina catalysts with Ir active sites were also studied. Catalysts with high performance, 5Ir/TH100 (5Ir/$Al_2O_3$), 5Ir/L3 (5Ir/La-$Al_2O_3$), and 5Ir/Sir10 (5Ir/Si-$Al_2O_3$) were investigated with in-situ X-ray Absorption Near Edge Spectroscopy (XANES), in-situ Extended X-ray Absorption Fine Structure (EXAFS), in-situ Fourier Transform Infrared Spectroscopy (in-situ FTIR),

Temperature Programmed Desorption (TPD), X-ray Diffraction (XRD), Transmission Electron Microscopy (TEM), Energy Dispersive X-ray (EDX), Pyridine adsorption via FTIR, CO Chemisorption, X-ray Photoelectron Spectroscopy (XPS) and X-ray Fluorescence (XRF) analysis techniques. Our findings revealed that 5Ir/TH100 and 5Ir/L3 catalysts favorably lowered the onset temperature of the ADN decomposition reaction, whereas 5Ir/Sir10 boosted the pressure generation during the reaction. The formation of mostly metallic Ir nanoparticles on 5Ir/TH100 and 5Ir/L3 enables the lowering of the activation energy of the reaction. On the other hand, enhancement in the pressure generation for 5Ir/Sir10 catalyst is associated with the generation of small oxidic $Ir_n^{x+}$ clusters which are strongly interacting with the $SiO_x$-$AlO_x$ surface domains of the support material. The fundamental structure-functionality relationships unraveled in the current work may allow design of novel catalytic systems for aerospace monopropellant propulsion systems with higher performance by simultaneous exploitation of Ir active sites with different electronic properties.

**Keywords:** Ir, ADN (ammonium dinitramide), monopropellant, hydrazine, catalytic decomposition

# ÖZET

## ENERJIK İYONİK SIVILARIN İRİDYUM BAZLI KATALİZÖRLER ÜZERİNDE EKZOTERMİK BOZUNMASI

Merve Kurt
Kimya, Doktora
Tez Danışmanı: Emrah Özensoy
Ocak 2022

Hidrazin ($N_2H_4$), yörüngedeki uzay araçları için, en yaygın olarak kullanılan iticidir. Bununla birlikte, uzay görevlerinde hidrazin kullanımı, sağlık, çevre ve güvenlik riskleriyle ilgili zorluklara sahiptir. Amonyum dinitramit (ADN) gibi enerjik iyonik sıvılar (EIS), çevre dostu alternatif yakıtlar olarak, umut vadeden seçenekler sunmaktadır. EIS'lar katalizör varlığında verimli ve güvenli bir şekilde bozunabilmektedir. Bu kapsamda, Ir ve $Al_2O_3$ içeren tek-metalli aktif sitelere sahip katalizörler, hem emdirme empregnasyonu, hem de nemlendirme empregnasyonu kullanılarak sentezlenmiş ve bu katalizörlerin yapısal özellikleri araştırılmıştır. $Al_2O_3$ destek malzemesinin Ir dağılımı ve katalitik ADN bozunması üzerindeki etkileri incelenmiştir. Ir dağılımını arttırmak için, katalizör sistemlerine La ve Ce gibi iyileştiriciler eklenmiş ve sentezlenen numunelere farklı ön işlem koşulları uygulanmıştır. Bunun dışında $LaMnO_3$ (perovskit) yapılarıyla zenginleştirilmiş, Ir aktif siteleri içeren katalizörler de hazırlanarak, performans özellikleri incelenmiştir. En yüksek aktivite gösteren, 5Ir/TH100 ($5Ir/Al_2O_3$), 5Ir/L3 ($5Ir/La\text{-}Al_2O_3$) ve 5Ir/Sir10 ($5Ir/Si\text{-}Al_2O_3$) formundaki katalizörler, yerinde X-ışını Absorpsiyon Yakın Kenar Spektroskopisi (XANES), yerinde Genişletilmiş X-ışını Soğurma İnce Yapısı (EXAFS), yerinde Fourier Dönüşümü Kızılötesi Spektroskopisi (yerinde FTIR), Sıcaklık Programlı Desorpsiyon (TPD), X-ışını Kırınımı (XRD), Geçirgen Elektron Mikroskopisi

(TEM), Enerji Dağılımlı X-ışını (EDX), Piridin adsorpsiyonu, CO kemisorpsiyonu, X-ışını Fotoelektron Spektroskopisi (XPS) ve X-ışını Floresan (XRF) analiz teknikleri ile araştırılmıştır. Bulgularımız, 5Ir/TH100 ve 5Ir/L3'ün, ADN bozunma reaksiyonunun başlangıç sıcaklığını olumlu şekilde düşürürken, 5Ir/Sir10'un reaksiyon sırasında basınç oluşumunu artırdığını ortaya koymaktadır. 5Ir/TH100 ve 5Ir/L3 için çoğunlukla metalik Ir nanoparçacıklarının oluşumu, reaksiyonun aktivasyon enerjisinin düşürülmesini sağlar. Öte yandan, 5Ir/Sir10 katalizörünün aktivitesi, destek malzemesinin, $SiO_x$-$AlO_x$, yüzeyi ile güçlü bir şekilde etkileşime giren küçük oksidik $Ir_n^{x+}$ kümelerinin üretilmesiyle ilişkilidir. Mevcut çalışmada ortaya konan katalitik temel yapı-işlevsellik ilişkileri, farklı elektronik özelliklere sahip aktif bölgelerin aynı anda kullanılmasıyla daha yüksek performansa sahip havacılık itki sevk sistemleri için yeni katalitik sistemlerin tasarlanmasına ışık tutmaktadır.

**Anahtar Kelimeler:** İridyum, ADN (amonyum dinitriamid), tek yakıtlı, hidrazin, katalitik bozunma.

# Acknowledgements

I would like to state my gratitude to many individuals who have provided me great support and helped me throughout my studies for my research project.

First and foremost, I would like to express my appreciation to my research supervisor Prof. Dr. Emrah Özensoy for providing me an opportunity to work on this research project. I would like to state my sincere thanks to him for his valuable guidance, encouragement, patience and supervision throughout my studies. It has been a pleasure studying in his research group.

I would like to thank my Ph.D. committee members Prof. Dr. Ömer Dağ, Prof. Dr. Ahmet Erhan Aksoylu, Prof. Dr. Ahmet Kerim Avcı and Asst. Prof. Ferdi Karadaş for their precious time.

I would like to thank to all Ozensoy research group members especially Kerem Emre Ercan, Sinem Şenol, and Zeynep Kap for their contribution to my research and the precious time that they shared with me during my Ph.D. studies. Sinem Senol and Zeynep Kap contributed to the material synthesis, XRD, BET and batch reactor measurements. Kerem Emre Ercan performed XANES/EXAFS measurements and analysis. I have received great support, encouragement and companionship from them in both my personal life and academic study during the past few years. I thank them all for their valuable friendship.

I acknowledge to Roketsan Company for their financial support. I would like to thank the project team Prof. Dr. Ahmet Erhan Aksoylu, Dr. Burcu Selen Çağlayan, Dr. Ahmet Koç, and Dr. Hacı Eşiyok.

Last but not the least, I wish to thank to my beloved family; my mother, Banu Doğaç, my father, Ali Doğaç, my husband, Erdem Kurt, my child, Karen Kurt, my sister, Melis Yüksel and my lovely dog, Roko. Nobody has been more important to me in the world than my family. There is no word to express my gratitude to my family for their love, support and

encouragement during my graduate studies. Their unconditional love and continuous support brought me where I am today. I owe them a lot for supporting me spiritually and genuinely throughout my life.

# Contents

**CHAPTER 1** ..... **1**
**1. INTRODUCTION** ..... **1**
1.1. Monopropellants ..... 2
1.1.1. HAN Propellants ..... 4
1.1.2. ADN Propellants ..... 5
1.2. Catalytic Systems ..... 7
1.2.1. Support Materials ..... 8
1.2.1.1. Al-based Support Materials ..... 8
1.2.1.1.1. Thermal stability of alumina upon doping ..... 10
1.2.1.1.2. Surface properties of the alumina upon doping ..... 12
1.2.1.2. Hexaluminates ..... 16
1.2.2. Catalytic Active Sites ..... 18
**CHAPTER 2** ..... **22**
**2. EXPERIMENTAL** ..... **22**
2.1. CUSTOM-DESIGN MICRO PROPULSION BATCH REACTOR ..... 22
2.1.1. Custom-design Micro Propulsion Batch Reactor Design Features ..... 22
2.1.2. Custom-design Micro Propulsion Batch Reactor Software ..... 34
2.1.2.1. Syringe pump software ..... 34
2.1.2.2. Data acquisition software ..... 38
2.1.3. Custom-design Micro Propulsion Batch Reactor Operating Procedures ..... 41
2.1.3.1. Reactor cleaning procedure before starting the experiment ..... 41
2.1.3.2. Adjusting the fuel dosing amount ..... 41
2.1.3.3. Gas dosing procedure ..... 42
2.1.3.4. Reactor cleaning procedure after measurement ..... 42
2.2. MATERIAL SYNTHESIS ..... 43
2.2.1. Support Materials ..... 43
2.2.2. Incorporation Catalytic Active Sites on the Alumina Support Materials ..... 45
2.2.2.1. Catalyst synthesis via wetness impregnation (WI) ..... 45
2.2.2.1.1. 5Ir/10LaMnO$_3$/SBa200 synthesis via WI ..... 47
2.2.2.2. Catalyst synthesis via incipient to wetness impregnation (IWI) ..... 48
2.2.2.2.1. Addition of 5 wt.% Ir via IWI ..... 49
2.2.2.2.2. Addition of La and Ce promoters via IWI synthesis method ..... 51

2.3. INSTRUMENTATION ..... 53
2.3.1. Ex-situ Characterization ..... 53
2.3.1.1. X-ray diffraction (XRD) ..... 53
2.3.1.2. $N_2$ adsorption measurements ..... 53
2.3.1.3. Transmission electron microscopy (TEM) images and energy dispersive X-ray (EDX) analyses ..... 54
2.3.1.4. Raman spectroscopy ..... 54
2.3.1.5. X-ray photoelectron spectroscopy (XPS) ..... 54
2.3.1.6. X-ray florescence (XRF) ..... 55
2.3.1.7. ADN adsorption experiments ..... 55
2.3.1.8. Gas phase decomposition products via FTIR ..... 55
2.3.2. In-Situ Experiments ..... 56
2.3.2.1. Pyridine adsorption experiments via in-situ FTIR ..... 56
2.3.2.2. CO chemisorption ..... 56
2.3.2.3. CO adsorption via in-situ FTIR spectroscopy and temperature programmed desorption (TPD) ..... 56
2.3.2.4. In-situ extended X-ray absorption fine structure (EXAFS) and in-situ X-ray absorption near edge spectroscopy (XANES) experiments ..... 57
2.3.3. Performance Measurements ..... 59
2.3.3.1. Differential Scanning Calorimetry/Thermal Gravimetric Analysis (DSC/TGA) ..... 59
2.3.3.2. Custom-design Micro Propulsion Batch Reactor Parameters ..... 61
**CHAPTER 3 ..... 63**
**3. CRYSTALLOGRAPHIC STRUCTURE AND THERMAL STABILITY OF THE SUPPORT MATERIALS: CHOICE OF THE ALUMINA SUPPORT ..... 63**
3.1. XRD analyses of the alumina support materials ..... 63
3.2. Specific surface area (SSA) values of the alumina support materials ..... 70
**CHAPTER 4 ..... 74**
**4. THERMAL DECOMPOSITION CHARACTERISTICS OF ADN BASED FUELS IN THE ABSENCE OF A CATALYST ..... 74**
4.1. Thermal decomposition characteristics of ADN mixtures (STY-120-X) in the absence of a catalyst via DSC/TGA ..... 74
4.2. Comparison of thermal decomposition characteristics of STY-126-X based ADN mixtures on SBa200 alumina in the absence of any catalytic active sites via custom-design micro propulsion batch reactor measurements ..... 75
**CHAPTER 5 ..... 78**

**5. CHARACTERIZATION AND CATALYTIC PERFORMANCE OF THE CATALYSTS SYNTHESIZED VIA WETNESS IMPREGNATION ..... 78**

5.1. PERFORMANCE OF THE CATALYSTS SYNTHESIZED VIA WI ..... 78

5.2. CHARACTERIZATION OF THE CATALYSTS SYNTHESIZED VIA WI .. 82

5.2.1. XRD analyses of the catalysts synthesized via WI ..... 82

5.2.2. Raman spectroscopic analyses of the catalysts synthesized via WI ..... 89

5.2.3. XPS Analyses of the catalysts synthesized via WI ..... 91

5.2.4. TEM and EDX measurements of the catalysts synthesized via WI ..... 93

5.2.5. ADN decomposition over Ir and perovskite-containing alumina supported catalysts prepared via WI method ..... 103

**CHAPTER 6 ..... 106**

**6. CHARACTERIZATION AND CATALYTIC PERFORMANCE OF THE CATALYSTS SYNTHESIZED VIA INCIPIENT TO WETNESS IMPREGNATION ..... 106**

6.1. XRD AND TEM ANALYSES OF THE CATALYSTS SYNTHESIZED VIA IWI ..... 106

6.1.1. XRD analyses of the catalysts synthesized via IWI ..... 106

6.1.1.1. XRD of CCR samples synthesized via IWI ..... 106

6.1.1.2. XRD of RR samples synthesized via IWI ..... 109

6.1.2. TEM analyses of the catalysts synthesized via IWI ..... 111

6.1.2.1. TEM of CCR samples synthesized via IWI ..... 111

6.1.2.2. TEM of RR samples synthesized via IWI ..... 115

6.2. PERFORMANCE RESULTS OF THE IWI CATALYSTS OBTAINED FROM CUSTOM-DESIGN MICRO PROPULSION BATCH REACTOR EXPERIMENTS ..... 116

6.3. DETAILED CHARACTERIZATION OF SELECTED CATALYSTS SYNTHESIZED VIA IWI ..... 119

6.3.1. Decomposition products via FTIR spectroscopy ..... 119

6.3.2. Specific surface area (SSA) of the selected catalysts synthesized via IWI .. 123

6.3.3. Composition of the catalysts synthesized via IWI from XRF ..... 124

6.3.4. Ir particle size of the catalysts synthesized via IWI from XRD and TEM analysis ..... 125

6.3.5. In-situ FTIR CO adsorption experiments for the analysis of Ir morphology and Ir oxidation state ..... 126

6.3.6. Surface acidity via pyridine adsorption and the extent of ADN uptake via FTIR measurements ..... 131

6.3.7. Ir oxidation state via XPS ..... 133

6.3.8. Determination of the relative number of exposed surface Ir species via CO chemisorption and CO-TPD experiments ..... 134
6.3.9. In-situ XANES/EXAFS experiments for analyzing Ir nearest neighbors and coordination ..... 136
**CHAPTER 7 ..... 141**
**7. CONCLUSIONS ..... 141**
**REFERENCES ..... 143**
**APPENDIX ..... 164**
Appendix A ..... 164
Appendix B ..... 176
Appendix C ..... 184
Appendix D ..... 191

# List of Figures

**Figure 1-1.** Molecular structures of ionic liquids used as monopropellants: a) ADN, b) HAN, c) HNF, and d) AN. ..... 4

**Figure 1-2.** Different forms of Al-based support materials. ..... 9

**Figure 1-3.** Temperature-dependent phase transformations of alumina materials [53]. Copyright (2014) Elsevier ..... 9

**Figure 1-4.** Changes of SSA of alumina with temperature under atmospheric pressure [52]. Copyright (1996) Elsevier ..... 10

**Figure 1-5.** Changes of the SSA with increasing temperature for 0 wt%, 2.5 wt%, 5 wt% and 10 wt% Si containing aluminas [72]. Copyright (2007) Elsevier ..... 11

**Figure 1-6.** Strong Bronsted acid sites in silica-alumina materials [80]. ..... 13

**Figure 1-7.** Electronic effects observed for weak metal support interaction (WMSI) and strong metal support interaction (SMSI) [84]. Copyright (2017) Elsevier ..... 14

**Figure 1-8.** Geometric effects in strong metal support interaction [84]. Copyright (2017) Elsevier ..... 14

**Figure 1-9.** Schematic representation of CO adsorption and oxidation over $Pd/Al_2O_3$ and $Pd/La/Al_2O_3$ in CO oxidation with $O_2$ [86]. Copyright (2017) American Chemical Society 15

**Figure 1-10.** Schematic representation of Pd and PdO on $La\text{-}Al_2O_3$ and $Al_2O_3$ [69]. Copyright (2013) Elsevier ..... 16

**Figure 1-11.** Hexaaluminate crystal structure [52]. Copyright (1996) Elsevier ..... 17

**Figure 1-12.** Behavior of Pt particles during HAN decomposition [103]. Copyright (1996) Elsevier ..... 19

**Figure 2-1.** Overall 3D view of the custom-design micro reactor system with 3 identical batch reactors that can be operated in parallel. ..... 23

**Figure 2-2.** Actual overall view of the batch reactors. ..... 24

**Figure 2-3.** View of a single batch reactor with its control box. ..... 25

**Figure 2-4.** 3D internal view of the cross-section of the batch reactor. ..... 27

**Figure 2-5.** Disassembled display of reaction compartment elements of the batch reactor. ..... 27

**Figure 2-6.** Thermocouple extending from the hole of the funnel to the reaction compartment. ..... 28

**Figure 2-7.** Alignment of the funnel shaped sample holder. ..... 28

**Figure 2-8.** Disassembled view of the batch reactor. ..... 29

**Figure 2-9.** Various components of the batch reactor. ..... 31

**Figure 2-10.** Components of the batch reactor control box. ..... 32

**Figure 2-11.** Data acquisition module and 24 VDC power supply. ..... 33

**Figure 2-12.** Login page. 34
**Figure 2-13.** Administrator window. 35
**Figure 2-14.** Admin connections port page. 35
**Figure 2-15.** Run tab. 36
**Figure 2-16.** Position adjustment button. 38
**Figure 2-17.** Main page of the DAQExpress data acquisition software. 39
**Figure 2-18.** Diagram tab. 39
**Figure 2-19.** Panel tab. 40
**Figure 2-20.** Wetness impregnation setup. 46
**Figure 2-21.** Box oven used in the calcination of catalysts in air. 47
**Figure 2-22.** (a) Incipient to wetness impregnation set up (b) updated version of the incipient to wetness impregnation set up system. 49
**Figure 2-23.** (a) Drying oven, (b) tubular flow furnace. 51
**Figure 2-24.** Typical heat flow and weight % plots obtained during ADN decomposition in a DSC/TGA measurement. 60
**Figure 2-25.** Typical temperature vs. time and pressure vs. time plots obtained during a catalytic anaerobic ADN decomposition run. 62
**Figure 3-1.** XRD patterns of SBa200 support material (a) after calcination at 550 °C, and (b) after thermal aging at 1100 °C. 64
**Figure 3-2.** XRD patterns of TH100 support material (a) after calcination at 550 °C, and (b) after thermal aging at 1100 °C. 65
**Figure 3-3.** XRD patterns of L3 support material (a) after calcination at 550 °C, and (b) after thermal aging at 1100 °C. 66
**Figure 3-4.** XRD patterns of SCFa140 support material (a) after calcination at 550 °C, and (b) after thermal aging at 1100 °C. 66
**Figure 3-5.** XRD patterns of MG5 support material (a) after calcination at 550 °C, and (b) after thermal aging at 1100 °C. 67
**Figure 3-6.** XRD patterns of Ce20 support material (a) after calcination at 550 °C, and (b) after thermal aging at 1100 °C. 68
**Figure 3-7.** XRD patterns of Sir5 support materials (a) after calcination at 550 °C, and (b) after thermal aging at 1100 °C. 69
**Figure 3-8.** XRD patterns of Sir10 support material (a) after calcination at 550 °C, and (b) after thermal aging at 1100 °C. 69
**Figure 3-9.** XRD patterns of Sir20 support material (a) after calcination at 550 °C, and (b) after thermal aging at 1100 °C. 70
**Figure 3-10.** SSA values of the fresh support materials. 71

**Figure 3-11.** SSA values for support materials calcined at (a) 1100 °C and (b) 1200 °C. ..... 72

**Figure 4-1.** Histograms showing the (a) $T_{Onset}$ and (b) Energy values of STY-120-1, STY-120-3, STY-120-4, STY-120-5 ADN mixtures in the absence of a catalyst. ..... 75

**Figure 4-2.** Comparison of (a) $T_{Onset}$ and (b) ΔP values of STY-126-2, STY-126-3, STY-126-4, STY-126-5, STY-126-6, STY-126-7, STY-126-8, STY-126-9 ADN mixtures measured with SBa200 alumina (in the absence of any catalytically active sites) in the custom-design micro propulsion batch reactor. ..... 76

**Figure 5-1.** Average $T_{Onset}$ values for the decomposition of ADN mixture on various 5 wt. % Ir loaded alumina catalysts prepared via WI method calcined at 550 °C, 900 °C, and 1100 °C measured with the DSC/TGA technique. Green bar represents $T_{Onset}$ value for the thermal decomposition of ADN mixture in the absence of a catalyst. ..... 79

**Figure 5-2.** Average generated energy values for the decomposition of ADN mixture on various 5 wt. % Ir loaded alumina catalysts prepared via WI method calcined at 550 °C, 900 °C, and 1100 °C measured with the DSC/TGA technique. Green bar represents energy value for the thermal decomposition of ADN mixture in the absence of a catalyst. ..... 81

**Figure 5-3.** XRD patterns of 5Ir/SBa200 catalyst prepared via WI method after calcination at 550 °C, 900 °C and 1100 °C. ..... 83

**Figure 5-4.** XRD patterns of 5Ir/SCFa catalyst prepared via WI method after calcination at 550 °C, 900 °C and 1100 °C. ..... 84

**Figure 5-5.** XRD patterns of 5Ir/MG5 catalyst prepared via WI method after calcination at 550 °C, 900 °C and 1100 °C. ..... 85

**Figure 5-6.** XRD patterns of of 5Ir/Ce20 catalyst prepared via WI method after calcination at 550 °C, 900 °C and 1100 °C. ..... 86

**Figure 5-7.** XRD patterns of of 5Ir/L3 catalyst prepared via WI method after calcination at 550 °C, 900 °C and 1100 °C. ..... 88

**Figure 5-8.** XRD patterns of of 5Ir/TH100 catalyst prepared via WI method after calcination at 550 °C, 900 °C and 1100 °C. ..... 89

**Figure 5-9.** Raman spectra of the Ir-containing catalysts prepared via WI method after calcination at (a) 550 °C (b) 900 °C, and (c) 1100 °C. ..... 90

**Figure 5-10.** Comparison of the percent surface atomic concentrations of Ir obtained via XPS on the catalyst surfaces prepared via WI method. ..... 93

**Figure 5-11.** (a-b) HRTEM images of 5Ir/SBa200-550C catalyst prepared via WI method. (c) HAADF-STEM image of the 5Ir/SBa200-550C catalyst prepared via WI method, (d) EDX spectrum of the 5Ir/SBa200-550C catalyst obtained from the marked area in (c). . 94

**Figure 5-12.** (a) HAADF-STEM image of the 5Ir/SBa200-900C catalyst prepared via WI method, (b-c) EDX spectra obtained from the marked areas 1, and 2 labeled in (a), respectively. ..... 95

**Figure 5-13.** (a) HAADF-STEM image of the 5Ir/SBa200-1100C catalyst prepared via WI method, (b) EDX spectrum of the area marked as 1 in (a). ..... 96

**Figure 5-14.** (a) HRTEM images of 5Ir/L3-550C catalyst prepared via WI method. (b) HAADF-STEM image of the 5Ir/L3-550C catalyst prepared via WI method, (c) EDX spectrum of the area marked as 1 in (b) ..... 96

**Figure 5-15.** (a) HAADF-STEM image of the 5Ir/L3-900C catalyst prepared via WI method, (b-c) corresponding EDX spectra obtained from the marked areas 1, 2 in (a), respectively. ..... 97

**Figure 5-16.** (a-c) HRTEM image of 5Ir/L3-1100C catalyst prepared via WI method (d) HAADF-STEM image of the 5Ir/L3-1100C catalyst prepared via WI method, (e) associated EDX spectrum obtained from the area marked as 2 in (d). ..... 98

**Figure 5-17.** (a) HAADF-STEM image, (b-f) Ir, O, Al, La, La+Ir elemental EDX maps of the 5Ir/L3-1100C catalyst prepared via WI method, respectively**.** ..... 99

**Figure 5-18.** (a) HRTEM image of 5Ir/Ce20-550C, (b) HAADF STEM image of the 5Ir/Ce20-550C catalyst prepared via WI method, (c) EDX spectrum of the material indicated by the marked area in (b)..... 100

**Figure 5-19.** (a) HAADF STEM image of the 5Ir/Ce20-900C catalyst prepared via WI method, (b) EDX spectra obtained from the indicated regions shown in (a). ..... 101

**Figure 5-20.** (a) HAADF STEM image of the 5Ir/Ce20-1100C catalyst prepared via WI method, (b) EDX spectrum obtained from the indicated region marked as 1 in (a)..... 102

**Figure 5-21.** In-situ FTIR spectra recorded after 5 Torr $NO_2$ (g) dosage at 323 K for 10 min on fresh $LaMnO_3$ [105]..... 104

**Figure 6-1.** XRD patterns of the catalysts prepared via CCR protocol of the IWI method. ..... 107

**Figure 6-2.** XRD patterns of the catalysts prepared via CCR protocol of the IWI method which were also additionally promoted with either 5 wt.% $La_2O_3$ or 5 wt.% $CeO_2$. ..... 109

**Figure 6-3.** XRD patterns of the catalysts prepared via RR protocol of the IWI method. ..... 110

**Figure 6-4.** XRD patterns of the catalysts prepared via RR protocol of the IWI method which were also additionally promoted with either 5 wt.% $La_2O_3$ or 5 wt.% $CeO_2$. ..... 110

**Figure 6-5.** (a) HRTEM image, (b) HAADF-STEM image, and (c) EDX spectrum of the area labeled as 1 in (b) of the 5Ir/L3-CCR catalyst synthesized via IWI. ..... 112

**Figure 6-6.** HRTEM image of the 5Ir/TH100-CCR catalyst synthesized via IWI. ..... 112

**Figure 6-7.** HRTEM images of the 5Ir/Sir10-CCR catalyst synthesized via IWI. ..... 113

**Figure 6-8.** (a) HRTEM image, (b) HAADF-STEM image, and (c) EDX spectrum of the region labeled as 1 in part (b) of the 5Ir/Sir20-CCR catalyst synthesized via IWI. ..... 113

**Figure 6-9.** (a-b) HAADF-STEM images, and (c) EDX spectrum of the region labeled as 1 in part (b) of the 5Ir/Mg5-CCR catalyst synthesized via IWI. ..... 114

**Figure 6-10.** (a-b) HAADF-STEM images, and (c) EDX spectrum of the region labeled as 1 in part (b) of the 5Ir/Ce20-CCR catalyst synthesized via IWI..... 114

**Figure 6-11.** (a) HRTEM image, (b) HAADF-STEM image, and (c) EDX spectrum of the region labeled as 1 in part (b) of the 5Ir/5La/L3-CCR catalyst synthesized via IWI. .... 115

**Figure 6-12.** HRTEM images of (a) 5Ir/L3-RR, (b) 5Ir/TH100-RR and (c)5Ir/Sir10-RR catalysts synthesized via IWI. ..... 116

**Figure 6-13.** Average $T_{Onset}$ values obtained in the anaerobic catalytic decomposition tests for ADN mixture with the synthesized catalysts via IWI and without a catalyst obtained during the custom-design micro propulsion batch reactor experiments. ..... 118

**Figure 6-14.** Average ΔP values obtained in the anaerobic catalytic decomposition tests for ADN mixture with the synthesized catalysts via IWI and without a catalyst obtained during the custom-design micro propulsion batch reactor experiments. ..... 118

**Figure 6-15.** Gas-phase FTIR spectra obtained for catalytic and non-catalytic decomposition of ADN mixture at the corresponding $T_{Onset}$ values. ..... 121

**Figure 6-16.** Gas-phase FTIR spectra for the thermal ADN decomposition products as a function of temperature. ..... 121

**Figure 6-17.** Gas-phase FTIR spectra for the catalytic ADN decomposition products as a function of temperature for (a) 5Ir/TH100-CCR and (b) 5Ir/TH100-RR synthesized via IWI. ..... 122

**Figure 6-18.** Gas-phase FTIR spectra for catalytic ADN decomposition products as a function of temperature for (a) 5Ir/L3-CCR and (b) 5Ir/L3-RR synthesized via IWI. ... 122

**Figure 6-19.** Gas-phase FTIR spectra for catalytic ADN decomposition products as a function of temperature for (a) 5Ir/Sir10-CCR and (b) 5Ir/Sir10-RR samples synthesized via IWI. ..... 123

**Figure 6-20.** SSAs for the synthesized catalysts via IWI. ..... 124

**Figure 6-21.** Ir particle size distribution for (a) 5Ir/TH100-RR, (b) 5Ir/L3-RR, and (c) 5Ir/Sir10-RR synthesized via IWI. ..... 125

**Figure 6-22.** Williamson-Hall plots for (a) 5Ir/TH100-CCR, (b) 5Ir/L3-CCR, and (c) 5Ir/Sir10-CCR samples synthesized via IWI. ..... 126

**Figure 6-23.** In-situ FTIR spectra for the synthesized CCR and RR catalysts via IWI upon CO adsorption at (a-b) 0.01 Torr, (c-d) 60 Torr. (e) Schematic representation of CO vibrational features observed for the CCR and RR catalysts. ..... 128

**Figure 6-24.** In-situ FTIR spectra corresponding to the stepwise CO adsorption at RT on (a) 5Ir/TH100-CCR, (b) 5Ir/L3-CCR, (c) 5Ir/Sir10-CCR, (d) 5Ir/TH100-RR, (e) 5Ir/L3-RR, (f) 5Ir/Sir10-RR samples synthesized via IWI. ..... 129

**Figure 6-25.** (a) In-situ FTIR spectra for pyridine adsorption on synthesized catalysts via IWI (b) the detailed view of 1588-1591 $cm^{-1}$ signals. ..... 132

**Figure 6-26.** (a) ATR spectrum of ADN/water mixture, (b) ATR spectrum of ADN adsorbed on synthesized catalysts via IWI, (c) the detailed view of the 1523 $cm^{-1}$ signal, (d) FTIR intensities of the 1523 $cm^{-1}$ IR signal shown in part (c). ..... 133

**Figure 6-27.** Ir 4f XPS data 5Ir/TH100-CCR, 5Ir/L3-CCR, 5Ir/Sir10-CCR, 5Ir/TH100-RR, 5Ir/L3-RR, and 5Ir/Sir10-RR. ..... 134

**Figure 6-28.** Integrated relative CO-TPD desorption signals and Ir surface dispersion values obtained from CO chemisorption experiments for the investigated catalysts synthesized via IWI with identical masses. ..... 135

**Figure 6-29.** CO TPD profiles for synthesized materials via IWI obtained after 5 Torr CO adsorption..... 136

**Figure 6-30.** EXAFS results for metallic Ir foil $L_{III}$ edge given with best fit results in the form of (a) Fourier-transform (FT) of the $k^2\chi(k)$ and imaginary part (Im[$\chi(R)$]) of the $\chi(R)$ spectra, (b) normalized XANES data for Ir $L_{III}$ edge..... 138

**Figure 6-31.** In-situ EXAFS data obtained (a-d) after the final reduction step of the catalyst preparation protocol via IWI and (e-h) consecutive exposure of these catalysts to $O_2$ flow (see text for details). (i-l) Corresponding Ir $L_{III}$ edge XANES data for the experiments shown in parts (a-h). ..... 139

# List of Tables

**Table 1-1.** SSA of the materials synthesized by Maleix et al. [104]. Copyright (2017) American Institute of Aeronautics and Astronautics ..... 21

**Table 2-1.** Abbreviations of the alumina support materials utilized in the current work. 45

**Table 2-2.** Synthesis conditions for the 5 wt. % Ir catalysts synthesized via IWI method. ..... 51

**Table 2-3.** Promoter and support amounts used in the IWI method. ..... 52

**Table 2-4.** Synthesis conditions for the La and Ce promoted samples synthesized via IWI method..... 53

**Table 3-1.** Crystalline phases and SSAs for different alumina types used in catalyst synthesis after calcination at 550 °C and 1100 °C. ..... 73

**Table 4-1.** $T_{Onset}$ and $\Delta P$ values of STY-126-X ADN mixtures measured with SBa200 alumina (in the absence of any catalytically active sites) in the custom-design micro propulsion batch reactor. ..... 77

**Table 5-1.** Surface atomic percentages of the elements obtained via XPS on the catalysts prepared via WI method..... 92

**Table 6-1.** Composition of the catalysts synthesized via IWI based on XRF measurements. ..... 124

**Table 6-2.** Parameters used for Ir dispersion calculations. ..... 136

**Table 6-3.** EXAFS best fitting parameters for the Ir $L_{III}$ edge of the 5Ir/L3-CCR, 5Ir/Sir10-CCR, 5Ir/L3-RR and 5Ir/Sir10-RR samples synthesized via IWI. ..... 140

# CHAPTER 1

## 1. INTRODUCTION

Satellites play an important and strategic role in today's communication and defense technologies. In the past, satellites were used mostly in military applications, however nowadays, they are also widely used for civilian purposes [1]. Satellites have many functions in telecommunication, intelligence, weather forecast, and space science applications. Upon placement of a satellite into the orbit, satellite's position and orientation corrections are done by small thrusts generated in the propulsion engines. These thrusts are created by the so called "propellants". Propellants are energetic compounds that can undergo rapid combustion/decomposition resulting in the production of large volumes of hot gases [2].

Propellants can be divided into three major categories as solid, liquid, and hybrid propellants. Solid propellants are typically composed of a fuel and an oxidant in powder form which are pressed together to form a pellet [3]. Once the solid propellant is chemically activated, triggered exothermic reaction continues until all the solid propellant is consumed. Hence, the amount of thrust cannot be readily controlled or stopped. On the other hand, fuel and oxidant co-existing in a liquid propellant can be placed in an external tank allowing the controlled injection of the liquid propellant into the combustion chamber for ignition and regulation of the generated amount of thrust. Solid and liquid propellants have their own advantages and disadvantages [4]. For example, motor design and construction for solid propellant rockets are much simpler and cheaper than their liquid propellant counterparts as the latter require additional fuel tank, valves and pumps [4]. Total weight and size of the propulsion system for liquid propellant rockets are also greater than that of the solid

propellant rockets. On the other hand, specific impulse ($I_{sp}$) is higher for liquid propellants than solid ones [4]. Moreover, synthesis routes and the exhaust products of solid propellant decomposition are typically more toxic than that of the liquid propellants [4]. The third type of propellants are hybrid propellants. Hybrid propellants consist of solid fuel and a liquid oxidizer. Solid fuel is vaporized by using an ignition system and high pressure of fuel is generated in the combustion chamber [5]. With the injection of oxidizer to the chamber, ignition starts and the thrust is generated. Hybrid propellants actually combine the advantages of the solid and liquid propellants such as start-stop capability.

Liquid propellants can be also classified into two sub-categories as monopropellants and bipropellants [6]. Monopropellants do not contain a secondary oxidizer, while bipropellants consist of an oxidizer and a fuel component. The distinction between monopropellants and bipropellants is made by the number of components injected into the engine for the combustion of the propellant. Monopropellants, which can consist of a single chemical or a mixture of several chemicals, are injected into the engine as a single formulation. In the bipropellant engine, fuel and oxidizer are injected or atomized into the combustion chamber as two separate formulations before combustion or decomposition process [7]. Bipropellants generally offer higher specific impulse than monopropellants [6]. Therefore, bipropellant systems are more efficient than monopropellant systems, but more complex and costly due to the need for extra hardware components on the satellite [6,8].

### 1.1. Monopropellants

The simplicity, reliability and low cost are the major priorities in monopropellant systems which are used when the total required thrust is low. Hydrazine, $N_2H_4$, one of the most common monopropellant used in space vehicles since 1960, maintains the orbit and

trajectory control of the satellites in low earth orbit [9,10]. However, hydrazine possesses significant health risks due to its high toxicity and carcinogenic nature [11]. In addition, storage, transport, refilling, and testing of hydrazine require not only complex but also costly processes and infrastructure. Accordingly, European Union (EU) Registration, Evaluation, Authorization and Restriction of Chemicals (REACH) regulation included hydrazine to the list of chemicals to be prohibited in the future by the European Chemicals Agency (ECHA) [12,13]. Along these lines, both National Aeronautics and Space Administration (NASA) and European Space Agency (ESA) declared interest in safe, high-performance, long-lasting, and environmentally friendly fuel alternatives called "Green Propellants" that can replace hydrazine in the future [14].

Ionic liquids (ILs) are used in many green technological applications [15]. Ionic liquid is a salt with a low melting point (i.e., $\leq 100$ ° C) consisting of an organic / inorganic cation and anion pair. Over the last decade, IL's have been widely used in innovative applications such as catalysis, separation, sensors, solid state physics, etc. due to their unique properties such as low vapor pressure, liquidity within a wide temperature range, high thermal stability, ionic conductivity, structural designability, adjustable viscosity / density / gas permeability [15]. Energetic Ionic Liquids (EILs) typically have high nitrogen and oxygen content, making them potentially useful in propulsion systems [8]. The unique properties of ionic liquids such as low melting point, wide pressure-temperature ranges within which they can stay as liquids, low viscosity and high thermal stability, make these materials a good alternative to traditional energetic materials. Furthermore, EILs usually have very low volatility reducing the evaporation-based material loss and vapor-based toxicity. In addition, storage, transportation and processing of EILs are safe, easy, and cost-effective.

Due to the reasons mentioned above, the use of EILs in satellite propulsion systems is a promising alternative as compared to the conventional propellant, hydrazine. The most preferred EIL formulations in such applications are hydroxylammonium nitrate (HAN), ammonium dinitramide (ADN), hydrazinium nitroformate (HNF), and ammonium nitrate (AN) [16]. **Figure 1-1** shows the molecular structures of these fuels. From the performance standpoint, the most active fuels are reported to be HAN and ADN [12,16–20].

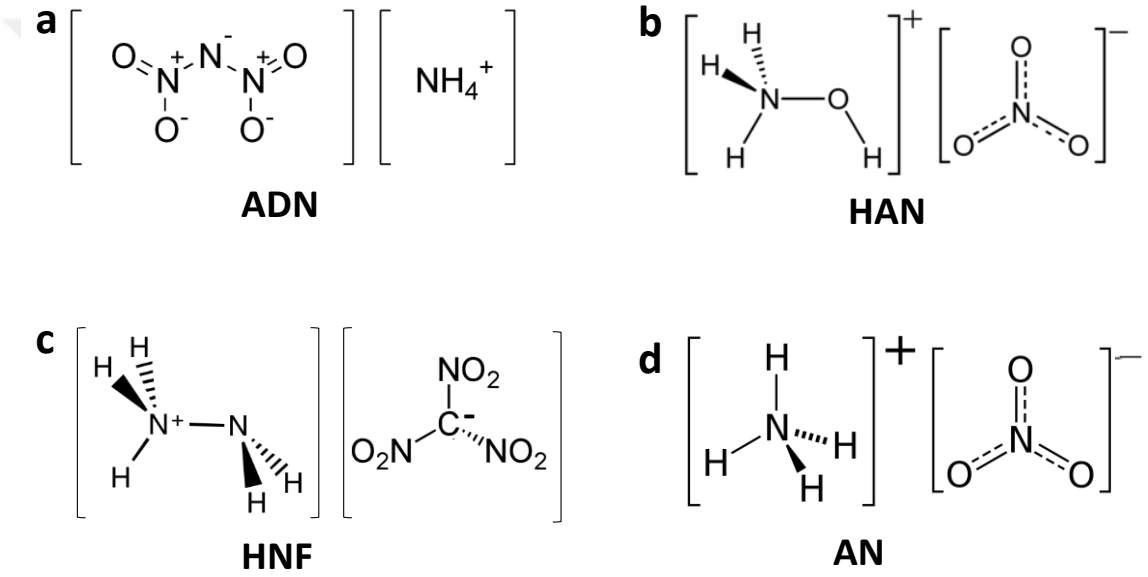



***Figure 1-1.*** *Molecular structures of ionic liquids used as monopropellants: a) ADN, b) HAN, c) HNF, and d) AN.*

### 1.1.1. HAN Propellants

HAN is a salt obtained from hydroxyl amine and nitric acid. It is a colorless solid with a high hygroscopicity. The melting temperature of HAN is 48 °C and is thermally stable up to 140 °C, depending on its purity [8]. The polar character of HAN makes it soluble in water and its solubility in water at 20 ° C is reported to be 95 wt. % [16]. This makes HAN a suitable candidate as a liquid propellant. The amount of energy release, adiabatic combustion

temperature, and physical-chemical properties of many propellants can be changed by tuning the amount of water in the fuel formulation [21]. AF-M315E is a HAN based propellant developed by the U.S. Air Force Research Laboratory in 1998. It has been used and tested as an alternative to hydrazine in the Green Propellant Infusion Mission (GPIM) program [22,23]. AF-M315E fuel consists of 44.5 wt. % HAN, 44.5 wt.% hydroxylethylhydrazine (HEHN), and 11 wt.% water [24]. Specific impulse and density of HAN is higher than that of hydrazine by 13 % and 63 %, respectively [25]. HAN fuels are currently being developed and used by NASA and are expected to be used in satellite propulsion systems in the medium term [26]. Such systems require combustion chambers and catalysts with high thermal durability. The other commercial HAN based fuel developed by Institute of Space and Astronautical Science (ISAS)/(JAXA) is called SHP163, which is composed of 73.6 wt.% HAN, 3.9 wt.% AN, 16.3 wt.% methanol, and 6.2 wt.% water [25]. Although HAN-based fuels have many advantages in terms of transportation, storage and human health, the adiabatic combustion temperature is around 1900 °C which is unfavorably high as compared to hydrazine with an adiabatic combustion temperature of only 900 °C [24,25].

### 1.1.2. ADN Propellants

ADN is a white-yellowish solid salt consisting ammonium cation ($NH_4^+$) and dinitramide anion ($N(NO_2)_2^-$) [27]. The melting temperature of ADN is 93 °C and its density is in the range of 1.80-1.84 g/cm$^3$ at 25 °C. Due to its high hygroscopicity, ADN solid tends to liquefy under high humidity and the ADN structure decomposes. Therefore, in the environment where ADN solid is present, the critical relative humidity value of 55.2% at 25 °C should not be exceeded [28]. Also, due to the photosensitive dinitramide anion, ADN needs to be protected from direct sunlight [8]. Complete thermal decomposition of ADN occurs at 200 °C

[29]. ADN has a high density, high positive oxygen balance (degree of oxidation of the explosive) and high solubility in water, therefore ADN-based ionic liquid fuels are promising candidates for aerospace applications.

There are many ADN fuel mixtures studied in the literature, with different fuel types and different ADN/water/fuel ratios. The most well-known of these AND fuel formulations are the LMP-103S and FLP-106 formulations produced by FOI, ECAPS, and EURENCO. Both fuels are non-toxic and suitable to be used in satellite propulsion systems. FLP-106 (FOI Liquid Fuel No:106) developed by FOI is an energetic ionic liquid containing 64.6 wt.% ADN, 23.9 wt.% water and 11.5 wt.% hydrocarbon fuel (F-6) [16,27].

LMP-103S is a storable liquid monopropellant developed in 1997 by the Swedish Space Corporation and the Swedish Defense Research Agency [30]. LMP-103S propellant consists of 63.0 wt.% ADN, 14.0 wt.% water, 18.4 wt.% methanol, and 4.6 wt.% ammonia. The evaporation of the components in the formulation, except ADN, results in solvent loss and consequently the change in the fuel content (ADN salt does not have a significant vapor pressure in its pure solid form when the solvent is absent). When the solution becomes saturated, solid ADN crystals begin to form in the liquid solution. For this reason, it is necessary to keep the fuel in a closed storage environment in order to maintain the physical properties of the ADN fuel including the propellant performance [30]. For the first time, LMP-103S fuel was used with hydrazine in the satellite PRISMA, which was sent into space in 2010 and was successfully tested during the satellite mission. LMP-103S fuel is also currently being used in satellites called Sky-Sat [19].

Limitations of ADN fuel were discussed extensively in the literature [19,31]. As in the case of HAN, the adiabatic combustion temperature of ADN is considerably higher than that of

hydrazine, and this value has been reported to be 1630 °C. For this reason, ADN systems require the use of expensive reactor housing materials with high temperature resistance. Another limitation of ADN-based thrusters is the so-called "cold start" requirement. For LMP-103S to activate, the catalyst must be preheated to 350 °C, and if the catalyst does not reach this temperature, combustion is not complete [31]. In contrast, hydrazine systems do not have the "cold start" problem allowing ignition without preheating. However, preheating is also often used in hydrazine propellants to extend the catalyst life [31–33].

### 1.2. Catalytic Systems

Monopropellants decompose both thermally (i.e., without the presence of a catalyst) and also catalytically. However, decomposition occurs much more efficiently and at lower temperatures in the presence of a catalyst. There are two different catalyst systems developed for hydrazine-based thrusters and they have been used safely in satellites for many years [34,35]. The first of these catalysts is the Shell 405 (S-405) catalyst produced by the Shell Development Company, USA [34,36]. The other is the H-KC12GA catalyst produced by the German company Heraeus [35]. The content of these two catalysts is quite similar and consist of 31-33 wt.% Ir active site and $Al_2O_3$ support material. It has been reported in the literature that only glycine-based HAN formulations (HANGLY26) show sufficient thermal catalyst stability and compatibility with Shell-405 catalyst [8]. For this reason, it is important to design and develop a new generation of thermally stable/durable/long-life catalysts. Catalysts to be designed for catalytically controlled combustion of EILs should have the following characteristics [37]:

1) The catalyst must trigger the decomposition of the monopropellant at low temperatures and this temperature must be lower than the propellant's own thermal decomposition temperature.

2) Nitrogen oxide (NO, $NO_2$, $N_2O$) formation during thermal decomposition must be limited for enhanced thrust.

3) At high temperatures, the catalyst must maintain its thermal stability and SSA.

4) During the flow of the propellant over the catalyst, loss of active sites in the catalyst should be prevented.

The most commonly used catalysts for the ADN and HAN decomposition reactions are metal-loaded aluminas and hexaaluminates [17,18,46–49,38–45]. These catalysts have two different components which are the support material and the active material. While the support material disperses the active material; active materials are involved in the efficient and sustainable decomposition of the fuel. Properties of the active material depend on the type of the precursor, type of the support material and introduction method of the active metal precursor which leads to different active phase-support interactions [50].

### 1.2.1. Support Materials

#### 1.2.1.1. Al-based Support Materials

Al-based support materials are one of the most commonly used type of support materials utilized in catalytic applications. **Figure 1-2** shows four different forms of Al-based support materials [51–53]. Transitional aluminas, which are the most preferred alumina structures in catalytic applications, can be also obtained via dehydration of AlOOH and $Al(OH)_3$ (**Figure 1-3**).

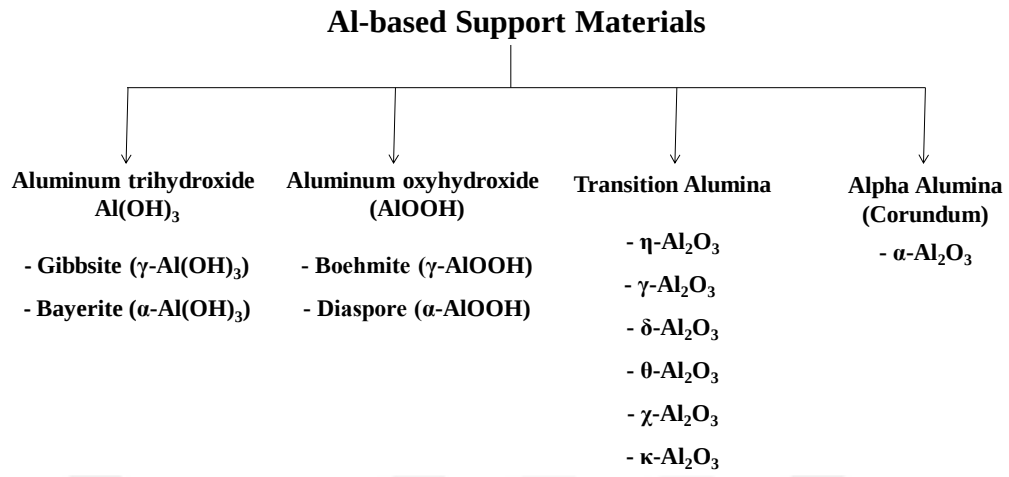



***Figure 1-2.*** *Different forms of Al-based support materials.*

Alumina support materials should show high thermal stability to be utilized in high temperature applications such as catalytic decomposition of hydrocarbons at high temperature, steam reforming of methane or catalytic decomposition of propellants in space applications [52,54–56]. Boehmite (AlOOH), is one of the most commonly preferred high SSA alumina precursors in catalytic applications. Upon calcination, boehmite is oxidized to form transitional aluminas leading to the following alumina phase transitions $\gamma \rightarrow \delta \rightarrow \theta \rightarrow \alpha$ shown in **Figure 1-3** [52,53]. During these phase transitions, the specific SSA (SSA) monotonically decreases (**Figure 1-4**) along with the porosity and the average pore size. α-$Al_2O_3$ (corundum) is thermodynamically the most stable phase of alumina [52,53,57].

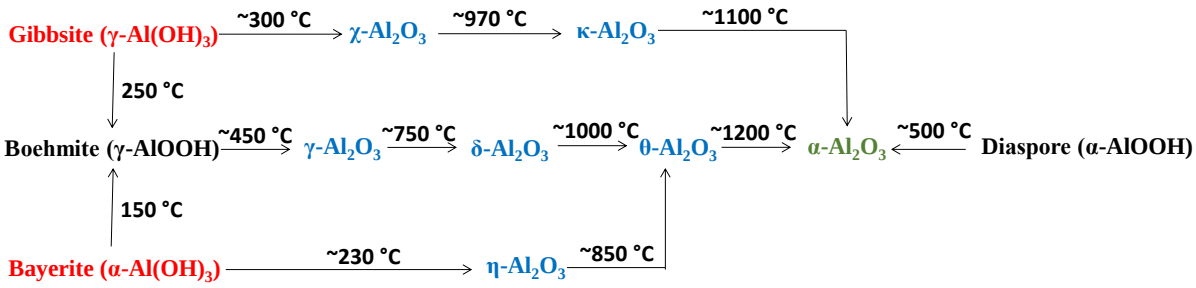



***Figure 1-3.*** *Temperature-dependent phase transformations of alumina materials* [53]. *Copyright (2014) Elsevier*

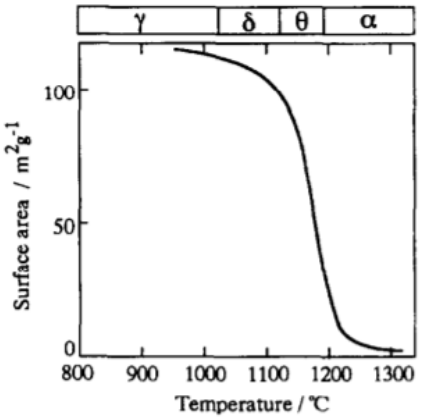



***Figure 1-4.*** *Changes of SSA of alumina with temperature under atmospheric pressure* [52]. *Copyright (1996) Elsevier*

Numerous studies exist in the literature on improving the thermal stability of alumina. Among these studies, some of the most effective results have been obtained by doping various elements into the alumina structure [37,41,64–67,52,54,58–63]. Doping different elements into the alumina structure not only increases the thermal stability but also alters the surface chemistry of the support materials [52,68].

#### 1.2.1.1.1. Thermal stability of alumina upon doping

Sintering process of oxide supports is a thermodynamically favorable process. Therefore, the most suitable method for stabilization of the alumina phase is to suppress the sintering kinetically with the help of dopants in order to hinder the construction of ordered phases [52]. It has been reported that the addition of metal and metal oxides containing Zr, La, Si, Ba, Sr, Ca, K, Li, Ce into alumina has a positive effect on the SSA, among which Si and La are the most promising ones [52].

In the studies of Shaper et al., SSA of pure $Al_2O_3$ and 5 mol% La doped $Al_2O_3$ calcined at 1100 °C were compared [66]. SSA of the La containing material was found to be 50 $m^2/g$, while the SSA of pure $Al_2O_3$ was less than 10 $m^2/g$. A five-fold increase in SSA was achieved

with La addition into the alumina phase [66]. Li et al. worked on the propane oxidation over $Pd/Al_2O_3$ and $Pd/La/Al_2O_3$ [69]. $Pd/Al_2O_3$ catalysts had a SSA of 60 $m^2/g$, whereas 5 wt.% La loading into alumina structure led to 82 $m^2/g$ SSA at 1100 °C [69]. Chen et al. also studied the thermal stability of the alumina after 3 mol% La-doping [70]. $Pd/La/Al_2O_3$ had a SSA of 51.6 $m^2/g$ which was 5 times higher than that of $Pd/Al_2O_3$ (4.46 $m^2/g$) at 1100 °C. The reason for the high thermal stability of La doped alumina was investigated by Oudet et al. [62]. Formation of $LaAlO_3$ species was reported to hinder the Al diffusion and suppress $\alpha$-$Al_2O_3$ formation.

Si doping can also be an effective strategy to increase the thermal stability of alumina. Xu et al. worked on the effect of Si addition into the alumina structure.[71] It was noted that after calcination at 1000 °C, 12 wt. % $Si/Al_2O_3$ had a SSA of 351 $m^2/g$ while pure alumina had SSA of 124 $m^2/g$. Osaka et al. also investigated the thermal stability of alumina with different loadings of Si (0 wt%, 2.5 wt%, 5 wt%, and 10 wt%) [72]. **Figure 1-5** illustrates that the SSA of undoped alumina material decreases drastically with increasing temperature and yielding a value below 4 $m^2/g$ at 1200 °C. On the other hand, Si insertion into alumina matrix significantly enhances the SSA and even at 1400 °C, the SSA is observed to be higher than 4 $m^2/g$.

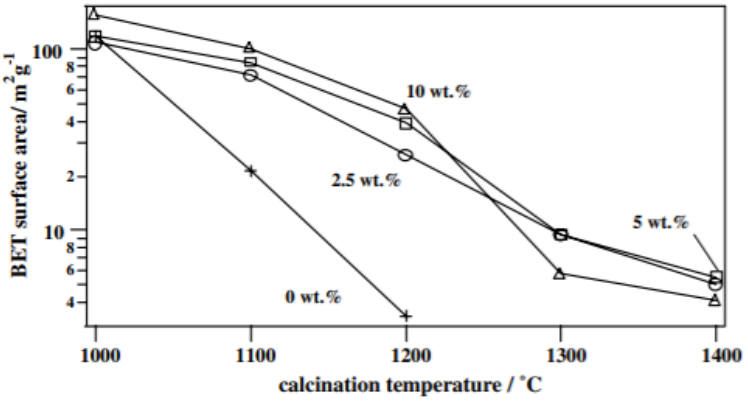



***Figure 1-5.*** *Changes of the SSA with increasing temperature for 0 wt%, 2.5 wt%, 5 wt% and 10 wt% Si containing aluminas* [72]*. Copyright (2007) Elsevier*

#### 1.2.1.1.2. Surface properties of the alumina upon doping

Surface Al-OH groups and coordinately unsaturated (cus) $Al^{3+}$ cationic sites make the γ-$Al_2O_3$ materials a good support and a good catalyst [73]. Hydroxyl groups on alumina generate weak Bronsted acid sites, whereas the cus $Al^{3+}$ sites are responsible for the Lewis acid properties of alumina [74]. The surface acidity of the alumina materials can be tuned via doping different elements in its structure [68]. La increases the basicity of alumina whereas Si makes the surface more acidic. Yamamoto et al. investigated the surface properties of rare earth metal doped alumina [75]. According to their studies, La species preferentially picked the Lewis acid sites of γ-$Al_2O_3$ causing a decrease in the strength of the Lewis acid sites as compared to γ-$Al_2O_3$. Moreover, the strength of the basicity of La-doped alumina materials can be adjusted by changing the calcination temperature. Surface basicity decreases with increasing temperature [76]. Stoyanovskii et al. studied the effect of La addition onto the alumina structure and Rh active sites in Rh/La/$Al_2O_3$ systems [77]. They observed that although the concentration of basic sites on alumina is higher compared to its lantana doped counterpart, the strength of the basic sites on La-$Al_2O_3$ is stronger than the pure alumina. Si doping leads to different trends as compared to La doping. For low Si loadings, the number of Lewis acid sites decreases slightly starting from the strongest sites, however the strength of the acidic sites increases as a result of inductive effects created by Si atoms [78]. Daniel et al. observed that upon Si doping up to 30 wt. % into alumina creates stronger Lewis acid sites than bare alumina via substitution of $Al^{3+}$ sites with $Si^{4+}$ and weak Bronsted acid sites resulting from bridging OH groups [79]. There are also high strength Bronsted acid sites in silica-alumina materials. The OH groups on $Si^{4+}$ sites which are in a close proximity to $Al^{4+}$ creates strong Bronsted acidity as shown in **Figure 1-6** [80]. However, at lower loadings of Si,

i.e., 1.5 wt.%, strong Bronsted acidity disappears and the surface behaves mostly like undoped alumina [78].

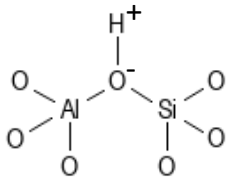



***Figure 1-6.*** *Strong Bronsted acid sites in silica-alumina materials* [80].

Catalytic active sites, their electronic properties and stability are also affected by the surface properties of alumina [69,77,81]. Doping different elements into alumina structure may change the acidity of the support material and induce an electronic effect on the active sites which is also called the strong metal support interaction (SMSI). [82,83]. SMSI not only changes the electronic properties of the active sites but also induces geometric modifications on the active sites and the support [84].

The interaction between support and active material can be either weak or strong as shown in **Figure 1-7**. The gray region in **Figure 1-7** is the reactive interface showing the degree of interaction between the metal center and the support material. At reactive interfaces, new bonds are formed between the metal and the support, where the electron transfer takes place. Hence, the electronic properties of the active metal center change. In the case of weak metal support interaction (WMSI), electronic properties of the metal remain unchanged.

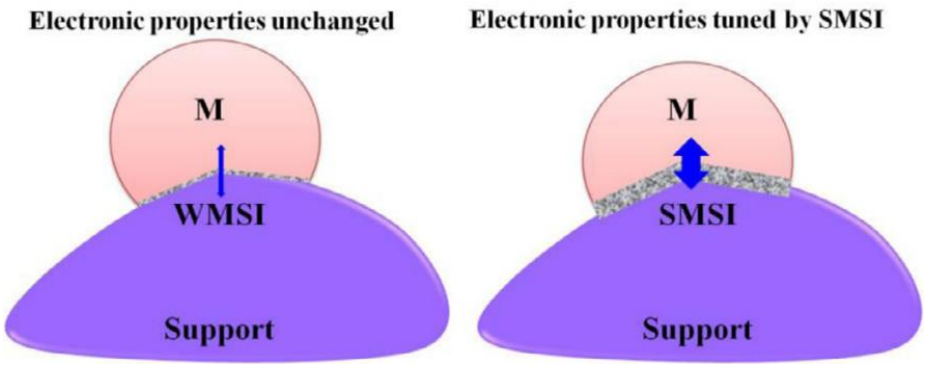



***Figure 1-7.*** *Electronic effects observed for weak metal support interaction (WMSI) and strong metal support interaction (SMSI)* [84]*. Copyright (2017) Elsevier*

Geometric effects, as a result of SMSI process, occur via partial/complete encapsulation/decoration of the active metal centers by the support material due to the reduction of the support (**Figure 1-8a**) [84]. The morphology of the metal particles may also change as shown in **Figure 1-8b**. Metal particles can be flattened and stabilized on the support so that the number of uncoordinated metal sites diminishes and the total surface free energy is minimized [84,85]. However, flattening via SMSI is generally valid for small metal clusters which have stronger and more extensive contact with the support surface.

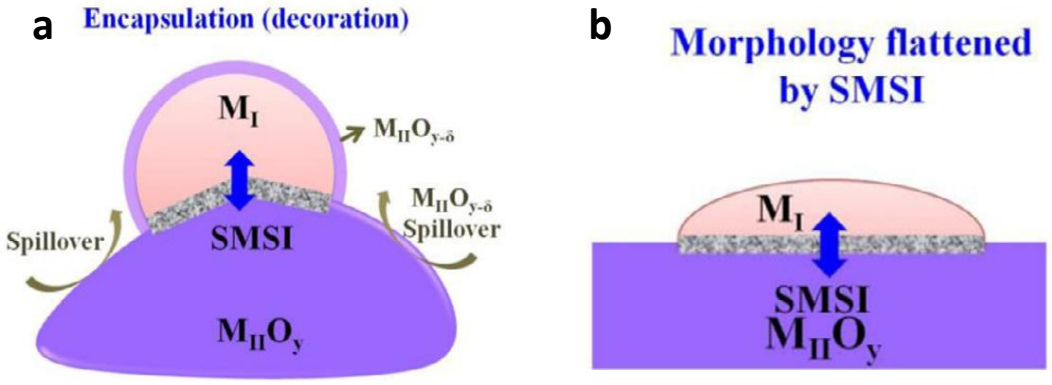



***Figure 1-8.*** *Geometric effects in strong metal support interaction* [84]*. Copyright (2017) Elsevier*

For Rh/La/$Al_2O_3$ catalyst, Rh species are preferentially located on lantana domains resulting in enhanced stability against thermal aging via SMSI [77]. On the other hand, Rh particles in La-free sample diffuse into alumina matrix during calcination at 1000 °C and are encapsulated inside the alumina structure with the formation of α-$Al_2O_3$. In the Gaudet et al.'s study, effect of La addition to alumina on Pd species were investigated by comparing the CO oxidation capability of Pd/$Al_2O_3$ and Pd/La/$Al_2O_3$ [86]. Pd particles on La-containing catalyst were smaller than the La-free counterpart. Pd/$Al_2O_3$ adsorbed CO on 3-fold Pd sites suppressing $O_2$ adsorption leading to the self-poisoning of the catalyst (**Figure 1-9)**. On the other hand, on the Pd/La/$Al_2O_3$ sample CO poisoning of the Pd-sites were not observed which yielded higher activity for CO oxidation. The reason for this behavior was argued to be associated with the Pd species created on the La-Al surface which behaved differently than the Pd on bare Al.

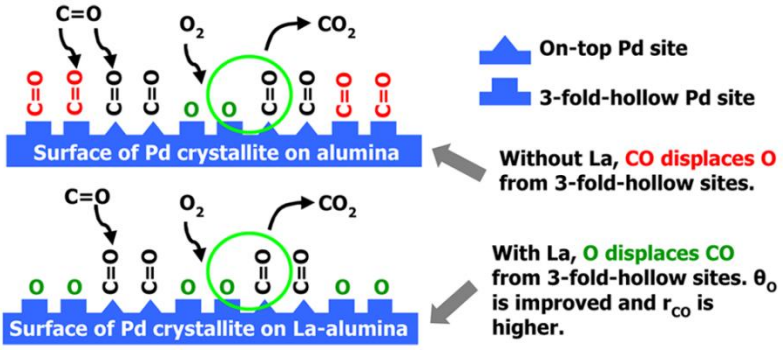



***Figure 1-9.*** *Schematic representation of CO adsorption and oxidation over Pd/$Al_2O_3$ and Pd/La/$Al_2O_3$ in CO oxidation with $O_2$ [86]. Copyright (2017) American Chemical Society*

Li et al investigated the thermal aging of the Pd/La/$Al_2O_3$ catalyst [69]. Upon cooling, basic supports favored PdO formation around metallic palladium which prevented the sintering of Pd particles (**Figure 1-10**). Moreover, La affected the electronic nature of Pd with the

formation of special electron-rich $PdO_{1-x}$ species. These Pd species were responsible for the high activity in propane oxidation.

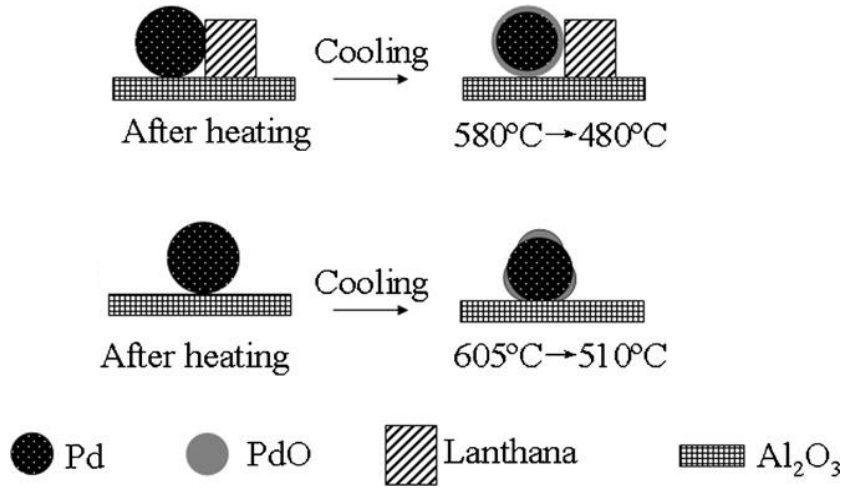



***Figure 1-10.*** *Schematic representation of Pd and PdO on La-$Al_2O_3$ and $Al_2O_3$* [69]*. Copyright (2013) Elsevier*

Zhao et al. studied the single site Pt catalysis over $Pt/Al_2O_3$, $Pt/SiO_2$ and $Pt/Si\text{-}Al_2O_3$ [87]. According to their studies, highly stable Pt single sites were only formed on the $Pt/Si\text{-}Al_2O_3$ sample having special $Al^v$ sites. These alumina sites also led to strong SMSI between Pt and $Si\text{-}Al_2O_3$ support material. On the other hand, Pt particles were in the form of nanoparticle for $Pt/Al_2O_3$ and $Pt/SiO_2$ materials lacked any $Al^v$ sites.

#### 1.2.1.2. Hexaluminates

Hexaaluminates are promising materials for catalytic reactions at high temperatures [88–93]. The hexaaluminate structure is made of $\gamma\text{-}Al_2O_3$ spinel blocks containing large cations (Ba, Ca, La and Sr) as shown in **Figure 1-11** [52].

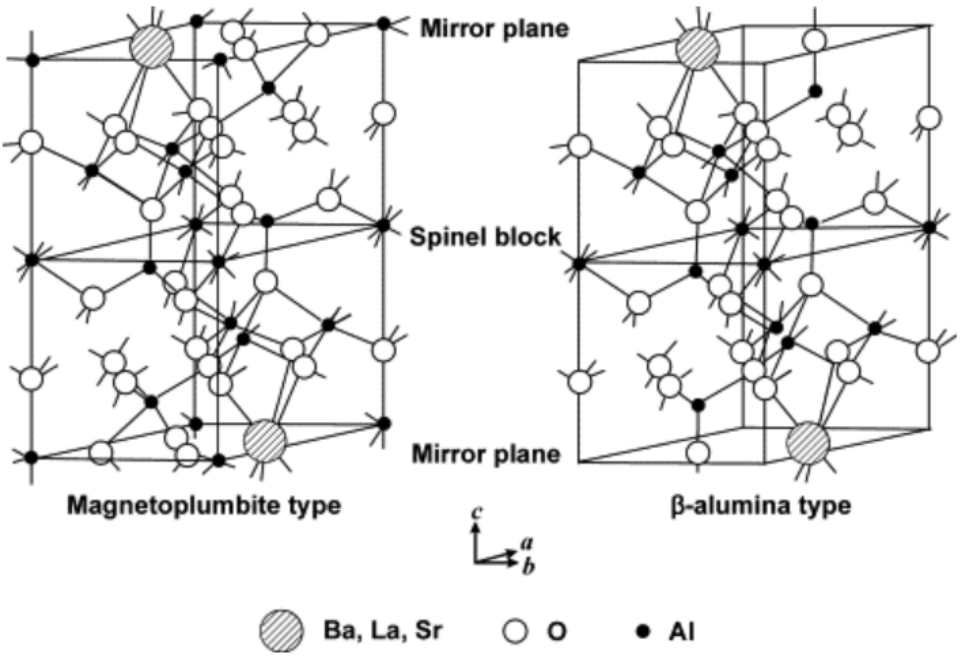



***Figure 1-11.*** *Hexaaluminate crystal structure [52]. Copyright (1996) Elsevier*

Tian et al. worked on La and Ba hexaaluminates in the form of $LaMn_xAl_{(12-x)}O_{19}$ and $BaMn_xAl_{(12-x)}O_{19}$ [88]. It was shown that barium containing hexaaluminates had much higher activity for the decomposition of $N_2O$ propellant as compared to hexaaluminates containing La. Ba-containing hexaaluminates were more resistant to thermal aging. Another example to hexaaluminate support materials used in the high temperature applications is SLMA ($Sr_{0.8}La_{0.2}MnAl_{11}O_{19}$) and SBLMA ($Sr_{0.3}Ba_{0.5}La_{0.2}MnAl_{11}O_{19}$) type materials [94]. Upon heating these materials from 1200 °C to 1300 °C, the decrease in the corresponding SSA values were 80% and 38% for SLMA and SBLMA, respectively. SBLMA had a higher SSA and a greater thermal stability than SLMA at high temperatures. This high thermal stability was attributed to the incorporation of barium into the SLMA structure which suppressed the collapse of the hexaaluminate structure at elevated temperatures leading to higher SSA of the material [52,94].

### 1.2.2. Catalytic Active Sites

Platinum group metals (PGM) are commonly used as active sites in catalyst formulations while metals such as Cu, Co, Zn, Fe, La, Ce are often used as co-catalysts or promoters. Among other PGM, Ir and Pt are the most frequently preferred active sites in aerospace applications [37,42,93,95–98]. Ir is also widely used in high temperature applications due to its high melting point and high Tammann temperature [99–102].

Courtheoux et al. investigated the effect of Pt active sites in Pt/Si-$Al_2O_3$ during HAN decomposition [103]. Three different Pt types of particles were reported on this catalyst. Namely; (i) Pt particles on alumina support, (ii) Small Pt particles on silica, (iii) Pt aggregates over alumina support. The catalyst showed stable activity up to 4000s during several catalytic performance tests (16 injections of fuel over the catalyst). Under strong oxidizing conditions (during decomposition of HAN), the following observations were reported (**Figure 1-12**):

1) Platinum migration from silica to alumina led to the formation of platinum nanoclusters that accumulated on the alumina surface.

2) Platinum migrated to another platinum particle on silica, causing Pt particles to grow.

3) Large platinum nanoclusters were redistributed over the surface.

4) Stable platinum nanoclusters were associated with the preservation of the activity of the catalysts.

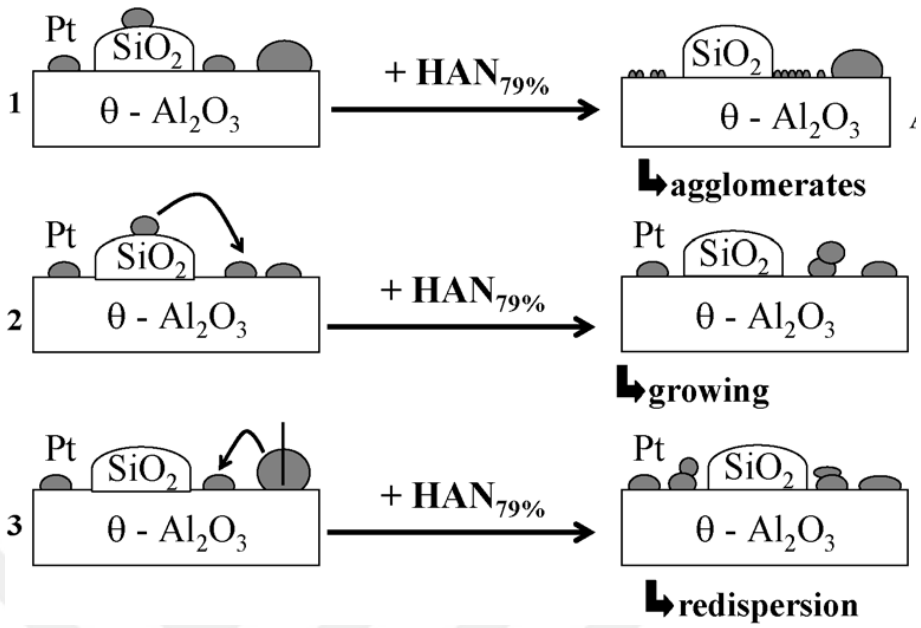



***Figure 1-12.*** *Behavior of Pt particles during HAN decomposition* [103]*. Copyright (1996) Elsevier*

Amrousse et al. investigated the decomposition of HAN and ADN monopropellant over Ir or Cu containing $La_2O_3/Al_2O_3$ support material [97]. 10 wt. % La-containing alumina support material was synthesized by the sol-gel method and the active metal addition was carried out by wetness impregnation. The synthesized catalysts were in the form of 10 wt.% Ir/10La-$Al_2O_3$ and 10 wt. % Cu/10La-$Al_2O_3$. La addition did not significantly affect the SSA of $Al_2O_3$ support material and the specific SSA of Ir and Cu containing catalysts were found to be 230 and 228 $m^2g^{-1}$, respectively. When the performance of the monopropellants was examined, it was observed that thermal decomposition of HAN caused higher energy release than ADN. On the other hand, decomposition temperature for ADN (113 °C) was lower than HAN (152 °C). The highest activity with low decomposition temperature, high reaction rate and high pressure for catalyst/monopropellant combinations were found for $HAN_{95\%}$: 10 wt. % Ir/10La-$Al_2O_3$ and for $ADN_{75\%}$: 10 wt. % CuO/10La-$Al_2O_3$.

Maleix et al. performed a detailed study on ADN (FLP106 and LMP103s) decomposition over PGM and Fe-Zn containing Si-$Al_2O_3$ support and Ir-based hexaaluminates [104]. The catalysts used in this study were as follows; Si-$Al_2O_3$ (DUS), Rh/DUS, Pd/DUS, Ir/DUS, Pt/DUS, Pt-Fe/DUS, Pt-Co/DUS, Pt-Ni/DUS, Pt-Cu/DUS, Pt-Zn/DUS, $BaAl_{12}O_{19}$(BHA), $LaAl_{11}O_{18}$ (LHA), Pt-Cu/BHA, $BaIr_{0.5}Fe_{0.5}Al_{11}O_{19}$ (BHIF), $BaIr_{0.5}Co_{0.5}Al_{11}O_{19}$(BHIC). SSA for some of these catalysts were given in **Table 1-1**. Thermal stability of Si-$Al_2O_3$ support material was very high at 1200 °C with a SSA of 92 $m^2/g$. However, the SSA value decreased drastically at 1500 °C. Ba-based hexaluminate had the highest SSA with value of 50 $m^2/g$ after calcination at 1500 °C. Ir addition was only performed onto the BHA support material. Lanthanum hexaaluminate, LHA, crystallized in perovskite structure, instead of a hexaaluminate structure, which led to a low SSA. The activities of these catalysts were measured in a fixed volume batch reactor and their performance was rated according to the catalytic decomposition temperature of ADN. Among the active metals, Pt was the most active one for decomposition of ADN based propellants and it reduced the decomposition temperature from 148 °C to 127 °C for FLP-106 and from 134 °C to 110 °C for LMP-103S. For this reason, Pt was selected as the active material to be tested with a second transition metal from the Fe-Zn group. The lowest activity was observed in Fe-containing bimetallic Pt-Fe catalyst. Ni or Zn did not show a significant difference in the attenuation of the decomposition temperature. Co addition did not alter the activity of LMP-103S decomposition. On the other hand, presence of Co in the catalyst system lowered the FLP-106 decomposition temperature by 14 °C. However, Cu addition to Pt showed improvement in both cases. Compared with the catalyst containing only Pt with that of bimetallic active sites, the Pt-Cu catalyst resulted in a 12 °C decrease in the decomposition temperature of

FLP-106 and a 5 °C decrease in that of LMP-103S. When the hexaaluminate containing Ir-Fe catalyst was examined, this catalyst reduced the decomposition temperature of FLP-106 by 37 °C, to that of LMP-103S by 6 °C. Ir and Fe exhibited very good activity on the hexaaluminate structure while exhibiting a low activity when impregnated on Si-$Al_2O_3$.

***Table 1-1.*** *SSA of the materials synthesized by Maleix et al.* [104]*. Copyright (2017) American Institute of Aeronautics and Astronautics*

| Sample | Thermal traitment | $a$ / $m^2$ $g^{-1}$ |
|---|---|---|
| DUS | 500 °C – 2 h | 379 |
| DUS | 1200 °C – 4 h | 92 |
| DUS | 1500 °C – 4 h | 3 |
| LHA | 1500 °C – 5 h | 7 |
| BHA | 1500 °C – 5 h | 50 |
| DUS - pellets | 600 °C – 2 h | 176 |
| DUS - pellets | 1600 °C – 2 h | < 0.1 |
| BHA - pellets | 600 °C – 2 h | 61 |
| BHA - pellets | 1600 °C – 2 h | 4 |
| BHIF | 1400 °C – 4 h | 6 |
| BHIC | 1400 °C – 4 h | 4 |
| Pt-Cu/DUS | 500 °C – 2 h | 192 |
| Pt-Cu/DUS – 1 FLP-106 decomp. | - | 107 |

# CHAPTER 2

## 2. EXPERIMENTAL

### 2.1. CUSTOM-DESIGN MICRO PROPULSION BATCH REACTOR

In Chapter 2, we focus on: i) the design and description of the custom-made micro propulsion reactor, ii) catalyst synthesis procedures, iii) instrumentation and parameters used in catalyst characterization, and iv) experimental protocols developed for the catalytic performance tests carried out with the custom-design micro propulsion reactor and the DSC/TGA system.

#### 2.1.1. Custom-design Micro Propulsion Batch Reactor Design Features

As a part of the current dissertation work, a custom-design micro propulsion reactor was designed, constructed and utilized in an attempt to test the catalytic performance of the synthesized catalysts in the anerobic ADN decomposition reaction. Experimental details, design features and the technical aspects of this setup is described in detail below.

The custom-made micro propulsion reactor consists of 3 identical batch reactors (labeled as Reactor A, B, C) that can be operated in parallel (**Figure 2-1** and **Figure 2-2**) and are made of 316 stainless steel. Each batch reactor contains an independent electronic control box (**Figure 2-3**) and a common electronic management utility operated by a single custom-design software.

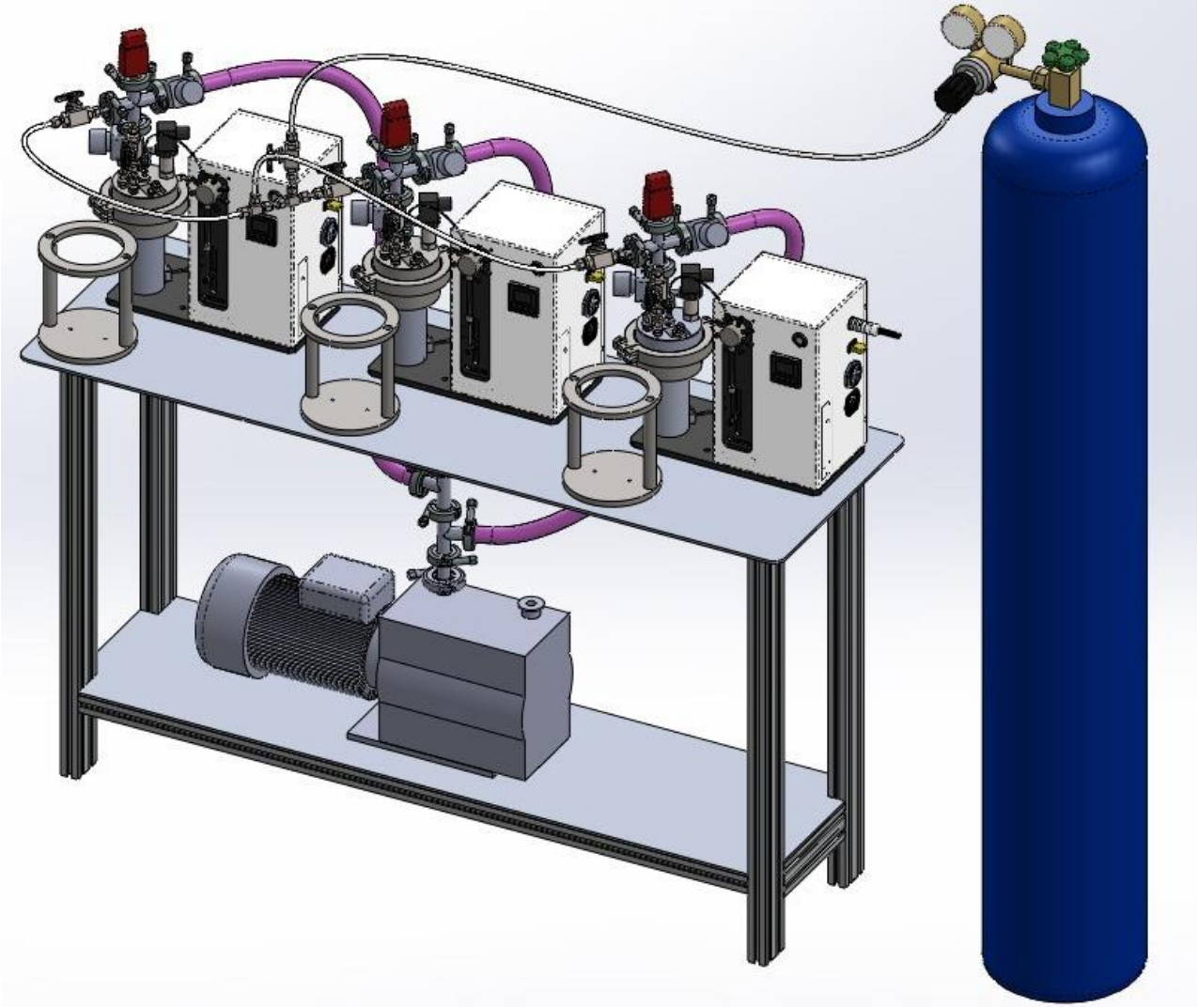


***Figure 2-1.*** *Overall 3D view of the custom-design micro reactor system with 3 identical batch reactors that can be operated in parallel.*




***Figure 2-2.*** *Actual overall view of the batch reactors.*

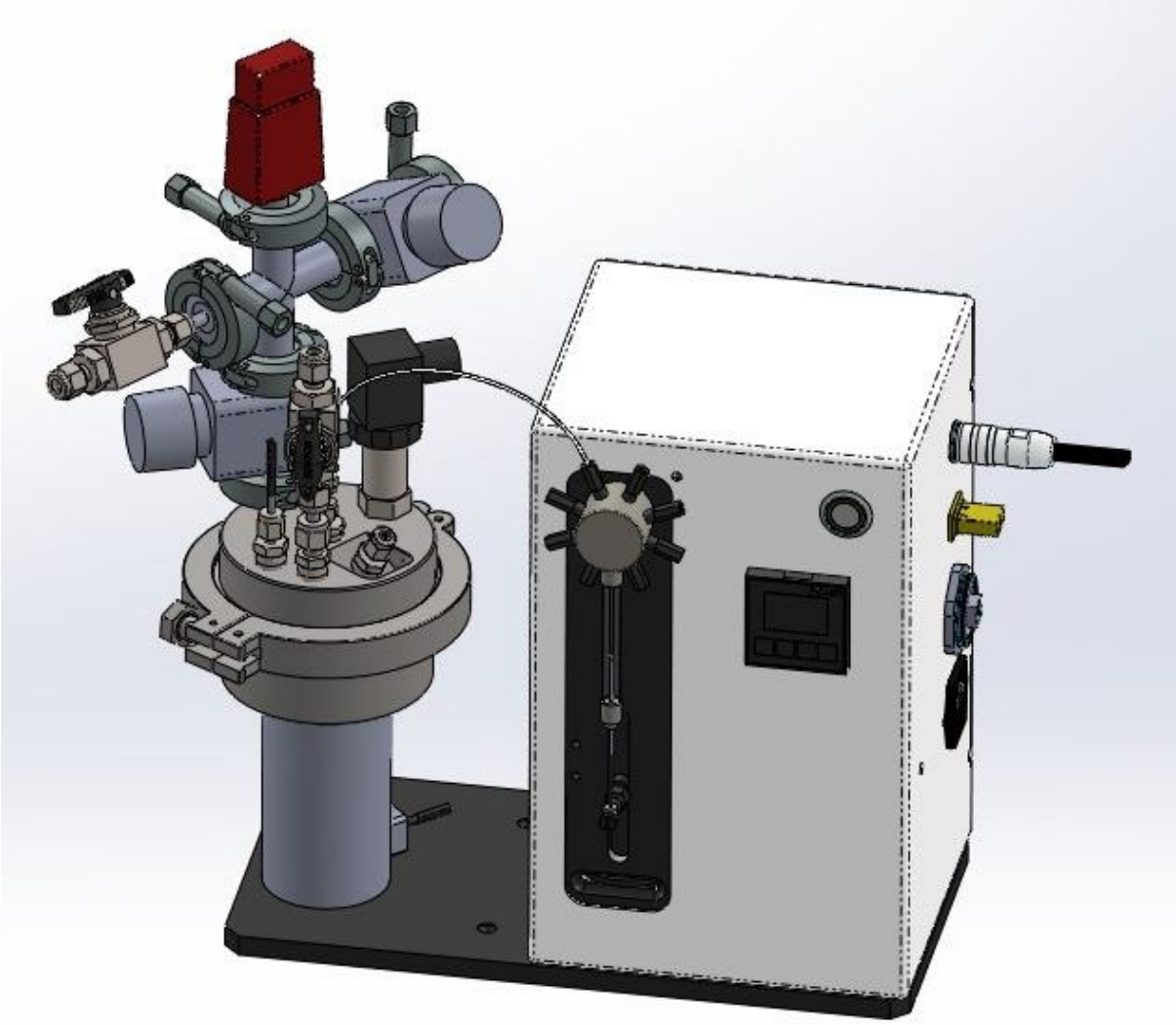


***Figure 2-3.*** *View of a single batch reactor with its control box.*

Batch reactors were designed and tested to withstand a maximum overall temperature of 400 °C and a pressure of 5 bar. In addition, an adjustable pressure safety valve was placed in each reactor in order to keep the system safe against any uncontrolled increase in pressure. The internal volume of each reactor was 175 ml. Inside each reactor, there is a reaction compartment heated by cartridge heaters located at the bottom section of the reactor (**Figure 2-4**). The sample holder consists of a funnel and a lid (**Figure 2-5**) which are positioned in the reaction compartment. Funnel shaped sample holder also minimizes the solid and liquid

scattering as a result of the highly exothermic ADN decomposition reaction. The hole on the side of the funnel allows the thermocouple (TC) to be extended into the reaction compartment (**Figure 2-6**). In addition, the pin on the funnel and the pin slot on the reactor allow the accurate and reproducible positioning of the funnel to the same location inside the reactor (**Figure 2-7**). Accordingly, TC can reach the reaction compartment by passing through two separate holes and the ¼″ NPT × ⅛″ fitting located on the reactor.

The properties of the TC are as follows:

- Outer diameter: 3 mm
- K-type
- Suitable for operation between -200 °C and 1200 °C
- SS316 cover with metal oxide filler
- The length of the bare TC: 1.5 mm

The design of the system allows execution of two different modes of experiments;

1. The reactant and catalyst can be loaded into the reaction compartment while the reactor is at room temperature, and temperature-programmed experiments can be performed by increasing the reactor temperature in a controlled manner (with a maximum temperature ramp of 20 °C/min).
2. Measurements can be carried out at a constant temperature by first increasing the temperature to a certain value and then injecting the desired amount of liquid from injection line to reaction compartment with the help of the syringe pump located in the control box of the reactor.

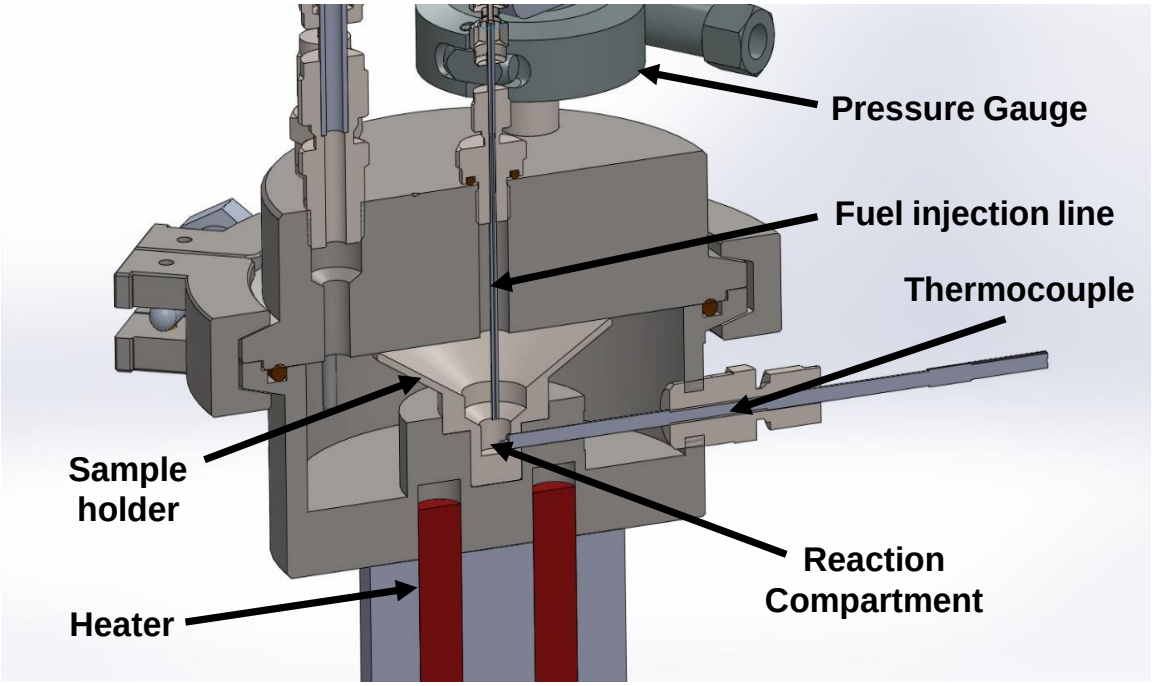



***Figure 2-4.*** *3D internal view of the cross-section of the batch reactor.*

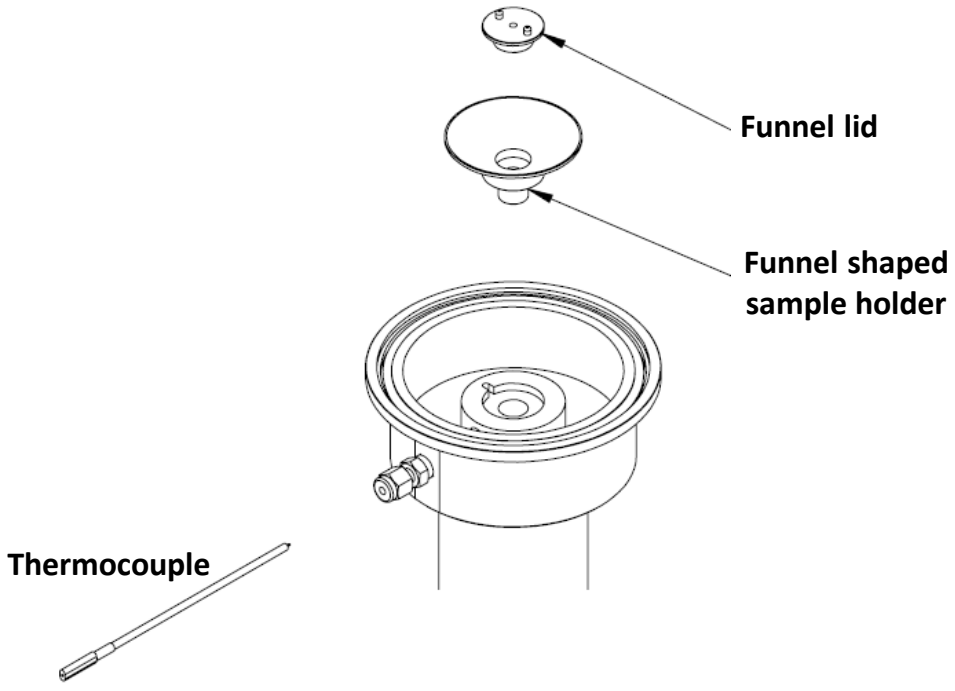



***Figure 2-5.*** *Disassembled display of reaction compartment elements of the batch reactor.*

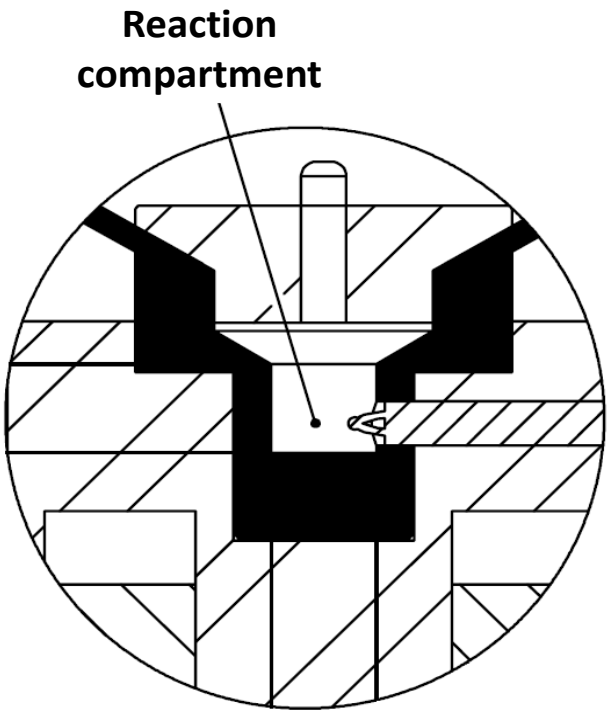



***Figure 2-6.*** *Thermocouple extending from the hole of the funnel to the reaction compartment.*

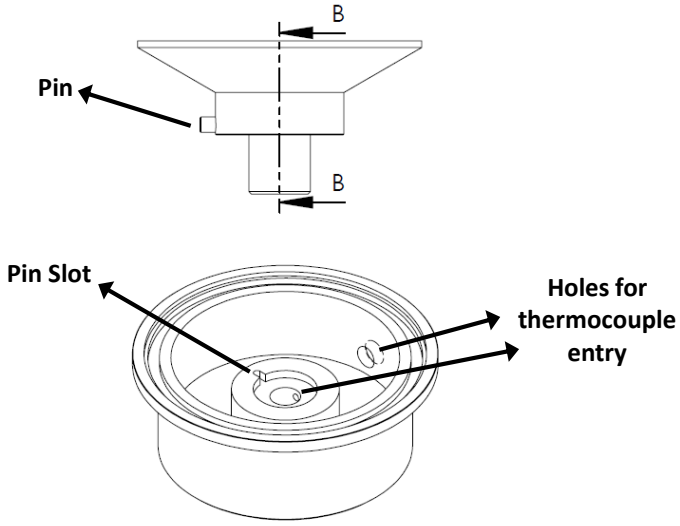



***Figure 2-7.*** *Alignment of the funnel shaped sample holder.*

All the connections of the reactors are durable and impermeable up to 2 bar pressure and $10^{-1}$ torr vacuum. O-rings inside the connections are made of viton with reasonable resistance to temperature and chemical degradation. The reactor cover was mounted on the reactor by placing an o-ring into the o-ring groove on the reactor and fixing them with a clamp as shown in **Figure 2-8**.

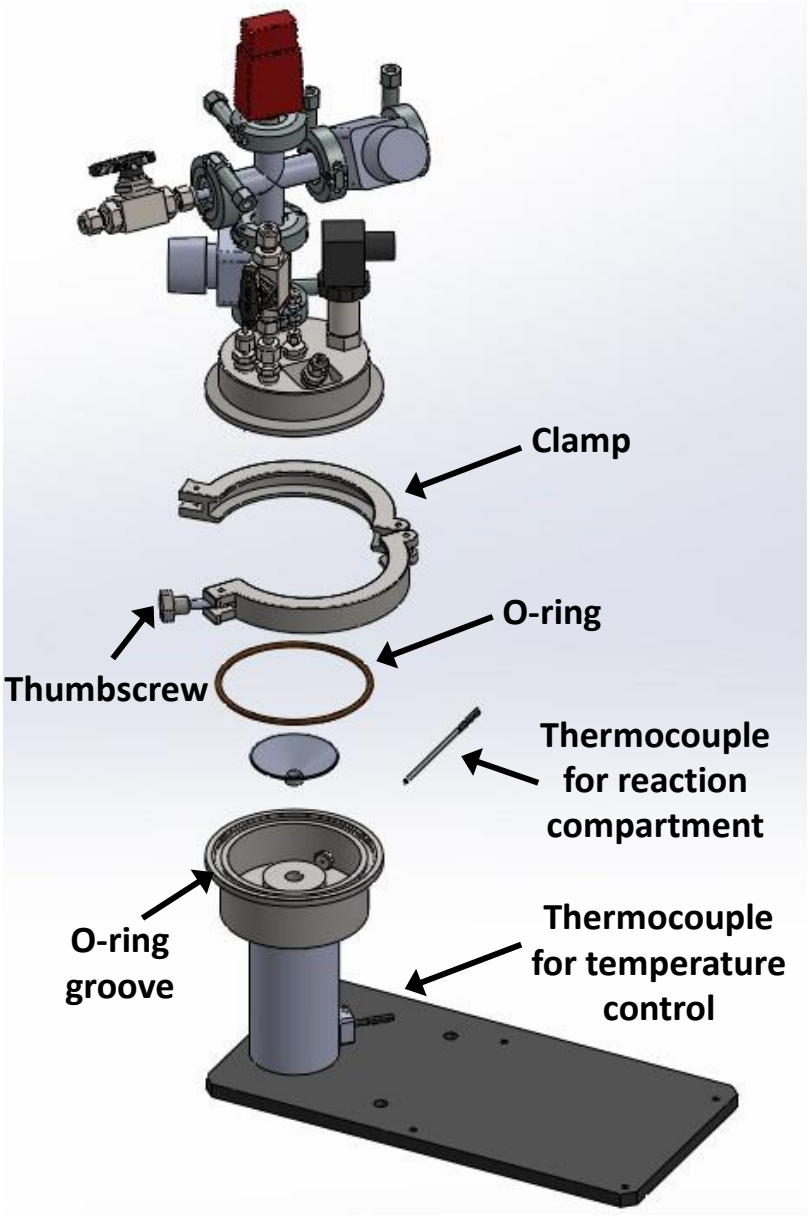



***Figure 2-8.*** *Disassembled view of the batch reactor.*

Components of a given batch reactor included (**Figure 2-9**);

- 1 pressure gauge (Edwards, APG100-XLC) for high-speed (2 kHz) measurement of the reactor pressure within 0.01-2.00 bar

- 1 pressure gauge (Keller, PAA-23SY) for measurement of low pressures ($10^{-4}$-1.00 mbar) upon evacuation

- 1 relief (safety) valve

- 2 vacuum regulation valves

- 2 on-off ball valves for gas inlets and outlets

- Liquid dosing port

- TC for measuring the temperature of gas phase section of the reaction compartment

- TC for measuring the temperature of reactor and the solid catalyst

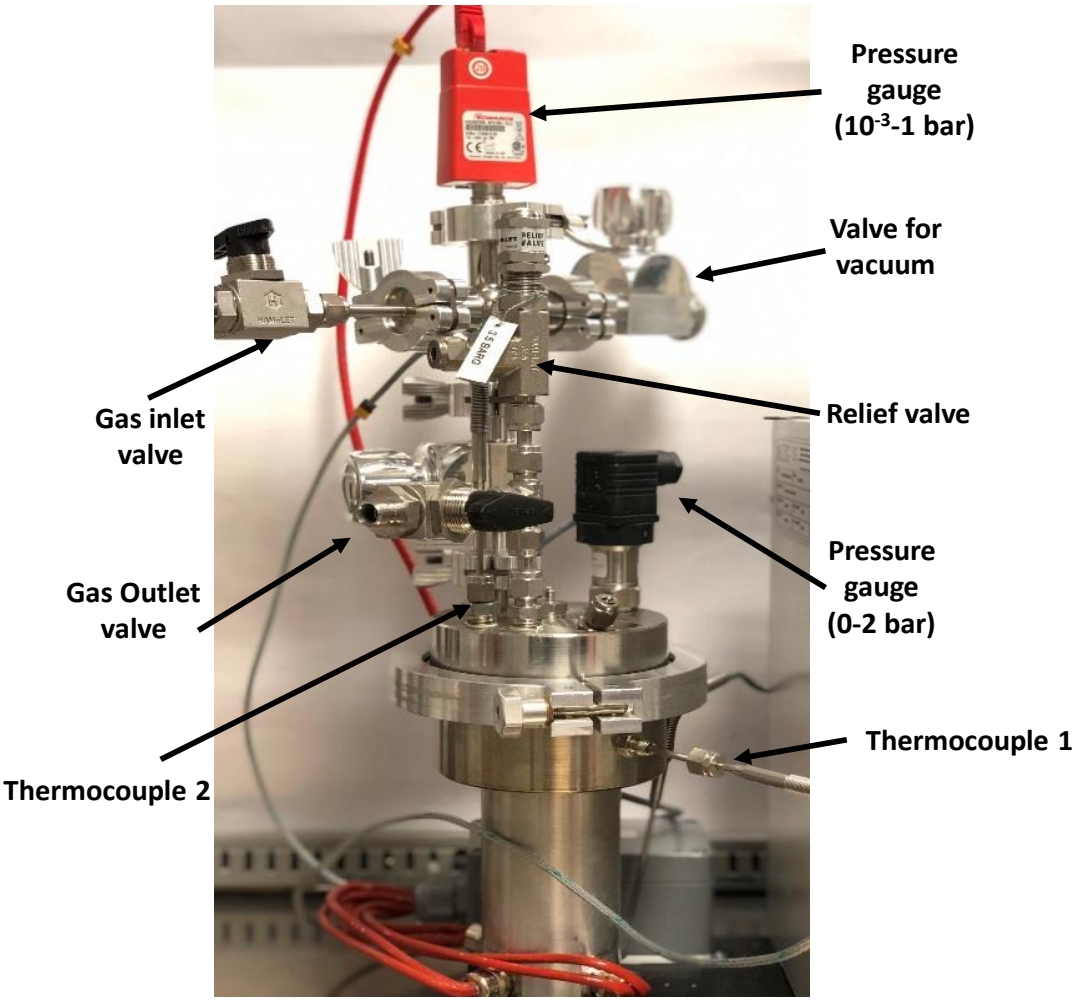



***Figure 2-9.*** *Various components of the batch reactor.*

**Figure 2-10** shows the control box of the reactor. It contains a computer-controlled and automated Kloehn syringe pump (V6 48K Syringe Drive Pump) which includes a position valve, a syringe and a syringe pump. This unique computer-controlled syringe pump allows injection of a total of 1 mL liquid in 48,000 identical portions (i.e., with 21 nL or 2.1 x $10^{-9}$ L portions). Moreover, control box also contains an Ordel (PC441) Proportional Integral Derivative (PID) temperature controller.

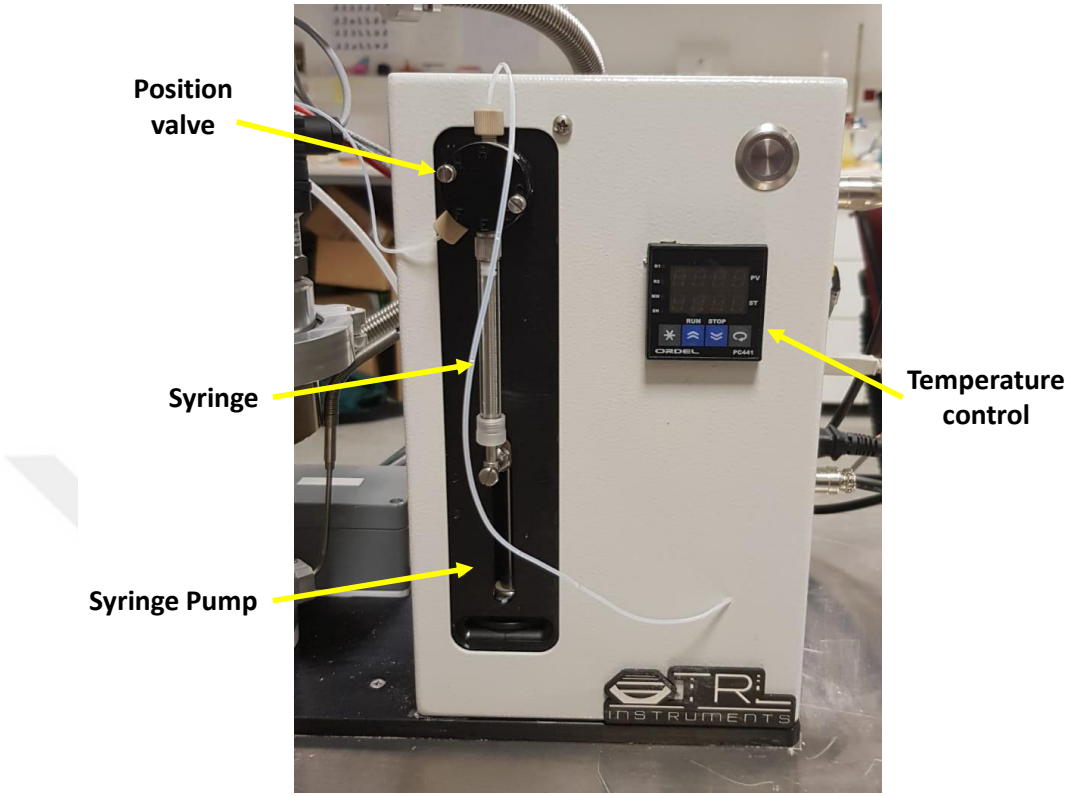



***Figure 2-10.*** *Components of the batch reactor control box.*

Custom design data acquisition module reads and records the data collected from six pressure gauges and six thermocouples in a simultaneous manner and is powered by a custom made 24 VDC power supply (**Figure 2-11**).




***Figure 2-11.*** *Data acquisition module and 24 VDC power supply.*

The materials used in the custom-design micro propulsion reactor are as follows:

• Reactor body: SS304

• Pressure gauge connections: SS316L

• Liquid dosing connection lines: 1/16″ PTFE hose

• Liquid injection needle: 1/16″ SS316 pipe

• Liquid injection needle fittings

- 1/16″ “bore-through” union SS316

- 1/16″ x 5/16-24 “bore-through” fitting SS316

• Gas distribution lines: 6 mm PTFE hose

• Pressure relief valve connections: 6 mm SS316

• Gas inlet and outlet valves connections: 6 mm SS316

• Gas outlet fitting: ¼″ NPT SS316

• Vacuum components (SS316)

- QF 16 X ¼″ pipe adapter

- QF 16 Cover

- QF 16 Tee Fitting

- QF 25 X QF 16 adapter

- QF 16 Viton O-ring and O-ring

- QF 25 Viton O-ring and O-ring

- 16 mm PVC hose

### 2.1.2. Custom-design Micro Propulsion Batch Reactor Software

Two separate software were utilized in the operation of the system as described below.

#### 2.1.2.1. Syringe pump software

The purpose of this software is to control the automated syringe pumps, which are capable of dosing a liquid with the syringe volume in 48000 equal steps. Moreover, the software enables the syringe pumps to dose the same amount of liquid into the reactor each time.

When the software is turned on, a login page appears as shown in **Figure 2-12**. Administrator must be selected in the "User Name" section and 1 must be entered in the "Password" section to enter the software.

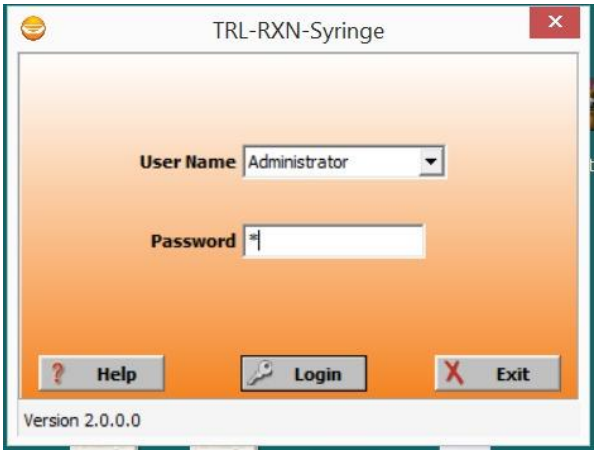



***Figure 2-12.*** *Login page.*

After logging into the software, the "Administrator window" shown in the **Figure 2-13** appears.




***Figure 2-13.*** *Administrator window.*

After logging into this page, "Parameters" button is pressed in order to establish the connection between the software and the reactor system. When this button is pressed, “Admin Connection Ports” page appears, where individual computer connection ports can be selected and saved for each of the 3 syringe pumps in the system (**Figure 2-14**).

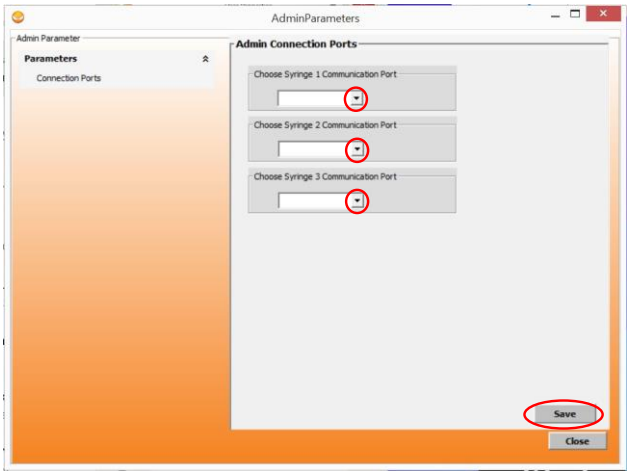



***Figure 2-14.*** *Admin connections port page.*

After pressing the “Run” button on the main page, the “Run” tab opens, and under this tab, one can specify the parameters of the syringe pumps to be used during the experiment and move the syringe pumps to their starting positions (**Figure 2-15**).

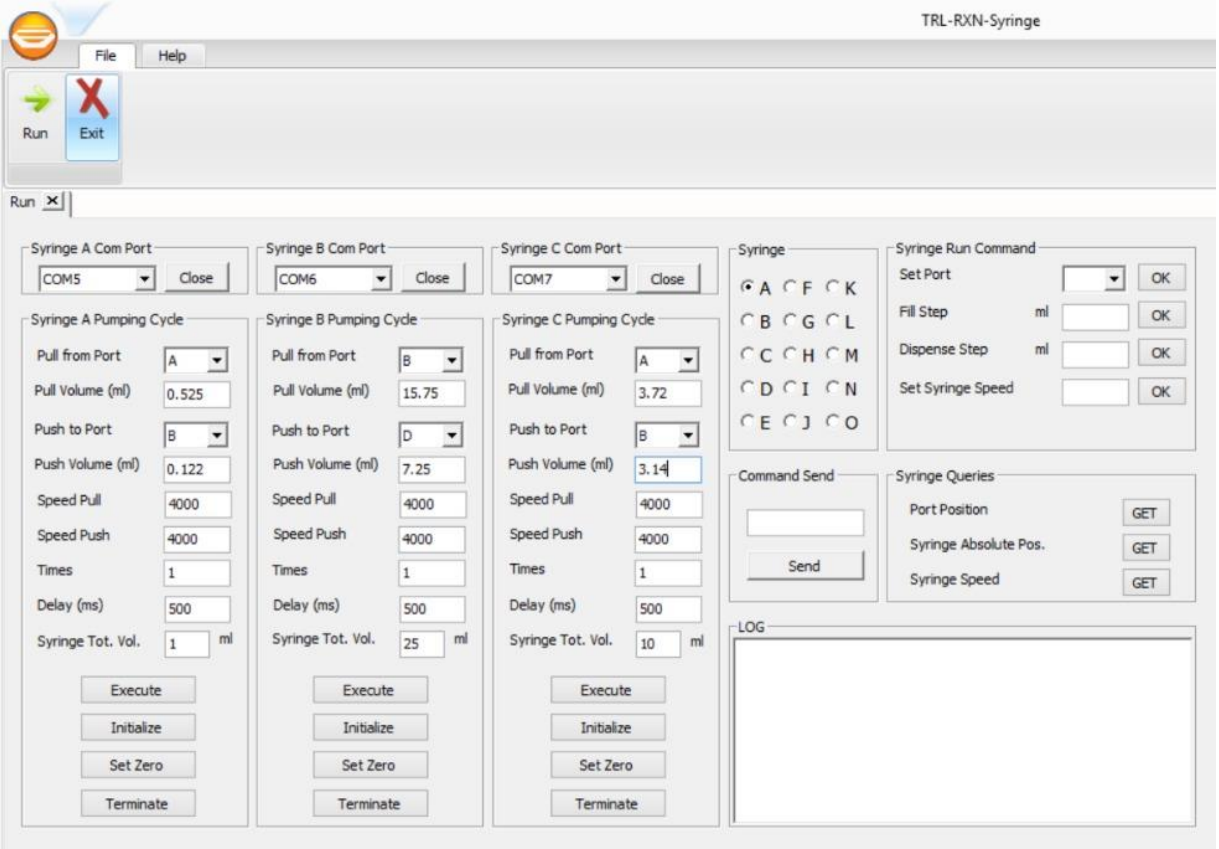



***Figure 2-15.*** *Run tab.*

The purpose of the remaining parameters on the Run tab shown in **Figure 2-15** are listed below.

***Pull from Port:*** determines the port on the valve of the syringe pump where the liquid will be drawn.

***Pull Volume (ml):*** determines how much liquid is drawn into the syringe in ml.

***Push to Port:*** determines the port on the valve of the syringe pump where the liquid will be injected.

***Push Volume (ml):*** determines how much liquid is injected from the syringe in ml.

***Speed Pull:*** determines the speed at which the liquid is drawn into the syringe (max. 4000).

***Speed Push:*** determines the speed at which the liquid is injected from the syringe (max. 4000).

***Times:*** determines how many times the liquid is drawn and injected.

***Delay (ms):*** determines how long the syringe pump waits (in ms) between drawing and injecting the liquid.

***Syringe Tot. Vol. (ml):*** specifies the total volume of the syringe connected to the syringe pump.

***Execute:*** starts the syringe pump operation.

***Initialize:*** moves the syringe pump to its starting position.

***Set Zero:*** defines the "0" position of the syringe pump. It is very important that the syringe is in the "0" position so that no air bubble is formed while the liquid is being drawn into the syringe. Before pressing this button, the position adjustment button on the syringe pump shown in **Figure 2-16** must be turned by hand and the syringe plunger must be brought up to the highest point. After this process is done, by pressing the "Set Zero" button, the "0" point is introduced to the syringe pump and the next operations are performed by accepting this position as "0".

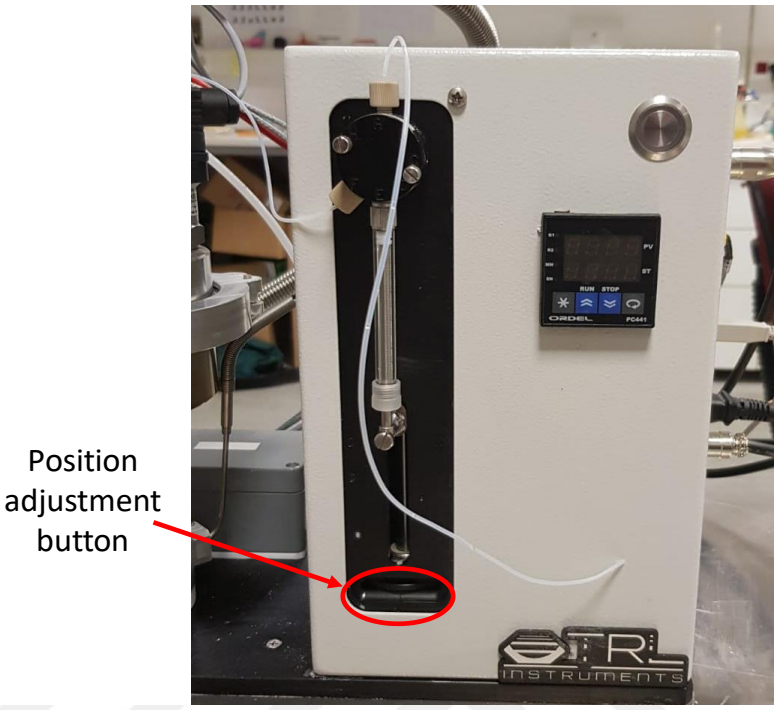



***Figure 2-16.*** *Position adjustment button.*

### 2.1.2.2. Data acquisition software

A software called DAQExpress is used for reading, saving and displaying the data acquired by the pressure gauges and thermocouples.

When the software is turned on, the "Home Page" shown in **Figure 2-17** will appear. On this page, open project is selected from the file tab in the upper left part, and then the project named “1 Batch Reaction.Ivproject” is selected.




***Figure 2-17.*** *Main page of the DAQExpress data acquisition software.*

In the 'Batch Reaction.gvi' file of the project, there is a 'Diagram' tab where the user can configure the modules connected to the system (**Figure 2-18**).

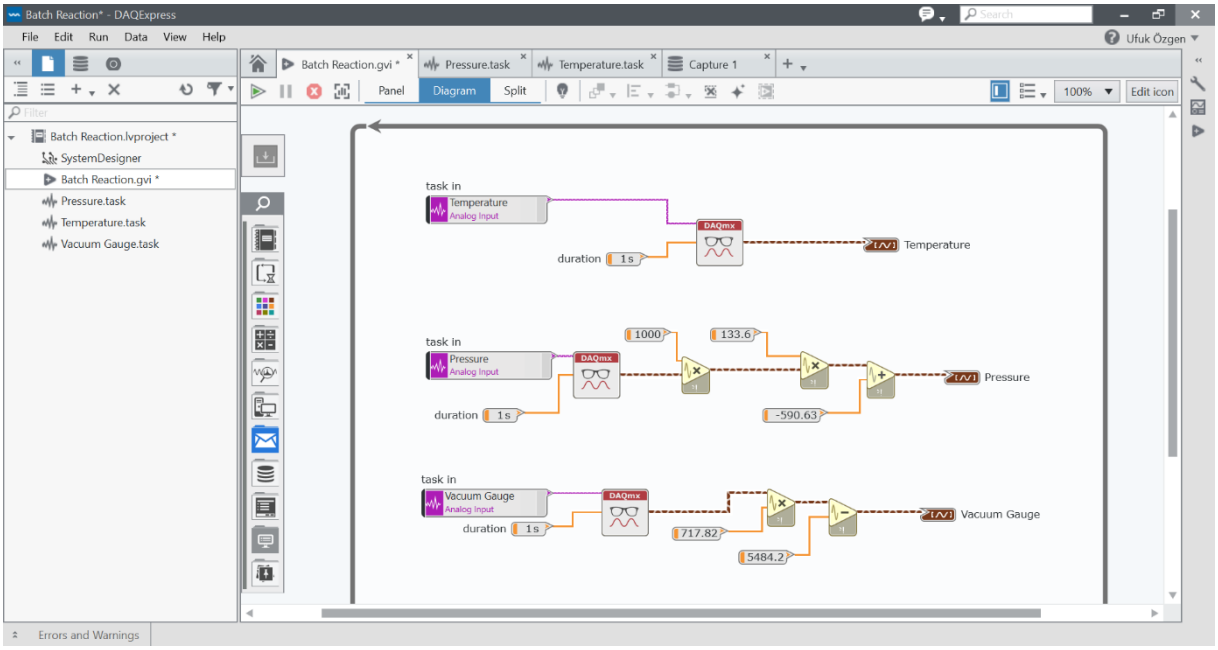



***Figure 2-18.*** *Diagram tab.*

On the left side of the 'Diagram' tab, there is the 'Panel' tab where the experiment can be run (**Figure 2-19**). In the 'Panel' tab, the parameters to be observed during the analysis can be viewed graphically. After clicking the parameter names section at the top right of each graph with the right mouse button, you can choose to hide and see the parameter.

To start and stop the analysis, the  button group is used. The meaning of these buttons are Run-Start, Pause-Stop, Abort-Cancel and Capture-Save, respectively. After clicking the Run button to start the analysis, the pressure vs. time and temperature vs. time can be seen real-time from the graphs. Data can be saved with the Capture button. Using the Capture function after finishing the experiment is recommended for high performance. The collected data can be viewed by clicking the  icon (**Figure 2-19**).

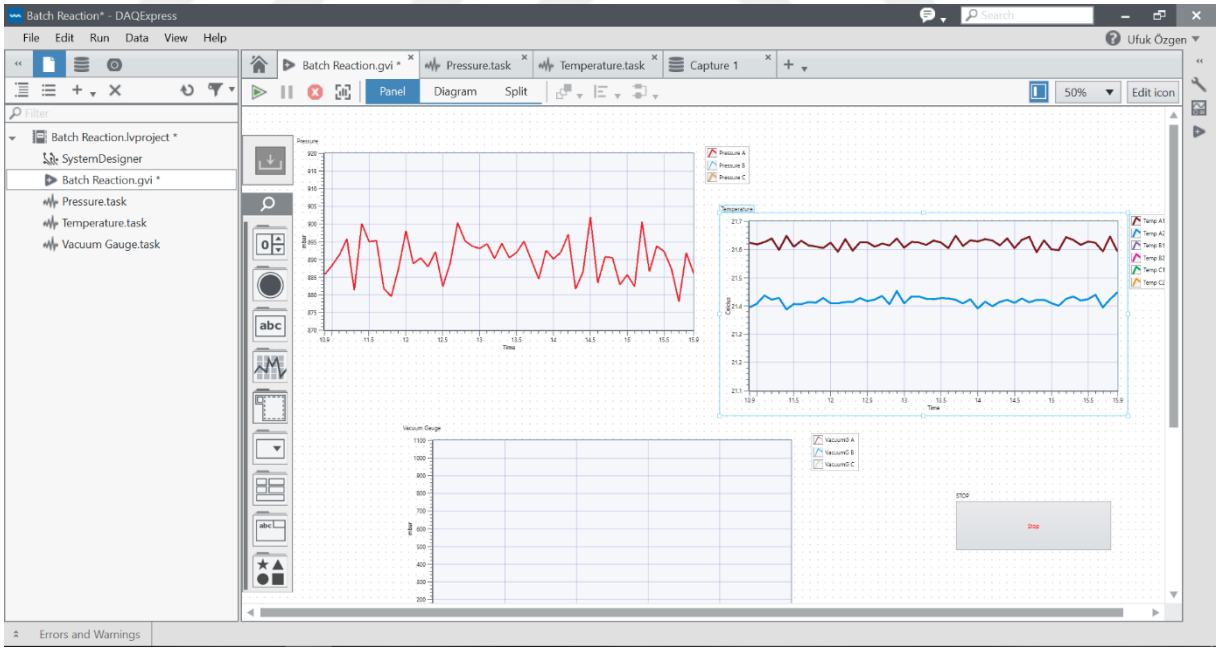



***Figure 2-19.*** *Panel tab.*

### 2.1.3. Custom-design Micro Propulsion Batch Reactor Operating Procedures

#### 2.1.3.1. Reactor cleaning procedure before starting the experiment

1) The funnel shaped sample holder in the reactor is cleaned by wiping with technical grade ethanol until there is no visible contamination.
2) The reactor cover, holes on the cover and the syringe tip which may be covered with catalyst powder and fuel residues after explosion, are cleaned by wiping first with deionized water and then with technical grade ethanol. Next, they are dried with an air gun.
3) The reactor is dried by heating at about 100 °C and then the system is cooled down to room temperature.
4) The powder catalyst sample is placed inside the funnel and by pressing firmly. The remaining powder residues in the middle of the funnel are cleaned. It is ensured that the TC is fully embedded inside the catalyst powder.
5) The syringe is cleaned from the fuel residues used in the previous experiment by injecting:
    a. 2 times 1 ml of deionized water
    b. 2 times 1 ml air
    c. 3 times 1 ml of ethanol
    d. 2 times 1 ml air
    e. 3 times 1 ml of fuel

#### 2.1.3.2. Adjusting the fuel dosing amount

1) Fuel is drawn into the syringe.

2) The injection trials of the fuel from the injection line are carried out by measuring the weight of the liquid drops and they are repeated until reproducible dripping is observed. Since the number of drops formed during the first injection step is misleading, this step is ignored. The reason for this is the small volumetric changes created by the rotation of computer-controlled multi-way valve, which provides liquid transfer.
3) If the repeatability is achieved in 3 successive injections, then the upper cover of the reactor is closed in order to fill the batch reactor with Ar(g). If reproducibility is not achieved, injection trials are repeated.

#### 2.1.3.3. Gas dosing procedure

1) While the valve of the catalyst chamber is opened and the vacuum valve is closed, the Ar(g) inlet valve is opened, allowing Ar(g) to fill the reactor until the pressure reading reaches to approximately 1.5 bar. For one minute, the change in the pressure value is monitored to check possible leaks.
2) The argon inlet valve is closed, the vacuum valve is opened in a controlled manner and the pressure is brought to approximately 1 bar with the help of the vacuum pump. When this value is reached, the vacuum valve is closed.
3) The first two processes are repeated 3 times. Afterwards, the vacuum valve and the valve of the catalyst chamber are closed, respectively, and then, the catalytic performance test is started after injecting the fuel into the reaction compartment.

#### 2.1.3.4. Reactor cleaning procedure after measurement

1) Vacuum valve and catalyst chamber valve are opened.

2) The vacuum pump is turned on for about 30 seconds, during this time the harmful gases released after the exothermic reaction are pumped out from the reactor and then vacuum pump is turned off.
3) In order to accelerate the cooling and to continue the pumping of the residual gases, the catalyst chamber valve and the vacuum valve are left open, and the reactor is allowed to cool.
4) When the temperature drops below 100 °C, the reactor cover is opened.
5) The funnel is cleaned with a funnel-compatible tipped broom.
6) This step is carried out depending on two different conditions;

i. If it is the last measurement of the day or if a new fuel is used;
    a. The syringe is pulled and pushed 10 times with 1 ml of deionized water.
    b. Before closing the reactor, 1 ml of deionized water is pulled once inside the syringe and left in it to prevent the formation of salt coming from the fuel residuals.

ii. If it is not the last measurement of the day and the same fuel is being used;
    a. The syringe pulled and pushed twice with 1 ml of fuel.
    b. Continue with the step of adjusting the fuel dosing amount.

7) At the end of the day, the reactor cover is left closed.

## 2.2. MATERIAL SYNTHESIS

### 2.2.1. Support Materials

In the catalyst synthesis, nine different alumina support materials obtained from SASOL Inc. were used as catalyst supports (i.e., SCFA140-L3, SCFA140, SBa200, TH100/150,

SCFA160-Ce20, PURAL-MG5, Siralox5, Siralox10, and Siralox20). Some of the alumina support materials such as SCFA140, SBa200, TH100/150 contained either no dopants or a very low level of dopants (e.g., < 2 wt.%). On the other hand, remaining alumina support materials were enriched with higher loadings of different dopants (i.e., SCFA140-L3: 3 wt.% La dopant, SCFA160-Ce20: 20 wt.% Ce dopant, PURAL-MG5: 5 wt.% Mg dopant, Siralox5: 5 wt.% Si dopant, Siralox10: 10 wt.% Si dopant, Siralox20: 20 wt.% Si dopant) in order to improve various functional properties such as thermal resistance, chemical behavior, surface acidity, precious metal dispersion. All the selected alumina materials have high porosity and high SSA values at room temperature. These different alumina structures have dissimilar thermal stabilities. For example, SCFA140-L3 and TH100/150 can maintain (at least to a certain extent) their crystal structures, porosities and SSA at relatively high temperatures (≥ 1200 ° C). Furthermore, the TH100/150 material has a relatively high porosity. SCFA140 is a standard alumina and was used as the control of the SCFA140-L3 sample which had a higher thermal stability than SCFA140. SBa200 is a widely used, high SSA and high catalytic performance alumina exploited in many catalytic processes such as automotive exhaust emission control systems. SCFA160-Ce20 sample contains 20 wt.% ceria inside the alumina structure and PURAL-MG5 is an alumina support material containing 5 wt.% Mg. Although this later two types of alumina are not widely used in high temperature processes, they have promising structural features for such applications. Currently utilized alumina support materials are abbreviated as shown in **Table 2-1**.

***Table 2-1.*** *Abbreviations of the alumina support materials utilized in the current work.*

| Support Name | Support Code |
|---|---|
| SBa200 | SBa200 |
| SCFa-140 | SCFa |
| SCFa-140 L3 | L3 |
| TH100/150 | TH100 |
| SCFa-160 Ce20 | Ce20 |
| Pural-MG5 | MG5 |
| Siralox5 | Sir5 |
| Siralox10 | Sir10 |
| Siralox20 | Sir20 |

### 2.2.2. Incorporation Catalytic Active Sites on the Alumina Support Materials

In the current work, we used two different synthetic strategies to incorporate Ir catalytic active sites on the chosen alumina support materials in order to optimize catalytic functionality, stability, and active site dispersion. The first synthetic approach that we exploited was the wetness impregnation (WI) method, while the second approach involved the incipient wetness impregnation (IWI) technique. Details regarding these two different catalytic active site incorporation routes, corresponding structures of the catalysts obtained, as well as their catalytic performance behaviors are described in detail in the forthcoming sections/chapters.

#### 2.2.2.1. Catalyst synthesis via wetness impregnation (WI)

Different types of catalysts containing 5 wt. % Ir was synthesized over various alumina support materials by using a single-step wetness impregnation method. Alumina support materials used for this synthesis method were SCFa140, SCFa140-L3, SBa200, TH100/150, SCFA160-Ce20, PURAL-MG5. First, the $Al_2O_3$ support was added to 20 ml of deionized water and mixed with the magnetic stirrer for 1 h. For a 250 mg of sample synthesis, 0.0194 g of $IrCl_3$ precursor material was added in the alumina suspension followed by the addition

of 10 ml deionized water. After stirring for 10 min, the mixture was heated and stirred at 80 °C on the magnetic stirrer to evaporate the water (water was evaporated in ca. 3 h). The wetness impregnation setup is shown in **Figure 2-20**. The obtained sample was finely ground in a mortar and pulverized, and then the sample was calcined for 5 h at 550 °C, 900 °C or 1100 °C, in a box oven shown in **Figure 2-21**.

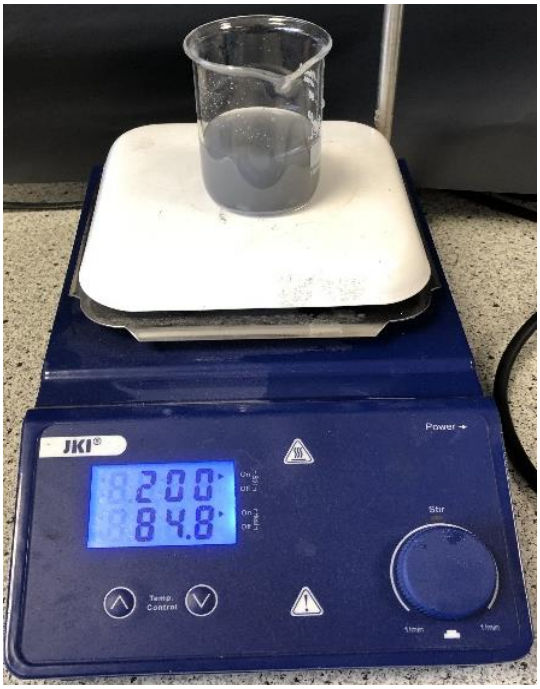



***Figure 2-20.*** *Wetness impregnation setup.*




***Figure 2-21.*** *Box oven used in the calcination of catalysts in air.*

#### 2.2.2.1.1. 5Ir/10LaMnO$_3$/SBa200 synthesis via WI

$LaMnO_3$ (perovskite) containing samples were synthesized using the citrate method [105,106]. First, 1.9116 g citric acid was dissolved in 82.7ml distilled water followed by addition of 1.7905 g $La(NO_3)_3.6H_2O$ and 1.0379 g $Mn(NO_3)_3.4H_2O$ precursors. Solutions were stirred for 1 h followed by heating at 80 °C with continuous stirring under ambient conditions. During heating, the solvent was slowly evaporated resulting in the gel formation which was heated in an oven at 90 °C overnight in air. Next, the sample was calcined in a box oven at 700 °C in air for 5 h.

Then, 1 g 10$LaMnO_3$/SBa200 sample was prepared by dispersing 0.1 g $LaMnO_3$ and 0.9 g SBa200 in 60 ml distilled water. After the suspensions were stirred for 10 min, they were heated at 80 °C on a magnetic stirrer to evaporate the water. After the water was evaporated,

the sample was dried and the resulting powder material was heated in the calcination furnace at 900 °C in air for 5 h.

For the Ir incorporation on the perovskite containing catalysts, the same procedure was applied as mentioned in **Section 2.2.2.1**.

#### 2.2.2.2. Catalyst synthesis via incipient to wetness impregnation (IWI)

The incipient to wetness impregnation (IWI) setup shown in **Figure 2-22** consists of a peristaltic pump (PT-500), a vacuum pump (DrVAC-600), a sonicator (United Jevelry Tool Supplies), a vacuum flask, and connection tubes (TYGON, LMT-55 SC0373T). Calibration of the peristaltic pump was performed before each impregnation using deionized water. Metal precursor solution was drawn into the device with the fast-filling mode and injection was carried out on the desired material with the continuous-filling mode.

The incipient to wetness impregnation setup was upgraded to allow more catalyst synthesis simultaneously, and the currently used synthesis setup is given in **Figure 2-22b**. In this system, there are 3 separate peristaltic pumps, allowing parallel synthesis.

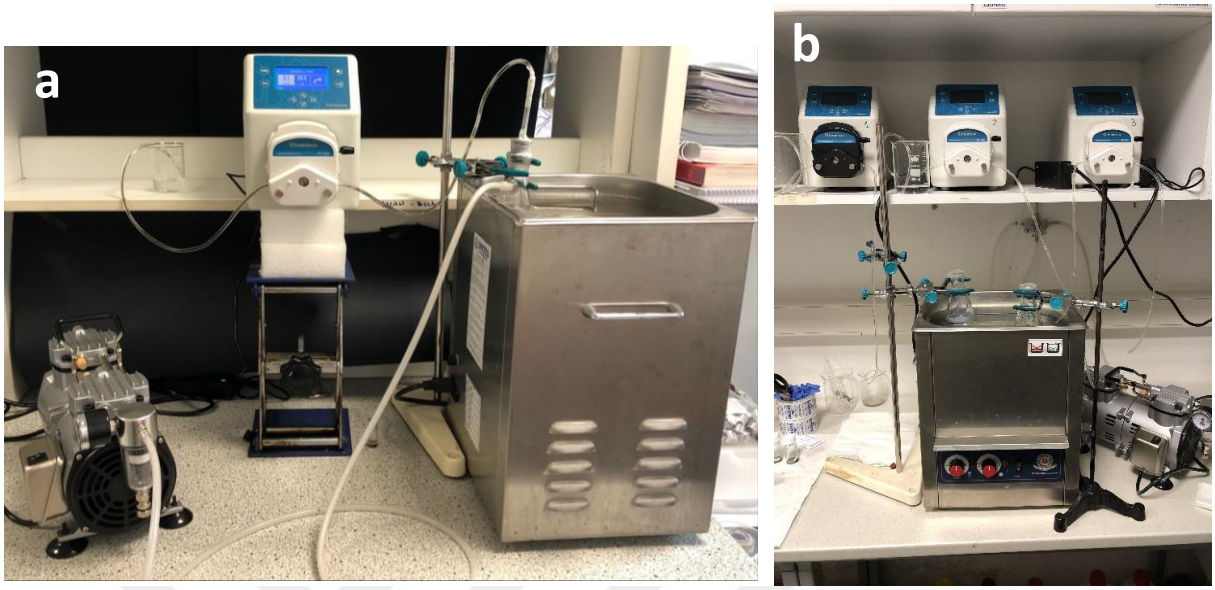



***Figure 2-22.*** *(a) Incipient to wetness impregnation set up (b) updated version of the incipient to wetness impregnation set up system.*

#### 2.2.2.2.1. Addition of 5 wt.% Ir via IWI

At the beginning of catalyst synthesis via IWI method, support material was weighed in the vacuum flask and then the bottom surface of the flask was placed into the sonicator. One end of the vacuum flask was connected to the vacuum pump and the other end was connected to the hose of the peristaltic pump using a pastor pipette. One of the three cylinders of the peristaltic pump was adjusted to be upward, so air contact was prevented. Then, the vacuum pump which was brought to the lowest speed (375 mmHg) was turned on and then the sonicator was switched on. The support material was kept under vacuum for 30 min to evacuate the pores of the material.

For 1.050 g of catalyst synthesis, 0.0407g of $IrCl_3$ precursor material (2.5 wt.% iridium) was dissolved in a plastic tube by adding 50 µl $NH_4OH$ in 1.5 ml of deionized water. The pH of the prepared solution was about 9.4. The metal solution was sonicated for 5-7 min to dissolve the Ir precursor salt.

Next, support material was kept under vacuum (375 Torr) for 30 min and the metal solution was drawn into the hose of the peristaltic pump, which was calibrated for dripping impregnation solution with a volumetric rate of 0.1 ml / min. The continuous filling mode was selected at the start of the dripping process and the metal solution was dripped onto the support material with the calibrated drip speed. During the dripping time, the vacuum was reduced to 150 Torr and the evaporation of the drop was prevented. This also enabled us to distribute the drops evenly in the vacuum flask. Then, the mixture of metal solution and support material was left under vacuum (375 Torr) for 30 min.

The synthesized materials were dried in a low-temperature oven (**Figure 2-23a**) at 60 °C for 8 h and then two different procedures were applied. Materials were either calcined at 400 °C in air for 3 h in a box oven (**Figure 2-21**) or reduced at 500 °C for 2 h in a tubular flow furnace (**Figure 2-23b**) in 5% $H_2$/Ar and later these materials were either labeled as CCR or RR, respectively, according to their pretreatment procedure.

To complete the serial impregnation cycle, the aforementioned dripping procedure was repeated with 1.5 ml of aqueous ammonia solution containing 2.5 wt. % Ir.

Then, the dried materials were;

(i) Calcined at 400 °C for 3 h in a box oven and then reduced at 500 °C for 2 h under 5% $H_2$/Ar for CCR samples, or

(ii) Reduced at 500 °C for 2 h under 5% $H_2$/Ar for RR samples

**Table 2-2** shows the synthesized materials and the pretreatment conditions used in the IWI method.

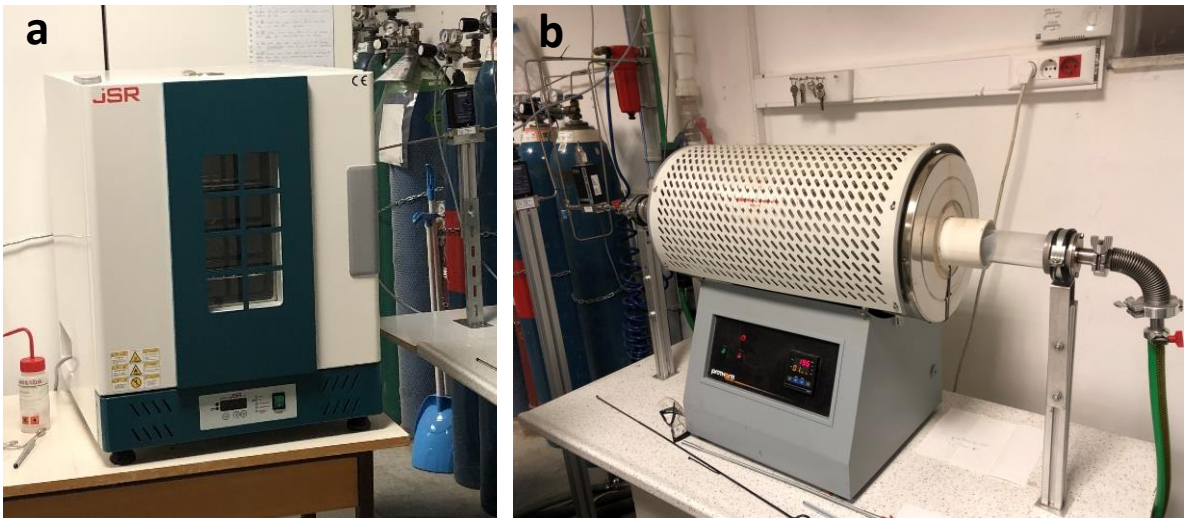



***Figure 2-23.*** *(a) Drying oven, (b) tubular flow furnace.*

***Table 2-2****. Synthesis conditions for the 5 wt. % Ir catalysts synthesized via IWI method.*

| Support Name | 1st $IrCl_3$ addition (2.5 wt%) | | | 2nd $IrCl_3$ addition (2.5 wt%) | | | Sample code |
|---|---|---|---|---|---|---|---|
| | Drying | Calcination | Reduction | Drying | Calcination | Reduction | |
| L3 | 60 °C, 3 h | 400 °C, 3 h | - | 60 °C, 8 h | 400 °C, 3 h | 500 °C, 2 h | 5Ir/L3-CCR |
| TH100 | 60 °C, 3 h | 400 °C, 3 h | - | 60 °C, 8 h | 400 °C, 3 h | 500 °C, 2 h | 5Ir/TH100-CCR |
| MG5 | 60 °C, 8 h | 400 °C, 3 h | - | 60 °C, 8 h | 400 °C, 3 h | 500 °C, 2 h | 5Ir/MG5-CCR |
| Sir5 | 60 °C, 8 h | 400 °C, 3 h | - | 60 °C, 8 h | 400 °C, 3 h | 500 °C, 2 h | 5Ir/Sir5-CCR |
| Sir10 | 60 °C, 8 h | 400 °C, 3 h | - | 60 °C, 8 h | 400 °C, 3 h | 500 °C, 2 h | 5Ir/Sir10-CCR |
| Sir20 | 60 °C, 8 h | 400 °C, 3 h | - | 60 °C, 8 h | 400 °C, 3 h | 500 °C, 2 h | 5Ir/Sir20-CCR |
| SBa200 | 60 °C, 8 h | 400 °C, 3 h | - | 60 °C, 8 h | 400 °C, 3 h | 500 °C, 2 h | 5Ir/SBa200-CCR |
| Ce20 | 60 °C, 8 h | 400 °C, 3 h | - | 60 °C, 8 h | 400 °C, 3 h | 500 °C, 2 h | 5Ir/Ce20-CCR |
| L3 | 60 °C, 3 h | | 500 °C, 2 h | 60 °C, 8 h | | 500 °C, 2 h | 5Ir/L3-RR |
| TH100 | 60 °C, 3 h | | 500 °C, 2 h | 60 °C, 8 h | | 500 °C, 2 h | 5Ir/TH100-RR |
| Sir10 | 60 °C, 3 h | | 500 °C, 2 h | 60 °C, 8 h | | 500 °C, 2 h | 5Ir/Sir10-RR |

#### 2.2.2.2.2. Addition of La and Ce promoters via IWI synthesis method

To synthesize 1 g of promoted support materials, first alumina support was placed in a vacuum flask and then located in the sonicator. One end of the vacuum flask was connected

to the vacuum pump and the other end was connected to the hose of the peristaltic pump using a pastor pipette, as mentioned before. Then the support material was left under vacuum for 30 min. 1.5 ml of aqueous solution of 5 wt. %, 10 wt. % $La(NO_3)_3 \cdot 6H_2O$ or 5 wt. %, 10 wt. % $Ce(NO_3)_3 \cdot 6H_2O$ was impregnated to the supports with the help of the peristaltic pump (calibrated for 0.1 ml/min). The corresponding amounts of alumina support and metal nitrate precursors are shown in **Table 2-3**. After impregnation, sample was left under vacuum for 40 min and then placed in a drying oven at 110 °C for 3 h. Sample was then calcined at 550 °C for 5 h (temperature ramp: 7.5 °C/min). For the Ir addition, the same procedure was applied as mentioned in **Section 2.2.2.2.1**. Synthesized samples and their pretreatment conditions are listed in **Table 2-4**.

***Table 2-3.*** *Promoter and support amounts used in the IWI method.*

| | **Support amount (g)** | **Promoter amount (g)** |
|---|---|---|
| 5 wt% La | 0.95 | 0.1261 |
| 10 wt% La | 0.90 | 0.2522 |
| 5 wt% Ce | 0.95 | 0.1329 |
| 10 wt% Ce | 0.90 | 0.2658 |

***Table 2-4.*** *Synthesis conditions for the La and Ce promoted samples synthesized via IWI method.*

| Support Name | La addition (5 wt%) | | Ce addition (5 wt%) | | 1st $IrCl_3$ addition (2.5 wt%) | | | 2nd $IrCl_3$ addition (2.5 wt%) | | | Sample code |
|---|---|---|---|---|---|---|---|---|---|---|---|
| | Drying | Calcination | Drying | Calcination | Drying | Calcination | Reduction | Drying | Calcination | Reduction | |
| L3 | 110 °C, 3 h | 550 °C, 5 h | - | - | 60 °C, 3 h | 400 °C, 3 h | - | 60 °C, 8 h | 400 °C, 3 h | 500 °C, 2 h | 5Ir/5La/L3-CCR |
| L3 | - | - | 110 °C, 3 h | 550 °C, 5 h | 60 °C, 3 h | 400 °C, 3 h | - | 60 °C, 8 h | 400 °C, 3 h | 500 °C, 2 h | 5Ir/5Ce/L3-CCR |
| TH100 | 110 °C, 3 h | 550 °C, 5 h | - | - | 60 °C, 8 h | 400 °C, 3 h | - | 60 °C, 8 h | 400 °C, 3 h | 500 °C, 2 h | 5Ir/5La/TH100-CCR |
| TH100 | - | - | 110 °C, 3 h | 550 °C, 5 h | 60 °C, 8 h | 400 °C, 3 h | - | 60 °C, 8 h | 400 °C, 3 h | 500 °C, 2 h | 5Ir/5Ce/TH100-CCR |
| Sir10 | 110 °C, 3 h | 550 °C, 5 h | - | - | 60 °C, 8 h | 400 °C, 3 h | - | 60 °C, 8 h | 400 °C, 3 h | 500 °C, 2 h | 5Ir/5La/Sir10-CCR |
| Sir10 | - | - | 110 °C, 3 h | 550 °C, 5 h | 60 °C, 8 h | 400 °C, 3 h | - | 60 °C, 8 h | 400 °C, 3 h | 500 °C, 2 h | 5Ir/5Ce/Sir10-CCR |
| L3 | 110 °C, 3 h | 550 °C, 5 h | - | - | 60 °C, 8 h | 400 °C, 3 h | - | 60 °C, 8 h | 400 °C, 3 h | 500 °C, 2 h | 5Ir/5La/L3-RR |
| L3 | - | - | 110 °C, 3 h | 550 °C, 5 h | 60 °C, 8 h | 400 °C, 3 h | - | 60 °C, 8 h | 400 °C, 3 h | 500 °C, 2 h | 5Ir/5Ce/L3-RR |
| TH100 | 110 °C, 3 h | 550 °C, 5 h | - | - | 60 °C, 3 h | | 500 °C, 2 h | 60 °C, 8 h | | 500 °C, 2 h | 5Ir/5La/TH100-RR |
| TH100 | - | - | 110 °C, 3 h | 550 °C, 5 h | 60 °C, 3 h | | 500 °C, 2 h | 60 °C, 8 h | | 500 °C, 2 h | 5Ir/5Ce/TH100-RR |
| Sir10 | 110 °C, 3 h | 550 °C, 5 h | - | - | 60 °C, 3 h | | 500 °C, 2 h | 60 °C, 8 h | | 500 °C, 2 h | 5Ir/5La/Sir10-RR |
| Sir10 | - | - | 110 °C, 3 h | 550 °C, 5 h | 60 °C, 3 h | | 500 °C, 2 h | 60 °C, 8 h | | 500 °C, 2 h | 5Ir/5Ce/Sir10-RR |

## 2.3. INSTRUMENTATION

### 2.3.1. Ex-situ Characterization

#### 2.3.1.1. X-ray diffraction (XRD)

X-ray diffraction (XRD) measurements were performed using a Panalytical X'PertPro Multipurpose X-Ray Diffractometer with a CuKα X-Ray source (40 kV, 45 mA, λ = 1.5405 Å). Williamson-Hall analysis was carried out by using the Rigaku Smartlab program.

#### 2.3.1.2. $N_2$ adsorption measurements

SSA of the samples were measured via the five-point Brunauer-Emmett-Teller (BET) method by low temperature isothermal adsorption/desorption of $N_2$(g) (purity > 99.99%, Linde GmbH). Prior to $N_2$ adsorption measurements, samples were degassed in vacuum at 300 °C for 2 h. $N_2$ adsorption analyses were carried out using a Micromeritics ASAP 2000 gas sorption and porosimetry system.

#### 2.3.1.3. Transmission electron microscopy (TEM) images and energy dispersive X-ray (EDX) analyses

Two different instruments were used for acquiring TEM images.

1) Bright field TEM images were obtained using a Hitachi HT7700 TEM with an electron beam energy of 120 kV.

2) FEI Technai G2 F30 TEM was used in both dark field (STEM HAADF) and bright field (HRTEM) mode. EDX measurements were carried out from multiple regions. A beam voltage of 300 kV was used for TEM imaging. Particle size estimations were done using the TEM images via ImageJ software, by including 100 particles.

#### 2.3.1.4. Raman spectroscopy

Raman measurements were performed using the WITech-alpha300 S Raman Spectrometer and a laser excitation with a wavelength of 532 nm.

#### 2.3.1.5. X-ray photoelectron spectroscopy (XPS)

X-ray photoelectron spectroscopy (XPS) experiments were performed with a SPECS PHOIBOS hemispheric energy analyzer. Monochromatic Al-Kα X-ray source (14 kV, 400 W) was used during the XPS data collection. Data analysis was performed using CasaXPS (v2.3.23rev1.1G)[107] software utilizing a Shirley background. Peak fits were achieved by using Gaussian–Lorentzian (GL) or Lorentzian Functional (LF) line shapes. Ir4f spectra were fitted with an energy difference of 3 eV within Ir $4f_{5/2}$ and Ir $4f_{7/2}$ peaks, and an area ratio of 0.75:1, respectively. Binding energy (B.E.) calibration was performed using the C1s signal at 284.8 eV.

#### 2.3.1.6. X-ray florescence (XRF)

Quantification of Ir loadings in the bulk of the catalysts were carried out via a Bruker S2 PUMA Energy Dispersive X-ray Fluorescence (EDXRF) spectrometer which was equipped with a silicon drift detector and a silver X-ray source (maximum power, 50 kV). For the XRF analysis, samples were packed in a loose powder form and measurements were performed under He atmosphere.

#### 2.3.1.7. ADN adsorption experiments

Relative ADN adsorption/uptake amounts of the catalyst samples were determined in a semi-quantitative fashion using a Bruker Alpha-II Platinum Attenuated Total Reflectance (ATR)-IR spectrometer. Prior to these measurements, 3 mg of a catalyst sample was mounted on a tungsten grid. Then, the samples were dipped into a saturated ADN-water mixture (7 g ADN dissolved in 10 ml water) for 1 min. Next, the catalyst sample was dried under air, followed by acquisition of the ATR-IR spectra.

#### 2.3.1.8. Gas phase decomposition products via FTIR

Gas phase decomposition products were investigated by connecting the heated Simultaneous Differential Scanning Calorimetry/Thermogravimetric Analysis (DSC/TGA) (TA instruments SDT 650 device) exhaust gas line to an online Bruker FTIR spectrometer equipped with an IR gas cell. During these measurements, 3 mg catalyst was placed into the hermetic aluminum pan which can resist up to 3 bar of internal pressure and 1 µl ADN-based fuel was introduced on to the catalyst with a micropipette. Samples were analyzed from RT to 250 °C with a heating rate of 4 °C/min in $N_2$ flow (30 ml/min). The FTIR spectra with 4 $cm^{-1}$ resolution and 32 scan were recorded every 4 min.

### 2.3.2. *In-Situ* Experiments

#### 2.3.2.1. Pyridine adsorption experiments via *in-situ* FTIR

Pyridine adsorption experiments via *in-situ* Fourier transform infrared (FTIR) spectroscopy were done by using a custom design *in-situ* FTIR cell equipped with a pyridine vapor doser and a rotary vane pump for evacuation. Samples were pressed on a tungsten grid and placed into the *in-situ* FTIR cell. Before pyridine adsorption experiments, each sample was annealed under vacuum at 500 °C for 5 min with a heating ramp of 12 °C /min to activate the surfaces. Approximately, 20 Torr pyridine vapor was dosed over the samples for 30 min. The *in-situ* FTIR spectra with 1 $cm^{-1}$ resolution and 256 scan were recorded after evacuation of pyridine for 15 min.

#### 2.3.2.2. CO chemisorption

Surface dispersion of Ir and the total number of Ir active sites on the catalyst surfaces were determined via CO chemisorption method by using a Hiden Analytical CATLAB mass spectroscopic instrument. Prior to measurements, samples were reduced *in-situ* at 500 °C under 5% $H_2$/He flow and then cooled to 35 °C. CO uptake measurements were performed at 35 °C under 60 ml/min He flow and injection of 0.1 ml pulses of 5% CO over the catalyst samples. In the dispersion calculations, a CO/Ir stoichiometry of 1 was assumed [108,109].

#### 2.3.2.3. CO adsorption via *in-situ* FTIR spectroscopy and temperature programmed desorption (TPD)

CO adsorption experiments via *in-situ* Fourier transform infrared (FTIR) spectroscopy were executed in transmission mode in a custom-design batch-type in-situ spectroscopic reactor coupled to a Bruker Tensor 27 FTIR spectrometer equipped with a liquid nitrogen-cooled mercury cadmium telluride (MCT) IR detector. The *in-situ* spectroscopic reactor was

also connected to a quadruple mass spectrometer (QMS, Stanford Research Systems, RGA 200) for temperature programmed desorption (TPD) measurements. Experimental details of the currently performed TPD experiments can be found elsewhere[110]. Before the CO adsorption experiments, each sample was activated via an initial treatment including annealing at 500 °C for 10 min in 5 wt.% $H_2$/Ar mixture (Linde GmbH) with a total pressure of 10 Torr. Then the sample was cooled to 50 °C and the reactor was evacuated to $10^{-3}$ Torr. Next, catalyst sample was exposed to various pressures ($P_{CO(g)}$ = 0.01, 0.04, 0.2, 0.9, 12, 36.5 Torr) of CO (g) (Linde GmbH, purity >99.99%) and kept at each pressure for 10 min at 50 °C. As the last adsorption step, sample was exposed to 60 Torr CO for 30 min to saturate the surface with CO. After each CO exposure, the spectroscopic reactor was evacuated and in-situ FTIR spectra were recorded with a frequency resolution of 1 $cm^{-1}$ and by averaging 128 scans per spectrum. CO TPD experiments were performed with 5 Torr CO at 50 °C for 30 min followed by evacuation of the reactor to $10^{-3}$ Torr. During the TPD runs, catalyst samples were heated from 50 °C to 500 °C with a linear heating rate of 12 °C /$min^{-1}$ in vacuum.

#### 2.3.2.4. *In-situ* extended X-ray absorption fine structure (EXAFS) and *in-situ* X-ray absorption near edge spectroscopy (XANES) experiments

*In-situ* extended X-ray absorption fine structure (EXAFS) and *in-situ* x-ray absorption near edge spectroscopy (XANES) experiments were designed and carried out at the ROCK beamline of the Soleil Synchrotron Facility (Saint-Aubin, France). EXAFS and XANES data were collected for the Ir $L_{III}$ edge of the synthesized catalysts. Quick EXAFS (QEXAFS) monochromator was utilized to monitor the time-resolved changes in the Ir $L_{III}$ edge as a function of treatment conditions[111]. The Ir $L_{III}$ edge energy (11215 eV) was calibrated using

a metallic Ir reference foil. Each XANES/EXAFS spectrum for a given catalyst sample was acquired by averaging 1200 scans. In the EXAFS analysis, the forward Fourier transform range was determined to be within 3-17 $Å^{-1}$, where 1-3 $Å^{-1}$ range was used as the fitting (backward Fourier transform) interval. Ir was chosen as the main absorber in the fitting of the EXAFS data. EXAFS/XANES data analysis were carried out by using the IFEFFIT tool of the Demeter software package[112]. For the in-situ EXAFS/XANES measurements, catalyst samples were mounted in a spectroscopic flow reactor equipped with a custom-design capillary flow cell which was heated via a gas blower heating system[113]. This setup allowed exposure of the catalyst surfaces to reducing or oxidizing conditions with a gas mixture of desired composition, flow rate and temperature during the XANES/EXAFS measurements.

*In-situ* XANES/EXAFS experiments were carried out using two different experimental procedures. The first procedure was designed to mimic the synthesis protocol of the catalysts classified with the "*CCR*" code. Here, the support materials were impregnated with 2.5 wt.% Ir, dried in air at 60 °C for 8 h and calcined in air at 400 °C for 3 h. This is followed by the second loading of 2.5 wt.% Ir and drying in air at 60 °C for 8 h. These samples were placed into the in-situ capillary XANES/EXAFS flow cell. Next, the sample was exposed to 20 % $O_2$/Ar gas mixture with a flow rate of 30 ml/min and heated from room temperature (RT) to 400 °C using a heating rate of 7 °C/min in this gas mixture. After waiting for 10 min at 400 °C, sample was cooled to RT and the gas mixture was switched to 5 % $H_2$/Ar (flow rate = 30 ml/min) and the catalyst was heated to 500 °C with a heating rate of 7 °C/min. Then the sample was cooled to RT in 5 % $H_2$/Ar after waiting fo 10 min at 500 °C, and in-situ XANES/EXAFS data were collected for the *CCR* samples at RT. To imitate the "re-oxidation" of the *CCR* samples under ambient conditions after the completion of the catalyst

synthesis protocol, gas composition was switched to 20 % $O_2$/Ar (flow rate = 30 ml/min) at RT and a second set of in-situ XANES/EXAFS data were collected at RT.

The second in-situ XANES/EXAFS experimental procedure was designed to mimic the synthesis protocol of the catalysts denoted with the "*RR*" code. In this procedure, the support materials were impregnated with 2.5 wt.% Ir, dried in air at 60 °C for 8 h and reduced under 100 ml/min 5% $H_2$/Ar flow at 500 °C for 2 h. This is followed by the second loading of 2.5 wt.% Ir and drying in air at 60 °C for 8 h. These samples were placed into the in-situ capillary XANES/EXAFS flow cell. Then, the catalysts were heated from RT to 500 °C with a heating rate of 7 °C/min in 5 % $H_2$/Ar (flow rate = 30 ml/min). Then the catalysts were kept at 500 °C for 10 min, followed by cooling to RT in this gas mixture, where the in-situ XANES/EXAFS data for the *RR* catalysts were collected. Re-oxidation of the *RR* samples were also investigated by switching the gas composition to 20 % $O_2$/Ar (flow rate = 30 ml/min) at RT and subsequent in-situ XANES/EXAFS data acquisition at RT.

### 2.3.3. Performance Measurements

#### 2.3.3.1. Differential Scanning Calorimetry/Thermal Gravimetric Analysis (DSC/TGA)

DSC/TGA measurements were carried out by using a TA Instruments Q600 SDT Simultaneous Thermal Analyzer. In these measurements, an open alumina pan was used. The amount of ADN mixture was fixed at 0.8 µl and the amount of catalyst was kept between 2.0-2.5 mg. DSC/TGA measurements were performed under a flow of 100 ml/min $N_2$ (g). Prior to the measurements, the system was stabilized 35 °C under nitrogen flow. The heating ramp was then started at 35 °C and reached to maximum 250 °C. In the DSC / TGA

experiments, the temperature ramp was set to 20 °C/min from 35 °C to 110 °C and 5 °C/min from 110 to 250 °C.

In order to compare the thermal decomposition characteristics of different ADN mixtures, two particular parameters were exploited. One of these parameters is the onset temperature (which will be denoted as $T_{Onset}$, given in °C, throughout the text) at which the reaction is initiated, and the second parameter is the *specific energy* generated per mass of the ADN mixture used (which will be denoted as *Energy*, given in J/g, throughout the text). An example DSC curve shown in **Figure 2-24** reveals the $T_{Onset}$ and Energy values as a result of ADN decomposition. $T_{Onset}$ is determined from the maximum point of the 1st derivative of the heat flow, while the area under the heat flow curve yields the Energy value.

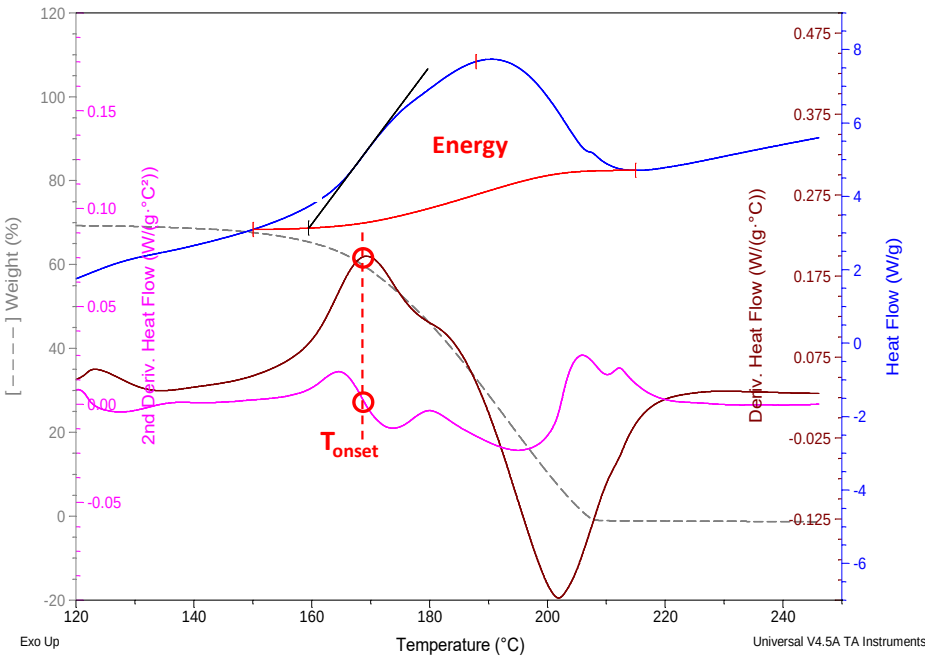



***Figure 2-24.*** *Typical heat flow and weight % plots obtained during ADN decomposition in a DSC/TGA measurement.*

#### 2.3.3.2. Custom-design Micro Propulsion Batch Reactor Parameters

In a typical catalytic ADN decomposition test, catalyst sample was placed in the reaction compartment of the batch reactor. Then, the reactor was filled with Ar(g) ($P_{Ar(g)}$ = 1 bar) to obtain an inert/anaerobic atmosphere and ADN was injected onto the catalyst powder at RT. Next, computer-controlled temperature ramp was initiated. Time-dependent pressure and temperature data were recorded during the heating ramp. **Figure 2-25** shows typical temperature vs. time and pressure vs. time plots obtained from one of the batch reactors during a catalytic ADN decomposition run. The onset temperature ($T_{Onset}$) value obtained from the temperature vs. time plot (revealing the triggering of the ADN decomposition reaction) and ΔP value acquired from the pressure vs. time plot (showing the extent of total pressure generation due to the ADN decomposition reaction) were used to compare relative performances of the catalysts in the catalytic anaerobic decomposition of ADN. A lower $T_{Onset}$ value signifies diminishing of the apparent activation energy of the reaction and a greater ΔP value contributes to an enhanced thrust.

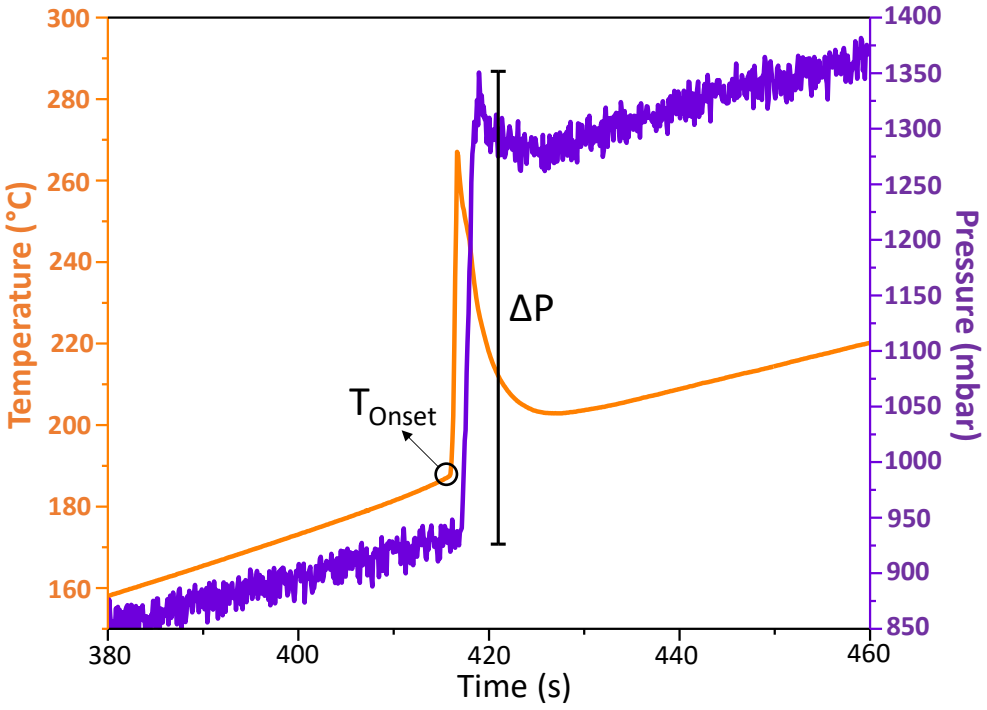



***Figure 2-25.*** *Typical temperature vs. time and pressure vs. time plots obtained during a catalytic anaerobic ADN decomposition run.*

# CHAPTER 3

## 3. CRYSTALLOGRAPHIC STRUCTURE AND THERMAL STABILITY OF THE SUPPORT MATERIALS: CHOICE OF THE ALUMINA SUPPORT

Some of the most important features in ADN/HAN decomposition catalysts are a) enhanced PGM dispersion and b) improved thermal stability of the support material [103,104,114,115]. As described in Chapter 3, in an attempt to choose the optimum alumina support material to be used in catalyst synthesis, we carried out XRD and $N_2$ adsorption studies which allowed us to determine the crystallographic phases and SSA values of fresh and thermally aged alumina support materials.

### 3.1. XRD analyses of the alumina support materials

Thermal stability and the phase changes of SBa200, TH100, L3, SCFa140, MG5, Ce20, Sir5, Sir10, and Sir20 support materials were investigated via XRD after thermal treatment at 550 °C and 1100 °C. As mentioned before, alumina materials derived from boehmite precursor consecutively acquires $\gamma \rightarrow \delta \rightarrow \theta \rightarrow \alpha$ crystallographic phases with increasing temperatures, where the corresponding SSA values monotonically decrease during these successive polymorphic phase transitions [52]. The $\gamma$-$Al_2O_3$ phase has the most disordered (amorphous) and porous structure with the largest SSA, while the $\alpha$- $Al_2O_3$ has the most ordered crystal structure with the lowest SSA [52,53]. Current XRD measurements reveal the following alumina phases with the PDF card numbers given in parentheses; $\gamma$-$Al_2O_3$ (PDF: 00-046-1212), $\theta$-$Al_2O_3$ (PDF: 00-056-0456), $\delta$-$Al_2O_3$ (PDF: 00-056-1186), $\alpha$-$Al_2O_3$ (PDF: 00- 056-0457), $CeO_2$ (PDF: 04-016-4868), $MgAl_2O_3$ (PDF: 00-021-1152).

**Figure 3-1a** and **Figure 3-1b** show the XRD patterns of the SBa200 support material calcined at 550 °C and 1100 °C, respectively. At 550 °C, the detected alumina phases are γ-$Al_2O_3$ and δ-$Al_2O_3$ as shown in **Figure 3-1a**. Calcination at 1100 °C leads to the collapse in alumina structure and the formation of α-$Al_2O_3$ and θ-$Al_2O_3$.

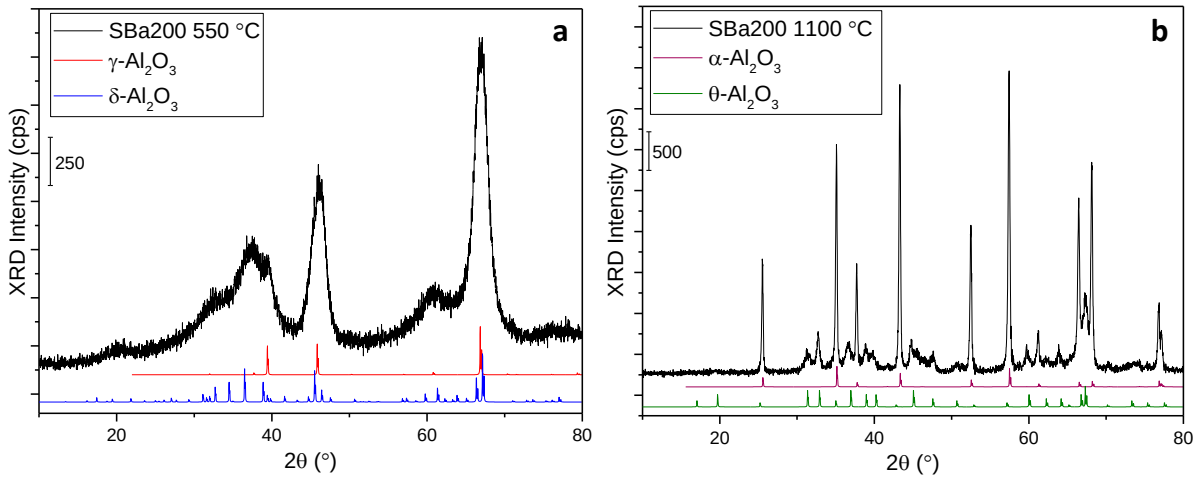



***Figure 3-1.*** *XRD patterns of SBa200 support material (a) after calcination at 550 °C, and (b) after thermal aging at 1100 °C.*

XRD patterns of TH100 support materials calcined at 550 °C and 1100 °C are given in **Figure 3-2a** and **Figure 3-2b**, respectively. TH100 support reveals γ-$Al_2O_3$ and δ-$Al_2O_3$ structures at 550 °C and these alumina phases transform to δ-$Al_2O_3$ and θ-$Al_2O_3$ after calcination at 1100 °C.

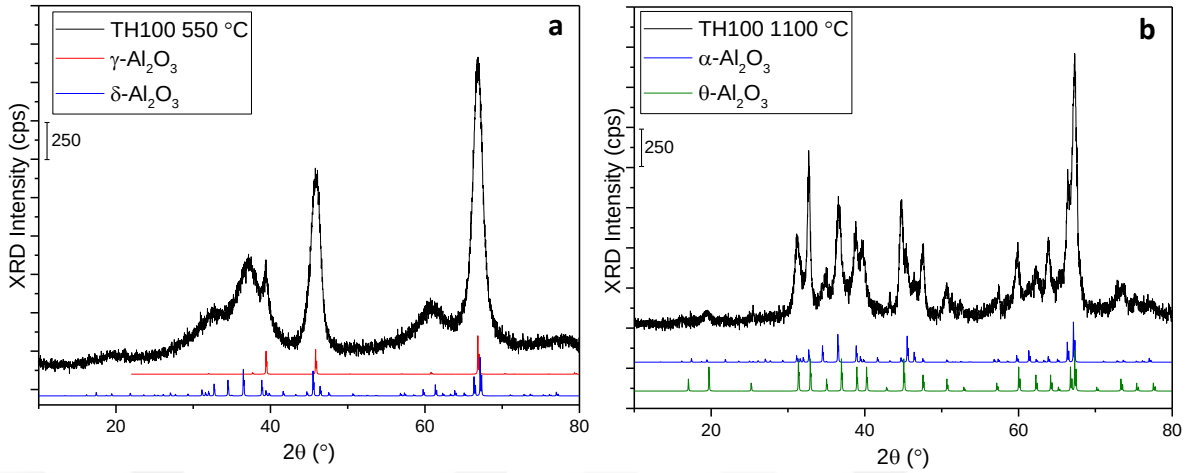



***Figure 3-2.*** *XRD patterns of TH100 support material (a) after calcination at 550 °C, and (b) after thermal aging at 1100 °C.*

**Figure 3-3a** and **Figure 3-3b** show the XRD patterns obtained after the calcination of 3 wt. % La loaded L3 support material at 550 °C and 1100 °C, respectively. The detected γ-$Al_2O_3$ and δ-$Al_2O_3$ phases at 550 °C (**Figure 3-3a**) undergo phase transitions to δ-$Al_2O_3$ and θ-$Al_2O_3$ at 1100 °C, respectively (**Figure 3-3b**) as in case of TH100 support material. No La-related phases were observed for the L3 support. This may be due to the low La loading and the formation of amorphous lantana-alumina mixed oxide phases.

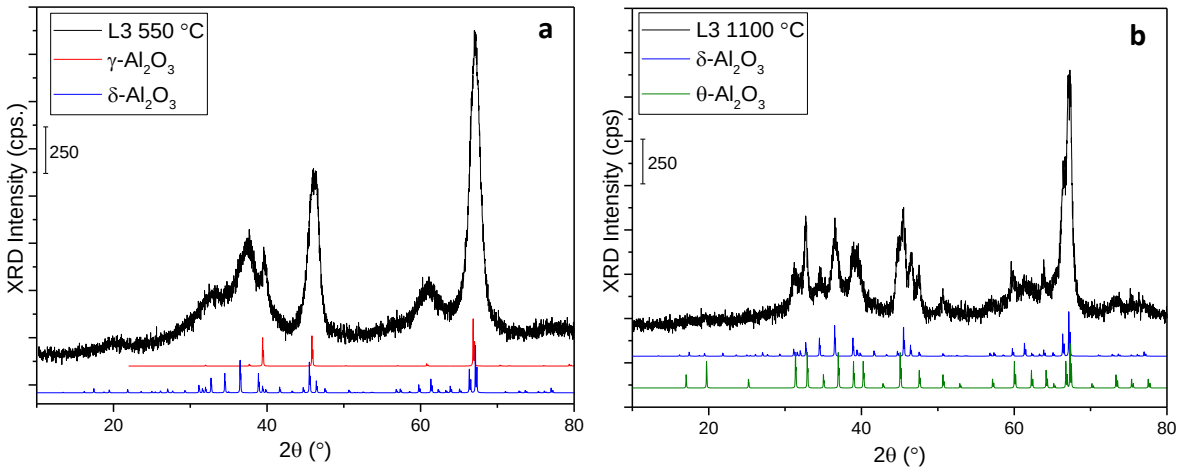



***Figure 3-3.*** *XRD patterns of L3 support material (a) after calcination at 550 °C, and (b) after thermal aging at 1100 °C.*

**Figure 3-4a** and **Figure 3-4b** show the XRD patterns of the SCFa140 support material calcined at 550 °C and 1100 °C, respectively. At 550 °C, $\gamma$-$Al_2O_3$ and $\delta$-$Al_2O_3$ phases were observed, whereas $\alpha$-$Al_2O_3$ and $\theta$-$Al_2O_3$ were detected at 1100 °C.

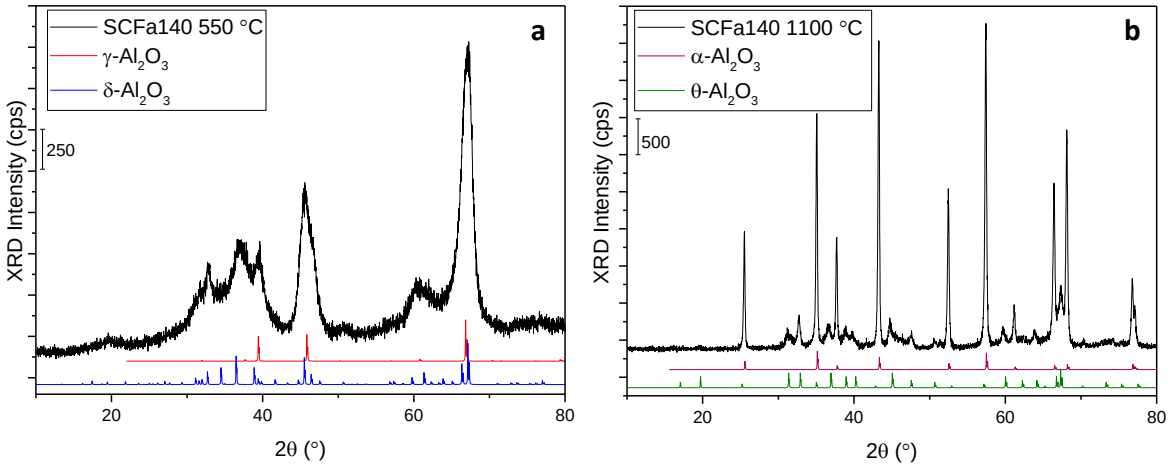



***Figure 3-4.*** *XRD patterns of SCFa140 support material (a) after calcination at 550 °C, and (b) after thermal aging at 1100 °C.*

XRD patterns of 5 wt.% Mg containing MG5 support material after calcination at 550 °C and 1100 °C are given in **Figure 3-5a** and **Figure 3-5b**, respectively. $\gamma$-$Al_2O_3$ and $\delta$-$Al_2O_3$

were the predominant phases at 550 °C on the MG5 support. As a result of thermal aging at 1100 °C, α-$Al_2O_3$ and $MgAl_2O_3$ phases emerged as shown in **Figure 3-5b**.

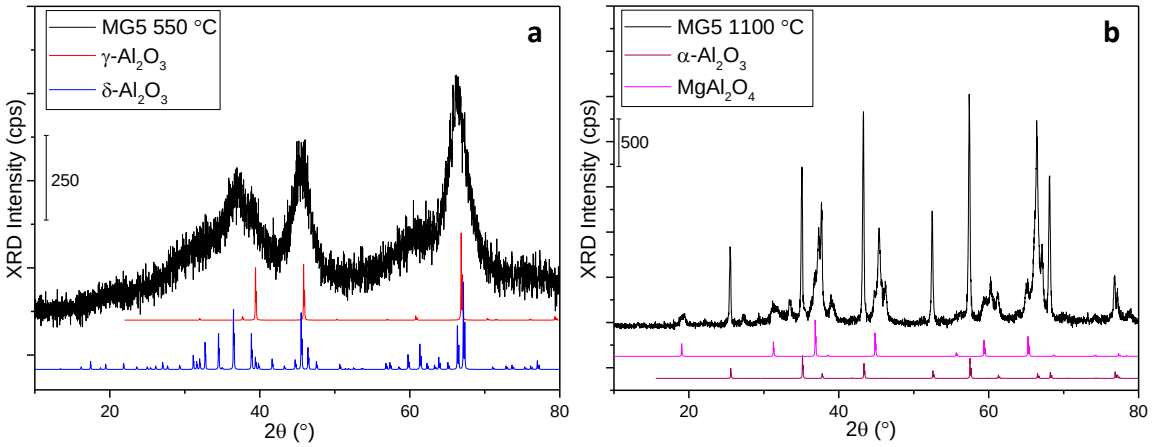



***Figure 3-5.*** *XRD patterns of MG5 support material (a) after calcination at 550 °C, and (b) after thermal aging at 1100 °C.*

**Figure 3-6a** and **Figure 3-6b** show the XRD patterns obtained after the calcination of 20 wt.% Ce containing Ce20 support material at 550 °C and 1100 °C, respectively. Before the high temperature thermal aging, γ-$Al_2O_3$, δ-$Al_2O_3$ and $CeO_2$ phases were observed (**Figure 3-6a**) whereas $CeO_2$ and θ-$Al_2O_3$ phases became dominant upon calcination at 1100 °C (**Figure 3-6b**).

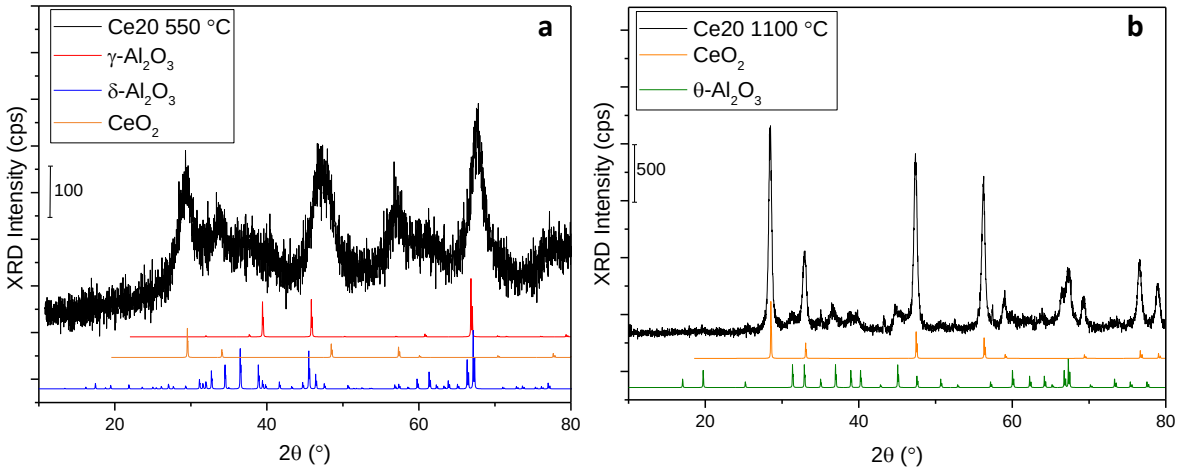



***Figure 3-6.*** *XRD patterns of Ce20 support material (a) after calcination at 550 °C, and (b) after thermal aging at 1100 °C.*

XRD patterns of 5 wt.% Si containing Sir5 support, 10 wt.% Si containing Sir10 support and 20 wt.% Si containing Sir20 support are given in **Figure 3-7**, **Figure 3-8** and **Figure 3-9**, respectively. The only detected phase was $\gamma$-$Al_2O_3$ for all silica containing support materials at 550 °C (**Figure 3-7a**, **Figure 3-8a**, **Figure 3-9a**). The small angle intensities of Sir10 samples are originated from the greater number of amorphous particles. After calcination at 1100 °C, both $\gamma$-$Al_2O_3$ and $\delta$-$Al_2O_3$ were observed for Sir5 (**Figure 3-7b**), Sir10 (**Figure 3-8b**), and Sir20 (**Figure 3-9b**).

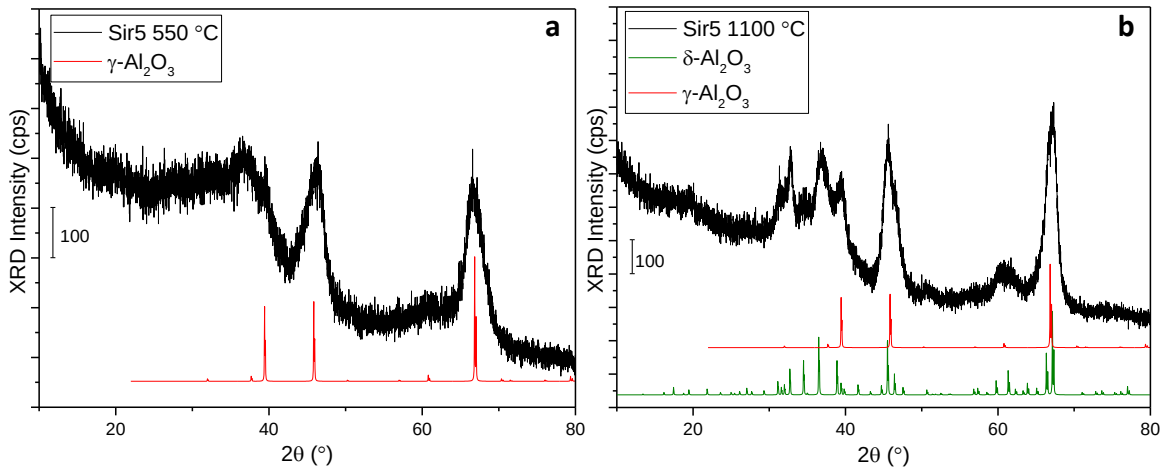



***Figure 3-7.*** *XRD patterns of Sir5 support materials (a) after calcination at 550 °C, and (b) after thermal aging at 1100 °C.*

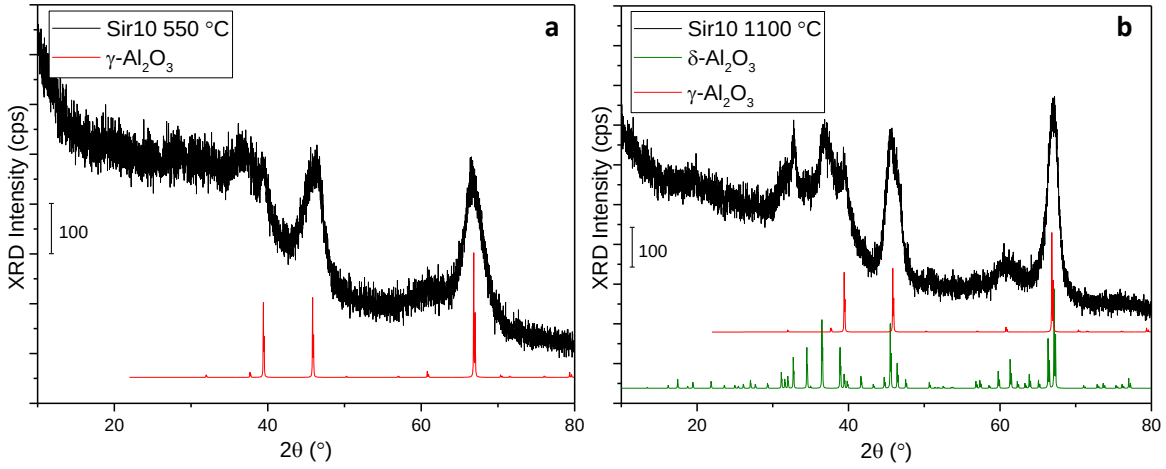



***Figure 3-8.*** *XRD patterns of Sir10 support material (a) after calcination at 550 °C, and (b) after thermal aging at 1100 °C.*

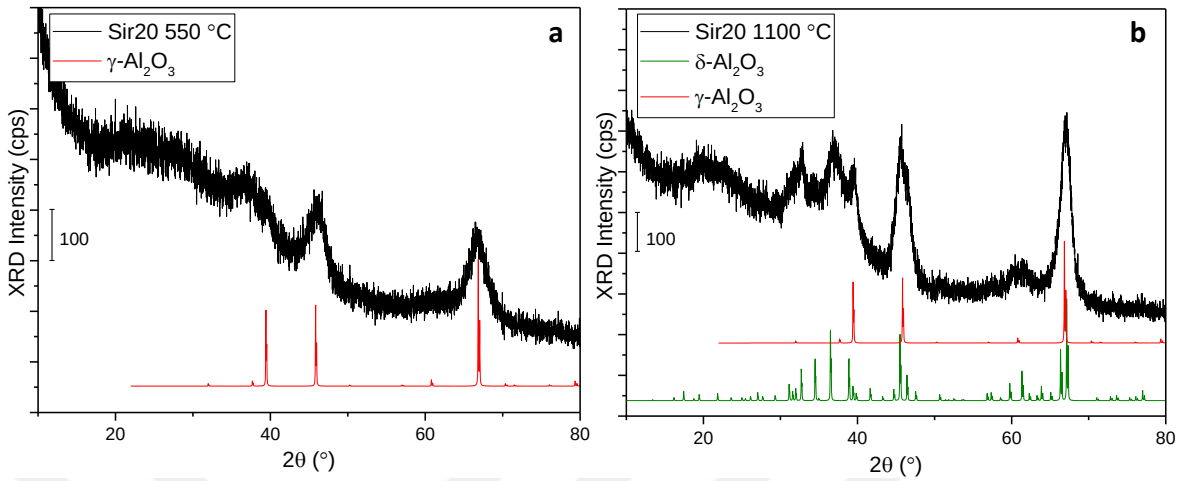



***Figure 3-9.*** *XRD patterns of Sir20 support material (a) after calcination at 550 °C, and (b) after thermal aging at 1100 °C.*

### 3.2. Specific surface area (SSA) values of the alumina support materials

SSA values of the fresh support materials are shown in **Figure 3-10** [116,117]. The Sir samples had higher SSA than other support materials and the highest SSA belonged to Sir20 (410 $m^2/g$). On the other hand, L3 and SCFa140 had the lowest SSA values (140 $m^2/g$). This observation is consistent with the aforementioned XRD measurements of the corresponding support materials. Sir samples result in only γ-$Al_2O_3$ phase, on the other hand, L3 and SCFa140 yield both δ-$Al_2O_3$ and γ-$Al_2O_3$ phases.

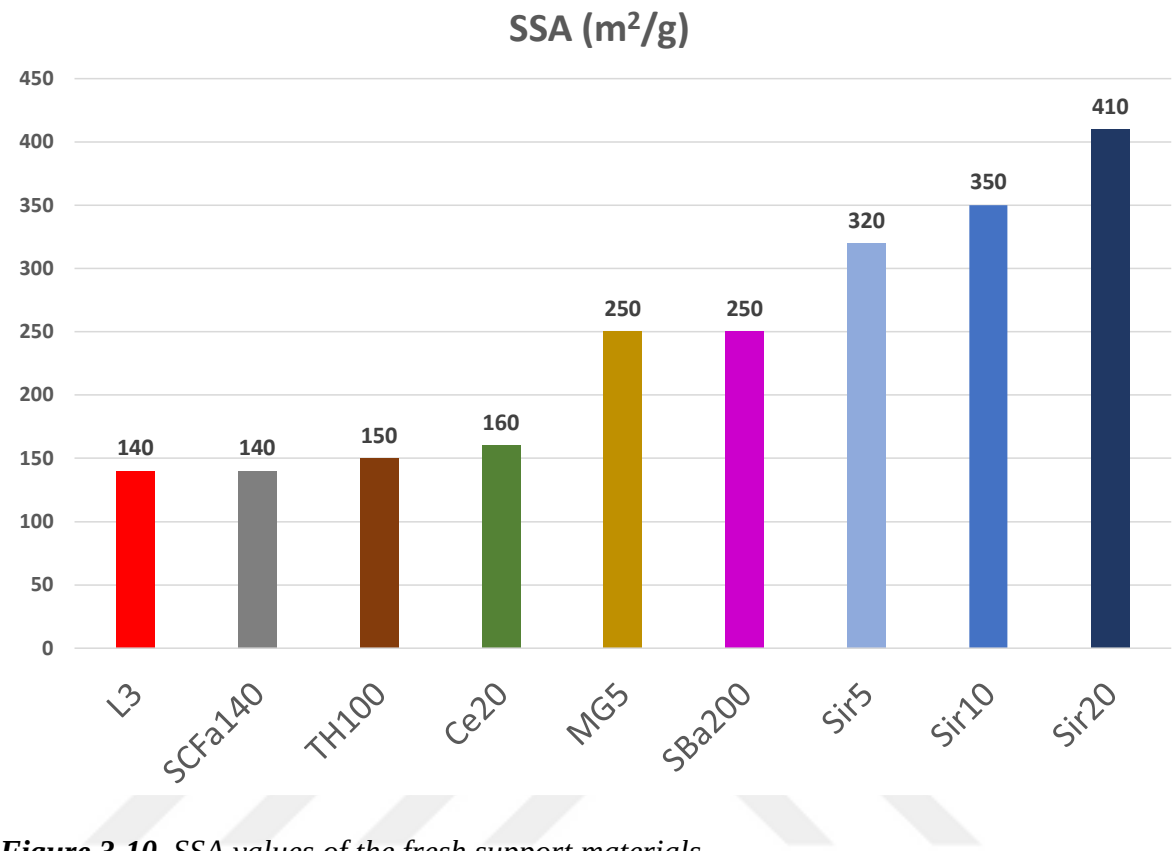



***Figure 3-10.*** *SSA values of the fresh support materials.*

**Figure 3-11a** and **Figure 3-11b** show the SSA values of the support materials after thermal aging at 1100 °C and 1200 °C, respectively. As in the case of the fresh support materials shown in **Figure 3-10**, Sir samples revealed higher SSA values than other support counterparts. Sir10 support had the highest SSA at both 1100 °C (150 $m^2/g$) and 1200 °C (80 $m^2/g$). Although the fresh L3 support had the lowest SSA value, it yielded significantly higher SSA than many other support materials after thermal aging. Current BET results for the thermally aged support materials are in good agreement with the XRD data shown in **Section 3.1**. Even at 1100 °C, Sir samples show γ-$Al_2O_3$ diffraction patterns which is the phase with the highest surface area of $Al_2O_3$ (**Figure 3-7**, **Figure 3-8**, and **Figure 3-9**).

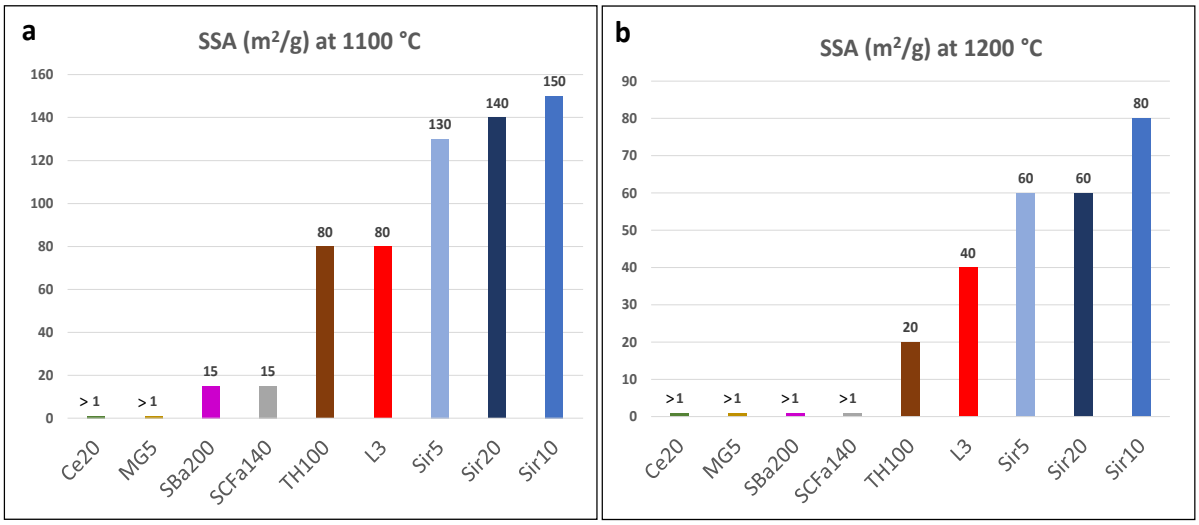



***Figure 3-11.*** *SSA values for support materials calcined at (a) 1100 °C and (b) 1200 °C.*

**Table 3-1** summarizes the crystalline phases and SSA values of the alumina support materials after calcination at 550 °C and 1100 °C. At 550 °C, γ-$Al_2O_3$ and δ-$Al_2O_3$ were observed for SBa200, L3, TH100, SCFa140, Ce20, MG5, whereas only γ-$Al_2O_3$ phase was observed for Sir5, Sir10, and Sir20. Moreover, among the fresh samples, silica containing supports (Sir5, Sir10, Sir20) had higher SSA than others. After calcination at 1100 °C, transition to more ordered δ, θ and α phases was observed depending on the support material. SBa200, SCFa140, MG5, Ce20 support materials formed θ/α-$Al_2O_3$ phases after thermal aging and lost a significant portion of their SSA as a result of the collapse of the alumina structure. On the other hand, the predominant alumina phase was δ/θ for TH100, L3 and γ/δ for Sir5, Sir10 and Sir20 supports. The highest SSA values were observed for Sir samples followed by L3 and TH100 at 1100 °C and 1200 °C. TH100, L3, Sir5, Sir10 and Sir20 support materials were found to be more resistant towards thermal aging. Therefore, rest of the experimental efforts were mostly focused on these support materials.

After getting detailed information about different support structures, we carried on our experiments by characterizing the different types of ADN mixtures provided by manufacturer.

***Table 3-1.*** *Crystalline phases and SSAs for different alumina types used in catalyst synthesis after calcination at 550 °C and 1100 °C.*

| | **550°C** | | **1100°C** | | **1200°C** |
|---|---|---|---|---|---|
| **Support Name** | **Phase** | **SSA ($m^2/g$)** | **Phase** | **SSA ($m^2/g$)** | **SSA ($m^2/g$)** |
| SBa200 | γ, δ | 250 | θ, α | 15 | - |
| TH100 | γ, δ | 150 | δ, θ | 80 | 20 |
| L3 | γ, δ | 140 | δ, θ | 80 | 40 |
| SCFa140 | γ, δ | 140 | θ, α | 15 | - |
| MG5 | γ, δ | 250 | α, $MgAl_2O_4$ | - | - |
| Ce20 | γ, δ | 160 | θ, $CeO_2$ | - | - |
| Sir5 | γ | 320 | γ, δ | 130 | 60 |
| Sir10 | γ | 350 | γ, δ | 150 | 80 |
| Sir20 | γ | 410 | γ, δ | 140 | 60 |

# CHAPTER 4

## 4. THERMAL DECOMPOSITION CHARACTERISTICS OF ADN BASED FUELS IN THE ABSENCE OF A CATALYST

Before starting the decomposition studies of ADN mixture in the presence of a catalyst, it was necessary to obtain information about its thermal (self) decomposition behavior. In this section, the investigation of different ADN mixtures given by the manufacturer was carried out by DSC/TGA and custom-made micro propulsion batch reactor measurements. While the batch reactor was in the design stage, the performances of the ADN mixtures were determined with DSC/TGA measurements.

### 4.1. Thermal decomposition characteristics of ADN mixtures (STY-120-X) in the absence of a catalyst via DSC/TGA

ADN mixtures labeled as STY-120-X (X= 1, 3, 4, 5) samples contained 60 wt.% ADN + 40 wt.% water, $NH_3$, methanol. Thermal decomposition characteristics of different ADN mixtures obtained via DSC/TGA measurements were compared based on $T_{Onset}$ and Energy values as defined in **Section 2.3.3.1**. Histogram given in **Figure 4-1** show $T_{Onset}$ and Energy values obtained from the thermal decomposition of STY-120-1, STY-120-3, STY-120-4, STY-120-5. The average $T_{Onset}$ values of "STY-120-1", "STY-120-3", "STY-120-4", "STY-120-5" ionic liquids were measured as 168.8 °C, 170 °C, 169.5 °C, 168.8 °C, respectively. Accordingly, the generated energy values were also measured as 1447 J/g, 1446 J/g, 1368 J/g and 1511 J/g for STY-120-1", "STY-120-3", "STY-120-4", "STY-120-5", respectively. The onset temperatures and generated energy values of all investigated ADN batches were found to be comparable.

Results of all DSC/TGA measurements performed for STY-120-1, STY-120-3, STY-120-4, STY-120-5 in the absence of a catalyst are presented in **Appendix A1-Appendix A5**.

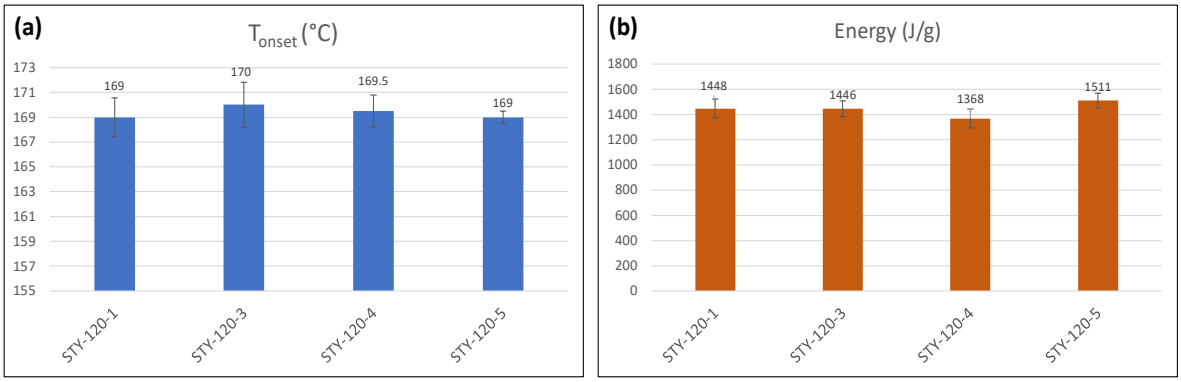



***Figure 4-1.*** *Histograms showing the (a) $T_{Onset}$ and (b) Energy values of STY-120-1, STY-120-3, STY-120-4, STY-120-5 ADN mixtures in the absence of a catalyst.*

## 4.2. Comparison of thermal decomposition characteristics of STY-126-X based ADN mixtures on SBa200 alumina in the absence of any catalytic active sites via custom-design micro propulsion batch reactor measurements

**Figure 4-2** and **Table 4-1** present the average $T_{Onset}$ and ΔP values obtained from custom-design micro propulsion batch reactor measurements for all STY-126 coded ADN mixtures. Definitions of $T_{Onset}$ and ΔP was given in **Section 2.3.3.2**. STY-126-7 revealed the lowest $T_{Onset}$ and triggered the ADN decomposition reaction at an earlier temperature than other ADN mixtures (**Figure 4-2a)** while the highest onset temperature value was observed for STY-126-4. In terms of ΔP values, STY-126-2 yielded the highest ΔP value, whereas STY-126-3 resulted in the lowest ΔP value (**Figure 4-2b**). Data given in **Figure 4-2** and **Table 4-1** reveal valuable information shedding light on the variations of the non-catalytic thermal decomposition characteristics of the ADN formulations possessing similar compositions but prepared with different synthetic protocols. While average $T_{Onset}$ and ΔP values of all STY-

126-X fuels are comparable, detectable differences in these values can also be identified in accurate experimental studies carried out in the custom-design micro propulsion batch reactor system.

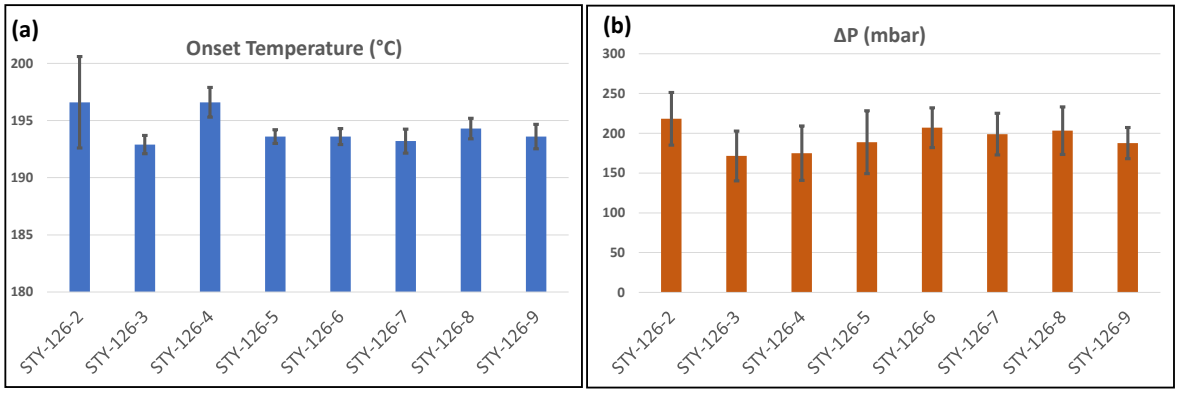



***Figure 4-2.*** *Comparison of (a) $T_{Onset}$ and (b) ΔP values of STY-126-2, STY-126-3, STY-126-4, STY-126-5, STY-126-6, STY-126-7, STY-126-8, STY-126-9 ADN mixtures measured with SBa200 alumina (in the absence of any catalytically active sites) in the custom-design micro propulsion batch reactor.*

***Table 4-1.*** *$T_{Onset}$ and ΔP values of STY-126-X ADN mixtures measured with SBa200 alumina (in the absence of any catalytically active sites) in the custom-design micro propulsion batch reactor.*

| NAME | $T_{onset}$ (°C) | Standard Deviation $T_{onset}$ | ΔP (mbar) | Standard Deviation ΔP |
|---|---|---|---|---|
| **STY-126-2** | 196.6 | 4.0 | 218.2 | 33.1 |
| **STY-126-3** | 192.9 | 0.8 | 171.5 | 31.3 |
| **STY-126-4** | 196.6 | 1.3 | 175 | 34.2 |
| **STY-126-5** | 193.6 | 0.6 | 188.8 | 39.5 |
| **STY-126-6** | 193.6 | 0.7 | 207 | 25.0 |
| **STY-126-7** | 193.2 | 1.0 | 199 | 26.2 |
| **STY-126-8** | 194.3 | 0.9 | 203.3 | 29.9 |
| **STY-126-9** | 193.6 | 1.1 | 187.7 | 19.6 |

In this section, thermal decomposition behavior of ADN mixtures delivered by the manufacturer was investigated. It was demonstrated that most of these ADN mixtures revealed comparable thermal decomposition characteristics. Therefore, these ADN mixtures were used upon availability at the time of the catalytic decomposition experiments which will be shown in the forthcoming sections.

# CHAPTER 5

## 5. CHARACTERIZATION AND CATALYTIC PERFORMANCE OF THE CATALYSTS SYNTHESIZED VIA WETNESS IMPREGNATION

In Chapter 5, performance of ADN decomposition on 5 wt. % Ir containing 6 different support materials synthesized via WI were determined by TGA/DSC measurements. The synthesized catalysts were prepared at three calcination different temperatures; 550 °C, 900 °C and 1100 °C. These three temperatures are intended to compare the behavior of the fresh catalyst (550 °C), a moderately thermally aged catalyst (900 °C), and a severely thermally thermal aged (1100 °C) catalyst. In addition to performance measurements, structural characterizations of the synthesized catalysts were carried out by XRD (X-Ray Diffraction), Raman Spectroscopy, XPS (X-Ray Photoelectron Spectroscopy) and TEM (Transmission Electron Microscopy) methods.

### 5.1. PERFORMANCE OF THE CATALYSTS SYNTHESIZED VIA WI

**Figure 5-1** compares the average $T_{Onset}$ values of thermal and catalytic ADN (STY-120-1) decomposition acquired by DSC/TGA technique. Green bar in **Figure 5-1** shows the average $T_{Onset}$ value for thermal ADN decomposition (i.e., in the absence of a catalyst). 5 wt.% Ir containing different alumina support catalysts calcined at 550, 900, and 1100 °C were prepared via WI method as mentioned in **Section 2.2.2.1**. Here, different calcination temperatures applied on the Ir-containing catalysts attempt to mimic the thermal aging of the catalysts and its effect on the average $T_{Onset}$ value.

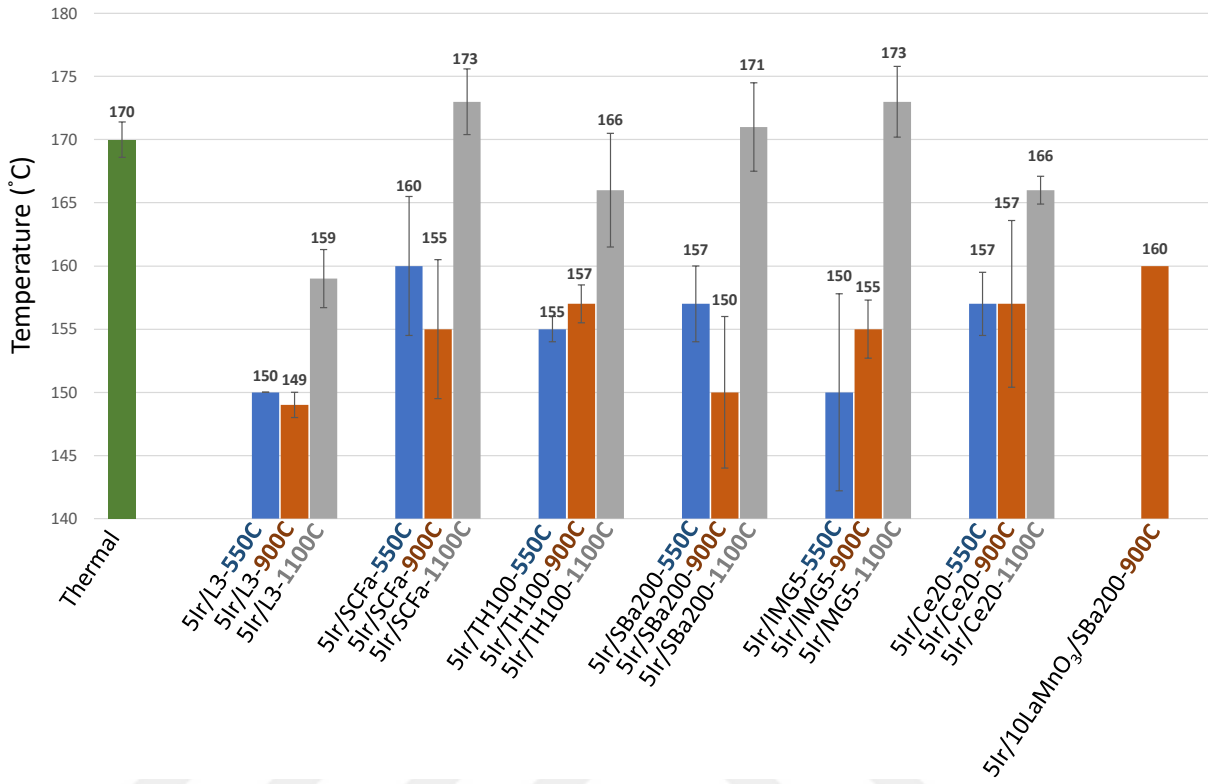



***Figure 5-1.*** *Average $T_{Onset}$ values for the decomposition of ADN mixture on various 5 wt. % Ir loaded alumina catalysts prepared via WI method calcined at 550 °C, 900 °C, and 1100 °C measured with the DSC/TGA technique. Green bar represents $T_{Onset}$ value for the thermal decomposition of ADN mixture in the absence of a catalyst.*

Ir-containing catalysts calcined at 550 °C (blue bars in **Figure 5-1**) can initiate the reaction at lower temperatures than the thermal decomposition of ADN mixture. This emphasizes that the catalysts have a favorable impact on the initiation of the decomposition process. The lowest $T_{Onset}$ (i.e., the most effective catalysts for triggering the ADN mixture decomposition) among the 6 different types of catalysts calcined at 550 °C belong to the 5Ir/L3 and 5Ir/MG5 samples. These catalysts can initiate the reaction at temperatures that are ca. 20 °C lower than the thermal decomposition of the ADN mixture. Calcination at 900 °C, leads to relatively moderate increase in $T_{Onset}$ values of the Ir-containing catalysts. This

observation indicates that even the simple and relatively primitive WI synthesis method can yield Ir-containing alumina catalysts with a reasonable thermal stability that can reveal fair catalytic activity after calcination at 900 °C. On the other hand, Ir-containing catalysts calcined at 1100 °C (gray bar in **Figure 5-1**) exhibit significant increase in $T_{Onset}$ values (i.e., a significant decrease in their ability to trigger the reaction). 5Ir/MG5 is one of the catalysts with the lowest $T_{Onset}$ at 550 °C, however, when it is calcined to 1100 °C, $T_{Onset}$ value is similar to that of the ADN mixture in the absence of a catalyst.

**Figure 5-1** clearly indicates that the calcination of the Ir-containing catalysts at elevated temperatures typically increases the $T_{Onset}$ of the ADN decomposition suggesting the thermal aging and performance degradation of the catalysts. The decrease in the $T_{Onset}$ with the increasing calcination temperature is lower for the 5Ir/L3 and 5Ir/TH100 samples than the remaining catalysts. L3 and TH100 alumina support material suppresses the variations in the $T_{Onset}$ and they have higher thermal stability which was also shown in **Section 3**.

Generated amounts of energy as a result of the thermal and catalytic ADN decomposition are presented in **Figure 5-2**. Energy value for thermal decomposition of ADN mixture was measured to be 1406 J/g. The presence of the catalyst increases the produced energy values except 5Ir/10$LaMnO_3$/$Al_2O_3$. As in the case of $T_{Onset}$ values shown in **Figure 5-1**, there is also detrimental effect of thermal aging on the produced energy values. In other words, as the catalyst calcination temperature increases, the energy release as a result of the ADN decomposition decreases.

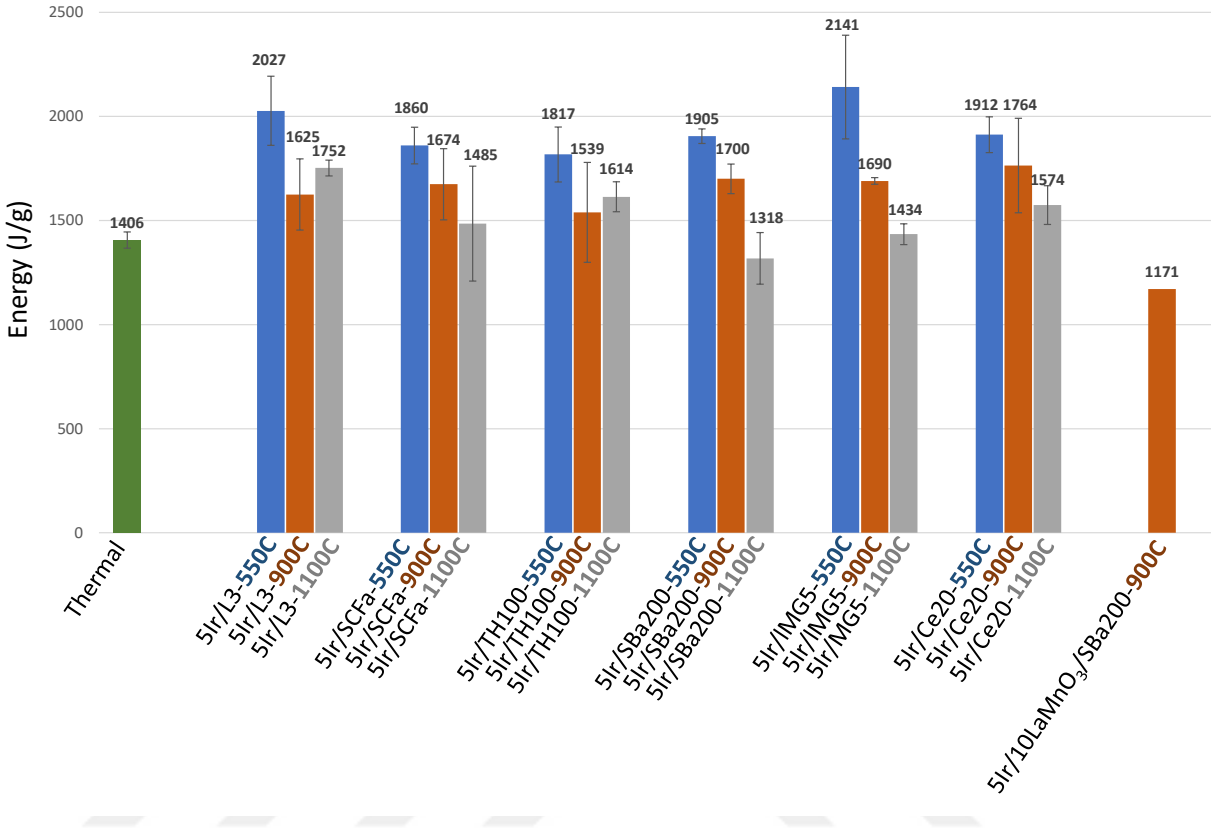



***Figure 5-2.*** *Average generated energy values for the decomposition of ADN mixture on various 5 wt. % Ir loaded alumina catalysts prepared via WI method calcined at 550 °C, 900 °C, and 1100 °C measured with the DSC/TGA technique. Green bar represents energy value for the thermal decomposition of ADN mixture in the absence of a catalyst.*

Comparison of the energy values upon ADN decomposition for the catalysts calcined at 550 °C reveals that the highest amount of energy was generated by the 5Ir/MG5 catalyst. However, this catalyst showed a loss of activity upon calcination at higher temperatures. In contrast, while the 5Ir/L3 and 5Ir/TH100 calcined at 550 °C produced a slightly lower energy than that of 5Ir/MG5, they demonstrated a more stable behavior after calcination at higher temperatures by preserving their energy generation values to a greater extent.

Corresponding experimental data associated with the average $T_{Onset}$ and Energy values presented in **Figure 5-1** and **Figure 5-2** are provided in **Appendix B1-Appendix B9** along with the relevant standard deviations and mean values.

**Figure 5-1** and **Figure 5-2** illustrates that calcination of the Ir-containing catalysts at 1100 °C suggesting severe deactivation and extreme thermal aging. Such a profound catalytic performance loss can be attributed to the following reasons:

- Excessive oxidation of metallic and partially oxidic Ir active sites to form $IrO_2$ and/or $Ir_2O_3$.
- Sintering of Ir active sites due to increased surface diffusion rate of adsorbed Ir species.
- Increased diffusion/sintering/volatility (i.e., loss) of oxidic iridium species (note that the melting point of $IrO_2$ is 1100 °C) [118].
- Loss/alteration of the favorable SMSI between alumina, promoters and Ir sites.
- Sub-surface diffusion of $Ir/IrO_x$ species into the support lattice and/or the covering/blocking of catalytic active sites [77].
- Decrease in SSA and closure of pores of the support material due to the structural collapse of the alumina lattice [53].

Thus, to investigate the relationship between the structure and the activity of these catalysts, detailed characterization studies were performed.

## 5.2. CHARACTERIZATION OF THE CATALYSTS SYNTHESIZED VIA WI

### 5.2.1. XRD analyses of the catalysts synthesized via WI

**Figure 5-3** shows the XRD patterns of the 5Ir/SBa200 catalyst prepared via WI method after calcination at 550 °C, 900 °C, and 1100 °C. For the 5Ir/SBa200-550C catalyst, support material exists in $\gamma$-$Al_2O_3$ phase prior to aging. However, as a result of thermal aging at 900

°C and 1100 °C, the γ-$Al_2O_3$ phase of the 5Ir/SBa200 catalyst is converted to δ-$Al_2O_3$ and α-$Al_2O_3$, respectively. Moreover, it is observed that Ir species on the 5Ir/SBa200-550C and 5Ir/SBa200-900C catalyst are in oxide form (i.e., $IrO_2$, PDF card no: 00-015-0870). After thermal aging at 1100 °C, the diffraction signals of the $IrO_2$ phase disappear as a result of the evaporation of $IrO_2$. The loss of the $IrO_2$ species from the catalyst structure at high temperatures is also supported by the Raman and XPS measurements, to be presented in the following sections.

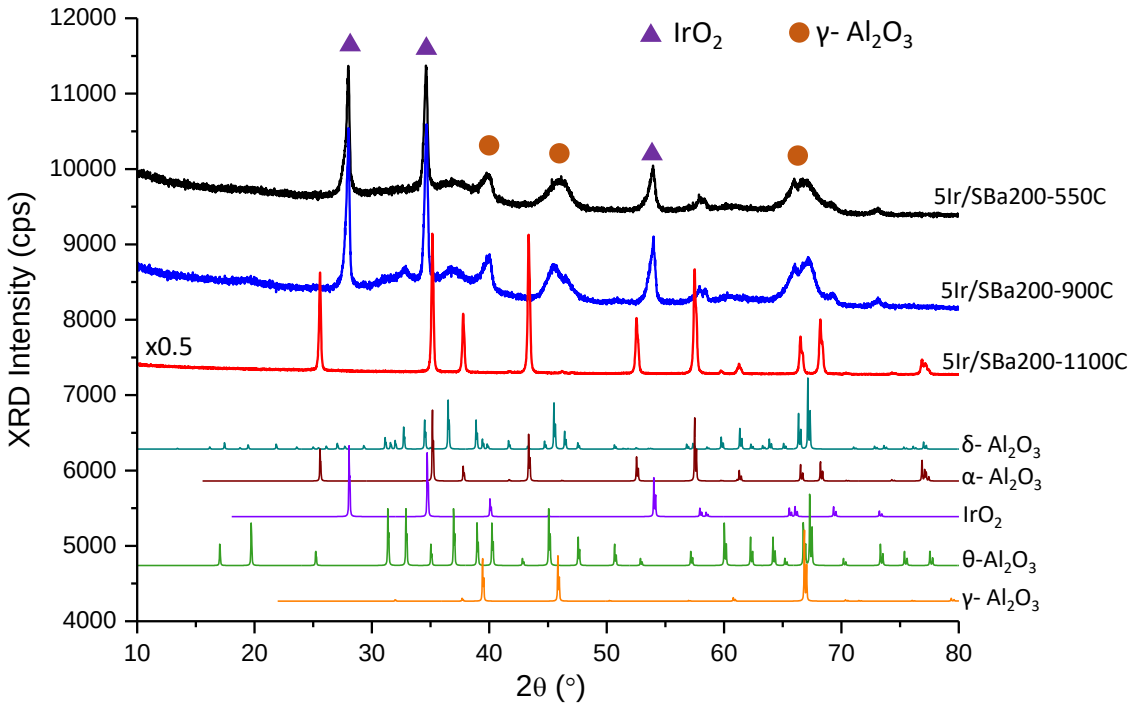



***Figure 5-3.*** *XRD patterns of 5Ir/SBa200 catalyst prepared via WI method after calcination at 550 °C, 900 °C and 1100 °C.*

XRD patterns of the 5Ir/SCFa catalyst prepared via WI method after various calcination temperatures are given in **Figure 5-4**. The support material of the 5Ir/SCFa catalyst at 550 °C was in γ-$Al_2O_3$ phase. After calcination at 900 °C, formation of δ-$Al_2O_3$ as a minority

phase was visible, while is γ-$Al_2O_3$ was still the predominant alumina phase. However, α-$Al_2O_3$ became prominent phase after thermal aging at 1100 °C indicating that the structure of the support material collapsed. Ir species existed in oxide ($IrO_2$) form for 5Ir/SCFa-550C and 5Ir/SCFa-900C. As in the case of the 5Ir/SBa200 catalyst, all $IrO_2$ diffraction signals disappeared after the thermal aging of the 5Ir/SCFa catalyst at 1100 °C.

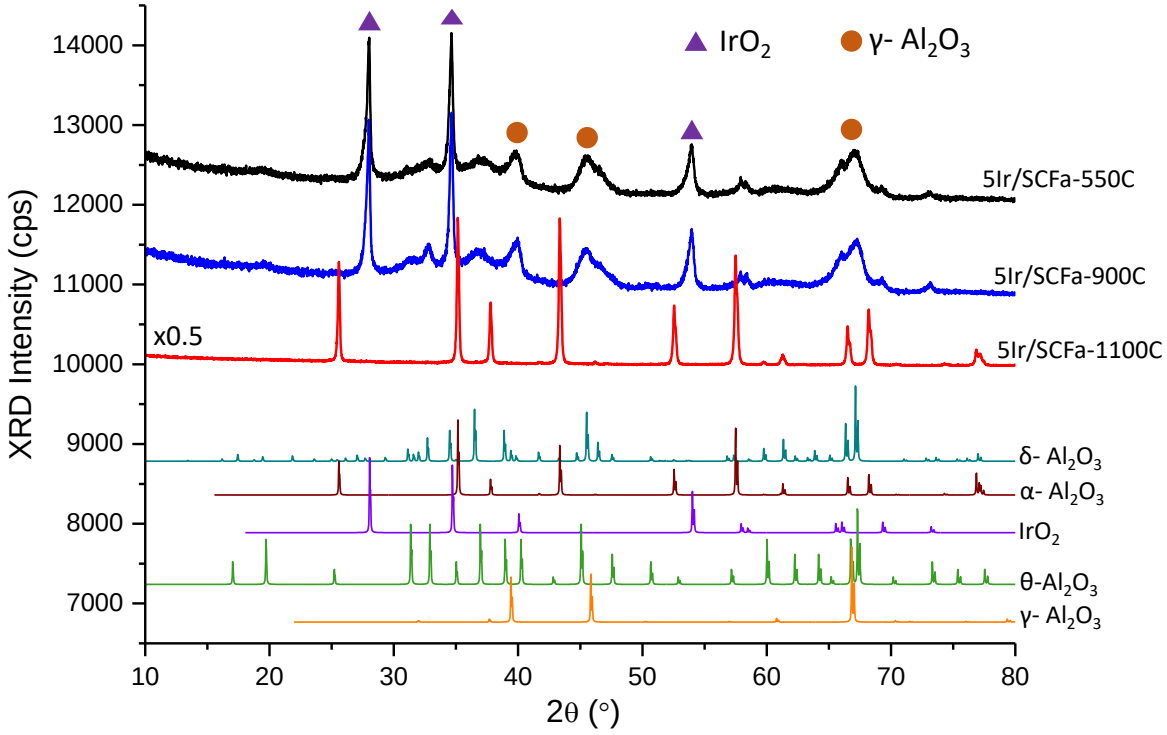



***Figure 5-4.*** *XRD patterns of 5Ir/SCFa catalyst prepared via WI method after calcination at 550 °C, 900 °C and 1100 °C.*

XRD patterns shown in **Figure 5-5** belong to the 5Ir/MG5 catalyst prepared with the WI method and calcined at various temperatures. 5Ir/MG5-550C catalyst revealed a γ-$Al_2O_3$ phase which was transformed into α-$Al_2O_3$ phase due to thermal aging. In addition, $MgAl_2O_4$ spinel phase was also observed after calcination at 1100 °C indicating severe structural alterations of the support material at elevated temperatures. $IrO_2$ diffraction signals were

detectable after calcination at 550 °C and 900 °C, whereas they vanished after calcination at 1100 °C. As shown in **Figure 5-1** and **Figure 5-2**, the degradation of the performance at high temperatures of 5Ir/SCFa, 5Ir/SBa200, and 5Ir/MG5 materials can be explained by both the sintering of the $IrO_2$ species followed by the loss/evaporation of Ir active sites from the surface[119] and collapse of the support material into α-$Al_2O_3$ phase [53].

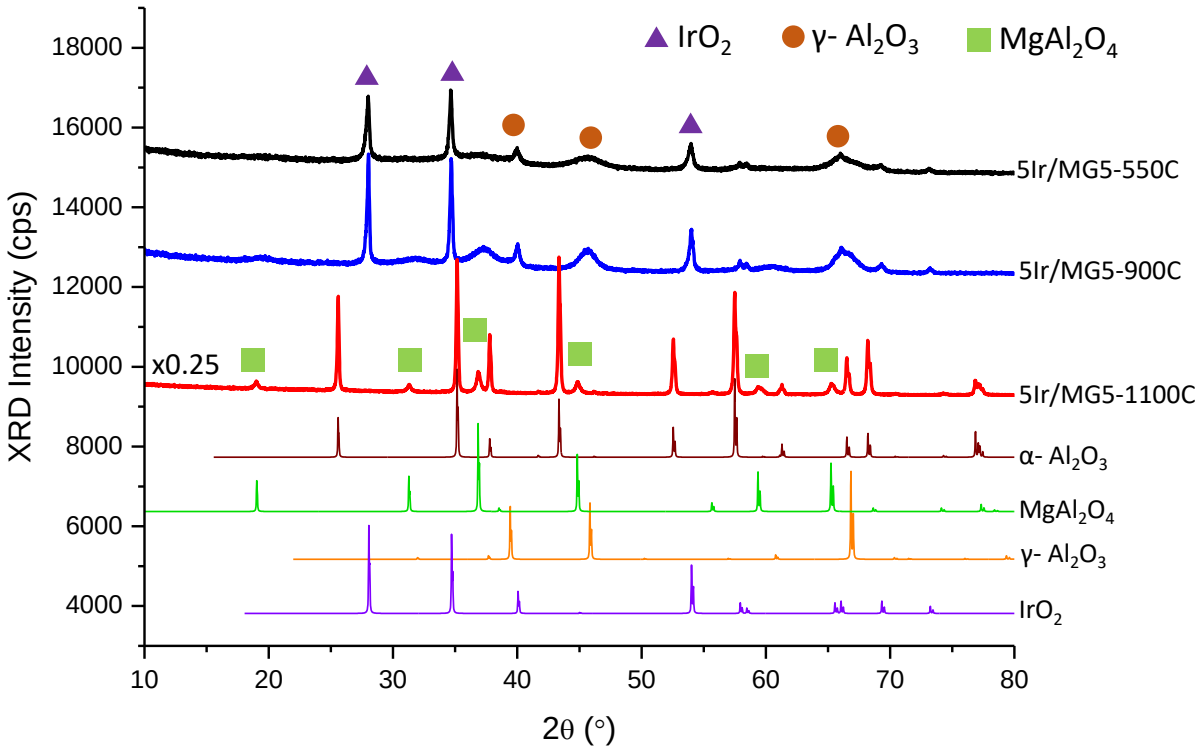



***Figure 5-5.*** *XRD patterns of 5Ir/MG5 catalyst prepared via WI method after calcination at 550 °C, 900 °C and 1100 °C.*

XRD patterns of the 5Ir/Ce20 catalyst prepared via WI method after calcination at various temperatures are shown in **Figure 5-6**. $CeO_2$ phase was visible for the 5Ir/Ce20-550C catalyst where the $CeO_2$ diffraction signals became sharper and stronger with increasing calcination temperature. This observation indicated that the ceria domains became more ordered and the corresponding particle size of the ceria domains increased. Apart from this,

alumina support material of the 5Ir/Ce20-550C and 5Ir/Ce20-900C catalysts revealed γ-$Al_2O_3$ phase, whereas after 1100 °C thermal aging, α-$Al_2O_3$ and δ-$Al_2O_3$ phases coexisted on the 5Ir/Ce20-1100C catalyst. $IrO_2$ phase was detected for the 5Ir/Ce20 catalysts calcined at 550 °C and 900 °C, while $IrO_2$ diffraction signals were no longer visible after calcination at 1100 °C.

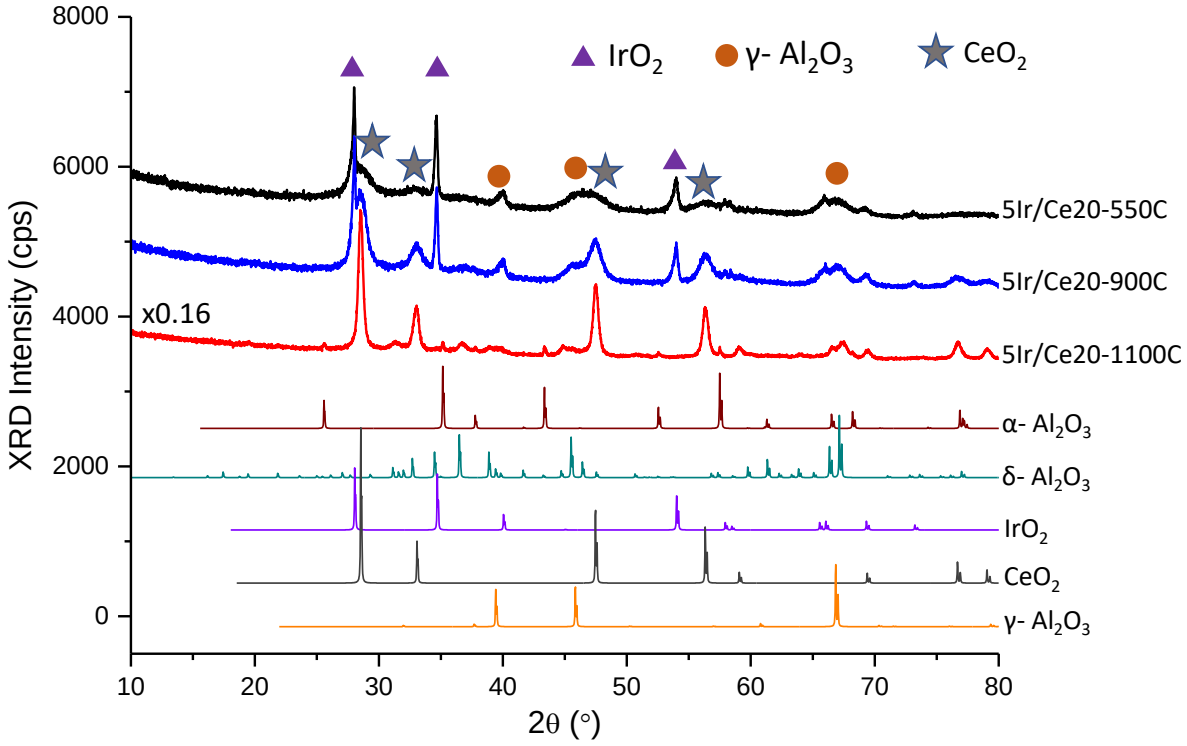



***Figure 5-6.*** *XRD patterns of of 5Ir/Ce20 catalyst prepared via WI method after calcination at 550 °C, 900 °C and 1100 °C.*

**Figure 5-7** shows the XRD patterns of the 5Ir/L3 catalyst prepared via WI method after calcination at various temperatures. Note that L3 and SCFa type alumina support materials were prepared via similar synthetic routes where the major difference between them is the La doping in L3, which is not present in SCFa. Lanthanum doping process stabilizes the alumina and increases the formation temperature of the α-$Al_2O_3$ phase during thermal aging

[61,66]. As can be seen in **Figure 5-7**, γ-$Al_2O_3$ and δ-$Al_2O_3$ phases predominantly co-existed on the 5Ir/L3-550C and 5Ir/L3-900C catalysts. After extreme thermal aging at 1100 °C, only δ-$Al_2O_3$ phase detectable on the 5Ir/L3-1100C catalyst, and α-$Al_2O_3$ phase was not observed. In addition, the 5Ir/L3-1100C catalyst still exhibited $IrO_2$ diffraction signals, indicating that the support material was able to stabilize the Ir active species in the catalyst structure via SMSI even after thermal aging at elevated temperatures [120]. Corresponding Raman spectroscopic measurements (**Figure 5-9**) presented in the later sections also show that $IrO_2$ Raman signals were observable on the 5Ir/L3-1100C sample. However, in the corresponding XPS measurements of the 5Ir/L3-1100C catalyst (**Figure 5-10**), no Ir-related XPS signals were detected. This is likely due to the fact that Raman spectroscopy and XRD techniques are not surface-sensitive techniques and provide information about the bulk structure of the material. On the other hand, the XPS technique is a surface-sensitive technique and reflects the composition of the first upper 10 nm of the surface. In other words, after the thermal aging at 1100 °C, while $IrO_2$ species were mostly removed from the 5Ir/L3-1100C catalyst surface (possibly either via evaporation or diffusion into the bulk), Ir species still remained to exist in the bulk [121].

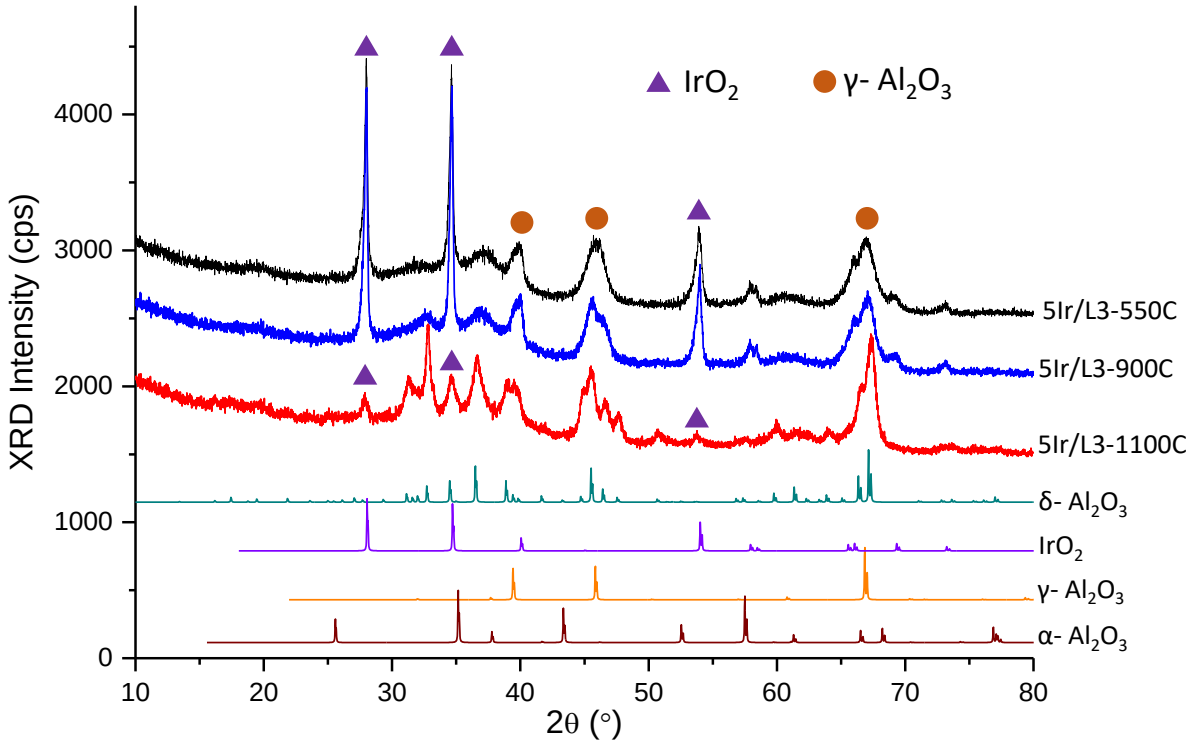



***Figure 5-7.*** *XRD patterns of of 5Ir/L3 catalyst prepared via WI method after calcination at 550 °C, 900 °C and 1100 °C.*

**Figure 5-8** shows XRD patterns of the 5Ir/TH100 catalyst exhibiting γ-$Al_2O_3$ and δ-$Al_2O_3$ phases at 550 °C. $IrO_2$ was also detected for the 5Ir/TH100 catalyst at all calcination temperatures. As the calcination temperature was increased to 900 °C, δ-$Al_2O_3$ phase became more prominent. After calcination at 1100 °C, δ-$Al_2O_3$ phase appeared as the most dominant phase. However, unlike the 5Ir/L3-1100C catalyst presented in **Figure 5-7**, 5Ir/TH100-1100C sample showed minor α-$Al_2O_3$ diffraction signals. 5Ir/TH100-1100C catalyst also revealed $IrO_2$ diffraction signals suggesting the presence of Ir species in the catalyst (bulk) structure.

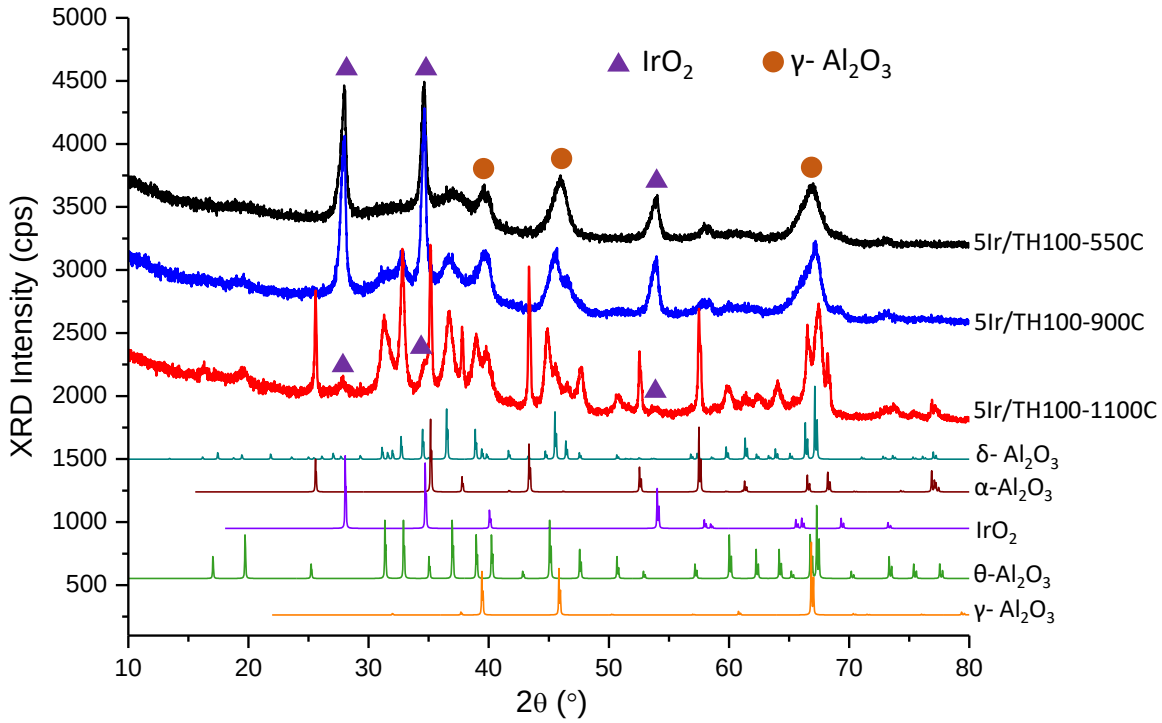



***Figure 5-8.*** *XRD patterns of of 5Ir/TH100 catalyst prepared via WI method after calcination at 550 °C, 900 °C and 1100 °C.*

In overall, $IrO_2$ was detected only for the 5Ir/L3-1100C and 5Ir/TH100-1100C catalysts after calcination at 1100 °C. Moreover, corresponding crystal structure of the alumina support of these catalysts were relatively less ordered (evident by broader XRD signals) indicating a lesser extent of the collapse of the alumina lattice structure to an ordered phase at elevated temperatures. Hence, 5Ir/L3 and 5Ir/TH100 catalysts revealed themselves as promising choices for the catalytic ADN decomposition reactions occurring at elevated temperatures.

### 5.2.2. Raman spectroscopic analyses of the catalysts synthesized via WI

Ir-containing catalysts synthesized using 6 different alumina support materials via WI method were also analyzed by Raman spectroscopy. Raman spectra shown in **Figure 5-9a**

belong to the samples calcined at 550 °C. 544 $cm^{-1}$ and 722 $cm^{-1}$ signals which were present for all 6 different catalysts were due to the phonon modes (i.e., Ir-O vibrations) of the $IrO_2$ species [122]. On the other hand, 455 $cm^{-1}$ signal present in the 5Ir/Ce20 sample was due to the Ce-O vibrations of $CeO_2$ domains [123].

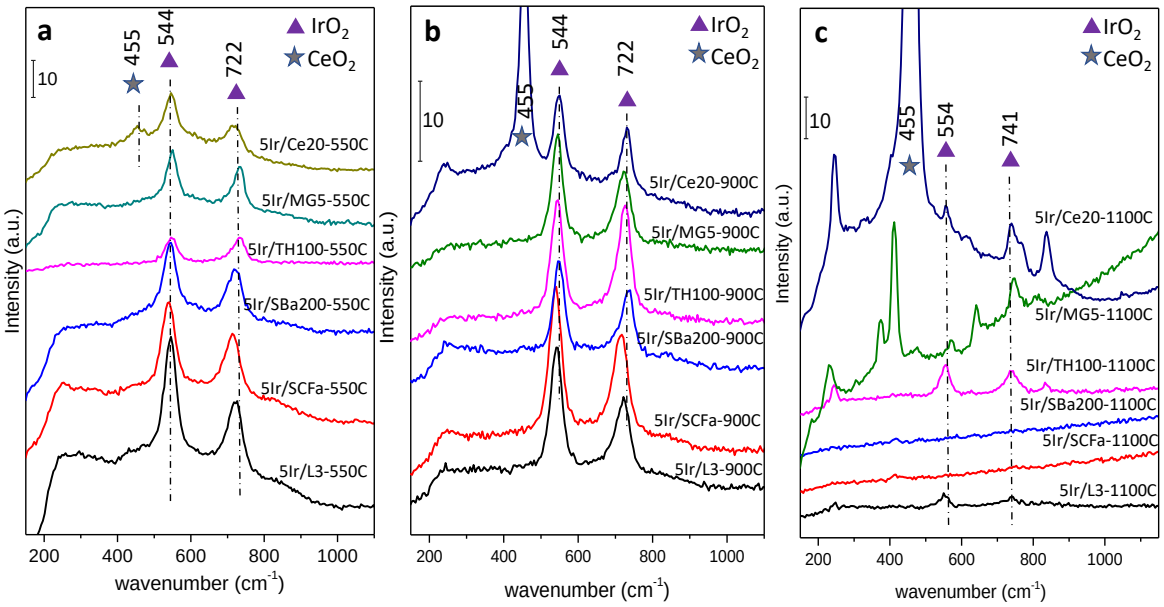



***Figure 5-9.*** *Raman spectra of the Ir-containing catalysts prepared via WI method after calcination at (a) 550 °C (b) 900 °C, and (c) 1100 °C.*

Raman spectra of the corresponding catalysts calcined at 900 °C are given in **Figure 5-9b**. General aspects of these spectra were rather similar to the that of **Figure 5-9a**. However, an increase in the 455 $cm^{-1}$ signal was visible in the 5Ir/Ce20-900C sample due to the ordering and growth of ceria domains.

**Figure 5-9c** shows the Raman spectra of the corresponding catalysts that were thermally aged at 1100 °C. These spectra show significant dissimilarities to that of the data given in **Figure 5-9a** and **Figure 5-9b** which corresponded to calcination at 550 °C and 900 °C, respectively. For the 5Ir/SCFa-1100C, 5Ir/SBa200-1100C, and 5Ir/MG5-1100C catalysts,

$IrO_2$ Raman features were not detectable. This result is in agreement with XRD data shown in **Figure 5-3**, **Figure 5-4**, **Figure 5-5**, where no $IrO_2$ diffraction signals were observed. On the other hand, $IrO_2$ Raman features were clearly discernible for the 5Ir/L3-1100C, 5Ir/TH100-1100C, and 5Ir/Ce20-1100C catalysts. Note that $IrO_2$ phase was also detected in the XRD patterns for 5Ir/L3-1100C (**Figure 5-7**) and 5Ir/TH100-1100C (**Figure 5-8**) but not for 5Ir/Ce20-1100C sample (**Figure 5-6**) which may due to the smaller size of the Ir particles. Presumably, relatively smaller particle size of the $IrO_2$ species on the 5Ir/Ce20-1100C catalyst precluded the detection of strong $IrO_2$ XRD signals.

### 5.2.3. XPS Analyses of the catalysts synthesized via WI

**Table 5-1** shows the surface weight percentages of the elements obtained via XPS measurements on the Ir-catalysts prepared via WI method after different calcination temperatures, while **Figure 5-10** particularly focuses on the surface Ir atomic % contents of these catalysts. Among the catalysts calcined at 550 °C, the maximum amount of iridium on the surface was observed for 5Ir/MG5-550C which is correlated with the high activity of this catalyst (**Figure 5-1** and **Figure 5-2**). However, when the calcination temperature was increased to 900 °C, the amount of Ir on the 5Ir/MG5-900C catalyst was observed to be only a half of the 5Ir/MG5-550C and a further increase in the calcination temperature to 1100 °C pushed the Ir surface atomic concentration below the detection limits of the XPS technique. This observation indicates that Ir species on the MG5 support do not possess a high thermal stability which is in line with the rapid decline in their corresponding activity as shown in **Figure 5-1** and **Figure 5-2**. **Table 5-1** and **Figure 5-10** indicate that the amount of Ir on the surface of all catalysts decreases when the calcination temperature was increased to 900 °C, except 5Ir/TH100 where the Ir content was almost invariant for 550 °C and 900 °C. After

thermal aging at 1100 °C, Ir content of all catalyst surfaces fell below the detection limit of XPS.

***Table 5-1.*** *Surface atomic percentages of the elements obtained via XPS on the catalysts prepared via WI method.*

| Sample Name | Al | Ir | O | La | Mg | Ce |
|---|---|---|---|---|---|---|
| 5Ir/SCFa-550C | 51.19 | **0.57** | 48.2 | | | |
| 5Ir/SCFa-900C | 49.53 | **0.51** | 49.96 | | | |
| 5Ir/SCFa-1100C | 54.54 | **0.01** | 45.5 | | | |
| 5Ir/L3-550C | 51.57 | **0.4** | 47.7 | 0.33 | | |
| 5Ir/L3-900C | 48.49 | **0.24** | 50.79 | 0.48 | | |
| 5Ir/L3-1100C | 54.34 | **0** | 45 | 0.62 | | |
| 5Ir/MG5-550C | 47.22 | **1.52** | 50.8 | | 0.45 | |
| 5Ir/MG5-900C | 47.32 | **0.70** | 51.74 | | 0.24 | |
| 5Ir/MG5-1100C | 51.84 | **0** | 47.6 | | 0.58 | |
| 5Ir/TH100-550C | 52.5 | **0.14** | 47.4 | | | |
| 5Ir/TH100-900C | 50.15 | **0.14** | 49.71 | | | |
| 5Ir/TH100-1100C | 55.1 | **0** | 44.9 | | | |
| 5Ir/SBa200-550C | 50.81 | **0.79** | 48.4 | | | |
| 5Ir/SBa200-900C | 49.70 | **0.61** | 49.69 | | | |
| 5Ir/SBa200-1100C | 55.06 | **0.01** | 44.9 | | | |
| 5Ir/Ce20-550C | 48.68 | **0.58** | 49.9 | | | 0.84 |
| 5Ir/Ce20-900C | 47.09 | **0.55** | 51.41 | | | 0.95 |
| 5Ir/Ce20-1100C | 52.53 | **0** | 46.8 | | | 0.67 |

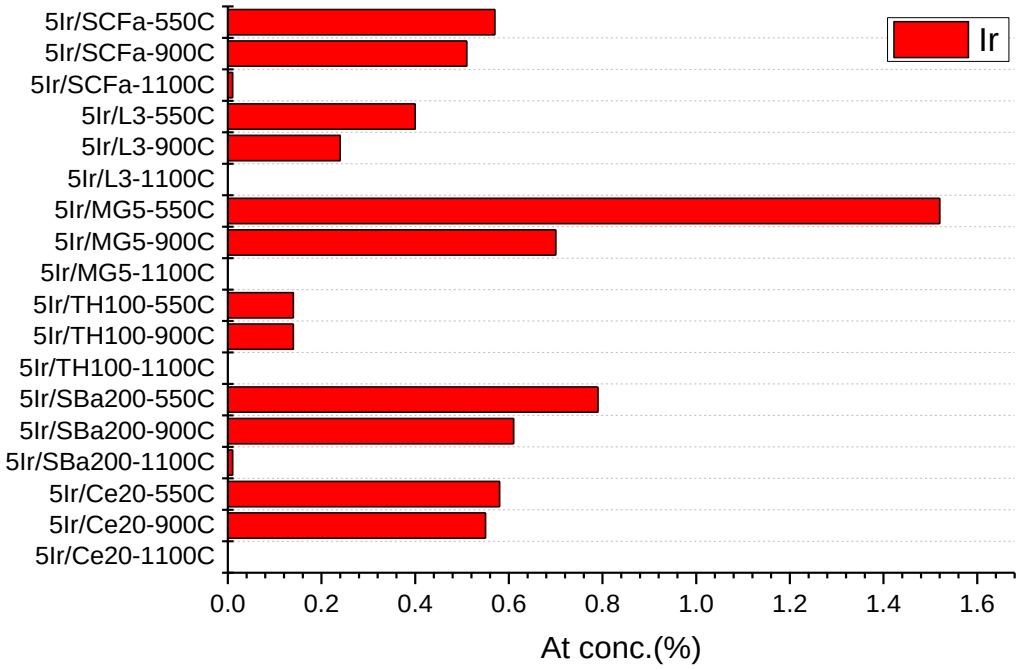



***Figure 5-10.*** *Comparison of the percent surface atomic concentrations of Ir obtained via XPS on the catalyst surfaces prepared via WI method.*

### 5.2.4. TEM and EDX measurements of the catalysts synthesized via WI

**Figure 5-11a-Figure 5-11b** shows the HRTEM images of the 5Ir/SBa200-550C sample revealing $IrO_2$ particles in the form of nanorods with ca. 200 nm in length. Ir dispersion is fairly poor on this sample even at low calcination temperatures. **Figure 5-11c** shows the HAADF-STEM image of the 5Ir/SBa200-550C material and the corresponding EDX spectrum obtained from the marked area verifying the presence of $IrO_2$ in the observed nanorods (**Figure 5-11d**).

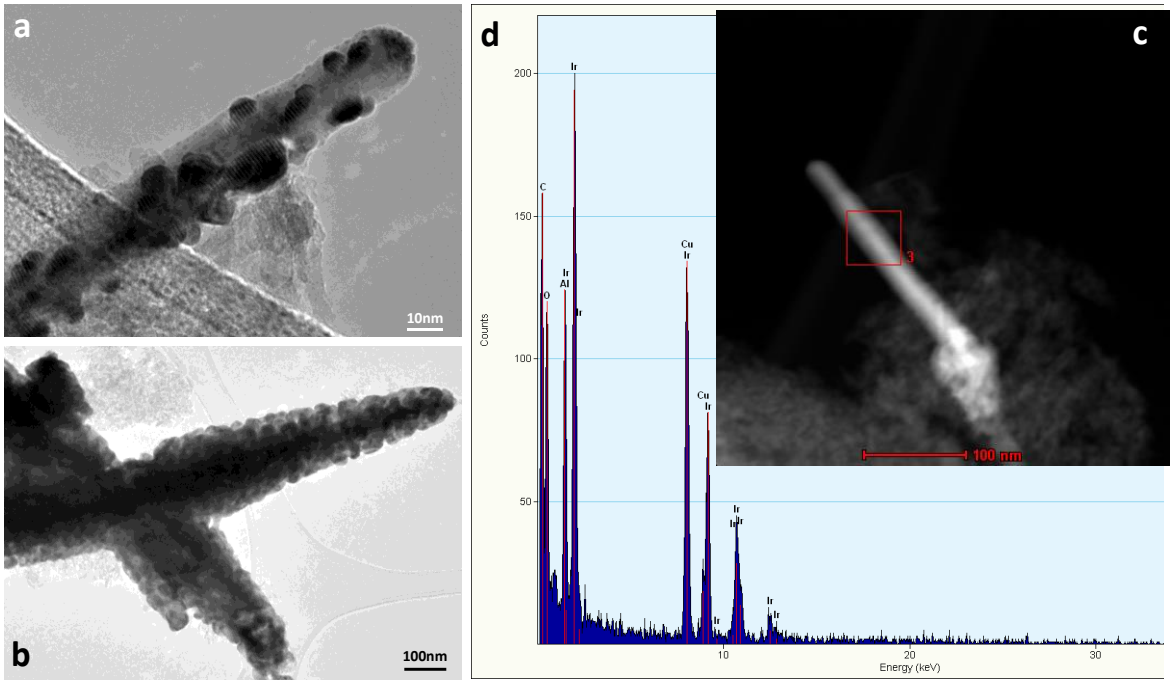



***Figure 5-11.*** *(a-b) HRTEM images of 5Ir/SBa200-550C catalyst prepared via WI method. (c) HAADF-STEM image of the 5Ir/SBa200-550C catalyst prepared via WI method, (d) EDX spectrum of the 5Ir/SBa200-550C catalyst obtained from the marked area in (c).*

HAADF-STEM image and the corresponding EDX spectrum illustrated in **Figure 5-12** correspond to the 5Ir-SBa200-900C catalyst. As a result of thermal aging at 900 $^{o}$C, larger $IrO_2$ nanorods (with lengths of ca. 500 nm) were observed on the 5Ir-SBa200-900C catalyst as compared to that of 5Ir-SBa200-550C.

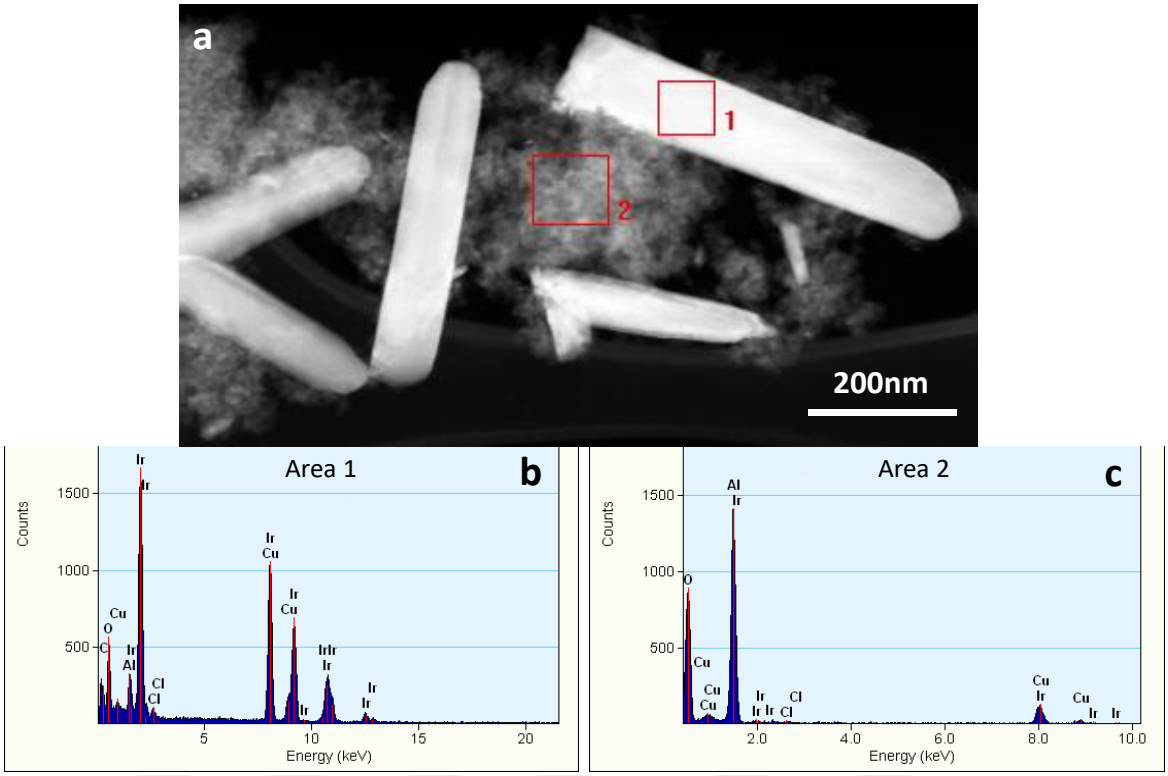



***Figure 5-12.*** *(a) HAADF-STEM image of the 5Ir/SBa200-900C catalyst prepared via WI method, (b-c) EDX spectra obtained from the marked areas 1, and 2 labeled in (a), respectively.*

**Figure 5-13** illustrates the HAADF-STEM image and the corresponding EDX analysis of the 5Ir/SBa200-1100 sample. XRD analysis of the 5Ir/SBa200-1100 catalyst (**Figure 5-3**) revealed the prominence of the α-$Al_2O_3$ phase which is in line with the loss of porosity, and elimination of surface disorder for this sample that are visible in **Figure 5-13a**. Furthermore, EDX analysis in **Figure 5-13b** is also consistent with the loss of Ir from the surface of 5Ir/SBa200-1100 at elevated temperatures.

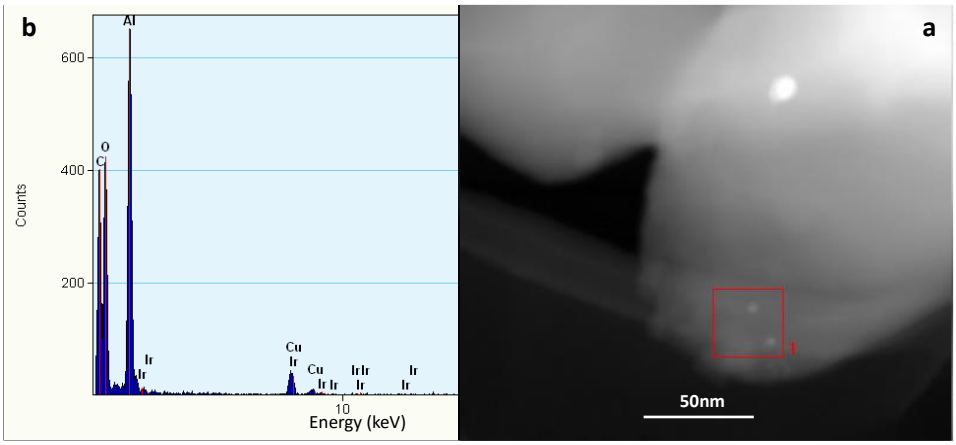



***Figure 5-13.*** *(a) HAADF-STEM image of the 5Ir/SBa200-1100C catalyst prepared via WI method, (b) EDX spectrum of the area marked as 1 in (a).*

**Figure 5-14** shows the HRTEM images of 5Ir/L3-550C catalyst. Although, the images show that the majority of the Ir particles have a diameter of ca. 20-30 nm, much bigger Ir particles with ca. 200 nm diameter are also encountered. **Figure 5-14** depicts the HAADF-STEM image and the corresponding EDX analysis of the 5Ir/L3-550C catalyst exhibiting $IrO_2$ species with ca. 10 nm diameter.

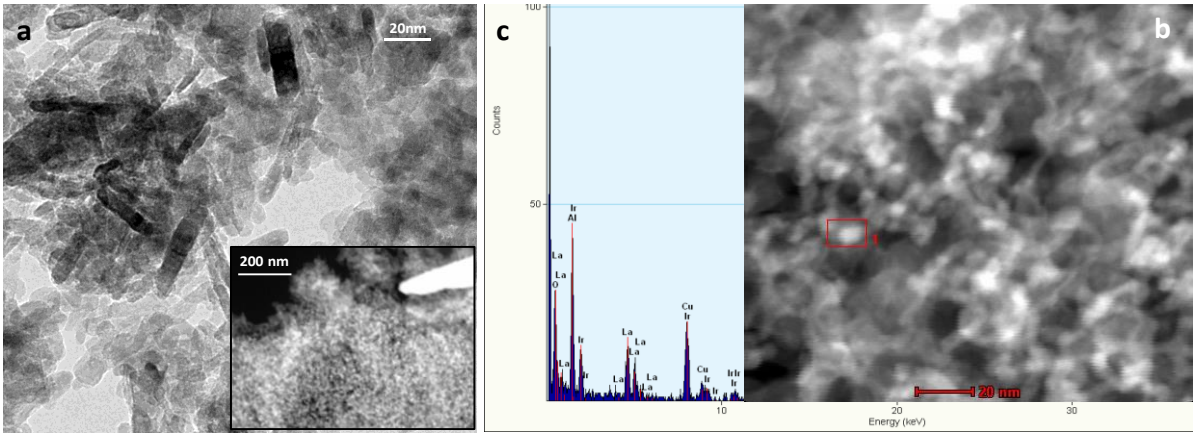



***Figure 5-14.*** *(a) HRTEM images of 5Ir/L3-550C catalyst prepared via WI method. (b) HAADF-STEM image of the 5Ir/L3-550C catalyst prepared via WI method, (c) EDX spectrum of the area marked as 1 in (b)*

**Figure 5-15** shows the HAADF-STEM image and the associated EDX analysis of the 5Ir/L3-900C catalyst. Upon increase in the calcination temperature to 900 °C, majority of the Ir particles severely sinter to form nanorods with an average length of ca. 500 nm.

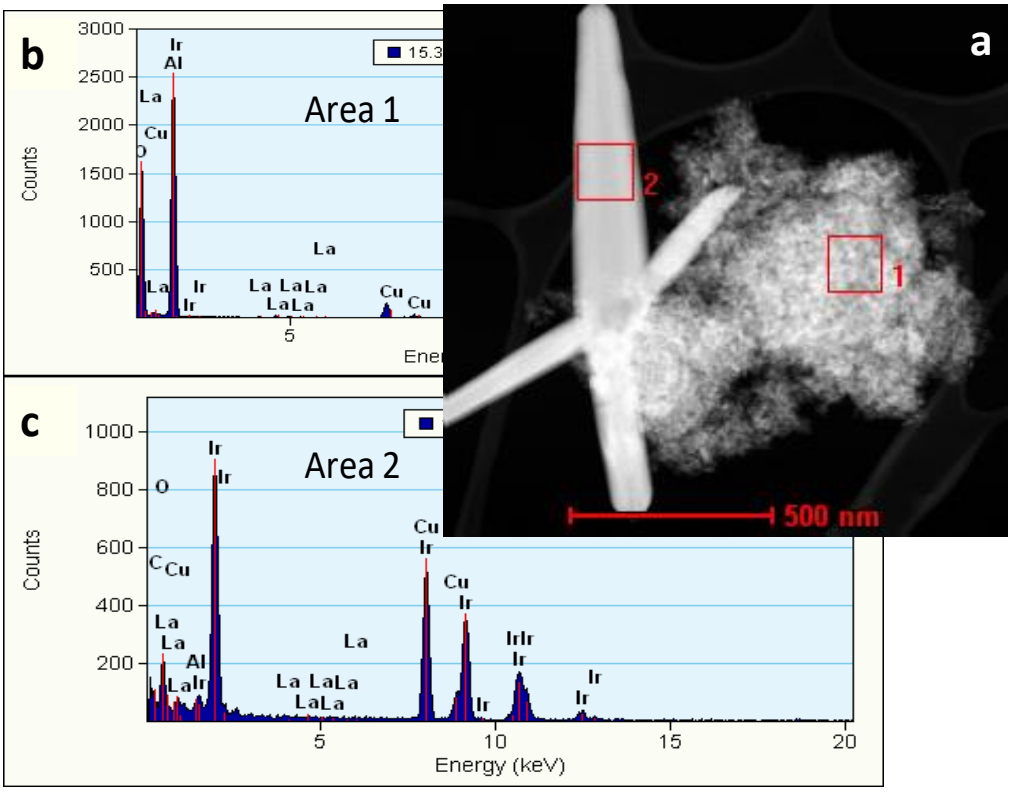



***Figure 5-15.*** *(a) HAADF-STEM image of the 5Ir/L3-900C catalyst prepared via WI method, (b-c) corresponding EDX spectra obtained from the marked areas 1, 2 in (a), respectively.*

**Figure 5-16a** and **Figure 5-16b** shows the HRTEM image of the 5Ir/L3-1100C sample showing the Ir particles on the La doped $Al_2O_3$ support material, which was exposed to thermal aging at 1100 °C. Ir particles still existed on the surface, and their size was found to be around 50-100 nm. **Figure 5-16e** and **Figure 5-16d** shows the HAADF image and the associated EDX analysis of 5Ir/L3-1100C suggesting that the La doped alumina support can sustain the Ir on the surface to a certain extent even at high temperatures as also observed in XRD (**Figure 5-7**) and Raman (**Figure 5-9c**) measurements. The EDX mapping analysis

shown in **Figure 5-17** for the same sample is also consistent with this argument. In the EDX map (**Figure 5-17**), Ir and La signals appear to overlap which may indicate that La-containing domains offer strong anchoring sites for Ir species and attenuate the Ir surface diffusion by boosting their adsorption strength to the catalyst support surface [77].

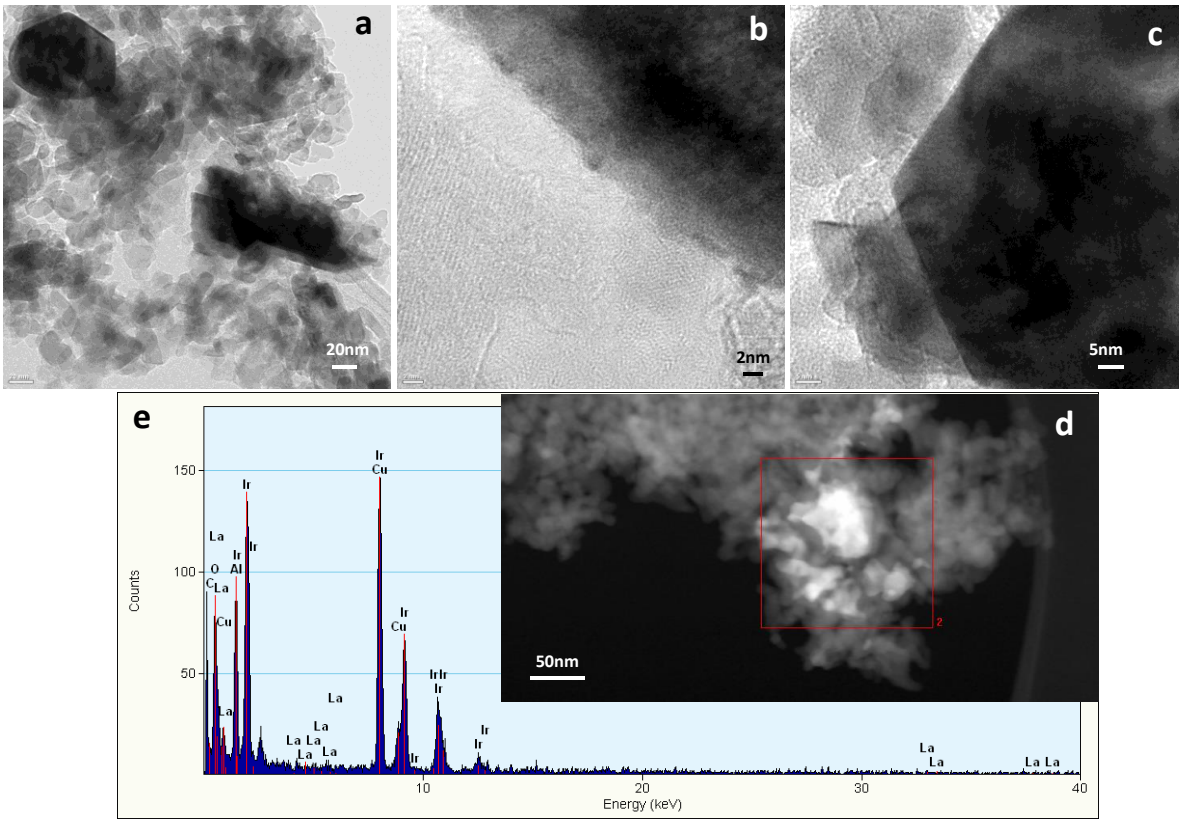



***Figure 5-16.*** *(a-c) HRTEM image of 5Ir/L3-1100C catalyst prepared via WI method (d) HAADF-STEM image of the 5Ir/L3-1100C catalyst prepared via WI method, (e) associated EDX spectrum obtained from the area marked as 2 in (d).*

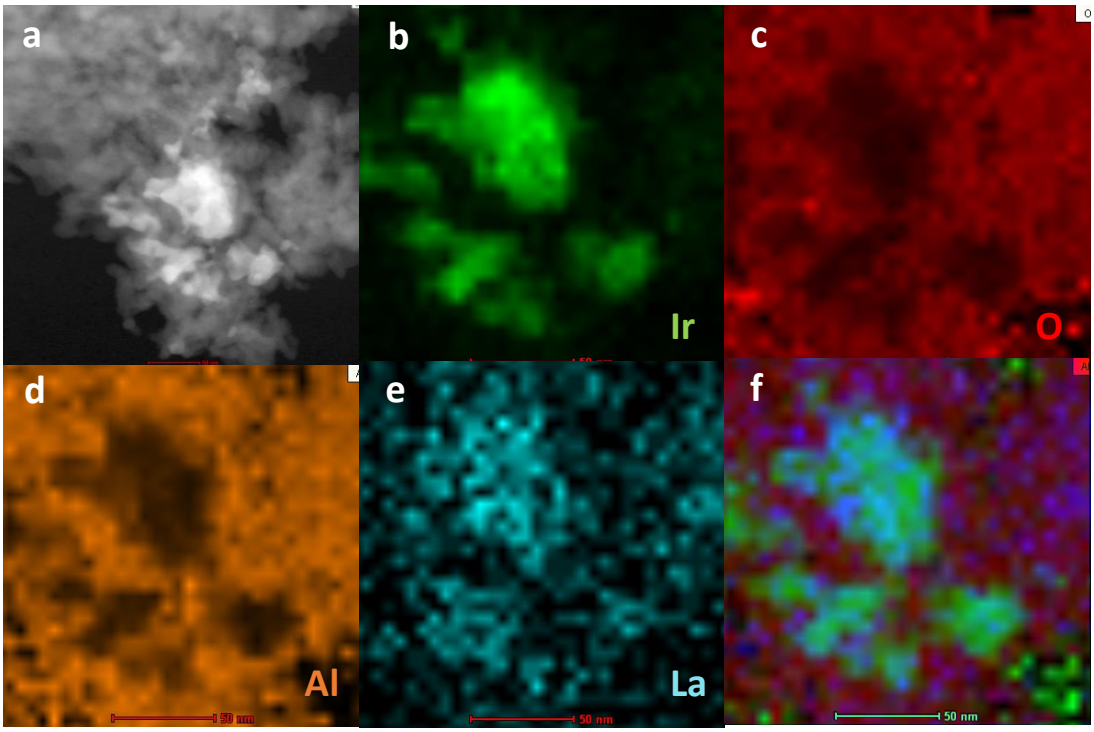



***Figure 5-17.*** *(a) HAADF-STEM image, (b-f) Ir, O, Al, La, La+Ir elemental EDX maps of the 5Ir/L3-1100C catalyst prepared via WI method, respectively.*

HRTEM image of the 5Ir/Ce20-550C sample is given in **Figure 5-18a**. **Figure 5-18b** and **Figure 5-18c** show the HAADF-STEM image and the corresponding EDX spectrum of the 5Ir/Ce20-550C catalyst. In some regions, the $IrO_2$ particles were found to exist as extremely long nanorods with lengths up to 1000 nm (**Figure 5-18b**), while on other parts of the 5Ir/Ce20-550C surface, $IrO_2$ existed as small nanoparticles with average diameters of < 5 nm (**Figure 5-18a**). In other words, on the 5Ir/Ce20-550C catalyst, $IrO_2$ species revealed a bimodal particle size distribution yielding two different types of particles with extremely small or extremely large diameters. Considering the presence of small $IrO_2$ particles on the 5Ir/Ce20-550C surface (**Figure 5-18a**), one can argue that ceria domains enhanced the Ir dispersion on the Ce-promoted alumina surface to a certain extent, however it also led to a

bimodal particle size distribution which resulted in the generation of extremely large Ir species on the surface (**Figure 5-18b**).

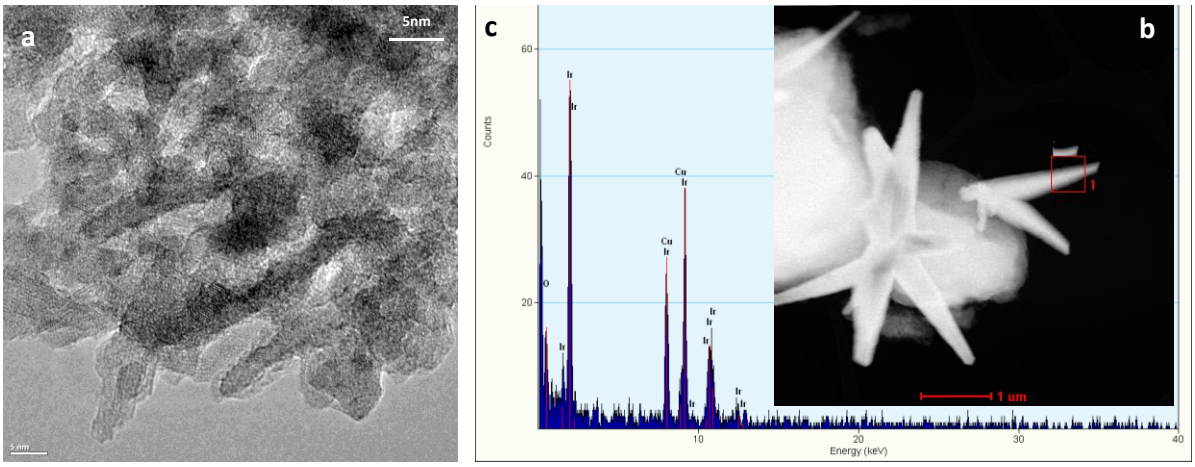



***Figure 5-18.*** *(a) HRTEM image of 5Ir/Ce20-550C, (b) HAADF STEM image of the 5Ir/Ce20-550C catalyst prepared via WI method, (c) EDX spectrum of the material indicated by the marked area in (b).*

HAADF-STEM image and the associated EDX spectra of the 5Ir/Ce20-900C catalyst are given in **Figure 5-19** . These results suggest that the Ir species tend to sinter and the number of Ir nanoparticles on the catalyst surface (i.e., Ir nanorod surface number density) decreases.

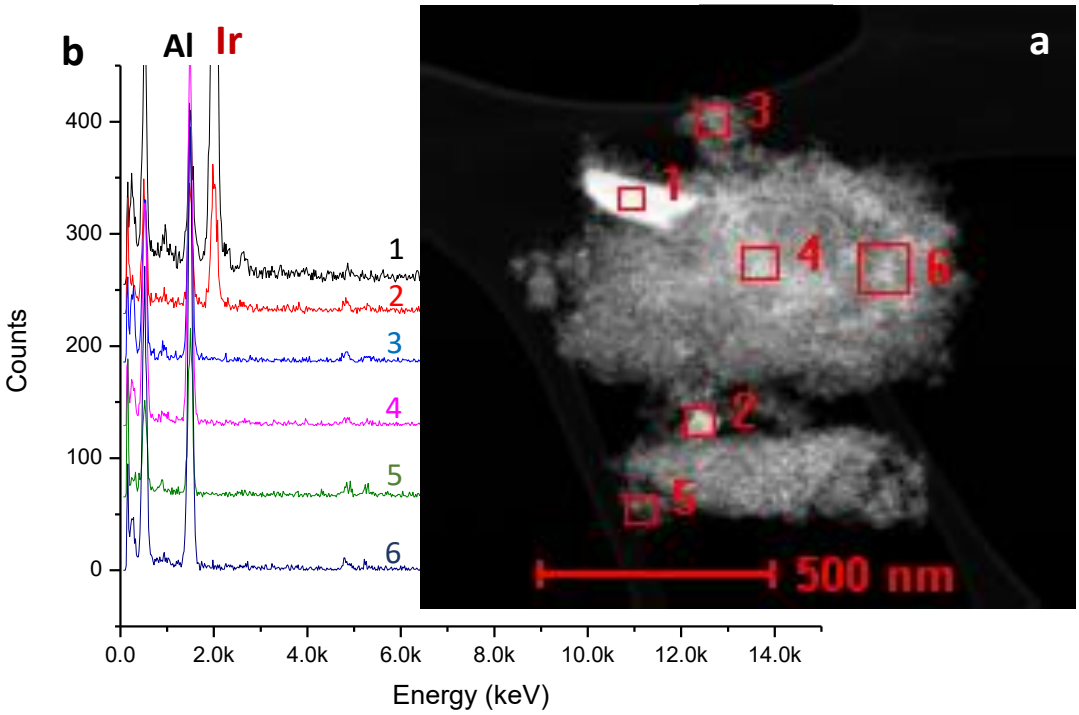



***Figure 5-19.*** *(a) HAADF STEM image of the 5Ir/Ce20-900C catalyst prepared via WI method, (b) EDX spectra obtained from the indicated regions shown in (a).*

**Figure 5-20** shows the HAADF-STEM image and the EDX spectrum of the 5Ir/Ce20-1100C catalyst. These findings indicate that some of the Ir species remain on the surface with moderate particle sizes even after high temperature thermal treatment which is consistent with the Raman analysis given in **Figure 5-9c**.

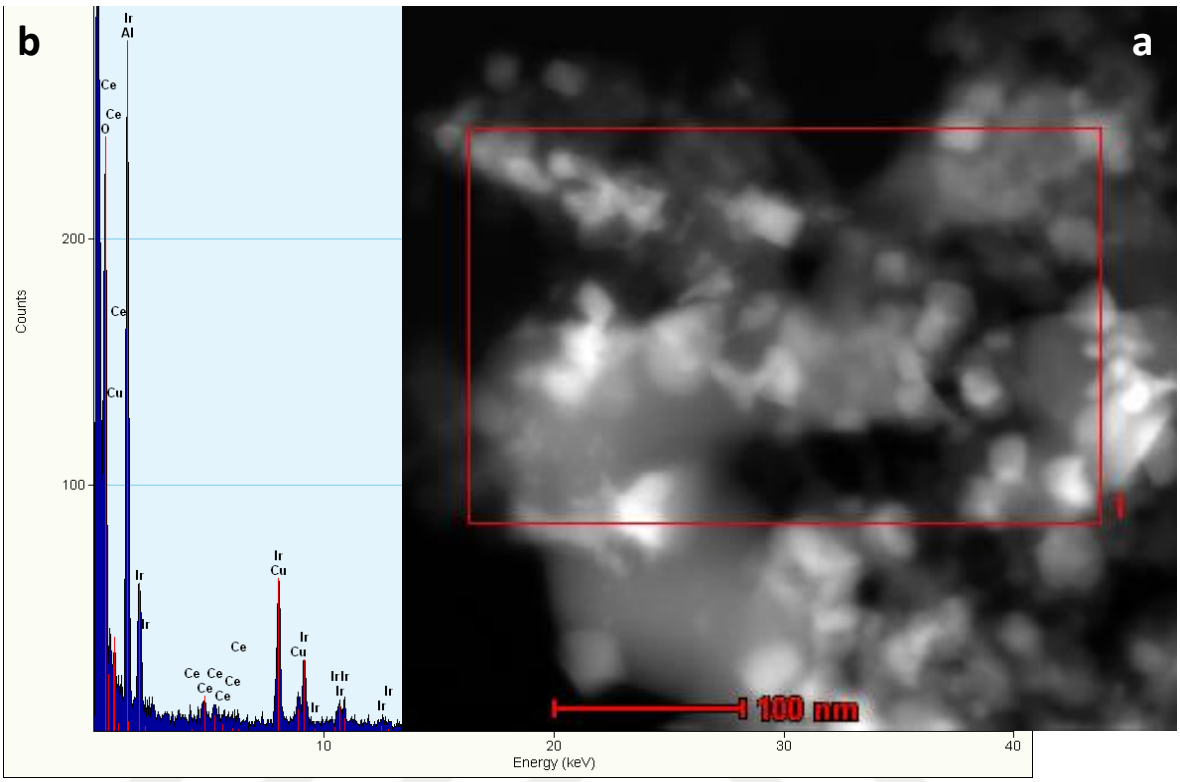



***Figure 5-20.*** *(a) HAADF STEM image of the 5Ir/Ce20-1100C catalyst prepared via WI method, (b) EDX spectrum obtained from the indicated region marked as 1 in (a).*

### 5.2.5. ADN decomposition over Ir and perovskite-containing alumina supported catalysts prepared via WI method

Perovskites are metal oxide structures with $ABO_3$ stoichiometry, which are widely used in catalysis [124]. It is well-known that $LaMnO_3$-based perovskites can readily activate N-O bonds and act as efficient catalysts in catalytic $DeNO_x$ applications relevant to automotive exhaust emission control technologies [125]. Furthermore, due to the high temperatures used in the synthesis of the perovskite catalysts, such systems may exhibit high thermal stability and high sinter resistance [124]. Since the ADN structure present in the currently investigated fuel formulations also contain N-O functionalities, we proposed that promotion of the alumina support material with $LaMnO_3$-based perovskites may be beneficial for the catalytic performance of the alumina supported Ir active sites. Along these lines, we exploited a synthesis protocol (i.e., citrate method), which we developed in a former study[106] to promote alumina materials with $LaMnO_3$-based perovskites synthesized via WI method as described in **Section 2.2.2.1.1**. We investigated the surface chemistry of the synthesized $LaMnO_3$-based perovskites in the absence of alumina by using $NO_2$ as a probe molecule and examined the $NO_2$ adsorption on $LaMnO_3$ via *in-situ* FTIR spectroscopy as a proxy to the ADN molecule.

**Figure 5-21** indicates the *in-situ* FTIR spectra obtained after $NO_2$ saturation of $LaMnO_3$ at 50 °C. IR features located at around 1649 $cm^{-1}$ and 1009 $cm^{-1}$ can be assigned to asymmetric and symmetric stretching modes of bridging nitrate species on the perovskite surfaces, respectively [126]. Features located at 1530 $cm^{-1}$ and 1269 $cm^{-1}$ can be attributed to stretching vibrations of monodentate nitrates. The IR features at 1568 $cm^{-1}$ and 1246 $cm^{-1}$ correspond to bidentate nitrates [127,128]. The characteristic features observed at 1434 and 1322

and can be ascribed to nitrito species on the perovskite surface [129–132]. In-situ FTIR spectra presented in **Figure 5-21** clearly demonstrates that in the absence of any other reagent, perovskite surface can catalytically activate $NO_2$ and initiate a disproportionation reaction to yield nitrate and nitrite species. Thus, these spectroscopic experiments provided reasonable insight that perovskite systems may be promising for ADN activation in Ir-alumina catalytic systems. However, as shown in the **Figure 5-1** and **Figure 5-2**, $LaMnO_3$-promoted Ir active sites supported with alumina prepared via WI method, led to limited catalytic performance results and thus, these catalysts were not further investigated.

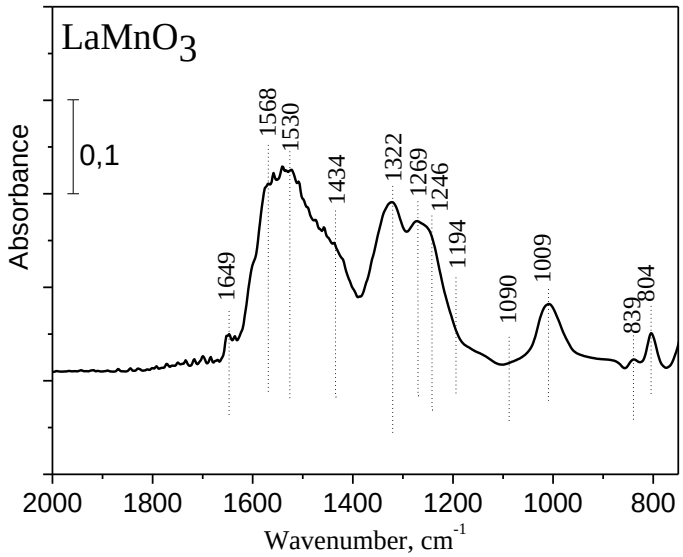



***Figure 5-21.*** *In-situ FTIR spectra recorded after 5 Torr $NO_2$ (g) dosage at 323 K for 10 min on fresh $LaMnO_3$* [105].

In this section, preliminary activity and structural properties of 5 wt. % Ir containing different alumina support materials synthesized via WI were investigated. It was found that fresh 5Ir/L3 and 5Ir/MG5 samples have higher Ir surface dispersion and catalytic performance than others. Moreover, 5Ir/L3 and 5Ir/TH100 possess high thermal resistance

after calcination to elevated temperatures (i.e., 1100 °C). However, WI synthesis method led to very low Ir dispersion even at low calcination temperatures (i.e., 550 °C). Next section introduces the performance and structural properties of catalysts synthesized with sequential Ir loading and IWI method. More realistic catalytic performance measurements with custom design micro propulsion batch reactor system will be also presented in the forthcoming section.

# CHAPTER 6

## 6. CHARACTERIZATION AND CATALYTIC PERFORMANCE OF THE CATALYSTS SYNTHESIZED VIA INCIPIENT TO WETNESS IMPREGNATION

*This section is reprinted (adapted) with permission of (Kurt, M.; Kap, Z.; Senol, S.; Ercan, K. E.; Sika-Nartey, A. T.; Kocak, Y.; Koc, A.; Esiyok, H.; Caglayan, B. S.; Aksoylu, A. E.; Ozensoy, E. Influence of La and Si Promoters on the Anaerobic Heterogeneous Catalytic Decomposition of Ammonium Dinitramide (ADN) via Alumina Supported Iridium Active Sites. Appl. Catal. A Gen.* ***2022****, 118500). Copyright (2022) Elsevier.*

In Chapter 6, we focus on the anaerobic ADN decomposition performances of the Ir containing catalysts synthesized via IWI by using custom design micro propulsion batch reactor. Moreover, different promoters such as La and Ce was added on to the alumina support materials prior to Ir addition and their effects on ADN decomposition performance and Ir particles size was investigated. Through detailed *in-situ*/*ex-situ* spectroscopic, diffraction and microscopic investigations, we demonstrate that different alumina support materials led to different types of catalytic performance enhancement of the Ir active sites.

### 6.1. XRD AND TEM ANALYSES OF THE CATALYSTS SYNTHESIZED VIA IWI

#### 6.1.1. XRD analyses of the catalysts synthesized via IWI

##### 6.1.1.1. XRD of CCR samples synthesized via IWI

XRD patterns of the 5 wt.% Ir-containing catalysts synthesized via CCR procedure of the IWI method described in **Section 2.2.2.2.1**. are presented in **Figure 6-1**. It is apparent that all of the CCR catalysts lead to sharp and strong metallic Ir diffraction signals (PDF Card no: 00-006-0598), suggesting the presence of relatively large Ir nanoparticles. Unfortunately, due to the overlap between alumina and Ir diffraction signals, reliable average

Ir particle size determination, via XRD data analysis, was not feasible. Also, note that no oxidic Ir species are visible in the XRD data given in **Figure 6-1**. It is important to mention that considering the large Ir loading (i.e., 5 wt.%) of the synthesized catalyst samples, presence of additional disordered metallic and/or oxidic Ir species with smaller particle sizes which are not detectable via XRD cannot be ruled out. This argument will be further verified via current TEM results presented in the forthcoming sections. Another important aspect of **Figure 6-1** is the difference in the alumina support crystal structure as a function of promoter type. It is apparent that while 5Ir/Sir5-CCR, 5Ir/Sir10-CCR, 5Ir/Sir10-CCR, 5Ir/Mg5-CCR and 5Ir/Ce20-CCR results in exclusively γ-$Al_2O_3$ phase, 5Ir/L3-CCR, 5Ir/TH100-CCR and 5Ir/SBa200-CCR yield both δ-$Al_2O_3$ and γ-$Al_2O_3$ phases. $CeO_2$ phase was also detected for the 5Ir/Ce20-CCR sample.

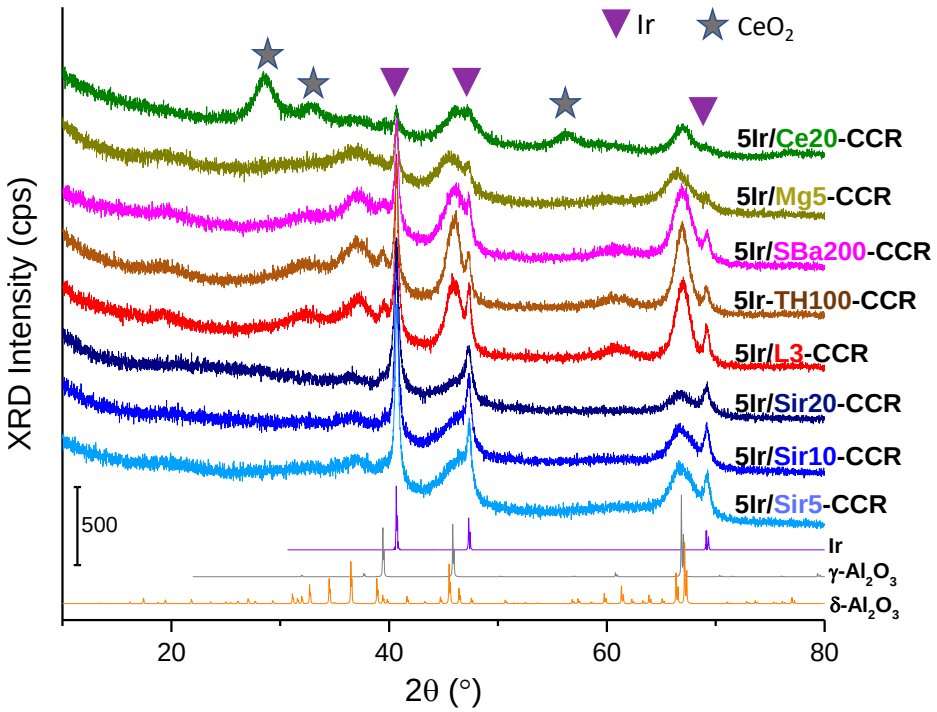



***Figure 6-1.*** *XRD patterns of the catalysts prepared via CCR protocol of the IWI method.*

In order to increase the dispersion of iridium particles on the catalyst support surfaces, L3, TH100 and Sir10 alumina support materials were additionally promoted with either $La_2O_3$ or $CeO_2$. XRD analysis of the corresponding 5 wt.% Ir containing catalysts prepared with the CCR protocol of the IWI method which were also additionally promoted with either 5 wt.% $La_2O_3$ or 5 wt.% $CeO_2$ are presented in **Figure 6-2**. It can be readily realized that all of the catalysts given in **Figure 6-2** contain metallic Ir phases except 5Ir/5La/L3-CCR.

**Figure 6-2a** shows that additional promotion of either 5 wt.% $La_2O_3$ or 5 wt.% $CeO_2$ on the L3-CCR system led to a decrease in the Ir particle size. However, decrease in the average Ir particle size was significantly more pronounced in the case of additional 5 wt.% $La_2O_3$ promotion. An analogous trend was also observed for the TH100-CCR catalysts (**Figure 6-2b**). Note that additional 5 wt.% $La_2O_3$ promotion of the TH100-CCR catalysts were not as effective as in the case of the L3-CCR system in terms of decreasing the Ir average particle size. In contrast to L3-CCR and TH100-CCR catalysts, neither additional $La_2O_3$ nor $CeO_2$ promotion led to a significant alteration in the Ir particle size in the case of the Sir10-CCR system (**Figure 6-2c**).

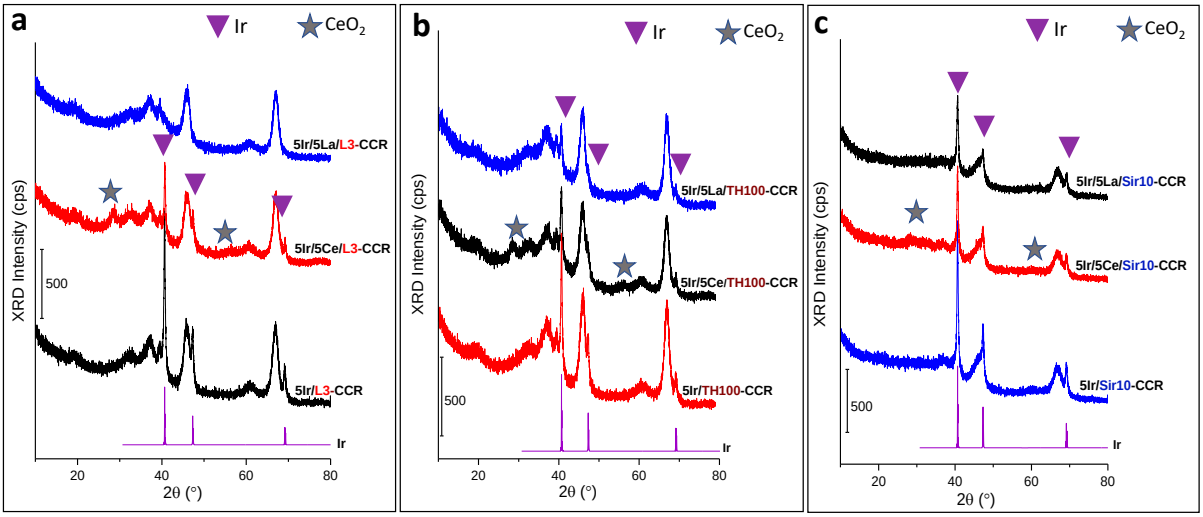



***Figure 6-2.*** *XRD patterns of the catalysts prepared via CCR protocol of the IWI method which were also additionally promoted with either 5 wt.% $La_2O_3$ or 5 wt.% $CeO_2$.*

### 6.1.1.2. XRD of RR samples synthesized via IWI

XRD patterns of the 5 wt.% Ir-containing catalysts synthesized via RR procedure of the IWI method described in **Section 2.2.2.2.1** are presented in **Figure 6-3**. XRD patterns of the RR catalysts depicted in **Figure 6-3** indicate a striking difference in the crystallographic structure of the Ir species on these catalysts as opposed to that of CCR catalysts given in **Figure 6-1**. It is visible in **Figure 6-3** that RR synthesis protocol does not lead to noticeable diffraction signals neither for metallic nor for oxidic Ir species. Similarly, Ir-related diffraction signals were also not detected for the additional promotion of either 5 wt.% $La_2O_3$ or 5 wt.% $CeO_2$ on the L3-RR, TH100-RR, Sir10-RR catalysts (**Figure 6-4**). These observations imply that Ir species predominantly exist as rather small (< 1 nm) clusters and to a lesser extent medium size (2-5 nm) nanoparticles on the RR catalysts.

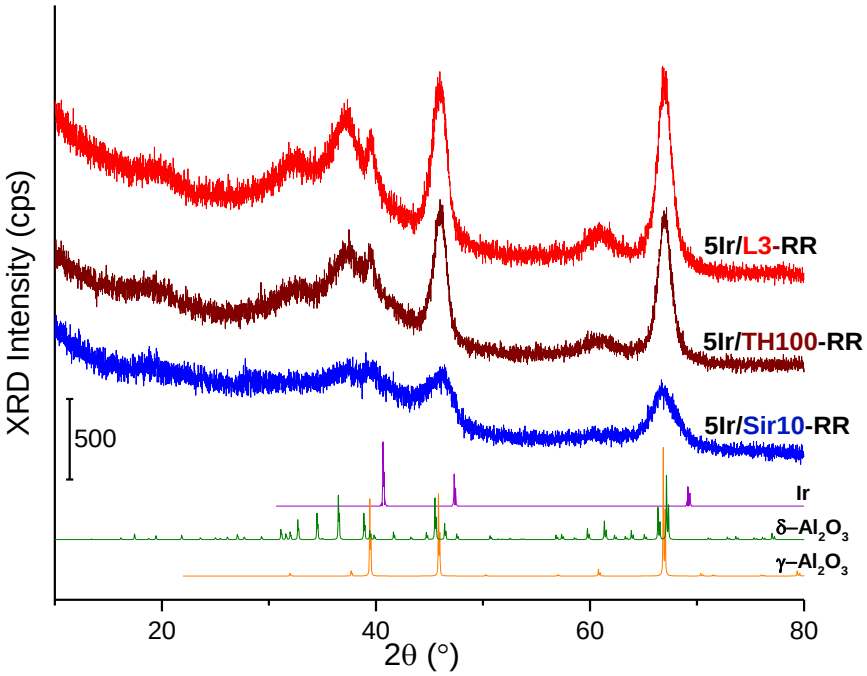



***Figure 6-3.*** *XRD patterns of the catalysts prepared via RR protocol of the IWI method.*

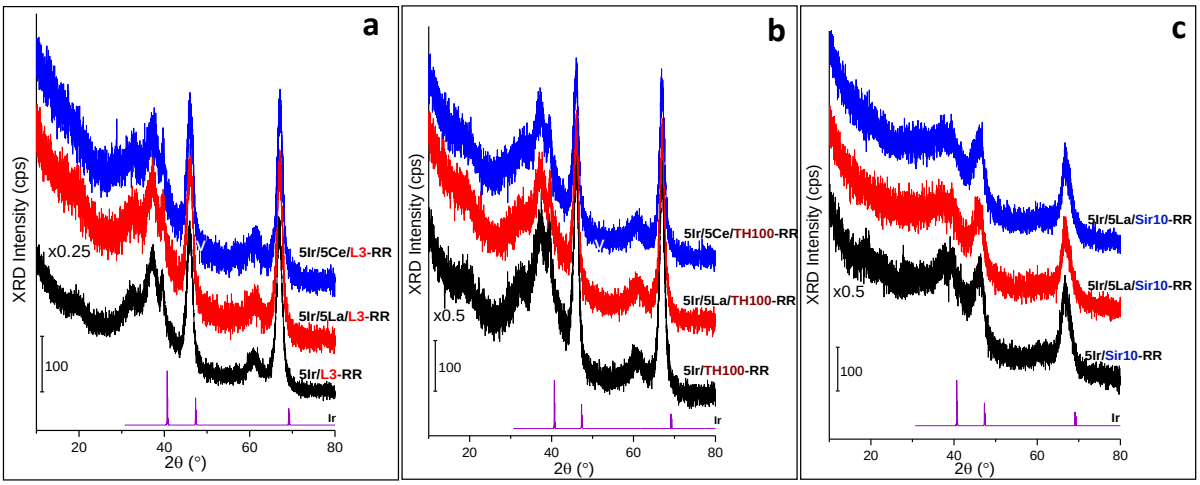



***Figure 6-4.*** *XRD patterns of the catalysts prepared via RR protocol of the IWI method which were also additionally promoted with either 5 wt.% $La_2O_3$ or 5 wt.% $CeO_2$.*

### 6.1.2. TEM analyses of the catalysts synthesized via IWI

#### 6.1.2.1. TEM of CCR samples synthesized via IWI

Typical particle sizes of Ir species and their distribution on the CCR materials were investigated via TEM shown in **Figure 6-5**, **Figure 6-6**, **Figure 6-7**, **Figure 6-8**, **Figure 6-9**, and **Figure 6-10**.

TEM images of the CCR catalysts indicate the presence of large Ir nanostructures having diameters ranging within 25-200 nm. This observation is also in accordance with the XRD data given in **Figure 6-1** revealing the presence of sharp and intense metallic Ir diffraction signals for CCR catalysts. However, it should be emphasized that the number density of such large Ir nanostructures on the CCR catalysts are rather low and additional Ir nanostructures are also visible with much smaller particle sizes (2-10 nm) indicating the existence of a multimodal distribution of Ir particles on all CCR catalysts. Furthermore, considering the high loading of Ir in the catalyst formulation as well as the overall low surface density of the large Ir nanostructures in TEM, presence of small Ir clusters with particle sizes less than 1 nm, which cannot be resolved with the currently used TEM, should not be ruled out for the CCR catalysts.

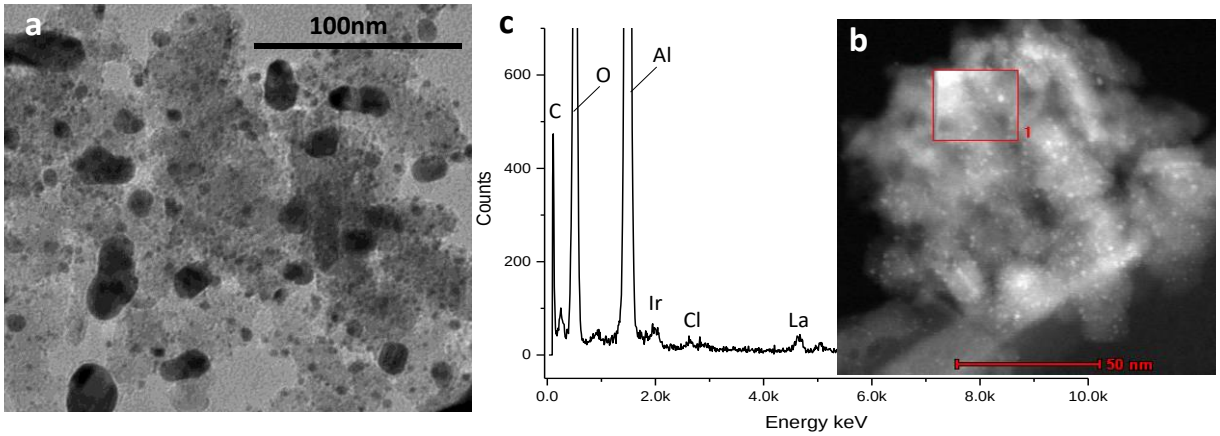



***Figure 6-5.*** *(a) HRTEM image, (b) HAADF-STEM image, and (c) EDX spectrum of the area labeled as 1 in (b) of the 5Ir/L3-CCR catalyst synthesized via IWI.*

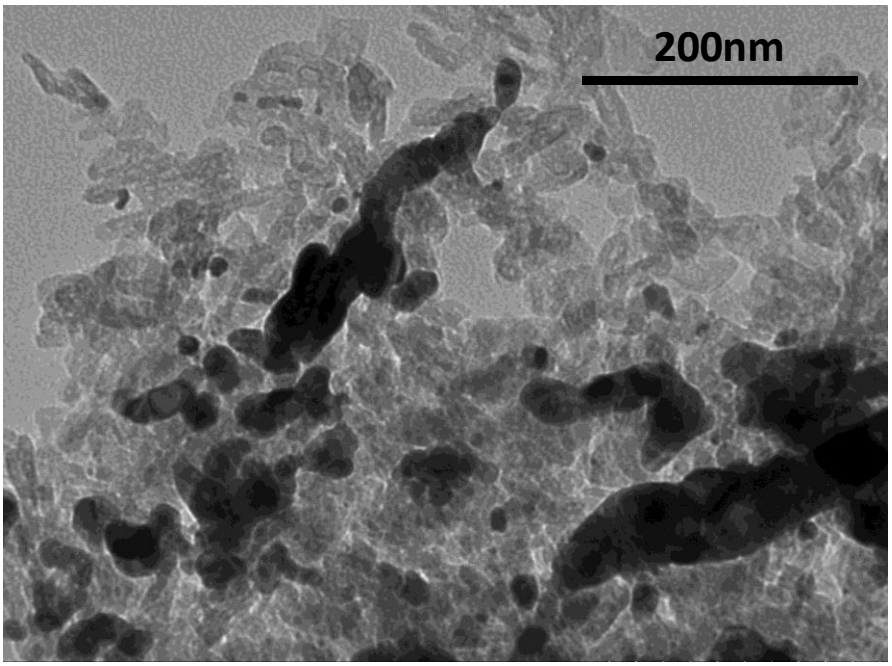



***Figure 6-6.*** *HRTEM image of the 5Ir/TH100-CCR catalyst synthesized via IWI.*

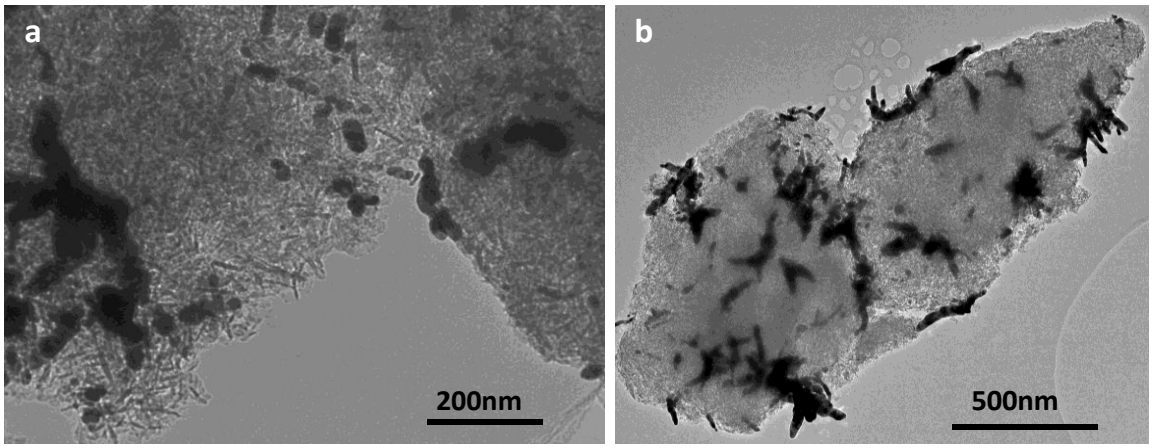



***Figure 6-7.*** *HRTEM images of the 5Ir/Sir10-CCR catalyst synthesized via IWI.*

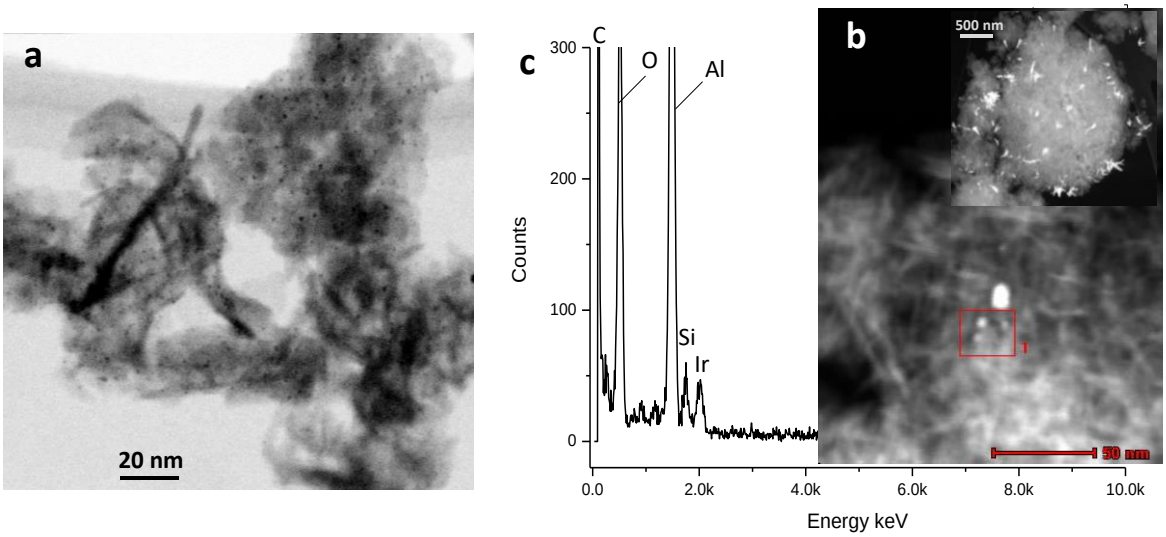



***Figure 6-8.*** *(a) HRTEM image, (b) HAADF-STEM image, and (c) EDX spectrum of the region labeled as 1 in part (b) of the 5Ir/Sir20-CCR catalyst synthesized via IWI.*

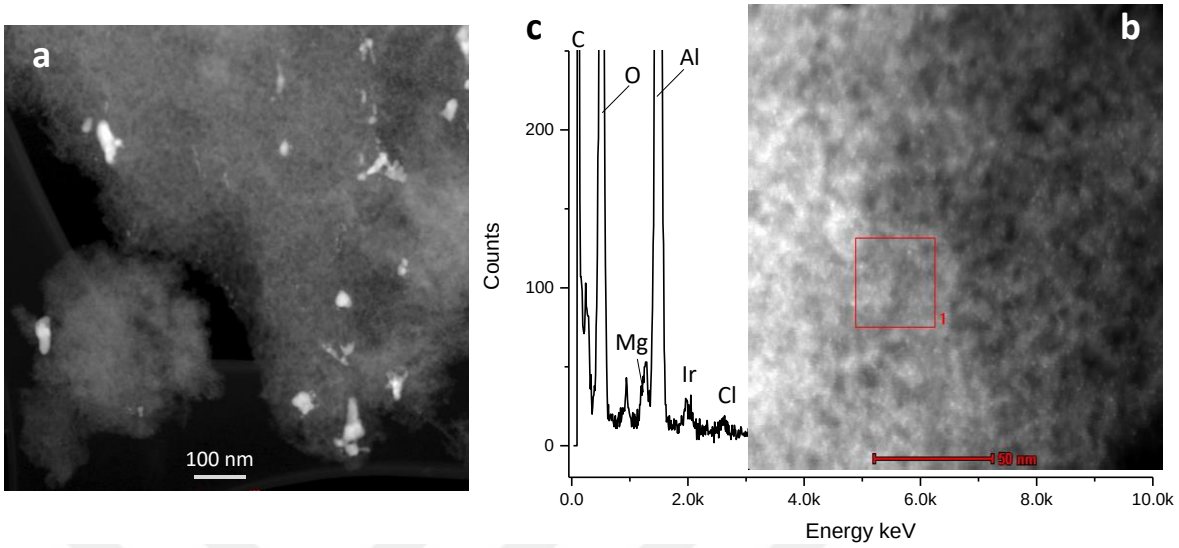



***Figure 6-9.*** *(a-b) HAADF-STEM images, and (c) EDX spectrum of the region labeled as 1 in part (b) of the 5Ir/Mg5-CCR catalyst synthesized via IWI.*

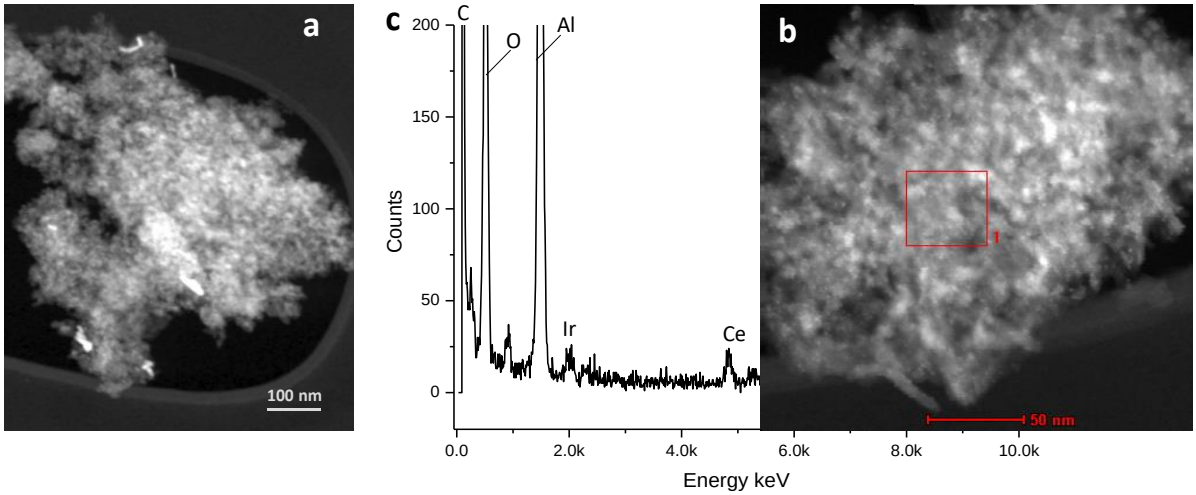



***Figure 6-10.*** *(a-b) HAADF-STEM images, and (c) EDX spectrum of the region labeled as 1 in part (b) of the 5Ir/Ce20-CCR catalyst synthesized via IWI.*

In order to demonstrate the favorable effect of additional 5 wt.% $La_2O_3$ promotion on the Ir dispersion on the L3-CCR catalyst system, we performed HRTEM, HAADF-STEM, and EDX analysis on the 5Ir/5La/L3-CCR catalyst as shown in **Figure 6-11**. Interestingly, on

the 5Ir/5La/L3-CCR catalyst, rather than a bimodal Ir particle size distribution, Ir species were found to exhibit only extremely small particles sizes (i.e., 2-3 nm), where bigger Ir particles (e.g. > 10 nm) do not exist. This observation is in very good agreement with the corresponding XRD pattern of the 5Ir/5La/L3-CCR catalyst (**Figure 6-2a**) which does not reveal any discernible metallic Ir diffraction signals suggesting the presence of only extremely small Ir particles.

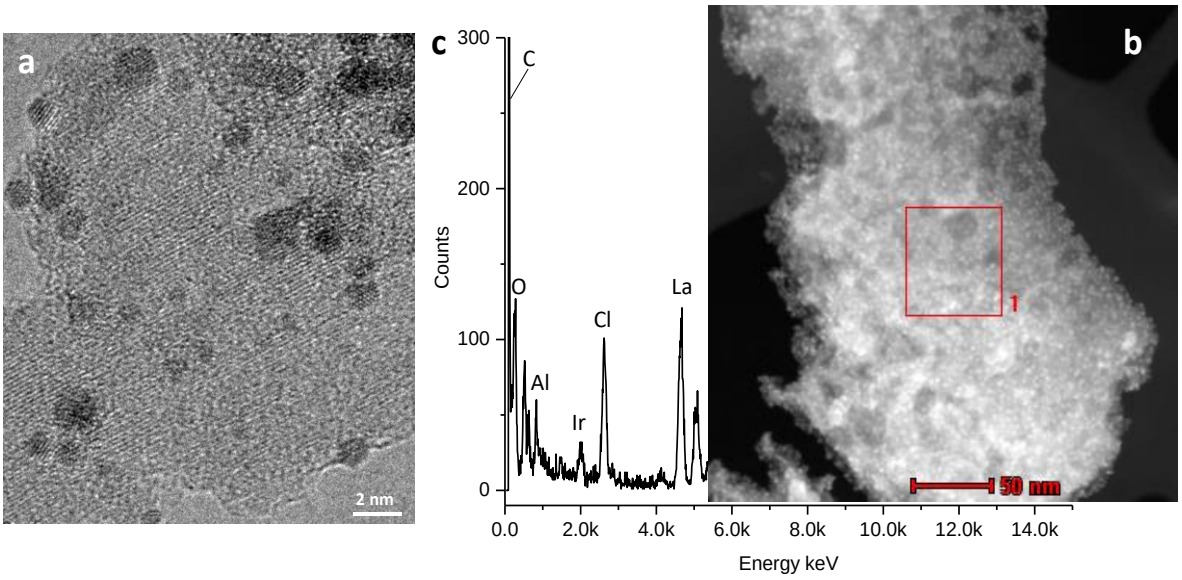



***Figure 6-11.*** *(a) HRTEM image, (b) HAADF-STEM image, and (c) EDX spectrum of the region labeled as 1 in part (b) of the 5Ir/5La/L3-CCR catalyst synthesized via IWI.*

### 6.1.2.2. TEM of RR samples synthesized via IWI

**Figure 6-12a**, **Figure 6-12b** and **Figure 6-12c** depict TEM images of RR catalysts. As expected from the lack of any discernible Ir diffraction signals in the corresponding XRD data of these catalysts (**Figure 6-3**), TEM images of the RR catalysts do not reveal any large Ir nanoparticles but instead are comprised of finely dispersed small (2-5 nm) Ir nanostructures. Again, possible existence of even smaller (< 1 nm) Ir clusters cannot be

precluded on the RR catalysts due to the high Ir loading used in the catalyst synthesis and the moderate spatial resolution of the currently used TEM.

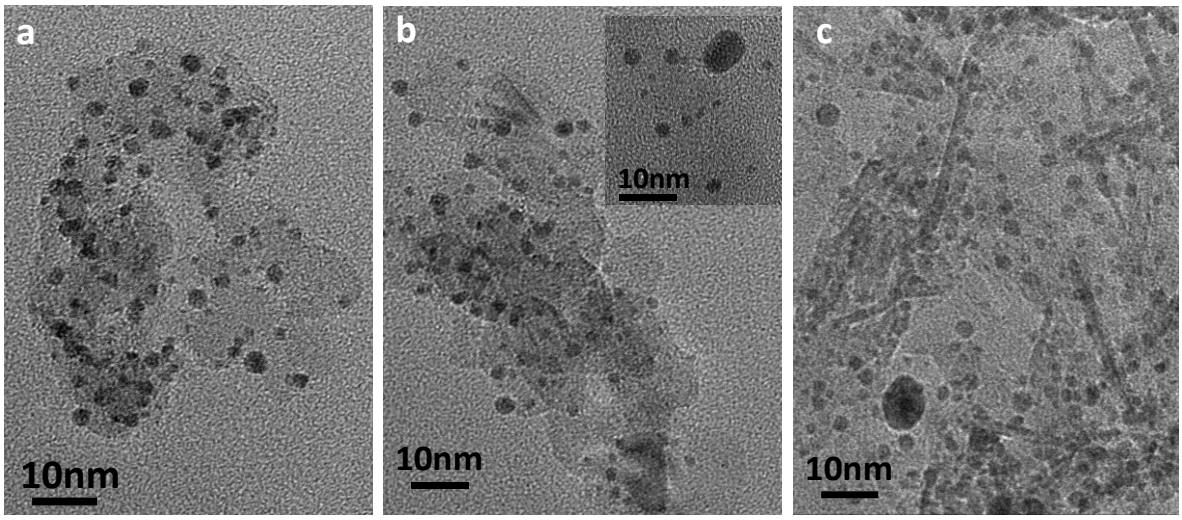



***Figure 6-12.*** *HRTEM images of (a) 5Ir/L3-RR, (b) 5Ir/TH100-RR and (c)5Ir/Sir10-RR catalysts synthesized via IWI.*

## 6.2. PERFORMANCE RESULTS OF THE IWI CATALYSTS OBTAINED FROM CUSTOM-DESIGN MICRO PROPULSION BATCH REACTOR EXPERIMENTS

**Figure 6-13** and **Figure 6-14** show the $T_{Onset}$ and $\Delta P$ values obtained during the anaerobic decomposition of ADN mixture in the presence of the synthesized catalysts as well as in the absence of a catalyst. In the absence of a catalyst, thermal decomposition of ADN mixture starts at 190 °C, yielding a decomposition related pressure generation of 220 mbar [2,115,133]. Corresponding temperature vs. time and pressure vs. time plots for these results are also presented **Appendix C1-Appendix C8.**

As can be seen in **Figure 6-13**, particular synthesis protocol (CCR vs. RR) of the catalysts prepared via IWI method has a relatively minor effect on $T_{Onset}$ whereas type of the support

significantly changes the $T_{Onset}$. Ce and La addition do not have a major effect on $T_{Onset}$ except Sir10-RR samples. Among the synthesized IWI catalysts, the lowest $T_{Onset}$ values belong to 5Ir/L3-RR, 5Ir/5Ce/L3-RR, 5Ir/TH100-RR, and 5Ir/5Ce/TH100-RR samples. On the other hand, only 5Ir/Sir10-RR sample is efficient in increasing $\Delta P$ value. Ce and La addition to 5Ir/Sir10-RR sample have negative effect on the amount of the pressure generation. These observations point out to a variety of factors which may be associated with the origins of these dissimilar promotional behaviors such as: i) variations in the crystallographic phases of different alumina supports, ii) distribution and particle size of Ir active sites on the support surfaces, iii) oxidation state of the Ir species, iv) interaction strength between the Ir active sites and the support material, and v) nature of the coordination of the Ir atoms. Thus, in an attempt to shed light on these important structural and electronic factors which cannot be simply explained by XRD and TEM results shown in **Section 6.1**, detailed *ex-situ* and *in-situ* characterization experiments were carried out on the selected catalysts (5Ir/L3-CCR, 5Ir/TH100-CCR, 5Ir/Sir10-CCR, 5Ir/L3-RR, 5Ir/TH100-RR, 5Ir/Sir10-RR) which will be described in the forthcoming sections.

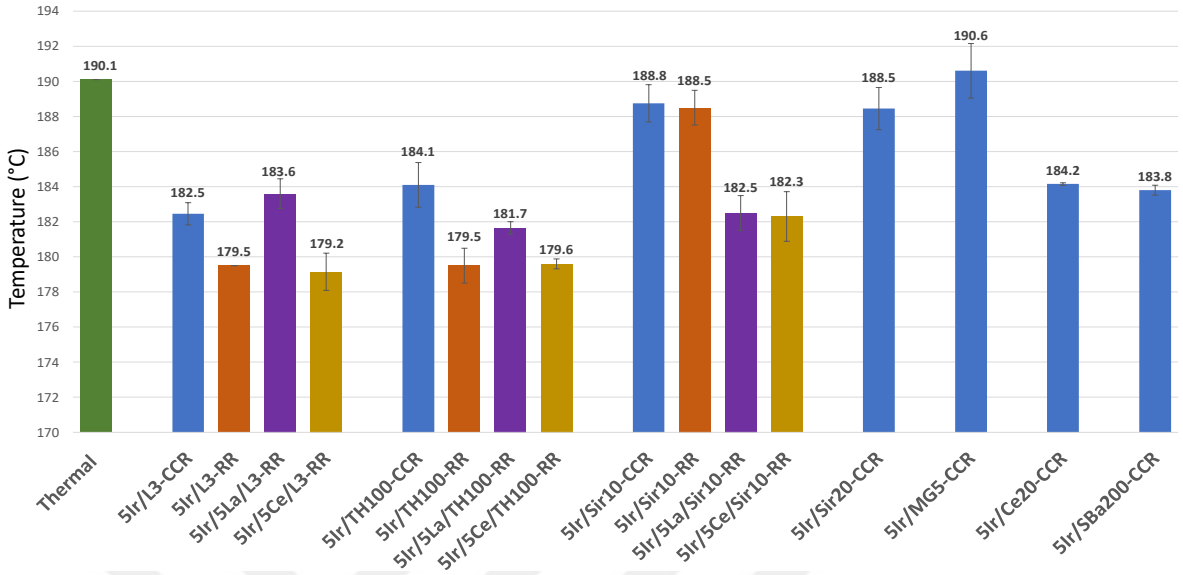



***Figure 6-13.*** *Average $T_{Onset}$ values obtained in the anaerobic catalytic decomposition tests for ADN mixture with the synthesized catalysts via IWI and without a catalyst obtained during the custom-design micro propulsion batch reactor experiments.*

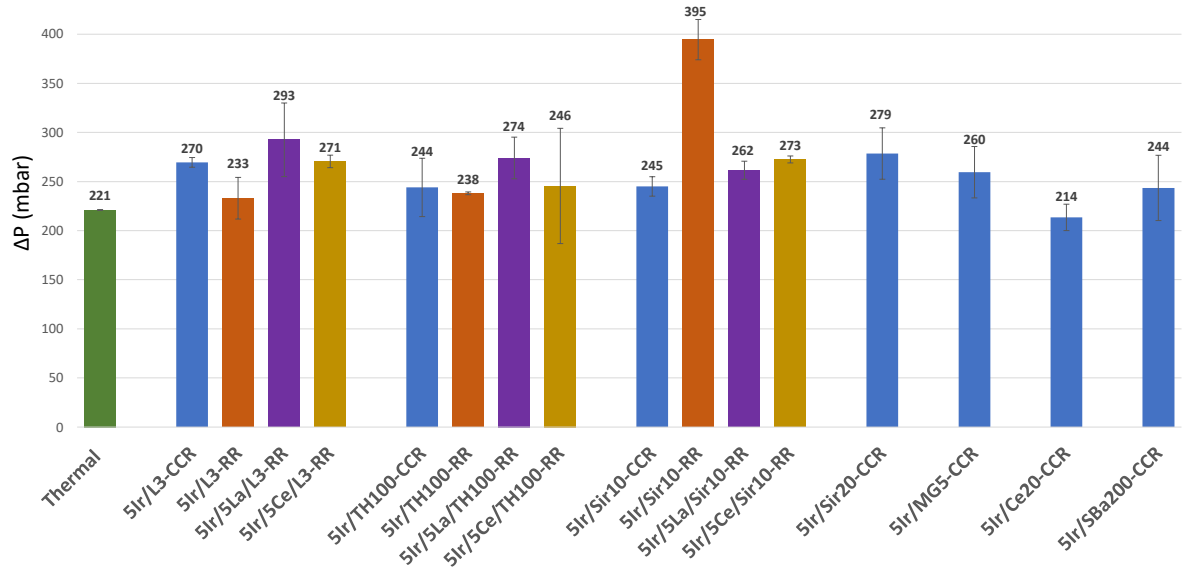



***Figure 6-14.*** *Average ΔP values obtained in the anaerobic catalytic decomposition tests for ADN mixture with the synthesized catalysts via IWI and without a catalyst obtained during the custom-design micro propulsion batch reactor experiments.*

## 6.3. DETAILED CHARACTERIZATION OF SELECTED CATALYSTS SYNTHESIZED VIA IWI

### 6.3.1. Decomposition products via FTIR spectroscopy

**Figure 6-15** illustrates the nature and the relative abundances of the produced gases during ADN decomposition in the absence of any catalyst and also in the presence of different catalysts at temperatures right after the initiation of the decomposition reaction. Corresponding temperature-dependent gas-phase FTIR spectra acquired at different temperatures revealing the evolution of the gaseous products generated upon ADN decomposition are also given in **Figure 6-16-Figure 6-19**. Gas phase FTIR spectra presented in **Figure 6-15** reveal characteristic vibrational signatures due to $N_2O$ (3500–3400 $cm^{-1}$ ($\upsilon_1$+ $\upsilon_3$), 2260–2100 $cm^{-1}$ (asymmetric stretching, $\upsilon_3$), and 1350–1200 $cm^{-1}$ (symmetric stretching $\upsilon_1$)), $NH_3$ (927 and 968 $cm^{-1}$), $CO_2$ (2400-2250 $cm^{-1}$), $CH_3OH$ (3550-3800 $cm^{-1}$(OH stretching, $\upsilon_{O-H}$), 3200-2700 $cm^{-1}$ (CH stretching, $\upsilon_{C-H}$), 1100-950 $cm^{-1}$(CO stretching, $\upsilon_{C-O}$)) a[134–136]. Note that within 1800-1400 $cm^{-1}$, NO, $NO_2$, and water vibrational signals heavily overlap. Former studies in the literature suggested that ADN (i.e., $NH_4N(NO_2)_2$) decomposition may start with any of the following reaction pathways [137];

$$NH_4N(NO_2)_2 \rightarrow NH_4NO_3 + N_2O \quad (1)$$

$$NH_4N(NO_2)_2 \rightarrow NH_3 + HNO_3 + N_2O \quad (2)$$

$$NH_4N(NO_2)_2 \rightarrow NH_3 + HN(NO_2)_2 \quad (3)$$

Moreover, Gronland et al. [6] and Zhang et al. [138] showed that after the initiation of the ADN decomposition via reaction *(1)*, reaction may proceed with the following steps;

$$NH_4NO_3 \rightarrow \tfrac{3}{4}\ N_2 + \tfrac{1}{2}\ NO_2 + 2\ H_2O \quad (4a)$$

$NO_2 \rightleftharpoons NO + ½\ O_2$ (4b)

$N_2O \rightarrow N_2 + O_{ads}$ (5)

$N_2O + O_{ads} \rightarrow N_2 + O_2$ (6)

$CH_3OH + NO_2 \rightarrow HCOOH + ½\ N_2 + H_2O$ (7)

$2\ CH_3OH + 3\ O_2 \rightarrow 2\ CO_2 + 4\ H_2O$ (8)

$HCOOH + ½\ O_2 \rightarrow CO_2 + H_2O$ (9)

When the relative IR signal intensity ratios of $I_{CH3OH}/I_{N2O}$ and $I_{NH3}/I_{N2O}$ shown in **Figure 6-15** are compared for different catalysts, it can be realized that relative formation of $NH_3$ and $CH_3OH$ gases is more pronounced for 5Ir/TH100-CCR and 5Ir/TH100-RR. This can be attributed to the prominence of ADN decomposition reaction pathways *(2)* and *(3)* for 5Ir/TH100-CCR and 5Ir/TH100-RR which do not yield $NH_4NO_3$, where the latter species is one of the required chemicals for $CH_3OH$ oxidation via reactions *(4a-b, 7-9)*. Observation of unreacted methanol in the exhaust is not preferable as it indicates incomplete combustion of the oxygenate in the ADN mixture. Limited extent of $CH_3OH$ oxidation on 5Ir/TH100-CCR and 5Ir/TH100-RR catalysts is also consistent with the relatively lower $CO_2$ formation (see the inset labeled with $CO_2$ in **Figure 6-15**) on these catalysts. For 5Ir/L3 and 5Ir/Sir10 catalysts, contribution of the ADN decomposition pathway (1) seems to be greater than that of the undoped 5Ir/TH100 catalysts, since the relative extents of formation of $CH_3OH$ and $NH_3$ are lower as compared to $N_2O$. Accordingly in **Figure 6-15**, smaller $I_{CH3OH}/I_{N2O}$ and $I_{NH3}/I_{N2O}$ FTIR intensity ratios are observed for the 5Ir/L3 and 5Ir/Sir10 catalysts than that of 5Ir/TH100. Moreover, the highest $N_2O$ to $CH_3OH$ ratio is observed for 5Ir/Sir10-RR which may explain the higher $\Delta P$ value for this particular sample (**Figure 6-14**) due to its high efficiency in the combustion of the oxygenate with ADN.

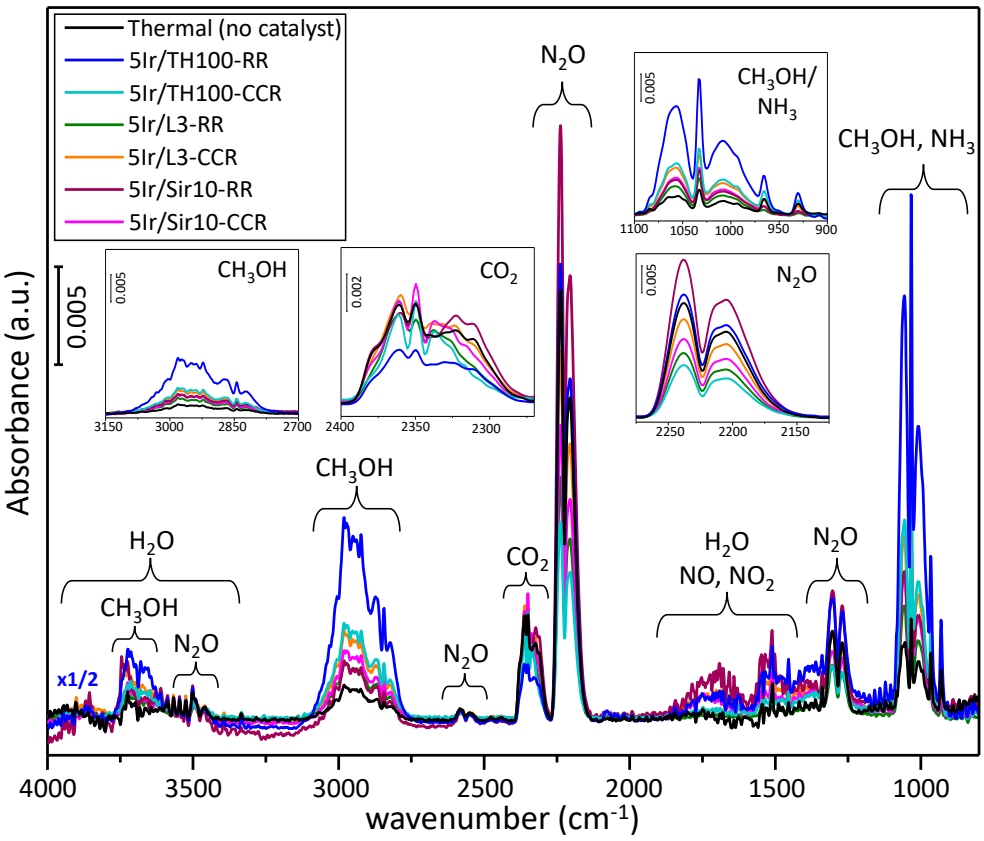



***Figure 6-15.*** *Gas-phase FTIR spectra obtained for catalytic and non-catalytic decomposition of ADN mixture at the corresponding* $T_{Onset}$ *values.*

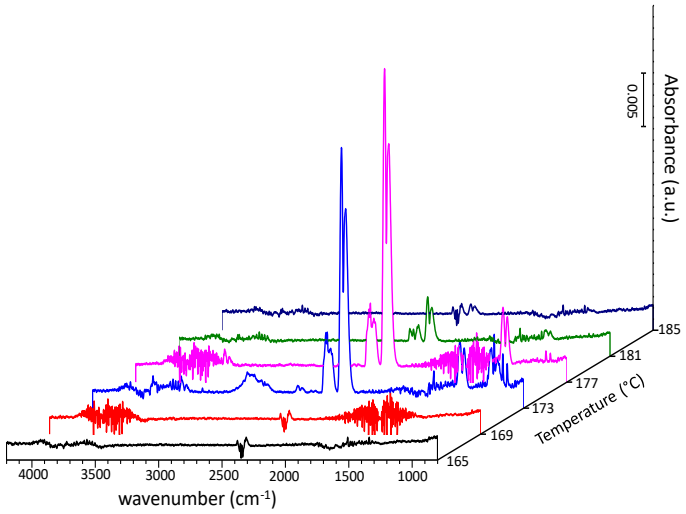



***Figure 6-16.*** *Gas-phase FTIR spectra for the thermal ADN decomposition products as a function of temperature.*

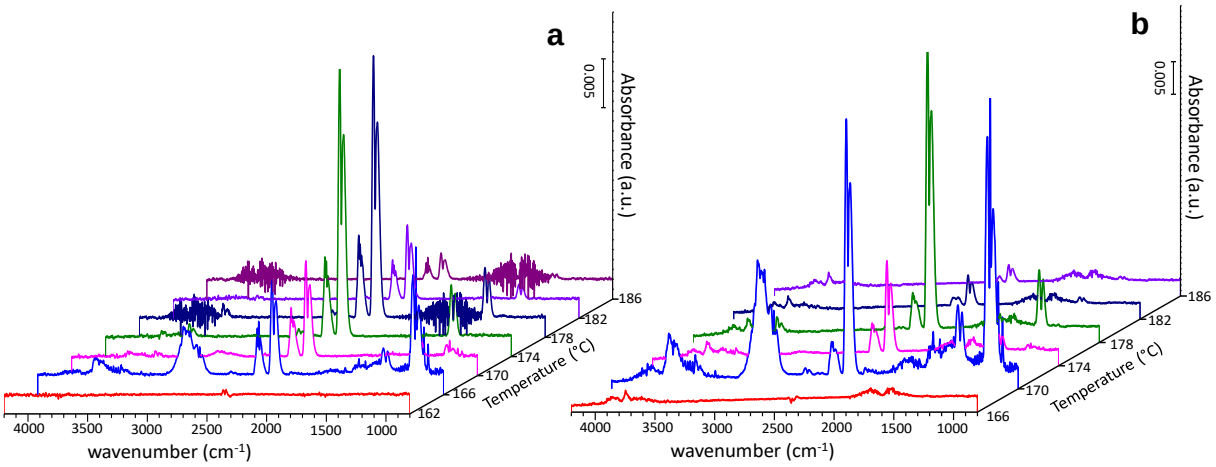



***Figure 6-17.*** *Gas-phase FTIR spectra for the catalytic ADN decomposition products as a function of temperature for (a) 5Ir/TH100-CCR and (b) 5Ir/TH100-RR synthesized via IWI.*

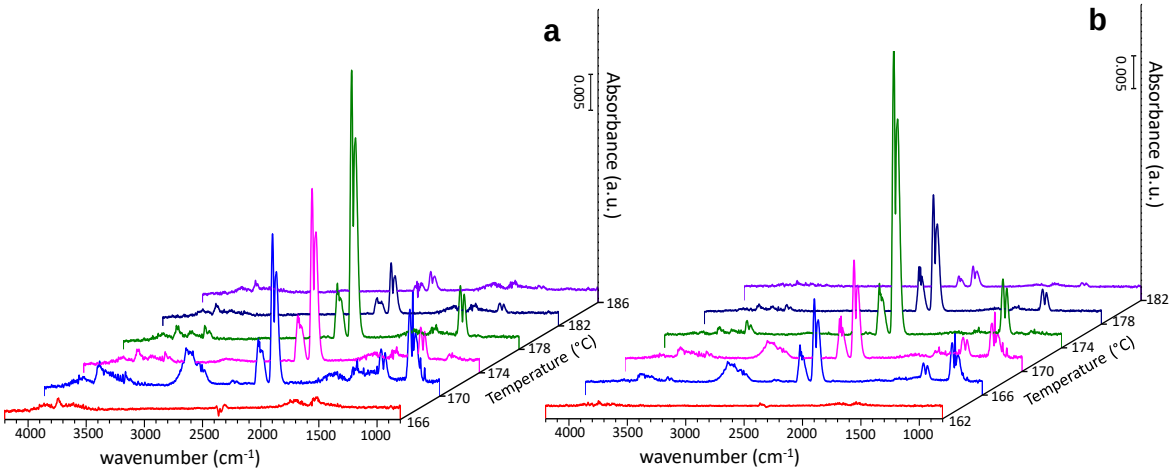



***Figure 6-18.*** *Gas-phase FTIR spectra for catalytic ADN decomposition products as a function of temperature for (a) 5Ir/L3-CCR and (b) 5Ir/L3-RR synthesized via IWI.*

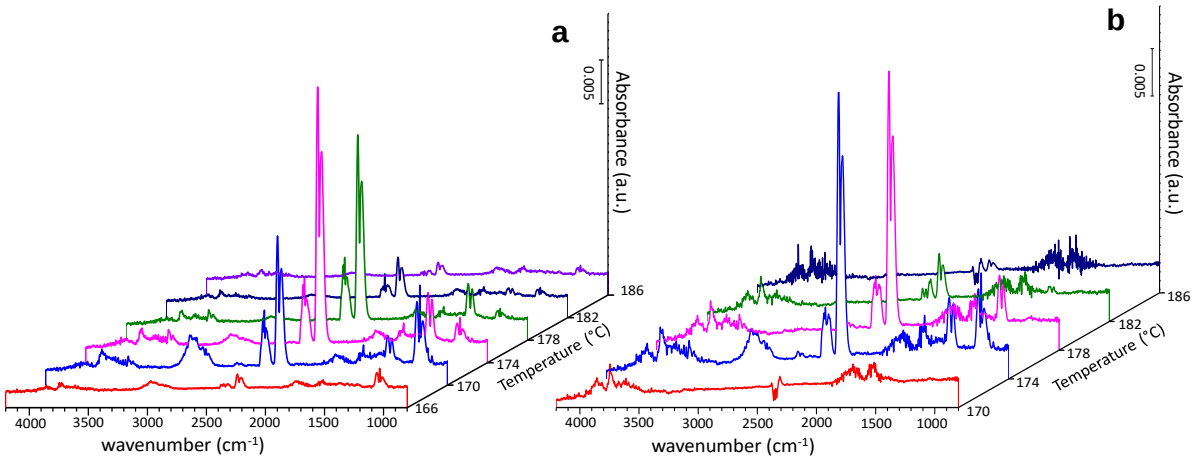



***Figure 6-19.*** *Gas-phase FTIR spectra for catalytic ADN decomposition products as a function of temperature for (a) 5Ir/Sir10-CCR and (b) 5Ir/Sir10-RR samples synthesized via IWI.*

### 6.3.2. Specific surface area (SSA) of the selected catalysts synthesized via IWI

SSA measurement results for the synthesized samples are presented in **Figure 6-20**. It is clearly discernible that the Si containing 5Ir/Sir10 samples have significantly higher SSA values than the 5Ir/TH100 and La promoted 5Ir/L3 catalysts. Also, variations in the synthesis protocol have a negligible effect on SSA. SSA values of the 5Ir/TH100 CCR and RR catalysts are 139 and 130 $m^2/g$, respectively. 5Ir/Sir10 CCR and RR catalysts possess SSA values of 231 and 223 $m^2/g$, whereas 5Ir/L3 CCR and RR catalysts have SSA values of 140 and 136 $m^2/g$, respectively. As discussed in the XRD results shown in **Figure 6-1** and **Figure 6-3**, observation of a $\delta$-$Al_2O_3$ phase for the 5Ir/L3 and 5Ir/TH100 catalysts is consistent with the lower SSA value of this catalyst, as compared to that of the higher SSA 5Ir/Sir10 catalyst, where no alumina phases other than $\gamma$-$Al_2O_3$ were detectable in the latter case.

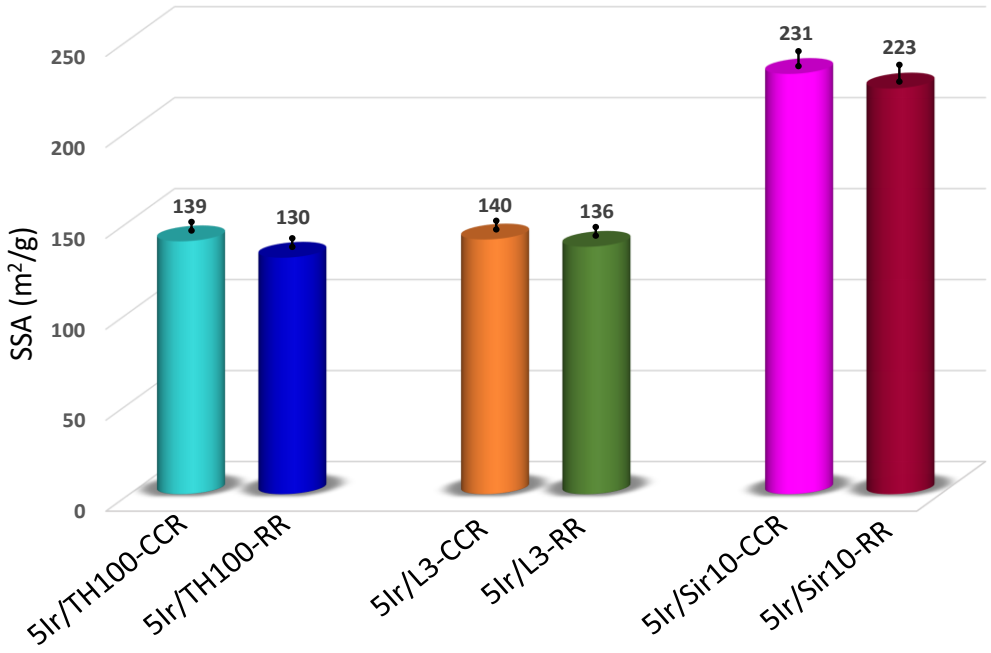



***Figure 6-20.*** *SSAs for the synthesized catalysts via IWI.*

### 6.3.3. Composition of the catalysts synthesized via IWI from XRF

The composition of the selected IWI catalysts obtained from XRF measurements are given in **Table 6-1**. The Ir loadings obtained from the XRF measurements were ca. 2.5 wt. % which is lower than the nominal Ir loading (5 wt. %) due to unknown amount of hydrate inside the Ir precursor and the limited solubility of the iridium precursor in the solution prepared for impregnation.

***Table 6-1.*** *Composition of the catalysts synthesized via IWI based on XRF measurements.*

| Sample Name | Ir (wt. %) | $La_2O_3$ (wt. %) | $SiO_2$ (wt. %) | Cl (wt. %) | $Al_2O_3$ (wt. %) | P (wt. %) | K (wt. %) | Mg (wt. %) |
|---|---|---|---|---|---|---|---|---|
| 5Ir/TH100-CCR | 2.5 | - | - | 0.6 | 93.2 | 2.7 | 0.2 | 0.6 |
| 5Ir/TH100-RR | 2.8 | - | - | 1.2 | 93.0 | 2.2 | 0.2 | 0.5 |
| 5Ir/L3-CCR | 2.7 | 3.1 | - | 0.9 | 90.7 | 1.6 | 0.2 | 0.6 |
| 5Ir/L3-RR | 2.4 | 3.2 | - | 1.2 | 90.5 | 1.6 | 0.2 | 0.7 |
| 5Ir/Sir10-CCR | 2.5 | - | 9.3 | 0.4 | 83.6 | 3.4 | 0.1 | 0.5 |
| 5Ir/Sir10-RR | 2.2 | - | 9.4 | 0.7 | 84.2 | 2.6 | 0.1 | 0.5 |

### 6.3.4. Ir particle size of the catalysts synthesized via IWI from XRD and TEM analysis

For the RR samples, ImageJ software was used to calculate the average Ir particle diameters from the TEM images shown in **Figure 6-3**. The average diameters of the Ir particles were found to be 2.3 nm, 1.5 nm, and 1.6 nm for 5Ir/TH100-RR, 5Ir/L3-RR, and 5Ir/Sir10-RR samples, respectively (**Figure 6-21**). On the other hand, because of the bimodal distribution of the Ir particles in CCR samples, we did not attempt to estimate the average Ir particle diameters for these samples via from TEM. Instead, Williamson-Hall method was used to determine the average Ir crystallite size by using the XRD data given in **Figure 6-1**. The mean Ir crystallite diameters were estimated to be 50 nm, 18 nm, and 11 nm for 5Ir/TH100-CCR, 5Ir/L3-CCR, and 5Ir/Sir10-CCR samples, respectively. (**Figure 6-22**).

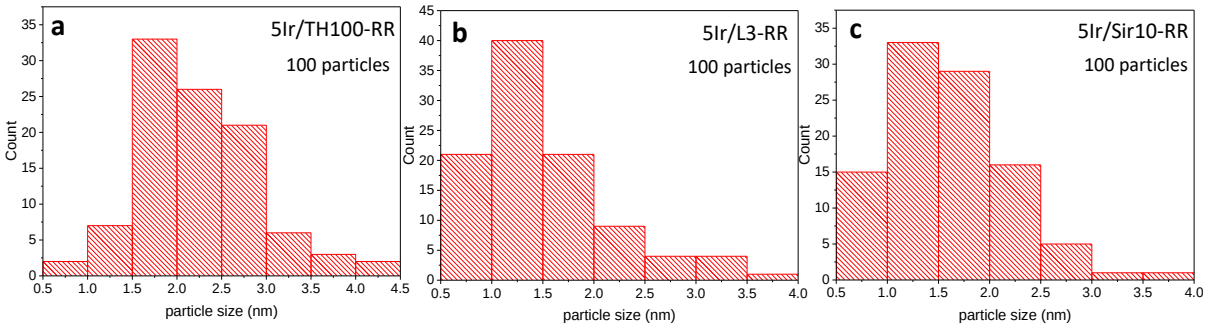



***Figure 6-21.*** *Ir particle size distribution for (a) 5Ir/TH100-RR, (b) 5Ir/L3-RR, and (c) 5Ir/Sir10-RR synthesized via IWI.*

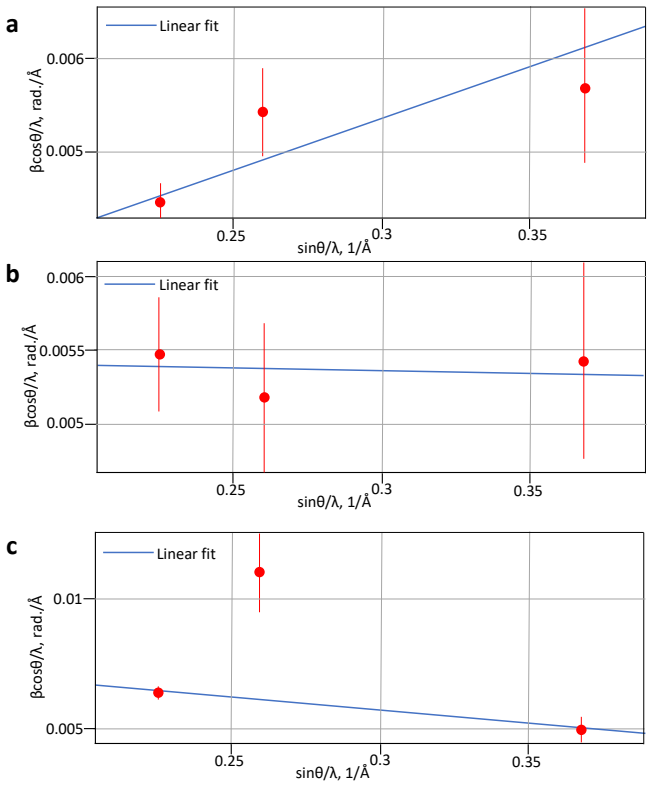



***Figure 6-22.*** *Williamson-Hall plots for (a) 5Ir/TH100-CCR, (b) 5Ir/L3-CCR, and (c) 5Ir/Sir10-CCR samples synthesized via IWI.*

### 6.3.5. *In-situ* FTIR CO adsorption experiments for the analysis of Ir morphology and Ir oxidation state

In an attempt to investigate the detailed electronic structure of the Ir active sites of the selected IWI catalysts and their surface morphology, CO(g) was used as a probe molecule and in-situ FTIR spectroscopic measurements were carried out upon CO adsorption on the selected IWI catalysts. Results of these experiments are shown in **Figure 6-23**. Additional in-situ FTIR data corresponding to stepwise increasing CO pressure on each catalyst sample are also provided in **Figure 6-24**.

In-situ FTIR spectra given in **Figure 6-23** reveal informative results enabling detailed analysis of the electronic structure of the Ir active sites on the synthesized catalyst surfaces.

Three different types of CO vibrational features can be identified in **Figure 6-23a-d** which are located at: i) 2091-2082 $cm^{-1}$, ii) 2062-2055 $cm^{-1}$, and iii) 2079-2070 $cm^{-1}$ + 2010-2006 $cm^{-1}$ (**Figure 6-23e**). The first of these vibrational features within 2091-2082 $cm^{-1}$ can be assigned to atop/ontop/linear adsorption of CO on small and highly dispersed oxidic iridium clusters ($Ir_n^{x+}$) as well as atomically dispersed $Ir^{x+}$ [139–144]. Extremely small full width at half maximum (FWHM) values (6-20 $cm^{-1}$) of this vibrational feature strongly indicates the structural homogeneity of these $Ir_n^{x+}$ sites which is consistent with the small number of Ir atoms in these clusters due to cluster diameters of less than 1 nm [145]. The second vibrational feature observed within 2062-2055 $cm^{-1}$ can be attributed to atop/ontop/linear adsorption of CO on metallic Ir sites ($Ir^0$) of relatively larger iridium nanoparticles (NP) [139,140,146–150]. The last vibrational feature consists of a pair of stretching located within 2079-2070 $cm^{-1}$ (symmetric stretch, *s*) and 2010-2006 $cm^{-1}$ (antisymmetric stretch, *as*) which is associated to gem carbonyls ($Ir(CO)_2$) [142,143,145,150–156]. Furthermore, using the expression: $I_{as}/I_s = tan^2(\theta/2)$ [143], one can estimate the OC-Ir-CO bond angle $(\theta)$ in these gem carbonyls to be $\leq 40°$.

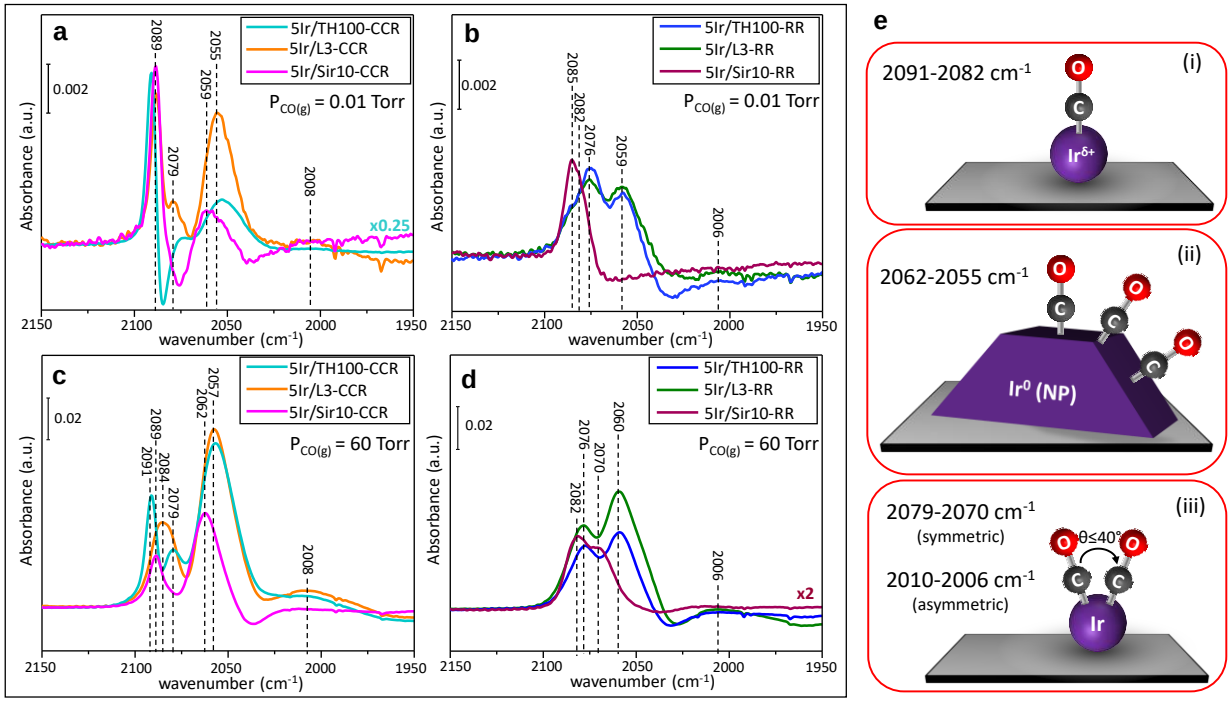



***Figure 6-23.*** *In-situ FTIR spectra for the synthesized CCR and RR catalysts via IWI upon CO adsorption at (a-b) 0.01 Torr, (c-d) 60 Torr. (e) Schematic representation of CO vibrational features observed for the CCR and RR catalysts.*

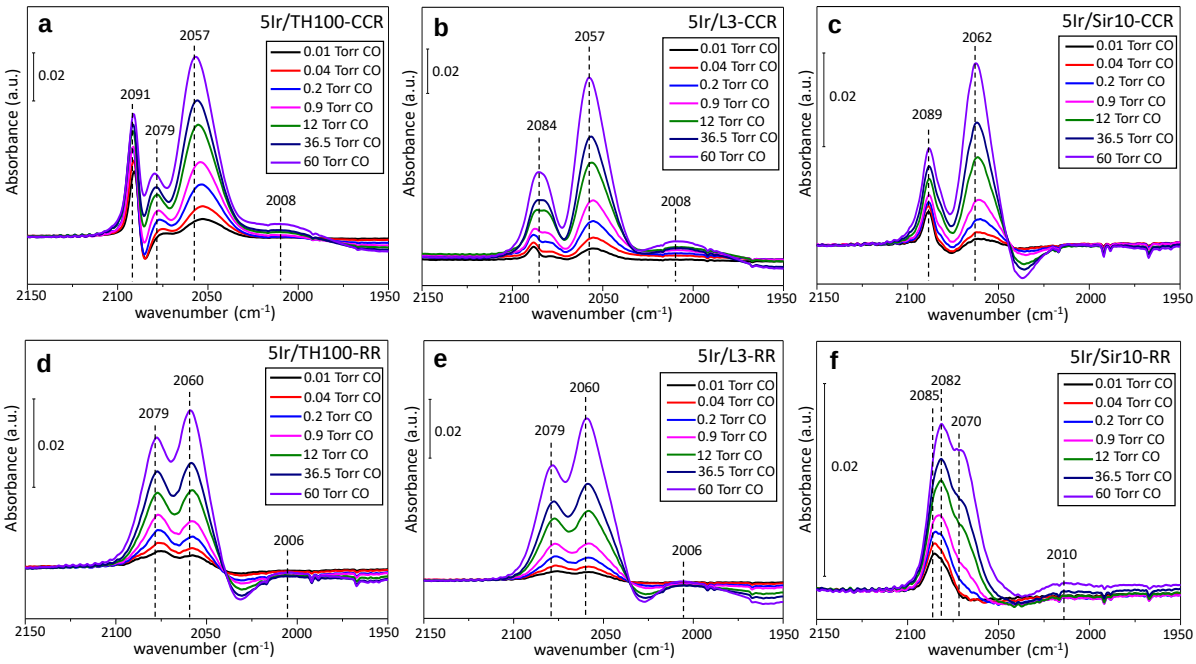



***Figure 6-24.*** *In-situ FTIR spectra corresponding to the stepwise CO adsorption at RT on (a) 5Ir/TH100-CCR, (b) 5Ir/L3-CCR, (c) 5Ir/Sir10-CCR, (d) 5Ir/TH100-RR, (e) 5Ir/L3-RR, (f) 5Ir/Sir10-RR samples synthesized via IWI.*

**Figure 6-23a** suggests that upon lower CO exposures (i.e., 0.01 Torr) on 5Ir/TH100-CCR, 5Ir/L3-CCR, and 5Ir/Sir10-CCR catalysts, coordinatively unsaturated $Ir_n^{x+}$ sites are predominantly populated with carbonyls, where CO adsorption on $Ir^0$ (NP) sites occurs to a lesser extent. Increasing the CO pressure to 60 Torr on these samples (**Figure 6-23c**) indicate saturation of the $Ir_n^{x+}$ sites with carbonyls, whereas $Ir^0$ (NP) sites continue to adsorb CO species in both samples and the gem carbonyls also become more visible for 5Ir/TH100-CCR and 5Ir/L3-CCR catalyst. These observations are in particularly good agreement with the current XRD data for the CCR catalysts revealing the presence of large metallic Ir NP (**Figure 6-1**) and the interpretation of the current TEM data (**Figure 6-5**, **Figure 6-6**, and

**Figure 6-7**) corresponding to a multimodal Ir surface distribution comprised of both large (>10 nm) and small (2-10 nm) Ir-NP, as well as even smaller Ir clusters of < 1 nm.

**Figure 6-23b** and **Figure 6-23d** present the corresponding in-situ FTIR spectra for the 5Ir/TH100-RR, 5Ir/L3-RR, and 5Ir/Sir10-RR catalysts. Interestingly, low pressure CO adsorption on the 5Ir/Sir10-RR catalyst shows an unusual behavior which is not observed in any of the other currently investigated catalysts. It is apparent that 5Ir/Sir10-RR catalyst reveals almost exclusively $Ir_n^{x+}$ sites belonging to small Ir clusters. Furthermore, overall FTIR signal intensities of the 5Ir/Sir10-RR sample for high CO coverages (i.e., 60 Torr) is much smaller than all other investigated samples. This is rather surprising since, 5Ir/Sir10-RR sample has a higher SSA than 5Ir/TH100-CCR and 5Ir/L3-CCR catalysts (**Figure 6-20**). This observation can be explained using the fact that Ir particles may be covered with $SiO_x$-$AlO_x$ domains via SMSI phenomena rendering them less accessible for CO adsorption [140,144,157]. Likewise, small $Ir_n^{x+}$ clusters also presumably interact strongly with the $SiO_x$-$AlO_x$ surface and become less exposed to CO(g) due to the partial immersion/diffusion of Ir sites into the $SiO_x$-$AlO_x$ matrix. This argument will be further verified with the current in-situ EXAFS measurements demonstrating a greater extent of Ir-O coordination for the 5Ir/Sir10-RR sample. Upon increasing the CO pressure to 60 Torr, 5Ir/Sir10-RR catalyst mostly reveals vibrational features due to $Ir_n^{x+}$ sites and $Ir(CO)_2$ (gem carbonyls), lacking any noticeable FTIR signals associated with $Ir^0$ NPs. Thus, the unusual $\Delta P$ values observed in the catalytic ADN decomposition tests for the 5Ir/Sir10-RR catalyst can be linked to the unique structural/electronic properties of the Ir/$SiO_x$-$AlO_x$ interfacial chemistry which is dominated by small $Ir_n^{x+}$ clusters strongly interacting with the $SiO_x$-$AlO_x$ domains.

*In*-situ FTIR data for the 5Ir/TH100-RR and 5Ir/L3-RR samples given in **Figure 6-23b** and **Figure 6-23d** indicate that on these catalysts, relative surface concentration of $Ir_n^{x+}$ sites are less than the remaining catalyst samples where atop/linear/ontop CO adsorption on $Ir^0$ NP sites and $Ir(CO)_2$ are the most prominent species. Accordingly, lower $T_{Onset}$ values observed for these catalysts can be attributed to the dominance of $Ir^0$ NP sites, where ADN decomposition presumably occurs with a lower activation energy.

### 6.3.6. Surface acidity via pyridine adsorption and the extent of ADN uptake via FTIR measurements

Si-promotion of alumina may have an influence on the interaction between the ADN mixture and the catalyst surface. It is known that $SiO_x$ promotion increases the surface acidity of alumina [158]. The higher surface acidity of the Si promoted samples was verified with pyridine adsorption experiments as shown in **Figure 6-25**. **Figure 6-25a** shows the in-situ FTIR spectra after pyridine adsorption on synthesized catalysts. Pyridine $\upsilon_{8a}$ and $\upsilon_{19b}$ IR stretching modes appear within 1632-1580 $cm^{-1}$ and 1455-1438 $cm^{-1}$, respectively. These stretching modes can be attributed to Lewis acid sites [159–162]. The Lewis acidity of metal oxides increases with increasing frequency of $\upsilon_{8a}$ IR stretching mode [159,161,162]. As seen from **Figure 6-25b**, the 1588 $cm^{-1}$ signal shifts to higher frequencies upon Si promotion. Accordingly, Lewis acidity of the samples are found to decrease in the following order: 5Ir/Sir10-CCR = 5Ir/Sir10-RR > 5Ir/TH100-RR > 5Ir/TH100-CCR = 5Ir/L3-CCR = 5Ir/L3-RR. Negative peaks are due to the reconstruction of surfaces upon pyridine adsorption.

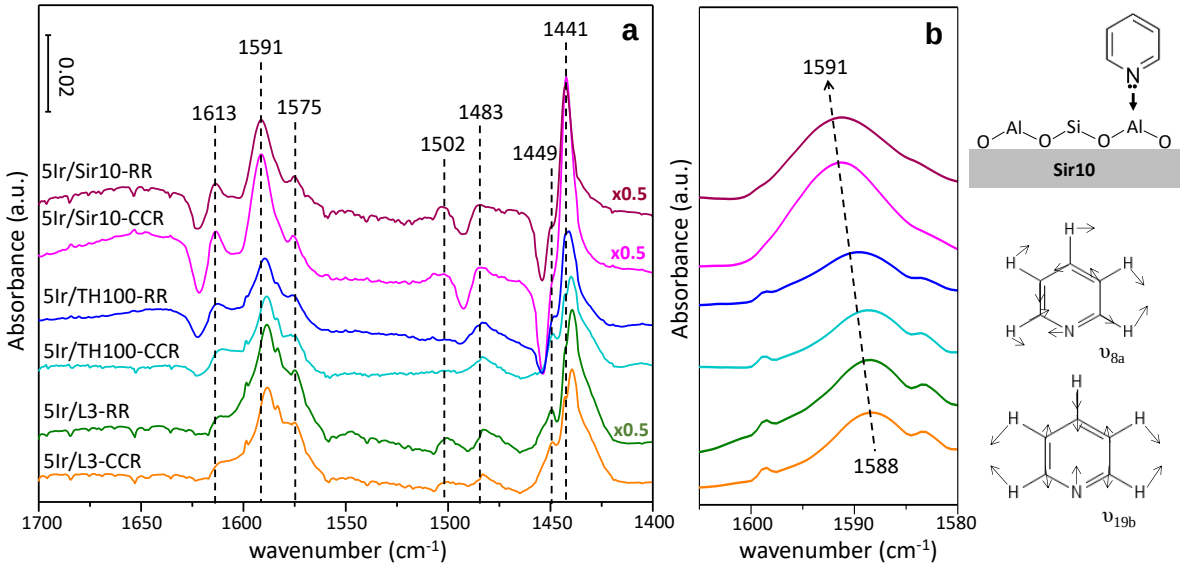



***Figure 6-25.*** *(a) In-situ FTIR spectra for pyridine adsorption on synthesized catalysts via IWI (b) the detailed view of 1588-1591 cm$^{-1}$ signals.*

Stabilizers used in the ADN fuel mixture such as ammonia led to a basic pH. Thus, increased surface acidity upon Si promotion may lead to poisoning of the 5Ir/Sir10-RR catalyst surface with strongly bound basic (ammonia/amine) groups as well as ADN species which may lead to an increased $T_{Onset}$ (**Figure 6-13**). ADN adsorption experiments shown in **Figure 6-26** also illustrate the greater amount of ADN uptake by 5Ir/Sir10 catalysts. However, upon sufficient thermal activation and liberation of catalytic active sites, basic ammonia/amine groups may desorb from the 5Ir/Sir10-RR catalyst surface and the remaining large amount of ADN strongly adsorbed on the small $Ir_n^{x+}$ clusters may lead to a high concentration of products resulting in a large ΔP generation (**Figure 6-14**). The lack of such a ΔP boost in the case of 5Ir/Sir10-CCR catalyst can be explained by simultaneous desorption of ADN and basic species from the small and large metallic Ir NP (due to the

presumably weaker adsorption of ADN on these latter Ir species) which are the predominant Ir species on this catalyst.

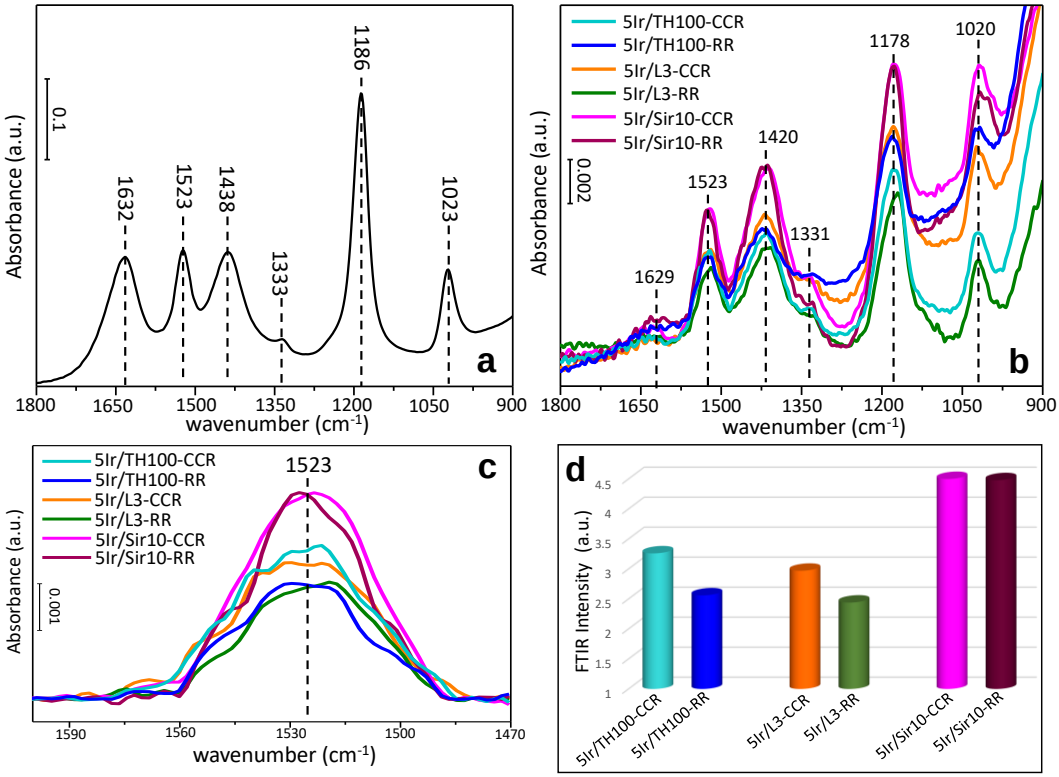



***Figure 6-26.*** *(a) ATR spectrum of ADN/water mixture, (b) ATR spectrum of ADN adsorbed on synthesized catalysts via IWI, (c) the detailed view of the 1523 $cm^{-1}$ signal, (d) FTIR intensities of the 1523 $cm^{-1}$ IR signal shown in part (c).*

### 6.3.7. Ir oxidation state via XPS

**Figure 6-27** depicts the Ir 4f XPS spectra of the investigated catalysts. Ir 4f signals were deconvoluted using three species: $Ir^0$, $Ir^{3+}$ and $Ir^{4+}$. Metallic iridium peaks are typically assigned to be within 60.6-61.1 eV [163–165], In the current work, we assign the metallic iridium peak at 60.8 ± 0.2 eV [165]. For 5 Ir/Sir10-RR sample, this peak appears at a higher B.E. (61.1 eV), which might indicate oxidation of Ir particles that are in accordance with the *in-situ* FTIR spectroscopic results given in **Figure 6-23.**

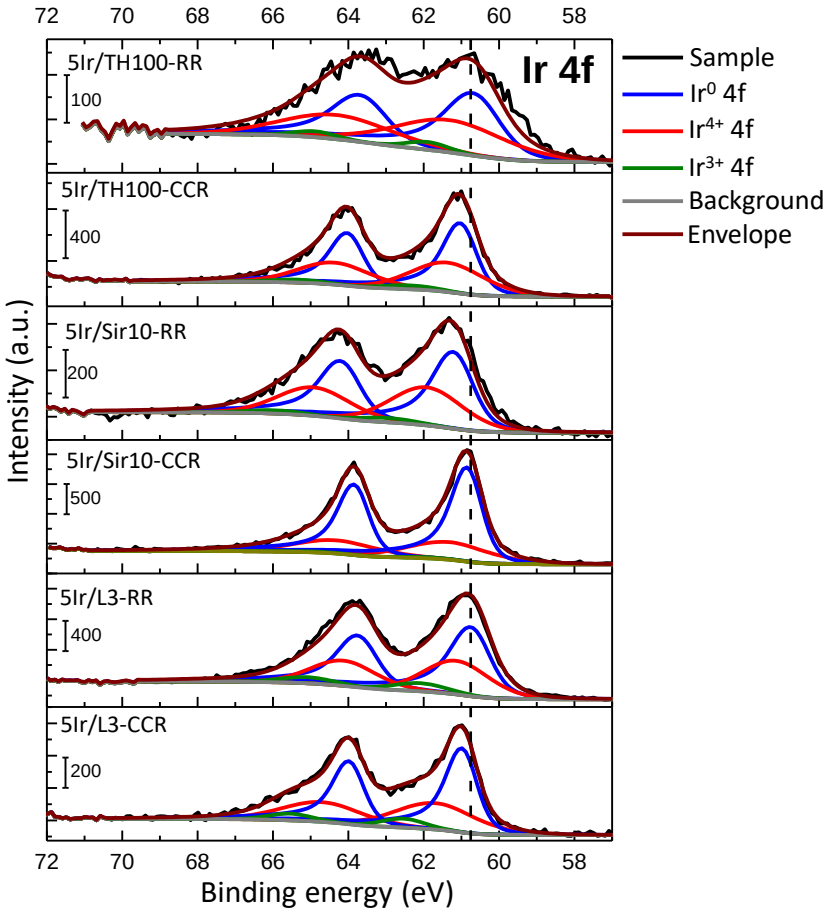



***Figure 6-27.*** *Ir 4f XPS data 5Ir/TH100-CCR, 5Ir/L3-CCR, 5Ir/Sir10-CCR, 5Ir/TH100-RR, 5Ir/L3-RR, and 5Ir/Sir10-RR.*

### 6.3.8. Determination of the relative number of exposed surface Ir species via CO chemisorption and CO-TPD experiments

In order to compare the relative number of Ir species on the synthesized catalyst surfaces that are exposed/accessible to CO adsorption, TPD experiments were executed for identical masses of catalysts (ca. 20 mg) and the results are presented in **Figure 6-28** and **Figure 6-29**. Furthermore, Ir surface dispersion percentages of the catalysts were also determined from the CO chemisorption experiments (**Figure 6-28** and **Table 6-2**). In accordance with the in-situ FTIR data given in **Figure 6-23**, despite the fact that 5Ir/Sir10 catalysts have

significantly higher SSA (**Figure 6-20**), they adsorb significantly lower amounts of CO and the Ir dispersion is lower as compared to that of 5Ir/TH100 and 5Ir/L3 samples. This can be explained by the relatively higher surface acidity of the Sir10 support material restricting CO uptake by the support, as well as the SMSI phenomena rendering Ir sites less accessible to CO due to blockage of Ir sites with $SiO_x$-$AlO_x$. The highest Ir dispersion and CO uptake is observed for the 5Ir/L3-RR sample which can be attributed to i) a less acidic L3 support material enabling direct CO uptake by the support as well as spill-over of CO from the L3 support to Ir active sites, ii) predominantly metallic Ir NP (**Figure 6-23d**) facilitating CO adsorption.

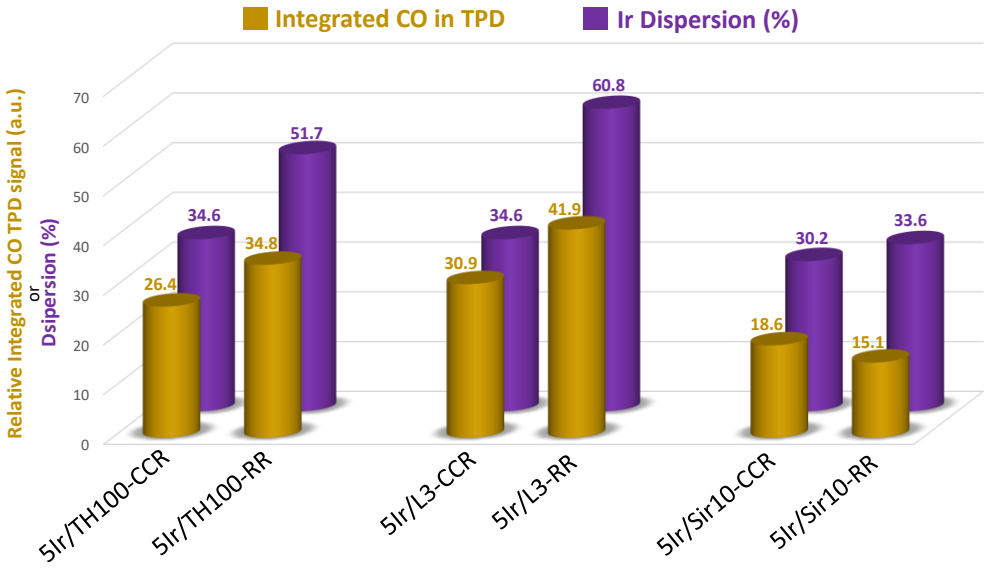



***Figure 6-28.*** *Integrated relative CO-TPD desorption signals and Ir surface dispersion values obtained from CO chemisorption experiments for the investigated catalysts synthesized via IWI with identical masses.*

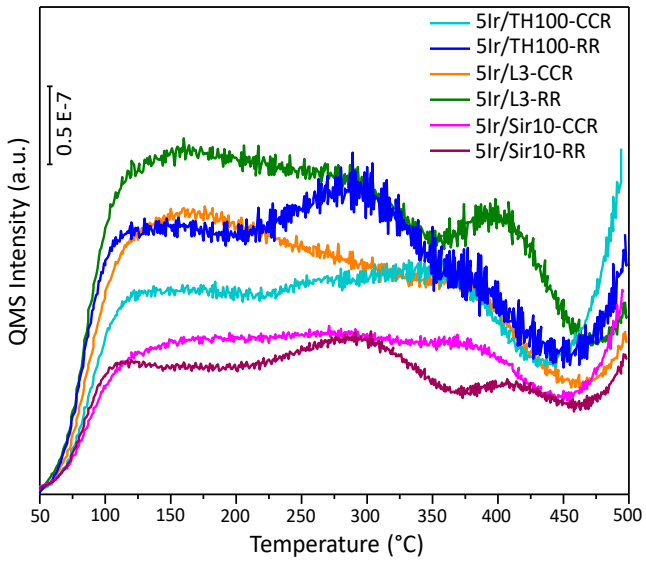



***Figure 6-29.*** *CO TPD profiles for synthesized materials via IWI obtained after 5 Torr CO adsorption.*

***Table 6-2.*** *Parameters used for Ir dispersion calculations.*

| Sample Name | Sample Weight (g) | CO Uptake (moles/g) | Nominal Ir Loading (wt%) | Ir Loading based on XRF (wt%) | Number of $CO_{ads}$ per Ir atom | **Ir dispersion (%) based on measured XRF Ir loadings** |
|---|---|---|---|---|---|---|
| 5Ir/TH100-CCR | 0.0754 | 4.50E-05 | 5 | 2.5 | 1 | 34.6 |
| 5Ir/TH100-RR | 0.0755 | 7.55E-05 | 5 | 2.8 | 1 | 51.7 |
| 5Ir/L3-CCR | 0.0758 | 4.87E-05 | 5 | 2.7 | 1 | 34.6 |
| 5Ir/L3-RR | 0.0751 | 7.61E-05 | 5 | 2.4 | 1 | 60.8 |
| 5Ir/Sir10-CCR | 0.0752 | 3.94E-05 | 5 | 2.5 | 1 | 30.2 |
| 5Ir/Sir10-RR | 0.0752 | 3.86E-05 | 5 | 2.2 | 1 | 33.6 |

### 6.3.9. *In-situ* XANES/EXAFS experiments for analyzing Ir nearest neighbors and coordination

Initial XANES/EXAFS experiments were carried out on a metallic Ir foil for energy calibration and optimization of the EXAFS fitting parameters (**Figure 6-30**). **Figure 6-30b** shows only the XANES region for $L_{III}$ edge. In the EXAFS analysis, the forward Fourier

transform range was determined to be within 3-17 $Å^{-1}$ (after edge extended to i.e., 850 eV for EXAFS analysis), where 1-3 $Å^{-1}$ range was used as the fitting (backward Fourier transform) interval. Details of the EXAFS best fitting parameters for all investigated catalysts also presented in **Table 6-3** and the corresponding XANES/EXAFS data are shown in **Figure 6-31a-l**. Ir1, Ir2, O1 and O2 in **Table 6-3** stands for the neighbor atoms of the Ir main absorber and different labeling is utilized due to the different atomic distances as a result of distortion in the structure. **Figure 6-31a-d** depict the EXAFS data obtained after the final reduction step of the in-situ catalyst synthesis protocol as described in the experimental section, while the EXAFS results presented in **Figure 6-31e-h** are associated with the consecutive exposure of these samples to $O_2$ flow at RT. Corresponding XANES spectra for these EXAFS results are given in **Figure 6-31i-l**.

Current EXAFS results (**Table 6-3** and **Figure 6-31a**) suggest that 5Ir/L3-RR catalyst is mostly comprised of metallic Ir species due to Ir-Ir coordination. This is in particularly good agreement with the corresponding in-situ FTIR data illustrated in **Figure 6-23b** and **Figure 6-23d**, revealing the lack of a large extent of $Ir_n^{x+}$ species. It is seen that exposure of this catalyst to $O_2$ leads to the partial oxidation of the Ir species evident by both EXAFS data (**Table 6-3** and **Figure 6-31e**) suggesting the generation of Ir-O coordination signals and the XANES data (**Figure 6-31i**) indicating an increase in the Ir $L_{III}$-edge white line intensity [166,167].

In stark contrast, 5Ir/Sir10-RR catalyst (**Table 6-3** and **Figure 6-31b**) possesses larger extent of Ir-O coordination which is in excellent accordance with the presence of $Ir_n^{x+}$ species suggested by the in-situ FTIR data depicted in Figure 6-23b and Figure 6-23d. As this particular catalyst did not undergo any calcination treatment, the oxide ions of the support

material are the only source for oxygen. This also indicates the presence of the strong interaction between Ir sites and the $SiO_x$-$AlO_x$ support surface. Oxidation of this sample in $O_2$ (**Table 6-3** and **Figure 6-31f**) also leads to the most oxidic Ir species among all other investigated catalysts, which is in line with the presence of a large concentration of highly reactive $Ir_n^{x+}$ clusters on the 5Ir/Sir10-RR catalyst that can readily undergo oxidation (**Figure 6-31j**).

EXAFS data for 5Ir/L3-CCR catalyst (**Table 6-3** and **Figure 6-31c**) reveals prominently metallic Ir species with Ir-Ir coordination and a limited extent of oxidic Ir species as expected from the current XRD (**Figure 6-1**) and in-situ FTIR spectroscopy (**Figure 6-23a** and **Figure 6-23c**) data. Oxidation of this sample augments the extent of Ir-O coordination (**Table 6-3** and **Figure 6-31g**) and increases the Ir oxidation state (**Figure 6-31k**).

Finally, 5Ir/Sir10-CCR catalyst possesses the second most oxidic Ir species (**Table 6-3** and **Figure 6-31d**). These iridium species can be further oxidized upon $O_2$ exposure (**Figure 6-31h** and **Figure 6-31l**).

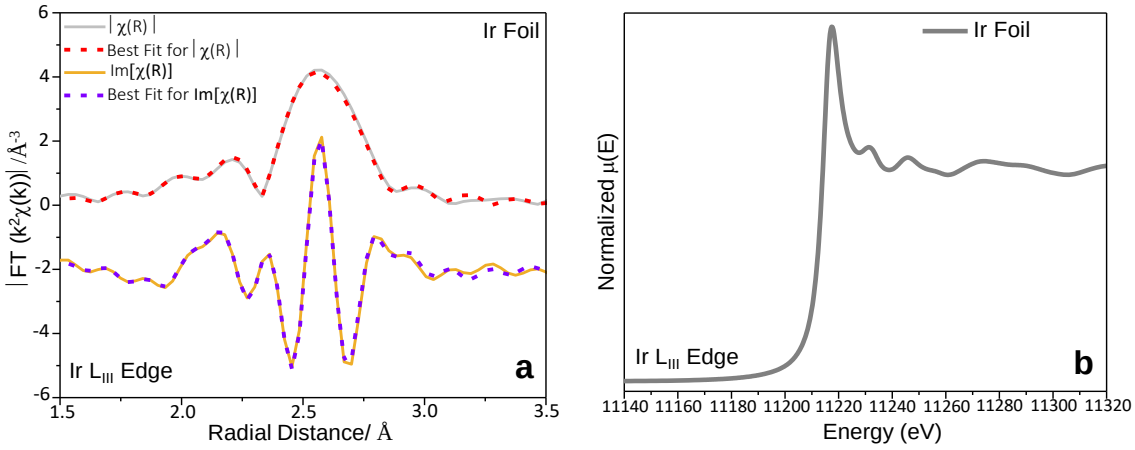



***Figure 6-30.*** *EXAFS results for metallic Ir foil $L_{III}$ edge given with best fit results in the form of (a) Fourier-transform (FT) of the $k^2\chi(k)$ and imaginary part (Im[$\chi$(R)]) of the $\chi$(R) spectra, (b) normalized XANES data for Ir $L_{III}$ edge.*

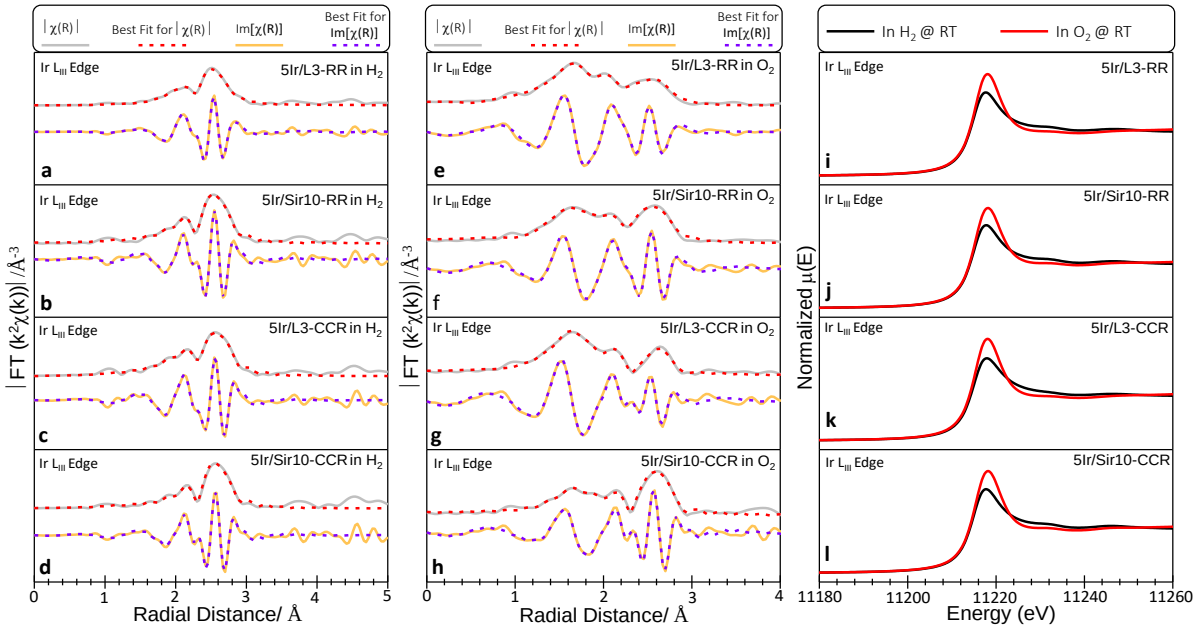



***Figure 6-31.*** *In-situ EXAFS data obtained (a-d) after the final reduction step of the catalyst preparation protocol via IWI and (e-h) consecutive exposure of these catalysts to $O_2$ flow (see text for details). (i-l) Corresponding Ir $L_{III}$ edge XANES data for the experiments shown in parts (a-h).*

***Table 6-3.*** *EXAFS best fitting parameters for the Ir $L_{III}$ edge of the 5Ir/L3-CCR, 5Ir/Sir10-CCR, 5Ir/L3-RR and 5Ir/Sir10-RR samples synthesized via IWI.*

| Sample Name | Path | N [a] | R (Å) [b] | $\sigma^2$ ($x10^{-3}$ Å$^2$) [c] | Δ E [d] (eV) | [e] R factor |
|---|---|---|---|---|---|---|
| Ir foil | Ir-Ir | 12.1 | 2.72 | 3.2 | 8.62 | 0.006 |
| 5Ir/L3-RR in $H_2$ | Ir-Ir | 9.3 | 2.68 | 5.9 | 6.5 | 0.007 |
| 5Ir/L3-RR in $O_2$ | Ir-Ir1 | 0.3 | 2.22 | 6.6 | 3.14 | 0.005 |
| 5Ir/L3-RR in $O_2$ | Ir-Ir2 | 7.2 | 2.66 | 8.8 | 3.14 | 0.005 |
| 5Ir/L3-RR in $O_2$ | Ir-O1 | 0.4 | 1.78 | 6.5 | 3.14 | 0.005 |
| 5Ir/L3-RR in $O_2$ | Ir-O2 | 3.1 | 1.99 | 6 | 3.14 | 0.005 |
| 5Ir/Sir10-RR in $H_2$ | Ir-Ir | 9.7 | 2.7 | 5.4 | 8.68 | 0.003 |
| 5Ir/Sir10-RR in $H_2$ | Ir-O | 3.5 | 2.01 | 40.5 | 8.68 | 0.003 |
| 5Ir/Sir10-RR in $O_2$ | Ir-Ir | 7.2 | 2.69 | 7 | 7.94 | 0.008 |
| 5Ir/Sir10-RR in $O_2$ | Ir-O1 | 3.3 | 1.72 | 35.9 | 7.94 | 0.008 |
| 5Ir/Sir10-RR in $O_2$ | Ir-O2 | 5.1 | 1.99 | 10.5 | 7.94 | 0.008 |
| 5Ir/L3-CCR in $H_2$ | Ir-Ir1 | 1.3 | 2.59 | 4.8 | 6.55 | 0.01 |
| 5Ir/L3-CCR in $H_2$ | Ir-Ir2 | 6.1 | 2.7 | 5 | 6.55 | 0.01 |
| 5Ir/L3-CCR in $H_2$ | Ir-O | 1.5 | 2.02 | 34 | 6.55 | 0.01 |
| 5Ir/L3-CCR in $O_2$ | Ir-Ir1 | 0.4 | 2.28 | 6.5 | 11.23 | 0.016 |
| 5Ir/L3-CCR in $O_2$ | Ir-Ir2 | 3.6 | 2.72 | 6 | 11.23 | 0.016 |
| 5Ir/L3-CCR in $O_2$ | Ir-O | 4.3 | 2.02 | 6 | 11.23 | 0.016 |
| 5Ir/Sir10-CCR in $H_2$ | Ir-Ir | 8.6 | 2.71 | 4.7 | 9.61 | 0.007 |
| 5Ir/Sir10-CCR in $H_2$ | Ir-O | 2.1 | 1.99 | 36.4 | 9.61 | 0.007 |
| 5Ir/Sir10-CCR in $O_2$ | Ir-Ir | 6.1 | 2.72 | 4.2 | 10.77 | 0.006 |
| 5Ir/Sir10-CCR in $O_2$ | Ir-O1 | 2 | 1.82 | 32.2 | 10.77 | 0.006 |
| 5Ir/Sir10-CCR in $O_2$ | Ir-O2 | 4.1 | 2.02 | 7.8 | 10.77 | 0.006 |

[a] Coordination number and amplitude reduction factor ($S_0^2$) is calculated as 0.7 from the iridium foil and same value was used for all the fits. [b] Distance between absorbing atom and the atom in the corresponding shell. [c] Debye-Waller value. [d] The energy shift between fit and the experimental data. [e] R-factor shows the conformity level of the fit and measured data.

# CHAPTER 7

## 7. CONCLUSIONS

In this study, thermal and catalytic decomposition processes of ADN monopropellants were investigated. The synthesized catalysts were in the form of 5 wt.% Ir active site supported on alumina. Among 9 different support materials, L3, TH100, Sir5, Sir10, Sir20 support materials were found to preserve their δ-$Al_2O_3$ structure and showed higher SSA values after thermal aging demonstrating the higher thermal durability of these support materials. Catalysts synthesized with wetness impregnation (WI) method led to the formation of large Ir particles even at low calcination temperatures. Hence, WI method were replaced by the incipient to wetness impregnation (IWI) method. Moreover, 5 wt.% Ir loading in a single step caused agglomeration of Ir particles, thus sequential Ir addition to the support materials were performed by using IWI synthesis method. Different pretreatment protocols (CCR vs. RR) were also applied to the samples synthesized via IWI method. Performance comparison of these catalysts were done with DSC/TGA and custom-design micro propulsion batch reactor measurements. Onset temperature, one of the catalyst performance criteria, was obtained from both DSC/TGA and batch reactor measurements. Other performance parameters which are Energy and Pressure release (ΔP) were acquired from the DSC/TGA and custom-design micro propulsion batch reactor measurement, respectively. The most active catalysts were found to be 5Ir/TH100, 5Ir/L3, and 5Ir/Sir10. Our detailed findings on the structure-functionality relationships on these latter catalysts can be summarized as follows;

5Ir/TH100 and 5Ir/L3: i) lead to lower $T_{Onset}$ but also smaller ΔP values where catalyst preparation protocols (CCR vs. RR) had a less significant effect on $T_{Onset}$, ii) form δ-$Al_2O_3$ and γ-$Al_2O_3$ phases with a relatively lower specific SSA, iii) result in the formation of predominantly metallic Ir nanoparticles along with oxidic $Ir^{x+}$ species as minority species and these metallic Ir species are dispersed on these materials in a multimodal manner lowering the activation energy ($E_a$) of the ADN decomposition reaction. While the catalytic ADN decomposition pathways are different for 5Ir/L3 and TH100, $T_{Onset}$ and ΔP values are similar. On the other hand, 5Ir/L3 have greater structural stability with the preservation of the SSA of the support at high temperatures.

5Ir/Sir10: i) yields higher $T_{Onset}$ values, but (particularly RR preparation protocol) leads to a significant boost in the ΔP and ΔH values, ii) results in the exclusive formation of γ-$Al_2O_3$ phase with extremely high SSA, iii) leads to the formation of oxidic $Ir_n^{x+}$ clusters which strongly interact with the $SiO_x$-$AlO_x$ domains leading to partial blocking/covering of the Ir sites with the $SiO_x$-$AlO_x$ domains via strong metal support interaction (SMSI).

Along these lines, it can be envisaged that next generation catalytic architectures can be designed for ADN decomposition using the fundamental molecular level insight provided in the current study where novel synthetic protocols can be developed to enable the preparation of bi-functional Ir active sites, including metallic Ir NPs lowering the $T_{Onset}$ and $E_a$ as well as oxidic Ir clusters ($Ir_n^{x+}$) capable of boosting ΔP to generate enhanced thrust.

# REFERENCES


(1) https://www.nasa.gov/audience/forstudents/k-4/stories/nasa-knows/what-is-a-satellite-k4.html.

(2) Batonneau, Y.; Brahmi, R.; Cartoixa, B.; Farhat, K.; Kappenstein, C.; Keav, S.; Kharchafi Farhat, G.; Pirault-Roy, L.; Saouabé, M.; Scharlemann, C. Green Propulsion: Catalysts for the European FP7 Project GRASP. *Top. Catal.* **2014**, *57* (6), 656–667.

(3) Solid and liquid fuel rockets https://www.esa.int/Education/Solid_and_liquid_fuel_rockets.

(4) Singh, H.; Shekhar, H. Solid Rocket Propellants; Royal Society of Chemistry: Cambridge, **2017.**

(5) Frota, O.; Ford, M. Review on Hybrid Propellants. In *ESA Special Publication*; **2004**, 557.

(6) Bergman, G.; Brandt, J.; Lyckfeldt, O.; Agrell, J.; Ersson, A.; Jaras, S.; Examiner, P.; Kim, T. Reactor for Decomposition of Ammonium Dinitramide-Based Liquid Monopropellants and Process for the Decomposition. US7137244B2, **2006**.

(7) Casiano, M. J.; Hulka, J. R.; Yang, V. Liquid-Propellant Rocket Engine Throttling: A Comprehensive Review. *J. Propuls. Power* **2010**, *26* (5), 897–923.

(8) Freudenmann, D.; Ciezki, H. K. ADN and HAN-Based Monopropellants – A Minireview on Compatibility and Chemical Stability in Aqueous Media. *Propellants, Explosives, Pyrotechnics*. **2019**, *44*, 1084– 1089.

(9) Schmidt, E. W.; Wucherer, E. J. Hydrazine (s) vs. Nontoxic Propellants—Where Do We Stand Now? In *2nd Conference (International) on Green Propellants for Space*

*Propulsion (ESA SP-557) Proceedings*; **2004**.

(10) Schmidt, E. W. *Hydrazine and Its Derivatives: Preparation, Properties, Applications, 2 Volume Set*; John Wiley & Sons, **2001**.

(11) Nguyen MC USAF, H. N.; Chenoweth MD MAS, J. A.; Bebarta MC USAF, V. S.; Albertson USA (Ret.), T. E.; Nowadly MC USAF, C. D. The Toxicity, Pathophysiology, and Treatment of Acute Hydrazine Propellant Exposure: A Systematic Review. *Mil. Med.* **2021**, *186* (3–4), e319–e326.

(12) Negri, M.; Wilhelm, M.; Hendrich, C.; Wingborg, N.; Gediminas, L.; Adelöw, L.; Maleix, C.; Chabernaud, P.; Brahmi, R.; Beauchet, R. New Technologies for Ammonium Dinitramide Based Monopropellant Thrusters–The Project RHEFORM. *Acta Astronaut.* **2018**, *143*, 105–117.

(13) European Chemicals Agency (ECHA), Hydrazine - substance information https://echa.europa.eu/substance-information/-/substanceinfo/100.005.560.

(14) Sackheim, R. L.; Masse, R. K. Green Propulsion Advancement: Challenging the Maturity of Monopropellant Hydrazine. *J. Propuls. Power* **2014**, *30* (2), 265–276.

(15) Zhang, Q.; Shreeve, J. M. Energetic Ionic Liquids as Explosives and Propellant Fuels: A New Journey of Ionic Liquid Chemistry. *Chem. Rev.* **2014**, *114* (20), 10527–10574.

(16) Wingborg, N.; Eldsäter, C.; Skifs, H. Formulation and Characterization of ADN-Based Liquid Monopropellants. In *ESA Special Publication*; **2004**, 557.

(17) Amrousse, R.; Katsumi, T.; Itouyama, N.; Azuma, N.; Kagawa, H.; Hatai, K.; Ikeda, H.; Hori, K. New HAN-Based Mixtures for Reaction Control System and Low Toxic Spacecraft Propulsion Subsystem: Thermal Decomposition and Possible Thruster

Applications. *Combust. Flame* **2015**, 162, 2686−2692.

(18) Courthéoux, L.; Rossignol, S.; Kappenstein, C.; Pillet, N. Improvement of Catalysts for the Decomposition of Han-Based Monopropellant - Comparison between Aerogels and Xerogels. *AIAA/ASME/SAE/ASEE 39th Joint Propulsion Conference and Exhibit*; **2003**.

(19) Friedhoff, P.; Anflo, K.; Thormahlen, P.; Persson, M. Growing Constellation of Ammonium Dinitramide (ADN) Based High Performance Green Propulsion (HPGP) Systems. *AIAA/ASME/SAE/ASEE Joint Propulsion Conference*, **2018.**

(20) Larsson, A.; Wingborg, N. Green Propellants Based on Ammonium Dinitramide (ADN). In *Advances in Spacecraft Technologies*; InTech, **2011**.

(21) Chang, Y. P.; Kuo, K. K. Assessment of Combustion Characteristics and Mechanism of Hydroxylammonium Nitrate-Based Liquid Monopropellant. *J. Propuls. Power* **2002,** 18, 1076-1085.

(22) Spores, R. A. GPIM AF-M315E Propulsion System. *AIAA/ASME/SAE/ASEE 51st Joint Propulsion Conference*, **2015**.

(23) McLean, C. H. Green Propellant Infusion Mission Program Overview. *AIAA/ASME/SAE/ASEE 49tht Joint Propulsion Conference*, **2013**.

(24) Fokema, M. D.; Torkelson, J. E. Thermally Stable Catalyst and Process for the Decomposition of Liquid Propellants. U.S. Patent No. 20070184971A1, **2007**.

(25) Nosseir, A. E. S.; Cervone, A.; Pasini, A. Review of State-of-the-Art Green Monopropellants: For Propulsion Systems Analysts and Designers. *Aerospace* **2021**, 8, 1– 21.

(26) Cavender, D. P.; Marshall, W. M.; Maynard, A. NASA Green Propulsion Roadmap.

*AIAA/ASME/SAE/ASEE 51st Joint Propulsion Conference*, **2018**.

(27) Wingborg, N.; de Flon, J.; Johnson, C.; Whitlow, W. Green Propellants Based on ADN. *Sp. Propuls.* **2008**, *2*, 5–8.

(28) Wingborg, N. Ammonium Dinitramide−Water: Interaction and Properties. *J. Chem. Eng. Data* **2006**, *51* (5), 1582–1586.

(29) Kumar, P. An Overview on Properties, Thermal Decomposition, and Combustion Behavior of ADN and ADN Based Solid Propellants. *Def. Technol.* **2018**, *14* (6), 661–673.

(30) Friedhoff, P.; Hawkins, A.; Carrico, J.; Dyer, J.; Anflo, K. On-Orbit Operation and Performance of Ammonium Dinitramide (ADN) Based High Performance Green Propulsion (HPGP) Systems. *AIAA/ASME/SAE/ASEE 53rd Joint Propulsion Conference*, **2017**, 4673.

(31) Negri, M.; Wilhelm, M.; Hendrich, C.; Wingborg, N.; Gediminas, L.; Adelöw, L.; Koopmans, R.-J.; Schuh, S.; Bartok, T.; Scharlemann, C. Technology Development for ADN-Based Green Monopropellant Thrusters–an Overview of the Rheform Project. Presented at the 7th EUCASS, Milan, IT, **2017**.

(32) Kesten, A. S. Analytical Study of Catalytic Reactors for Hydrazine Decomposition. *Tech. Rep., NASA UARL G* **1969**, 910438–910461.

(33) Pavoine, C.; Passagot, G.; Pages, X. Characterization in Endurance of the SNECMA 1N Hydrazine Thruster. In *Spacecraft Propulsion* **2000**, *465*, 271.

(34) McRight, P.; Popp, C.; Pierce, C.; Turpin, A.; Urbanchock, W.; Wilson, M. Confidence Testing of Shell-405 and S-405 Catalysts in a Monopropellant Hydrazine Thruster; **2005**.

(35) Ley, W.; Wittmann, K.; Hallmann, W. *Handbook of Space Technology*; **2009**.

(36) Wucherer, E. J.; Cook, T.; Stiefel, M.; Humphries, R.; Parker, J. Hydrazine Catalyst Production - Sustaining S-405 Technology. *AIAA/ASME/SAE/ASEE 39th Joint Propulsion Conference* **2003**.

(37) Courtheoux, L.; Popa, F.; Gautron, E.; Rossignol, S.; Kappenstein, C. Platinum Supported on Doped Alumina Catalysts for Propulsion Applications. Xerogels versus Aerogels. *J. Non. Cryst. Solids* **2004**, *350*, 113–119.

(38) Kappenstein, C.; Brahmi, R.; Amariei, D.; Batonneau, Y.; Rossignol, S.; Joulin, J. P. Catalytic Decomposition of Energetic Compounds-Influence of Catalyst Shape and Ceramic Substrate. *AIAA/ASME/SAE/ASEE 42nd Joint Propulsion Conference*, **2006**.

(39) Kappenstein, C.; Courthéoux, L.; Eloirdi, R.; Rossignol, S.; Duprez, D.; Pillet, N. Catalytic Decomposition of HAN-Water Binary Mixtures. *AIAA/ASME/SAE/ASEE 38th Joint Propulsion Conference*, **2002**.

(40) Eloirdi, R.; Rossignol, S.; Kappenstein, C.; Duprez, D.; Pillet, N. Design and Use of a Batch Reactor for Catalytic Decomposition of Propellants. *J. Propuls. Power* **2003**, *19* (2), 213–219.

(41) Rossignol, S.; Kappenstein, C. Effect of Doping Elements on the Thermal Stability of Transition Alumina. *Int. J. Inorg. Mater.* **2001**, *3* (1), 51–58.

(42) Zhu, Y.; Wang, X.; Zhang, Y.; Wang, J.; Huang, Y.; Kappenstein, C.; Zhang, T. Effect of Ir Crystallographic Site on the Catalytic Performance of Ir-Substituted Barium Hexaferrites for N2O Decomposition. *Appl. Catal. A Gen.* **2011**, *409–410*, 194–201.

(43) Farhat, K.; Cong, W.; Batonneau, Y.; Kappenstein, C. Improvement of Catalytic Decomposition of Ammonium Nitrate with New Bimetallic Catalysts. *AIAA/ASME/SAE/ASEE 45th Joint Propulsion Conference*, **2009**.

(44) Courtheoux, L.; Amariei, D.; Rossignol, S.; Kappenstein, C. Thermal and Catalytic Decomposition of HNF and HAN Liquid Ionic as Propellants. *Appl. Catal. B Environ.* **2006**, *62* (3–4), 217–225.

(45) Courthéoux, L.; Amariei, D.; Rossignol, S.; Kappenstein, C. Facile Catalytic Decomposition at Low Temperature of Energetic Ionic Liquid as Hydrazine Substitute. *Eur. J. Inorg. Chem.* **2005**, *12*, 2293-2295.

(46) Courthéoux, L.; Popa, F.; Gautron, E.; Rossignol, S.; Kappenstein, C. Platinum Supported on Doped Alumina Catalysts for Propulsion Applications. Xerogels versus Aerogels. *J. Non-Cryst. Solid*. **2004**, *350*, 113-119

(47) Amariei, D.; Rossignol, S.; Kappenstein, C.; Joulin, J. P. Shape Forming of Pt/Al2O3Si Sol-Gel Catalysts for Space Applications. Stud. Surf. Sci. Catal. **2006,** *162*, 969–976.

(48) Popa, A. F.; Courthéoux, L.; Gautron, E.; Rossignol, S.; Kappenstein, C. Aerogel and Xerogel Catalysts Based on θ-Alumina Doped with Silicon for High Temperature Reactions. *Eur. J. Inorg. Chem.* **2005,** 543.

(49) Amariei, D.; Courtheoux, L.; Rossignol, S.; Kappenstein, C. Catalytic and Thermal Decomposition of Ionic Liquid Monopropellants Using a Dynamic Reactor: Comparison of Powder and Sphere Shaped Catalysts. *Chem. Eng. Process.* **2007**, *46*, 165−174.

(50) Trueba, M.; Trasatti, S. P. Γ-Alumina as a Support for Catalysts: A Review of

Fundamental Aspects. *Eur. J. Inorg. Chem.* **2005**, *2005* (17), 3393–3403.

(51) Euzen, P.; Raybaud, P.; Krokidis, X.; Toulhoat, H.; Le Loarer, J.-L.; Jolivet, J.-P.; Froidefond, C. Alumina. *Handbook of Porous Solids*. **2002**, 1591–1677.

(52) Arai, H.; Machida, M. Thermal Stabilization of Catalyst Supports and Their Application to High-Temperature Catalytic Combustion. *Appl. Catal. A Gen.* **1996**, *138* (2), 161–176.

(53) Busca, G. The Surface of Transitional Aluminas: A Critical Review. *Catal. Today* **2014**, *226*, 2–13.

(54) Popa, A. F.; Rossignol, S.; Kappenstein, C. Influence of Drying Technique on Silicon Insertion into [Gamma]-Alumina and Consequences for the Homogeneity and Thermal Stability of Silica-Alumina Aquagels. *J. Mater. Chem.* **2002**, *12* (10), 2866–2868.

(55) Arai, H.; Fukuzawa, H., Research and Development on High Temperature Catalytic Combustion. *Catal. Today* **1995**, *26* (3–4), 217–221.

(56) Schliebs, R. Hydrazine and Its Derivatives. Preparation, Properties, Applications. VonE. W. Schmidt. Wiley, Chichester. *Angew. Chemie* **1985**, *97* (4), 360–360.

(57) Ishizuka, S.; Kimura, Y.; Sakon, I.; Kimura, H.; Yamazaki, T.; Takeuchi, S.; Inatomi, Y. Sounding-Rocket Microgravity Experiments on Alumina Dust. *Nat. Commun.* **2018**, *9* (1), 3820.

(58) Schaper, H.; Doesburg, E. B. M.; De Korte, P. H. M.; Van Reijen, L. L. Thermal Stabilization of High Surface Area Alumina. *Solid State Ionics* **1985**, *16*, 261−265.

(59) Niwa, M.; Katada, N.; Murakami, Y. Thin Silica Layer on Alumina: Evidence of the Acidity in the Monolayer. *J. Phys. Chem.* **1990**, *94* (16), 6441–6445.

(60) Beguin, B.; Garbowski, E.; Primet, M. Stabilization of Alumina toward Thermal Sintering by Silicon Addition. *J. Catal.* **1991**, *127* (2), 595–604.

(61) Beguin, B.; Garbowski, E.; Primet, Stabilization of Alumina by Addition of Lanthanum. *Appl. Catal.* **1991**, *75* (1), 119–132.

(62) Oudet, F.; Courtine, P.; Vejux, A. Thermal Stabilization of Transition Alumina by Structural Coherence with LnAlO3 (Ln = La, Pr, Nd). *J. Catal.* **1988**, *114* (1), 112–120.

(63) Levy, R. M.; Bauer, D. J. The Effect of Foreign Ions on the Stability of Activated Alumina. *J. Catal.* **1967**, *9* (1), 76–86.

(64) Johnson, M. F. L., Surface Area Stability of Aluminas. *J. Catal.* **1990**, *123* (1), 245–259.

(65) Schaper, H. E.; Amesz, D. J.; Doesburg, E. B. M.; van Reijen, L. L., The Influence of High Partial Steam Pressures on the Sintering of Lanthanum Oxide Doped Gamma Alumina. *Appl. Catal.* **1984**, *9* (1), 129–132.

(66) Schaper, H. E.; Doesburg, E. B. M.; van Reijen, L. L., The Influence of Lanthanum Oxide on the Thermal Stability of Gamma Alumina Catalyst Supports. *Appl. Catal.* **1983**, *7* (2), 211–220.

(67) Burtin,P.; Brunelle,J.P. ;Pijolat,M. ;Soustelle,M. Influence of Surface Area and Additives on the Thermal Stability of Transition Alumina Catalyst Supports. II: Kinetic Model and Interpretation. *Appl. Catal.* **1987**, *34*, 239–254.

(68) Bernal, S.; Blanco, G.; Gatica, J. M.; Pérez-Omil, J. A.; Pintado, J. M.; Vidal, H. Chemical Reactivity of Binary Rare Earth Oxides. In *Binary rare earth oxides*; Springer, **2004**, 9–55.

(69) Li, M.; Weng, D.; Wu, X.; Wan, J.; Wang, B. Importance of Re-Oxidation of Palladium by Interaction with Lanthana for Propane Combustion over Pd/Al2O3 Catalyst. *Catal. Today* **2013**, *201*, 19–24.

(70) Chen, T.; Chen, H.; Chen, H.; Wang, L.; Shi, J. Effect of La on the Thermal Stability of Pd/γ-Al2O3 Catalytic Membranes. *Ceram. Int.* **2001**, *27* (8), 883–887.

(71) Xu, B.; Yang, Y.; Xu, Y.; Han, B.; Wang, Y.; Liu, X.; Yan, Z. Synthesis and Characterization of Mesoporous Si-Modified Alumina with High Thermal Stability. *Microporous Mesoporous Mater.* **2017**, *238*, 84–89.

(72) Osaki, T.; Nagashima, K.; Watari, K.; Tajiri, K. Silica-Doped Alumina Cryogels with High Thermal Stability. *J. Non. Cryst. Solids* **2007**, *353* (24), 2436–2442.

(73) Basset, J.-M.; Gates, B. C.; Candy, J.-P.; Choplin, A.; Leconte, M.; Quignard, F.; Santini, C. *Surface Organometallic Chemistry: Molecular Approaches to Surface Catalysis*; Springer Science & Business Media, **2012**, 231.

(74) Ballinger, T. H.; Yates, J. T. IR Spectroscopic Detection of Lewis Acid Sites on Al2O3 Using Adsorbed CO. Correlation with Al-OH Group Removal. *Langmuir* **1991**, *7* (12), 3041–3045.

(75) Yamamoto, T.; Tanaka, T.; Matsuyama, T.; Funabiki, T.; Yoshida, S. Alumina-Supported Rare-Earth Oxides Characterized by Acid-Catalyzed Reactions and Spectroscopic Methods. *J. Phys. Chem. B* **2001**, *105* (9), 1908–1916.

(76) Boukha, Z.; Fitian, L.; López-Haro, M.; Mora, M.; Ruiz, J. R.; Jiménez-Sanchidrián, C.; Blanco, G.; Calvino, J. J.; Cifredo, G. A.; Trasobares, S.; Bernal, S. Influence of the Calcination Temperature on the Nano-Structural Properties, Surface Basicity, and Catalytic Behavior of Alumina-Supported Lanthana Samples. *J. Catal.* **2010**,

*272* (1), 121–130.

(77) Stoyanovskii, V. O.; Vedyagin, A. A.; Volodin, A. M.; Kenzhin, R. M.; Shubin, Y. V; Plyusnin, P. E.; Mishakov, I. V. Peculiarity of Rh Bulk Diffusion in La-Doped Alumina and Its Impact on CO Oxidation over Rh/Al2O3. *Catal. Commun.* **2017**, *97*, 18–22.

(78) Busca, G. Silica-Alumina Catalytic Materials: A Critical Review. *Catal. Today* **2020**, *357*, 621–629.

(79) Daniell, W.; Schubert, U.; Glöckler, R.; Meyer, A.; Noweck, K.; Knözinger, H. Enhanced Surface Acidity in Mixed Alumina–Silicas: A Low-Temperature FTIR Study. *Appl. Catal. A Gen.* **2000**, *196* (2), 247–260.

(80) Goldsmith, B. R.; Peters, B.; Johnson, J. K.; Gates, B. C.; Scott, S. L. Beyond Ordered Materials: Understanding Catalytic Sites on Amorphous Solids. *ACS Catal.* **2017**, *7* (11), 7543–7557.

(81) Montanari, T.; Matarrese, R.; Artioli, N.; Busca, G. FT-IR Study of the Surface Redox States on Platinum-Potassium-Alumina Catalysts. *Appl. Catal. B Environ.* **2011**, *105* (1–2), 15–23.

(82) Ramaker, D. E.; Oudenhuijzen, M. K.; Koningsberger, D. C. Strong Support Effects on the Insulator to Metal Transition in Supported Pt Clusters as Observed by X-Ray Absorption Spectroscopy. *J. Phys. Chem. B* **2005**, *109* (12), 5608–5617.

(83) Stakheev, A. Y.; Zhang, Y.; Ivanov, A. V; Baeva, G. N.; Ramaker, D. E.; Koningsberger, D. C. Separation of Geometric and Electronic Effects of the Support on the CO and H2 Chemisorption Properties of Supported Pt Particles: The Effect of Ionicity in Modified Alumina Supports. *J. Phys. Chem. C* **2007**, *111* (10), 3938–

3948.

(84) Pan, C.-J.; Tsai, M.-C.; Su, W.-N.; Rick, J.; Akalework, N. G.; Agegnehu, A. K.; Cheng, S.-Y.; Hwang, B.-J. Tuning/Exploiting Strong Metal-Support Interaction (SMSI) in Heterogeneous Catalysis. *J. Taiwan Inst. Chem. Eng.* **2017**, *74*, 154–186.

(85) Gonzalez-DelaCruz, V. M.; Holgado, J. P.; Pereñíguez, R.; Caballero, A. Morphology Changes Induced by Strong Metal–Support Interaction on a Ni–Ceria Catalytic System. *J. Catal.* **2008**, *257* (2), 307–314.

(86) Gaudet, J. R.; de la Riva, A.; Peterson, E. J.; Bolin, T.; Datye, A. K. Improved Low-Temperature CO Oxidation Performance of Pd Supported on La-Stabilized Alumina. *ACS Catal.* **2013**, *3* (5), 846–855.

(87) Zhao, Y.; Wang, L.; Kochubei, A.; Yang, W.; Xu, H.; Luo, Y.; Baiker, A.; Huang, J.; Wang, Z.; Jiang, Y. Formation and Location of Pt Single Sites Induced by Pentacoordinated Al Species on Amorphous Silica–Alumina. *J. Phys. Chem. Lett.* **2021**, *12* (10), 2536–2546.

(88) Tian, M.; Wang, A.; Wang, X.; Zhu, Y.; Zhang, T. Effect of Large Cations (La3+ and Ba2+) on the Catalytic Performance of Mn-Substituted Hexaaluminates for N2O Decomposition. *Appl. Catal. B Environ.* **2009**, *92* (3–4), 437–444.

(89) Svensson, E. E. ; Boutonnet M.; Järås S. G. Stability of Hexaaluminate-Based Catalysts for High-Temperature Catalytic Combustion of Methane. *Appl. Catal. B Environ.* **2008**, *84* (1–2), 241–250.

(90) Baylet, A.; Royer, S.; Marecot, P.; Tatibouet, J. M.; Duprez, D. Effect of Pd Precursor Salt on the Activity and Stability of Pd-Doped Hexaaluminate Catalysts for the CH4 Catalytic Combustion. *Appl. Catal. B Environ.* **2008**, *81* (1–2), 88–96.

(91) Kikuchi, R.; Iwasa, Y.; Takeguchi, T.; Eguchi, K. Partial Oxidation of CH4 and C3H8 over Hexaaluminate-Type Oxides. *Appl. Catal. A Gen.* **2005**, *281* (1–2), 61–67.

(92) Utaka, T.; Al-Drees, S. A.; Ueda, J.; Iwada, Y.; Takeguchi, T.; Kikuchi, R.; Eguchi, K. Partial Oxidation of Methane over Ni Catalysts Based on Hexaaliminate- or Perovskite-Type Oxides. *Appl. Catal. A Gen.* **2003**, *247* (1), 125–131.

(93) Zhu, S.; Wang, X.; Wang, A.; Cong, Y.; Zhang, T. A Novel Ir-Hexaaluminate Catalyst for N2O as a Propellant. *Chem. Commun.* **2007**, No. 17, 1695–1697.

(94) Yeh, T.-F.; Bi, J.-L.; Lee, H.-G.; Chu, K.-S.; Wang, C.-B. Phase Transformation and Catalytic Activity of Hexaaluminates upon High Temperature Pretreatment. *J. Alloys Compd.* **2006**, *425* (1), 353–356.

(95) Wang, Z. L.; Petroski, J. M.; Green, T. C.; El-Sayed, M. A. Shape Transformation and Surface Melting of Cubic and Tetrahedral Platinum Nanocrystals. *J. Phys. Chem. B* **1998**, *102* (32), 6145–6151.

(96) Hecker, S. S.; Rohr, D. L.; Stein, D. F. Brittle Fracture in Iridium. *Metall. Mater. Trans. A* **1978**, *9* (4), 481–488.

(97) Amrousse, R.; Hori, K.; Fetimi, W.; Farhat, K. HAN and ADN as Liquid Ionic Monopropellants: Thermal and Catalytic Decomposition Processes. *Appl. Catal. B Environ.* **2012**, *127*, 121–128.

(98) Zhu, S.; Wang, X.; Wang, A.; Zhang, T Superior Performance of Ir-Substituted Hexaaluminate Catalysts for N2O Decomposition. *Catal. Today* **2008**, *131* (1–4), 339–346.

(99) Newton, N. C.; Rice Jr, P. R.; Huxtable, D. D. *Shell 405 Catalyst Improvement*

*Substrate Evaluation*; AIR FORCE ROCKET PROPULSION LAB EDWARDS AFB CA, 1972.

(100) W.E. Armstrong, L.B. Ryland, H.H. Voge, US Patent 4,124,538, 1978.

(101) Baker, R. T. K.; Sherwood, R. D. Catalytic Oxidation of Graphite by Iridium and Rhodium. *J. Catal.* **1980**, *61* (2), 378–389.

(102) Seymour, R. J.; O'Farrelly, J. Platinum-Group Metals. *Kirk-Othmer Encyclopedia of Chemical Technology*. **2012**, *13*, 1–37.

(103) Courtheoux, L.; Gautron, E.; Rossignol, S.; Kappenstein, C. Transformation of Platinum Supported on Silicon-Doped Alumina during the Catalytic Decomposition of Energetic Ionic Liquid. *J. Catal.* **2005**, *232* (1), 10–18.

(104) Maleix, C.; Chabernaud, P.; Artault, M.; Brahmi, R.; Beauchet, R.; Batonneau, Y. X.; Kappenstein, C. Development and Activity Assessment of New Catalytic Materials for Decomposition of ADN-Based Monopropellants. In *53rd AIAA/SAE/ASEE Joint Propulsion Conference*; **2017**, 4754.

(105) Kurt, M.; Say, Z.; Ercan, K. E.; Vovk, E. I.; Kim, C. H.; Ozensoy, E. Sulfur Poisoning and Regeneration Behavior of Perovskite-Based NO Oxidation Catalysts. *Top. Catal.* **2017**, *60* (1–2), 40–51.

(106) Say, Z.; Dogac, M.; Vovk, E. I.; Kalay, Y. E.; Kim, C. H.; Li, W.; Ozensoy, E. Palladium Doped Perovskite-Based NO Oxidation Catalysts: The Role of Pd and B-Sites for NOx Adsorption Behavior via in-Situ Spectroscopy. *Appl. Catal. B Environ.* **2014**, *154–155*, 51–61.

(107) Fairley, N.; Fernandez, V.; Richard-Plouet, M.; Guillot-Deudon, C.; Walton, J.; Smith, E.; Flahaut, D.; Greiner, M.; Biesinger, M.; Tougaard, S.; Morgan, D.;

Baltrusaitis, J. Systematic and Collaborative Approach to Problem Solving Using X-Ray Photoelectron Spectroscopy. *Appl. Surf. Sci. Adv.* **2021**, *5*, 100112.

(108) Saadun, A. J.; Zichittella, G.; Paunović, V.; Markaide-Aiastui, B. A.; Mitchell, S.; Pérez-Ramírez, J. Epitaxially Directed Iridium Nanostructures on Titanium Dioxide for the Selective Hydrodechlorination of Dichloromethane. *ACS Catal.* **2020**, *10* (1), 528–542.

(109) Hinokuma, S.; Iwasa, T.; Kon, Y.; Taketsugu, T.; Sato, K. Effects of Support Materials and Ir Loading on Catalytic N2O Decomposition Properties. *Catal. Commun.* **2021**, *149*, 106208.

(110) Kayhan, E.; Andonova, S. M.; Şentürk, G. S.; Chusuei, C. C.; Ozensoy, E. Fe Promoted NOx Storage Materials: Structural Properties and NOx Uptake. *J. Phys. Chem. C* **2010**, *114* (1), 357–369.

(111) ROCK | French national synchrotron facility. https://www.synchrotron-soleil.fr/en/beamlines/rock

(112) Ravel, B.; Newville, M. ATHENA, ARTEMIS, HEPHAESTUS: Data Analysis for X-Ray Absorption Spectroscopy Using IFEFFIT. *J. Synchrotron Radiat.* **2005**, *12* (4), 537–541.

(113) SAMBA | French national synchrotron facility. https://www.synchrotron-soleil.fr/en/beamlines/samba.

(114) Mary, S.; Kappenstein, C.; Balcon, S.; Rossignol, S.; Gengembre, E. Monopropellant Decomposition Catalysts. I. Ageing of Highly Loaded Ir/Al2O3 Catalysts in Oxygen and Steam. Influence of Chloride Content *Appl. Catal. A Gen.* **1999**, *182* (2), 317–325.

(115) Maleix, C.; Chabernaud, P.; Brahmi, R.; Beauchet, R.; Batonneau, Y.; Kappenstein, C.; Schwentenwein, M.; Koopmans, R.-J.; Schuh, S.; Scharlemann, C. Development of Catalytic Materials for Decomposition of ADN-Based Monopropellants. *Acta Astronaut.* **2019**, *158*, 407–415.

(116) https://products.sasol.com/pic/products/home/grades/ZA/5puralox-and-siralox-doped/index.html.

(117) https://products.sasol.com/pic/products/home/grades/AS/5puralox-and-catalox/index.html.

(118) https://www.chemicalbook.com/ChemicalProductProperty_US_CB9760372.aspx.

(119) Dalla Betta, R. A. Catalytic Combustion Gas Turbine Systems: The Preferred Technology for Low Emissions Electric Power Production and Co-Generation. *Catal. Today* **1997**, *35* (1), 129–135.

(120) Bi, W.; Hu, Y.; Jiang, H.; Yu, H.; Li, W.; Li, C. In-Situ Synthesized Surface N-Doped Pt/TiO2 via Flame Spray Pyrolysis with Enhanced Thermal Stability for CO Catalytic Oxidation. *Appl. Surf. Sci.* **2019**, *481*, 360–368.

(121) Talo, A.; Lahtinen, J.; Hautojärvi, P. An XPS Study of Metallic Three-Way Catalysts: The Effect of Additives on Platinum, Rhodium, and Cerium. *Appl. Catal. B Environ.* **1995**, *5* (3), 221–231.

(122) Liao, P. .; Chen, C. .; Ho, W. .; Huang, Y. .; Tiong, K. . Characterization of IrO2 Thin Films by Raman Spectroscopy. *Thin Solid Films* **1997**, *301* (1–2), 7–11.

(123) Say, Z.; Vovk, E. I.; Bukhtiyarov, V. I.; Ozensoy, E. Influence of Ceria on the NOx Reduction Performance of NOx Storage Reduction Catalysts. *Appl. Catal. B Environ.* **2013**, *142–143*, 89–100.

(124) Peña, M. A.; Fierro, J. L. G. Chemical Structures and Performance of Perovskite Oxides. *Chem. Rev.* **2001**, *101* (7), 1981–2018.

(125) Kim, C. H.; Qi, G.; Dahlberg, K.; Li, W. Strontium-Doped Perovskites Rival Platinum Catalysts for Treating NOx in Simulated Diesel Exhaust. *Science* **2010**, *327* (5973), 1624–1627.

(126) López-Suárez, F. E. E.; Illán-Gómez, M. J. J.; Bueno-López, A.; Anderson, J. A. NOx Storage and Reduction on a SrTiCuO3 Perovskite Catalyst Studied by Operando DRIFTS. *Appl. Catal. B Environ.* **2011**, *104* (3–4), 261–267.

(127) Martinez-Arias, A.; Soria, J.; Conesa, J. C. J. C.; Seoane, X. L. X. L.; Arcoya, A.; Cataluna, R.; Martínez-Arias, A.; Soria, J.; Conesa, J. C. J. C.; Seoane, X. L. X. L.; Arcoya, A.; Cataluña, R. NO Reaction at Surface Oxygen Vacancies Generated in Cerium Oxide. *J. Chem. Soc. Faraday Trans.* **1995**, *91* (11), 1679–1687.

(128) Klingenberg, B.; Vannice, M. A. A. NO Adsorption and Decomposition on La2O3 Studied by DRIFTS. *Appl. Catal. B Environ.* **1999**, *21* (1), 19–33.

(129) Hadjivanov, K. I. Identification of Neutral and Charged N x O y Surface Species by IR Spectroscopy. *Catal. Rev.* **2000**, *42* (1–2), 71–144.

(130) Prinetto, F.; Ghiotti, G.; Nova, I.; Lietti, L.; Tronconi, E.; Forzatti, P. FT-IR and TPD Investigation of the NOx Storage Properties of BaO/Al2O3 and Pt−BaO/Al2O3 Catalysts. *J. Phys. Chem. B* **2001**, *105* (51), 12732–12745.

(131) Ghiotti, G.; Chiorino, A. An IR Study of NO Adsorption on a CrOx/ZrO2 Catalyst. *Spectrochim. Acta Part A Mol. Spectrosc.* **1993**, *49* (9), 1345–1359.

(132) Low, M. J. D. D.; Yang, R. T. Reactions of Gaseous Pollutants with Solids. V. Infrared Study of the Sorption of NO on CaO. *J. Catal.* **1974**, *34* (3), 479–489.

(133) Heo, S.; Kim, M.; Kim, W.; Jo, Y. M.; Park, Y.-K.; Jeon, J.-K. Catalytic Decomposition of an Ionic Liquid Monopropellant Over Ir/Hexaaluminate Catalysts. *J. Nanosci. Nanotechnol.* **2019**, *19* (12), 7906–7910.

(134) Jing, L.; Huo, J.; Wang, H.; You, X.; Zhu, M.; Yang, Y.; Yao, Z. Experimental Investigation on the Evaporation and Combustion Processes of Ammonium-Dinitramide-Based Liquid Propellant. *J. Propuls. Power* **2016**, *33* (2),

(135) Löbbecke, S.; Krause, H. H.; Pfeil, A. Thermal Analysis of Ammonium Dinitramide Decomposition. *Propellants, Explos. Pyrotech.* **1997**, *22* (3), 184–188.

(136) https://webbook.nist.gov

(137) Yang, R.; Thakre, P.; Yang, V. Thermal Decomposition and Combustion of Ammonium Dinitramide (Review). *Combust. Explos. Shock Waves* **2005**, *41* (6), 657–679.

(138) Zhang, T.; Li, G.; Yu, Y.; Sun, Z.; Wang, M.; Chen, J. Numerical Simulation of Ammonium Dinitramide (ADN)-Based Non-Toxic Aerospace Propellant Decomposition and Combustion in a Monopropellant Thruster. *Energy Convers. Manag.* **2014**, *87*, 965–974.

(139) Toolenaar, F. J. C. M.; Bastein, A. G. T. M.; Ponec, V. The Effect of Particle Size in the Adsorption of Carbon Monoxide on Iridium: An Infrared Investigation. *J. Catal.* **1983**, *82* (1), 35–44.

(140) Cao, W.; Lin, L.; Qi, H.; He, Q.; Wu, Z.; Wang, A.; Luo, W.; Zhang, T. In-Situ Synthesis of Single-Atom Ir by Utilizing Metal-Organic Frameworks: An Acid-Resistant Catalyst for Hydrogenation of Levulinic Acid to γ-Valerolactone. *J. Catal.* **2019**, *373*, 161–172.

(141) Haneda, M.; Fujitani, T.; Hamada, H. Effect of Iridium Dispersion on the Catalytic Activity of Ir/SiO2 for the Selective Reduction of NO with CO in the Presence of O2 and SO2. *J. Mol. Catal. A Chem.* **2006**, *256* (1), 143–148.

(142) Ivanov, A. V; Kustov, L. M. State of Iridium Supported on SO4/ZrO2. *Russ. Chem. Bull.* **1998**, *47* (11), 2124–2128.

(143) Lu, Y.; Wang, J.; Yu, L.; Kovarik, L.; Zhang, X.; Hoffman, A. S.; Gallo, A.; Bare, S. R.; Sokaras, D.; Kroll, T.; Dagle, V.; Xin, H.; Karim, A. M. Identification of the Active Complex for CO Oxidation over Single-Atom Ir-on-MgAl2O4 Catalysts. *Nat. Catal.* **2019**, *2* (2), 149–156.

(144) Chen, L.; Ali, I. S.; Sterbinsky, G. E.; Zhou, X.; Wasim, E.; Tait, S. L. Ligand-Coordinated Ir Single-Atom Catalysts Stabilized on Oxide Supports for Ethylene Hydrogenation and Their Evolution under a Reductive Atmosphere. *Catal. Sci. Technol.* **2021**, *11* (6), 2081–2093.

(145) Hoffman, A. S.; Fang, C.-Y.; Gates, B. C. Homogeneity of Surface Sites in Supported Single-Site Metal Catalysts: Assessment with Band Widths of Metal Carbonyl Infrared Spectra. *J. Phys. Chem. Lett.* **2016**, *7* (19), 3854–3860.

(146) McVicker, G. B.; Baker, R. T. K.; Garten, R. L.; Kugler, E. L. Chemisorption Properties of Iridium on Alumina Catalysts. *J. Catal.* **1980**, *65* (1), 207–220.

(147) Lynds, L. Infrared Spectra of Carbon Monoxide Chemisorbed on Iridium and Ruthenium. *Spectrochim. Acta* **1964**, *20* (9), 1369–1372.

(148) Gélin, P.; Auroux, A.; Taarit, Y. Ben; Gravelle, P. C. Infrared and Calorimetric Studies of the Adsorption of Carbon Monoxide on Zeolite-Supported Iridium Catalysts. *Appl. Catal.* **1989**, *46* (2), 227–240.

(149) Solymosi, F.; Novák, É.; Molnár, A. Infrared Spectroscopic Study on CO-Induced Structural Changes of Iridium on an Alumina Support. *J. Phys. Chem.* **1990,** 94, 7250−7255.

(150) Beutel, T.; Kawi, S.; Purnell, S. K.; Knoezinger, H.; Gates, B. C. Tetra- and Hexanuclear Iridium Clusters in NaY Zeolite: Characterization by Infrared Spectroscopy. *J. Phys. Chem.* **1993**, *97* (28),

(151) Kawi, S.; Chang, J. R.; Gates, B. C. Tetrairidium Clusters Supported on .Gamma.-Alumina: Formation from [Ir4(CO)12] and Carbon Monoxide-Induced Morphology Changes. *J. Phys. Chem.* **1993**, *97* (20), 5375–5383.

(152) Li, F.; Gates, B. C. Metal Carbonyl Cluster Synthesis in Nanocages: Spectroscopic Evidence of Intermediates in the Formation of Ir4(CO)12 in Zeolite NaY. *J. Phys. Chem. B* **2004**, *108* (31), 11259–11264.

(153) Tanaka, K.; Watters, K. L.; Howe, R. F. Characterization of Supported Iridium Catalysts Prepared from Ir4(CO)12. *J. Catal.* **1982**, *75* (1), 23–38.

(154) Gelin, P.; Coudurier, G.; Taarit, Y. B.; Naccache, C. Formation of Iridium Carbonyl Complex in NaY Zeolite. *J. Catal.* **1981**, *70* (1), 32–40.

(155) Hernández-Cristóbal, O.; Díaz, G.; Gómez-Cortés, A. Effect of the Reduction Temperature on the Activity and Selectivity of Titania-Supported Iridium Nanoparticles for Methylcyclopentane Reaction. *Ind. Eng. Chem. Res.* **2014**, *53* (24), 10097–10104.

(156) Mihaylov, M.; Ivanova, E.; Thibault-Starzyk, F.; Daturi, M.; Dimitrov, L.; Hadjiivanov, K. New Types of Nonclassical Iridium Carbonyls Formed in Ir-ZSM-5: A Fourier Transform Infrared Spectroscopy Investigation. *J. Phys. Chem. B*

**2006**, *110* (21), 10383–10389.

(157) Reyes, P.; Aguirre, M. C.; Pecchi, G.; Fierro, J. L. G. Crotonaldehyde Hydrogenation on Ir Supported Catalysts. *J. Mol. Catal. A Chem.* **2000**, *164* (1), 245–251.

(158) Rascón, F.; Wischert, R.; Copéret, C. Molecular Nature of Support Effects in Single-Site Heterogeneous Catalysts: Silica vs. Alumina. *Chem. Sci.* **2011**, *2* (8), 1449–1456.

(159) Phung, T. K.; Lagazzo, A.; Rivero Crespo, M. Á.; Sánchez Escribano, V.; Busca, G. A Study of Commercial Transition Aluminas and of Their Catalytic Activity in the Dehydration of Ethanol. *J. Catal.* **2014**, *311*, 102–113.

(160) Kline, C. H.; Turkevich, J. The Vibrational Spectrum of Pyridine and the Thermodynamic Properties of Pyridine Vapors. *J. Chem. Phys.* **1944**, *12* (7), 300–309.

(161) Busca, G. Spectroscopic Characterization of the Acid Properties of Metal Oxide Catalysts. *Catal. Today* **1998**, *41* (1), 191–206.

(162) Busca, G. The Surface Acidity of Solid Oxides and Its Characterization by IR Spectroscopic Methods. An Attempt at Systematization. *Phys. Chem. Chem. Phys.* **1999**, *1* (5), 723–736.

(163) Chakrapani, K.; Sampath, S. The Dual Role of Borohydride Depending on Reaction Temperature: Synthesis of Iridium and Iridium Oxide. *Chem. Commun.* **2015,** *51*, 9690−9693.

(164) Hetterscheid, D. G. H.; Van Der Ham, C. J. M.; Diaz-Morales, O.; Verhoeven, M. W. G. M.; Longo, A.; Banerjee, D.; Niemantsverdriet, J. W.; Reek, J. N. H.; Feiters,

M. C. Early Stages of Catalyst Aging in the Iridium Mediated Water Oxidation Reaction. *Phys. Chem. Chem. Phys.* **2016,** *18*, 10931−10940.

(165) Freakley, S. J.; Ruiz-Esquius, J.; Morgan, D. J. The X-Ray Photoelectron Spectra of Ir, IrO2 and IrCl3 Revisited. *Surf. Interface Anal.* **2017**, *49* (8), 794−799.

(166) Gracia, F. J.; Bollmann, L.; Wolf, E. E.; Miller, J. T.; Kropf, A. J. In Situ FTIR, EXAFS, and Activity Studies of the Effect of Crystallite Size on Silica-Supported Pt Oxidation Catalysts. *J. Catal.* **2003**, *220* (2), 382–391.

(167) Jiang, K.; Luo, M.; Peng, M.; Yu, Y.; Lu, Y.-R.; Chan, T.-S.; Liu, P.; de Groot, F. M. F.; Tan, Y. Dynamic Active-Site Generation of Atomic Iridium Stabilized on Nanoporous Metal Phosphides for Water Oxidation. *Nat. Commun.* **2020**, *11* (1), 2701.

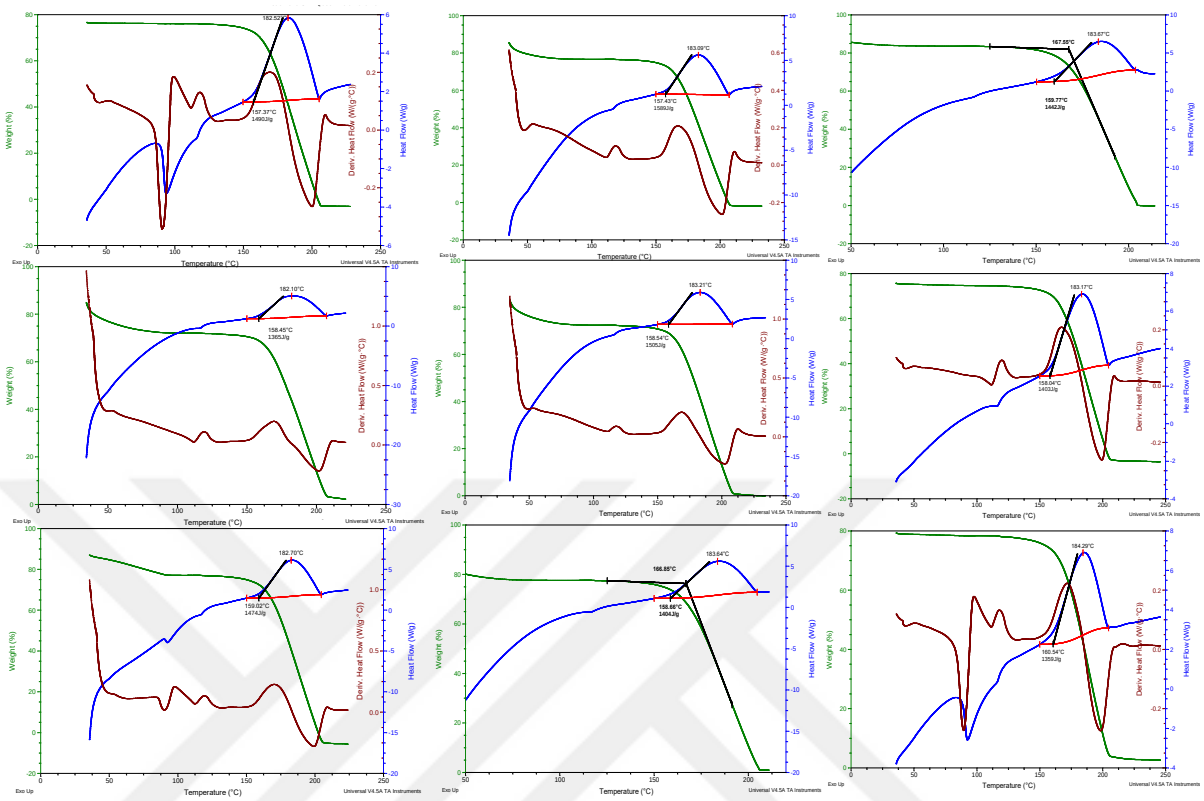
# APPENDIX

## Appendix A

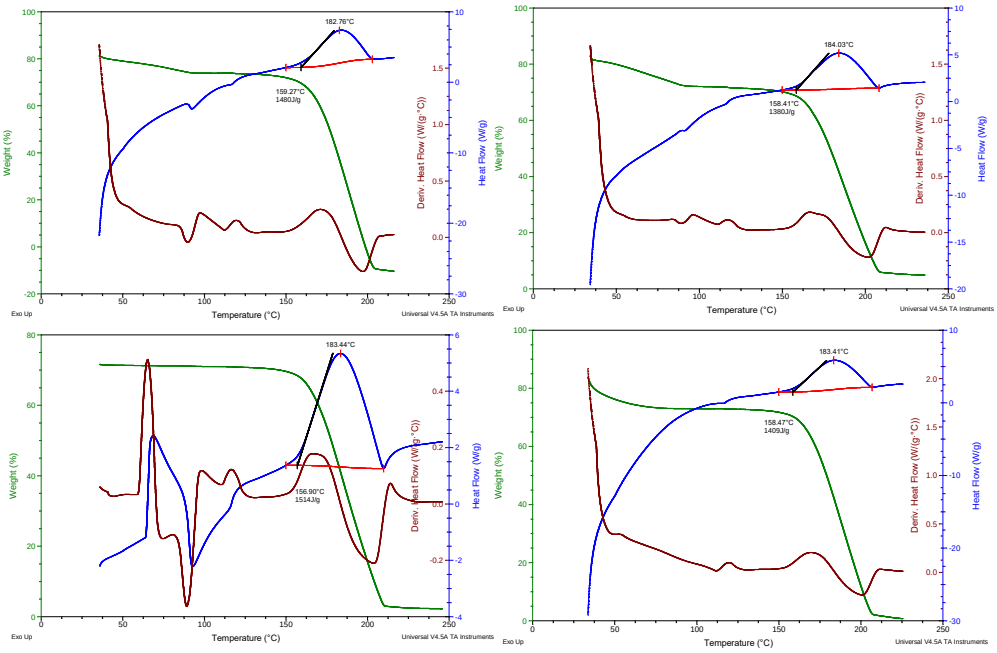
**Thermal decomposition characteristics of STY-120-X coded ionic liquids in the absence of a catalyst via DSC/TGA.**

***Appendix A1.*** *$T_{Onset}$ and Energy values of STY-120-X coded fuels in the absence of a catalyst.*

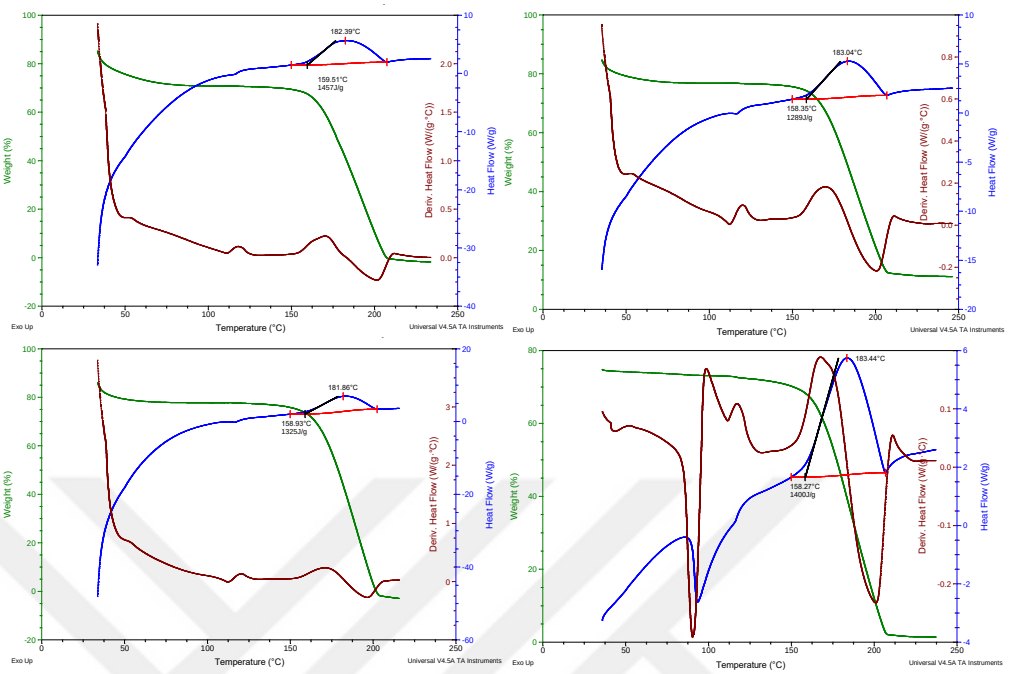
| | **STY-120-1** | | **STY-120-3** | | **STY-120-4** | | **STY-120-5** | |
|---|---|---|---|---|---|---|---|---|
| | $T_{onset}$ (°C) | Energy (J/g.IL) | $T_{onset}$ (°C) | Energy (J/g.IL) | $T_{onset}$ (°C) | Energy (J/g.IL) | $T_{onset}$ (°C) | Energy (J/g.IL) |
| 1 | 167 | 1404 | 168 | 1514 | 168 | 1400 | 169 | 1469 |
| 2 | 168 | 1442 | 171 | 1380 | 170 | 1289 | 168 | 1545 |
| 3 | 169 | 1490 | 172 | 1480 | 171 | 1325 | 169 | 1574 |
| 4 | 168 | 1589 | 169 | 1409 | 169 | 1457 | 169 | 1455 |
| 5 | 170 | 1474 | | | | | | |
| 6 | 167 | 1403 | | | | | | |
| 7 | 172 | 1359 | | | | | | |
| 8 | 169 | 1505 | | | | | | |
| 9 | 169 | 1365 | | | | | | |
| Average | 168.8 | 1447.9 | 170 | 1445.8 | 169.5 | 1367.8 | 168.8 | 1510.8 |
| Std. | 1.56 | 74.5 | 1.82 | 61.9 | 1.29 | 75.35 | 0.5 | 57.80 |



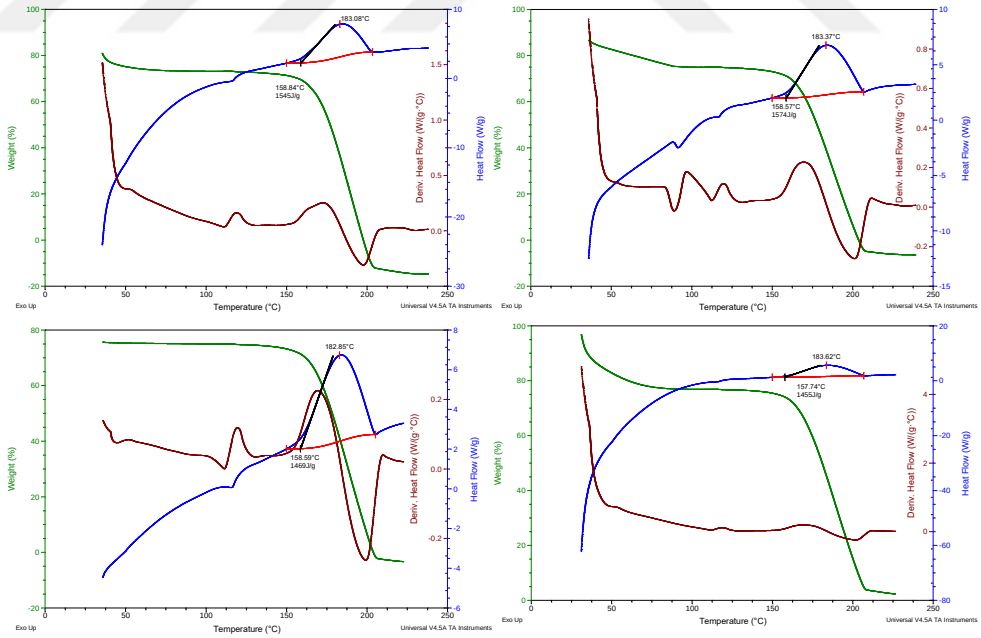
***Appendix A2.*** *DSC/TGA data of nine identical measurements for STY-120-1.*



***Appendix A3.*** *DSC/TGA data of four identical measurements for STY-120-3.*




***Appendix A4.*** *DSC/TGA data of four identical measurements for STY-120-4.*

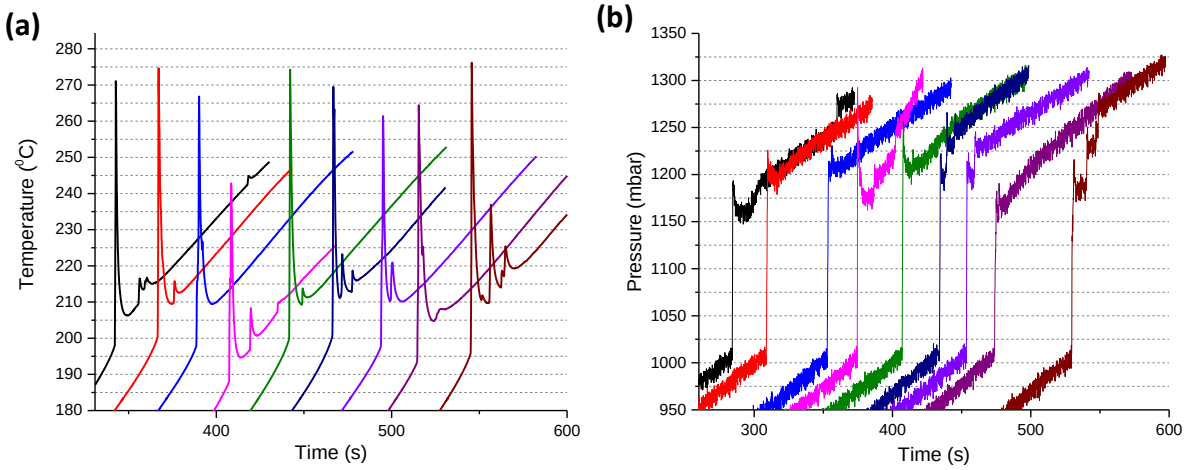



***Appendix A5.*** *DSC/TGA data of four identical measurements for STY-120-5*

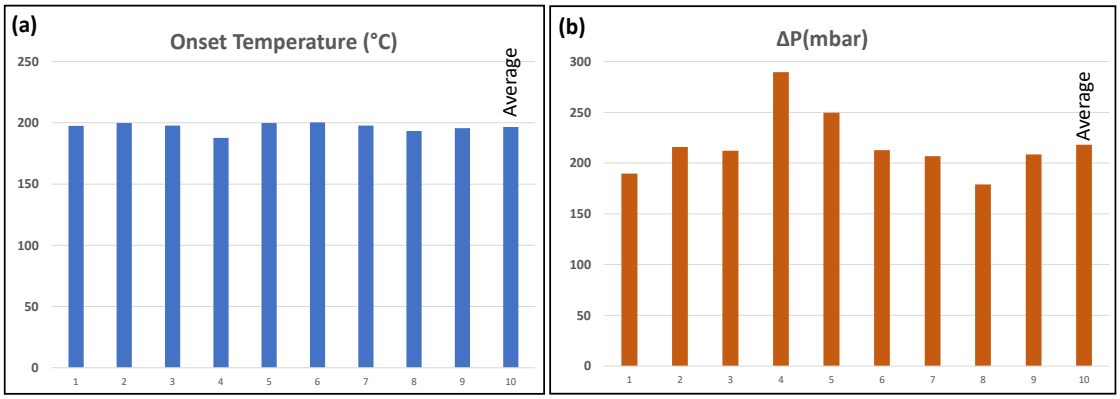
**Thermal decomposition characteristics STY-126-X based ADN mixtures in the absence of a catalyst via custom-design micro propulsion batch reactor measurements**

The STY-126-X (X = 2-9) coded fuels contained 60 wt. % ADN and a 40 wt. % mixture of water, $NH_3$, and $CH_3OH$, and prepared with different synthetic parameters.

These set of experiments were carried out in the custom-design micro propulsion batch reactor by dosing the STY-126-X fuel formulation onto the SBa200 alumina support material lacking any catalytically active component. During the measurements, the weight of the alumina powder was fixed to 125 mg, and the volume of ADN fuel was set to ca. 125 µl. As a result of these measurements, the fuel formulation with the highest exothermicity was determined.



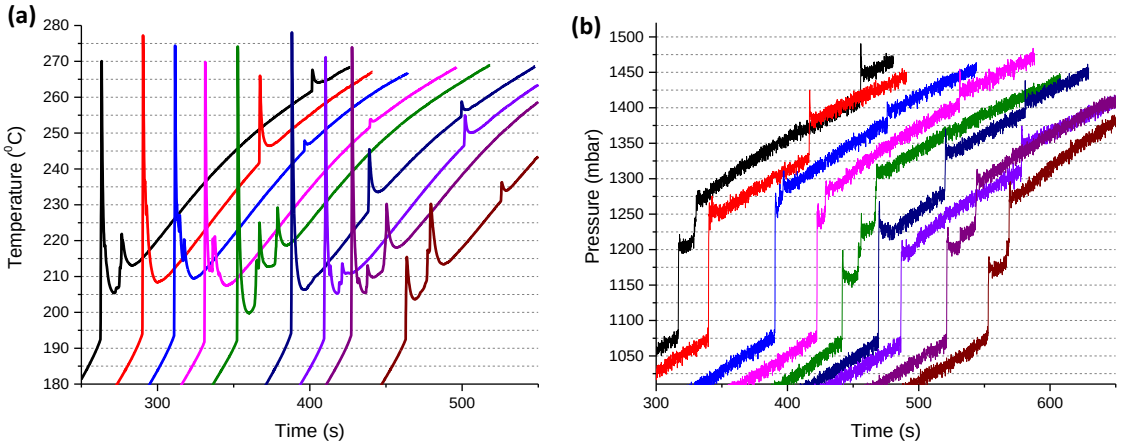

***Appendix A6.*** *(a) Temperature vs. Time and (b) Pressure vs. Time curves obtained from the custom-design micro propulsion batch reactor during thermal STY-126-2 decomposition on SBa200 alumina.*



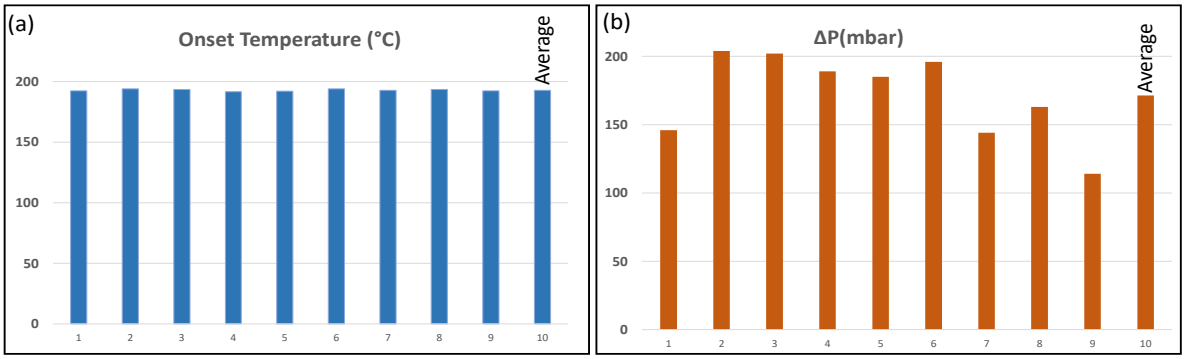

***Appendix A7.*** *Histograms showing the (a) $T_{Onset}$ and (b) ΔP values for STY-126-2 thermal decomposition on SBa200 alumina in the custom-design micro propulsion batch reactor.*

***Appendix A8.*** *$T_{Onset}$ and ΔP values for STY-126-2 on SBa200 obtained from the custom-design micro propulsion batch reactor data.*

| | 1 | 2 | 3 | 4 | 5 | 6 | 7 | 8 | 9 | Average | Standard Deviation |
|---|---|---|---|---|---|---|---|---|---|---|---|
| $T_{onset}$ (°C) | 197.6 | 199.9 | 197.8 | 187.7 | 199.8 | 200.3 | 197.7 | 193.4 | 195.6 | 196.6 | 4.01 |
| ΔP (mbar) | 189.6 | 215.7 | 212.1 | 289.7 | 249.5 | 212.7 | 206.8 | 178.9 | 208.6 | 218.2 | 33.1 |



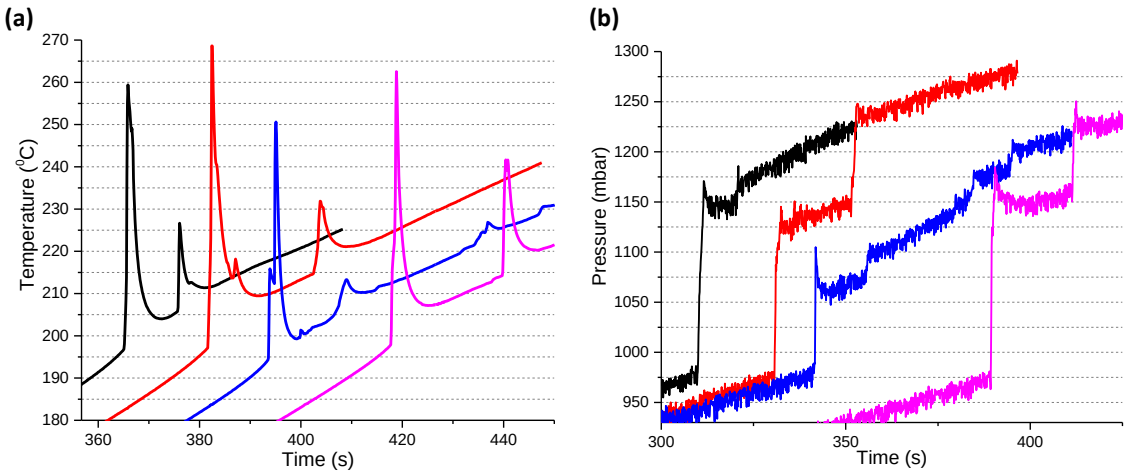

***Appendix A9.*** *(a) Temperature vs. Time and (b) Pressure vs. Time curves obtained from the custom-design micro propulsion batch reactor during thermal STY-126-3 decomposition on SBa200 alumina.*



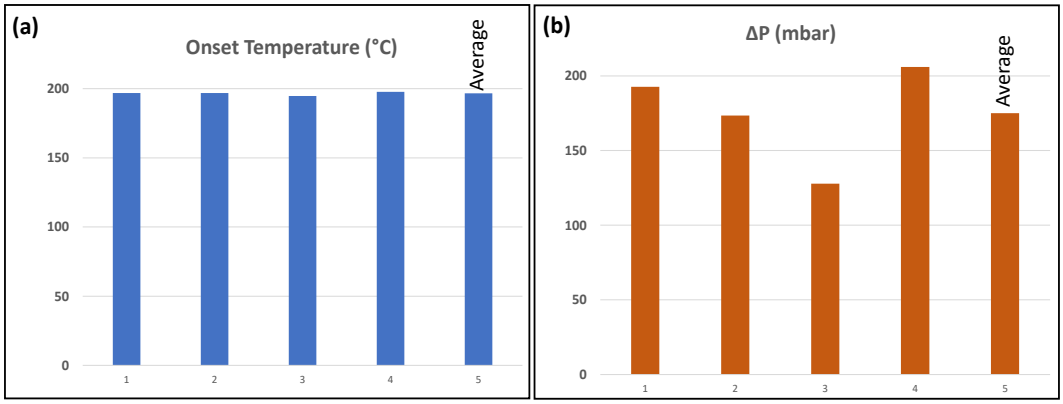

***Appendix A10.*** *Histograms showing the (a) $T_{Onset}$ and (b) ΔP values for STY-126-3 thermal decomposition on SBa200 alumina in the custom-design micro propulsion batch reactor.*

***Appendix A11.*** *$T_{Onset}$ and ΔP values for STY-126-3 on SBa200 obtained from the custom-design micro propulsion batch reactor data.*

| | 1 | 2 | 3 | 4 | 5 | 6 | 7 | 8 | 9 | Average | Standard Deviation |
|---|---|---|---|---|---|---|---|---|---|---|---|
| $T_{onset}$ (°C) | 192.3 | 193.9 | 193.4 | 191.7 | 192.1 | 194.1 | 192.7 | 193.6 | 192.4 | 192.9 | 0.8 |
| ΔP (mbar) | 146 | 204 | 202 | 189 | 185 | 196 | 144 | 163 | 114 | 171.4 | 31.3 |



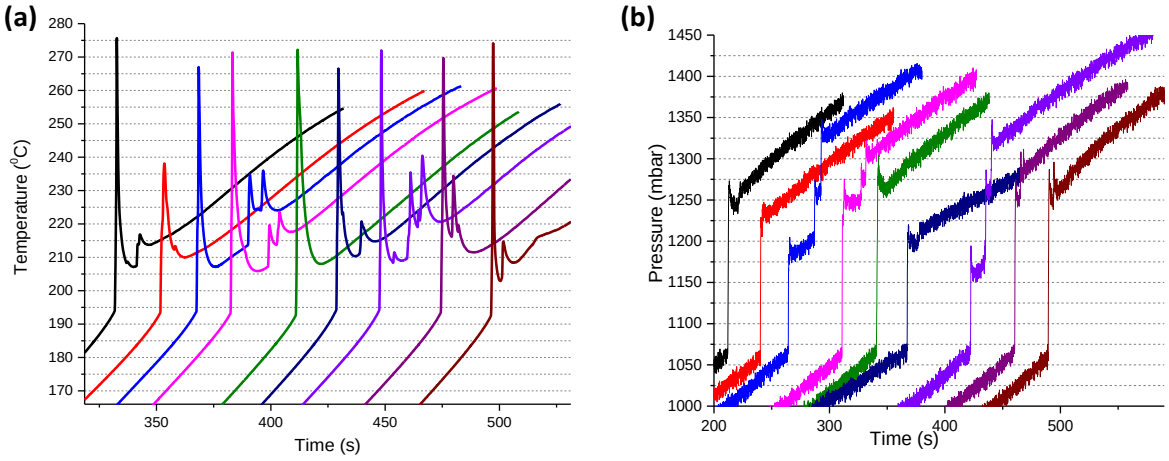

***Appendix A12.*** *(a) Temperature vs. Time and (b) Pressure vs. Time curves obtained from the custom-design micro propulsion batch reactor during thermal STY-126-4 decomposition on SBa200 alumina.*



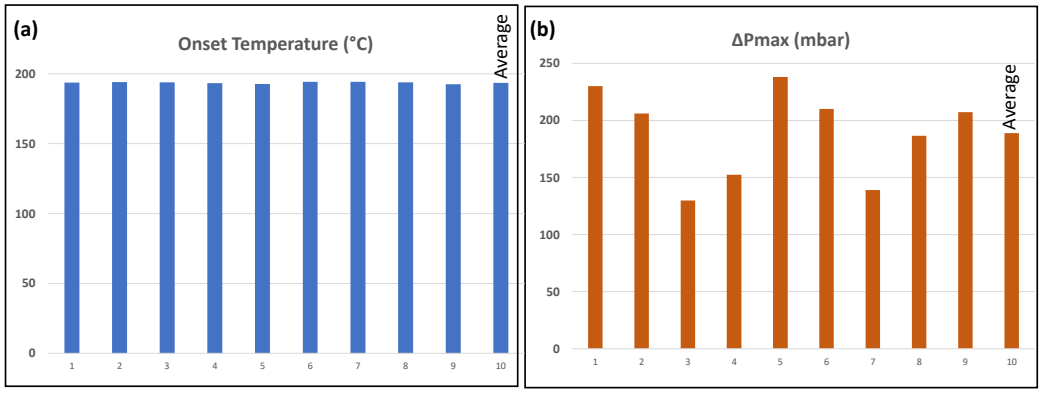

***Appendix A13.*** *Histograms showing the (a) $T_{Onset}$ and (b) ΔP values for STY-126-4 thermal decomposition on SBa200 alumina in the custom-design micro propulsion batch reactor.*

***Appendix A14.*** *$T_{Onset}$ and ΔP values for STY-126-4 on SBa200 obtained from the custom-design micro propulsion batch reactor data.*

| | 1 | 2 | 3 | 4 | Average | Standard Deviation |
|---|---|---|---|---|---|---|
| $T_{onset}$ (°C) | 196.9 | 196.9 | 194.8 | 197.8 | 196.6 | 1.3 |
| ΔP (mbar) | 192.8 | 173.4 | 127.9 | 206.1 | 175 | 34.2 |



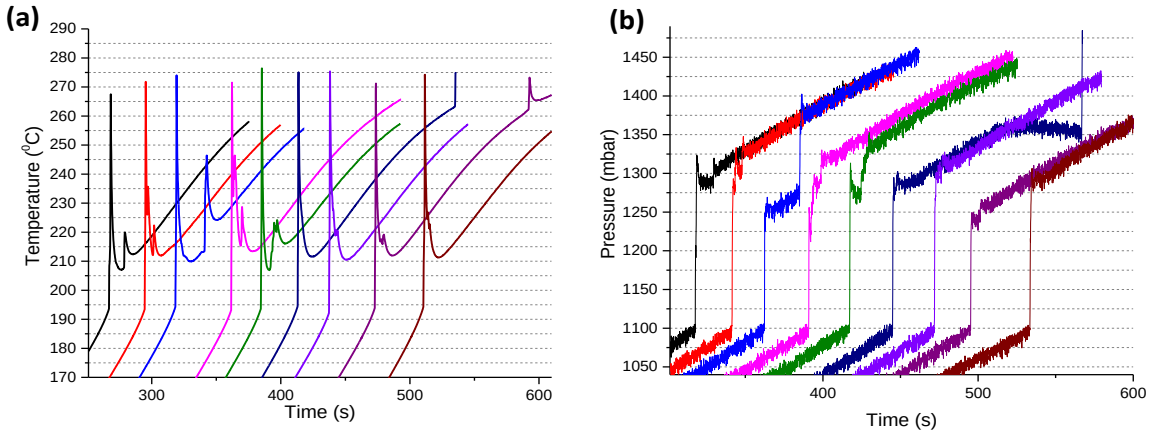

***Appendix A15.*** *(a) Temperature vs. Time and (b) Pressure vs. Time curve obtained from the custom-design micro propulsion batch reactor during thermal STY-126-5 decomposition on SBa200 alumina.*



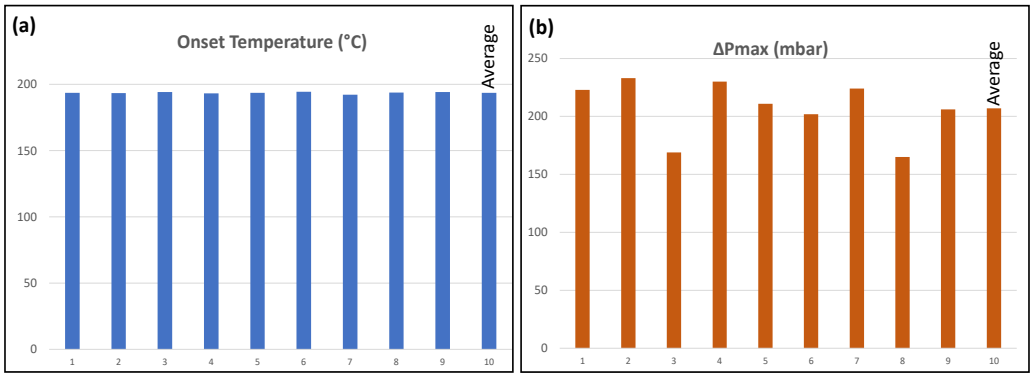

***Appendix A16.*** *Histograms showing the (a) $T_{Onset}$ and (d) ΔP values for STY-126-5 thermal decomposition on SBa200 alumina in the custom-design micro propulsion batch reactor*

***Appendix A17.*** *$T_{Onset}$ and ΔP values for STY-126-5 on SBa200 obtained from the custom-design micro propulsion batch reactor data.*

| | 1 | 2 | 3 | 4 | 5 | 6 | 7 | 8 | 9 | Average | Standard Deviation |
|---|---|---|---|---|---|---|---|---|---|---|---|
| $T_{onset}$ (°C) | 193.7 | 194 | 193.8 | 193.3 | 192.8 | 194.2 | 194.2 | 193.8 | 192.6 | 193.6 | 0.6 |
| ΔP (mbar) | 230 | 206 | 129.9 | 152.4 | 238.2 | 210.2 | 139 | 186.6 | 207.2 | 188.8 | 39.5 |



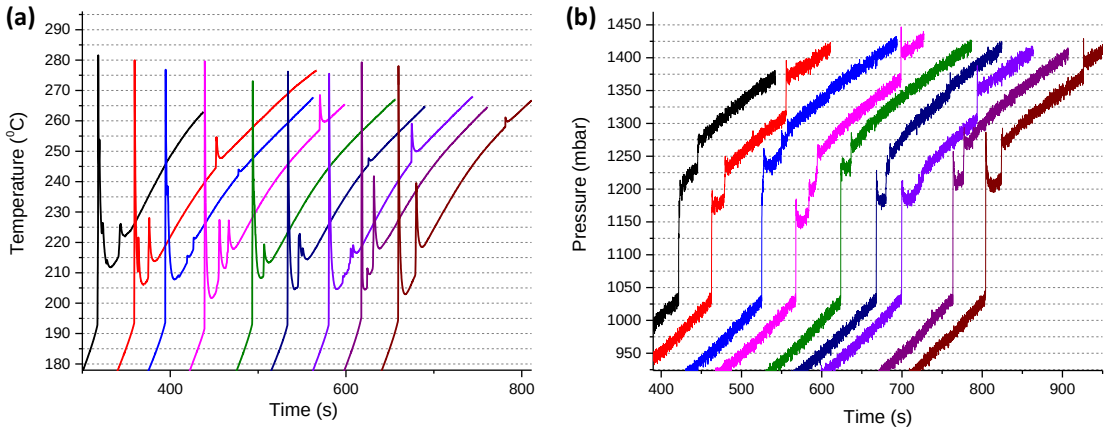

***Appendix A18.*** *(a) Temperature vs. Time and (b) Pressure vs. Time curve obtained from the custom-design micro propulsion batch reactor during thermal STY-126-6 decomposition on SBa200 alumina.*



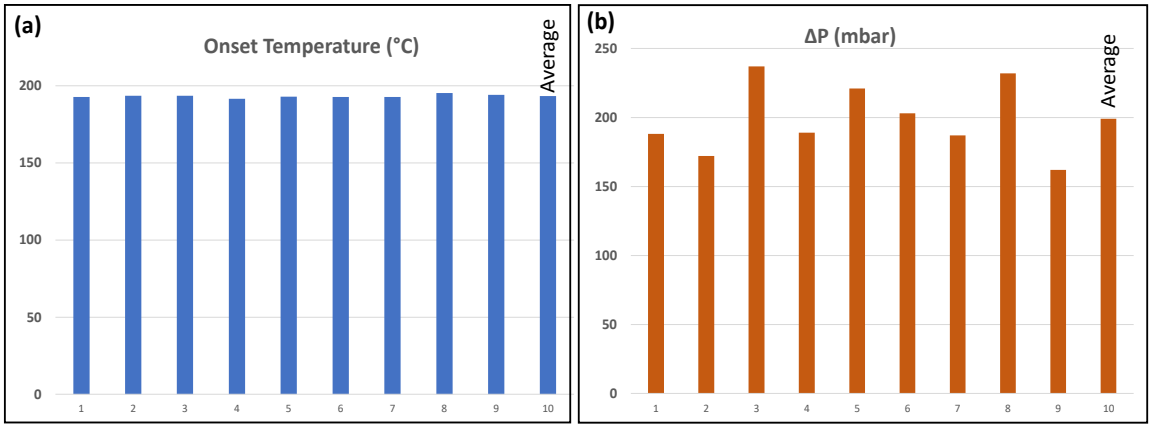

***Appendix A19.*** *Histograms showing the (a) $T_{Onset}$ and (b) ΔP values for for STY-126-6 thermal decomposition on SBa200 alumina in the custom-design micro propulsion batch reactor.*

***Appendix A20.*** *$T_{Onset}$ and ΔP values for STY-126-5 on SBa200 obtained from the custom-design micro propulsion batch reactor data.*

| | 1 | 2 | 3 | 4 | 5 | 6 | 7 | 8 | 9 | Average | Standard Deviation |
|---|---|---|---|---|---|---|---|---|---|---|---|
| $T_{onset}$ (°C) | 193.6 | 193.4 | 194.2 | 193.1 | 193.6 | 194.4 | 192.1 | 193.8 | 194.1 | 193.6 | 0.7 |
| ΔP (mbar) | 223 | 233 | 169 | 230 | 211 | 202 | 224 | 165 | 206 | 207 | 25 |



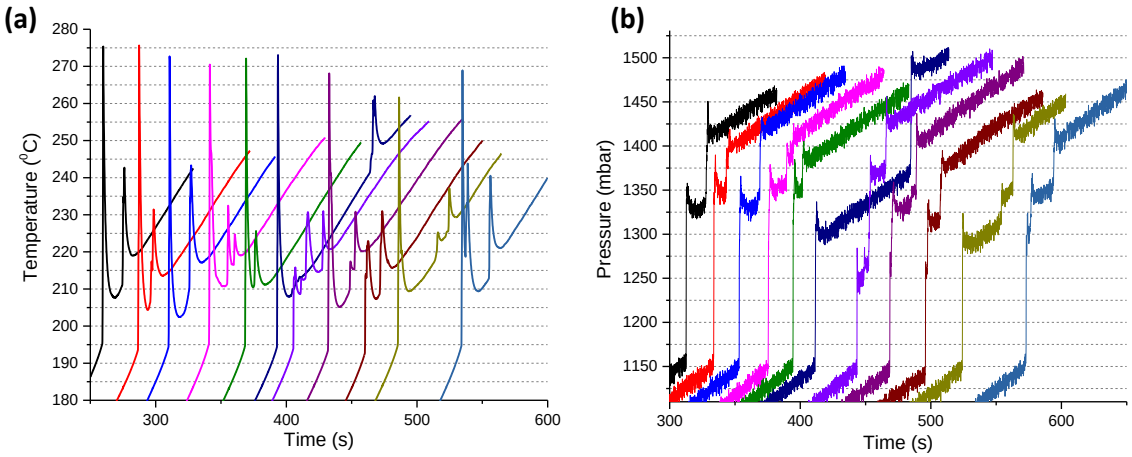

***Appendix A21.*** *(a) Temperature vs. Time and (b) Pressure vs. Time curve obtained from the custom-design micro propulsion batch reactor during thermal STY-126-7 decomposition on SBa200 alumina.*



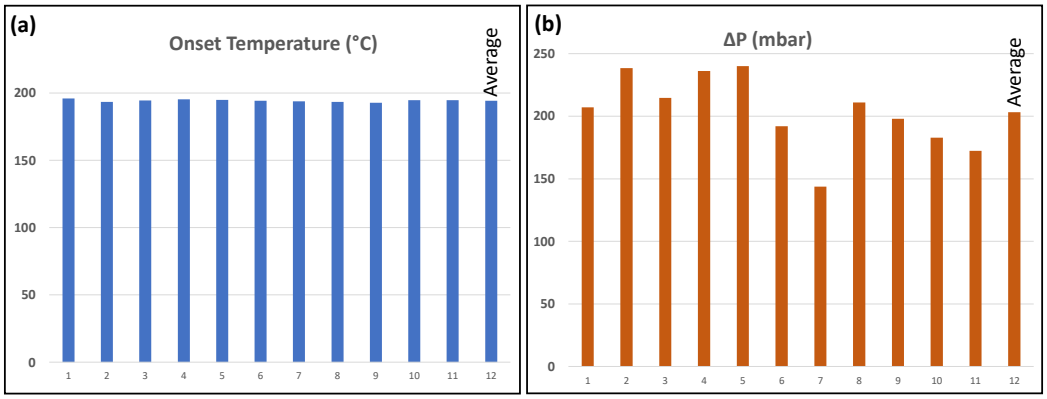

***Appendix A22.*** *Histograms showing the (a) $T_{Onset}$ and (b) ΔP values for for STY-126-7 thermal decomposition on SBa200 alumina in the custom-design micro propulsion batch reactor.*

**Appendix A23.** $T_{Onset}$ and ΔP values obtained from all measurements with STY-126-7.

| | 1 | 2 | 3 | 4 | 5 | 6 | 7 | 8 | 9 | Average | Standard Deviation |
|---|---|---|---|---|---|---|---|---|---|---|---|
| $T_{onset}$ (°C) | 192.8 | 193.5 | 193.6 | 191.5 | 192.9 | 192.8 | 192.7 | 195.2 | 194.2 | 193.2 | 1.04 |
| ΔP (mbar) | 188 | 172 | 237 | 189 | 221 | 203 | 187 | 232 | 162 | 199 | 26.2 |



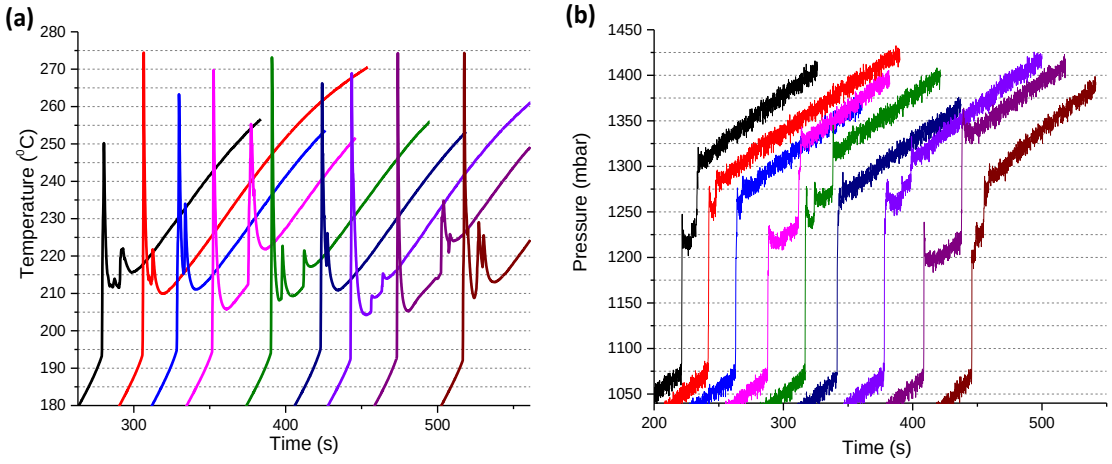

***Appendix A24.*** *(a) Temperature vs. Time and (b) Pressure vs. Time curve obtained from the custom-design micro propulsion batch reactor during thermal STY-126-8 decomposition on SBa200 alumina.*



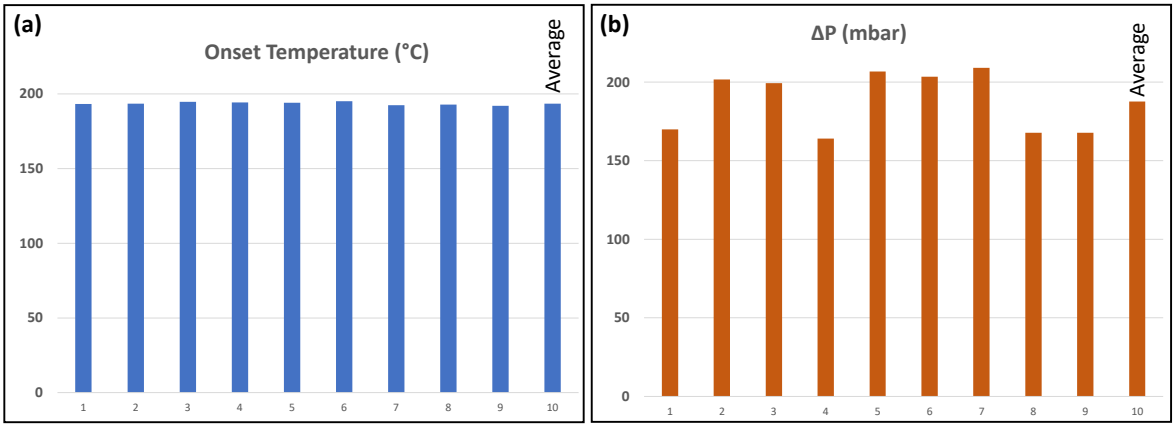

***Appendix A25.*** *Histograms showing the (a) $T_{Onset}$ and (b) ΔP values for for STY-126-8 thermal decomposition on SBa200 alumina in the custom-design micro propulsion batch reactor.*

***Appendix A26.*** *$T_{Onset}$ and ΔP values obtained from all measurements with STY-126-8.*

| | 1 | 2 | 3 | 4 | 5 | 6 | 7 | 8 | 9 | 10 | 11 | Average | Standard Deviation |
|---|---|---|---|---|---|---|---|---|---|---|---|---|---|
| $T_{onset}$ (°C) | 195.9 | 193.5 | 194.4 | 195.3 | 194.8 | 194.2 | 193.9 | 193.4 | 192.7 | 194.7 | 194.7 | 194.3 | 0.9 |
| ΔP (mbar) | 207.1 | 238.5 | 214.7 | 236.1 | 240 | 191.9 | 143.7 | 210.9 | 198 | 182.8 | 172.3 | 203.3 | 29.9 |




***Appendix A27.*** *(a) Temperature vs. Time and (b) Pressure vs. Time curve obtained from the custom-design micro propulsion batch reactor during thermal STY-126-9 decomposition on SBa200 alumina.*



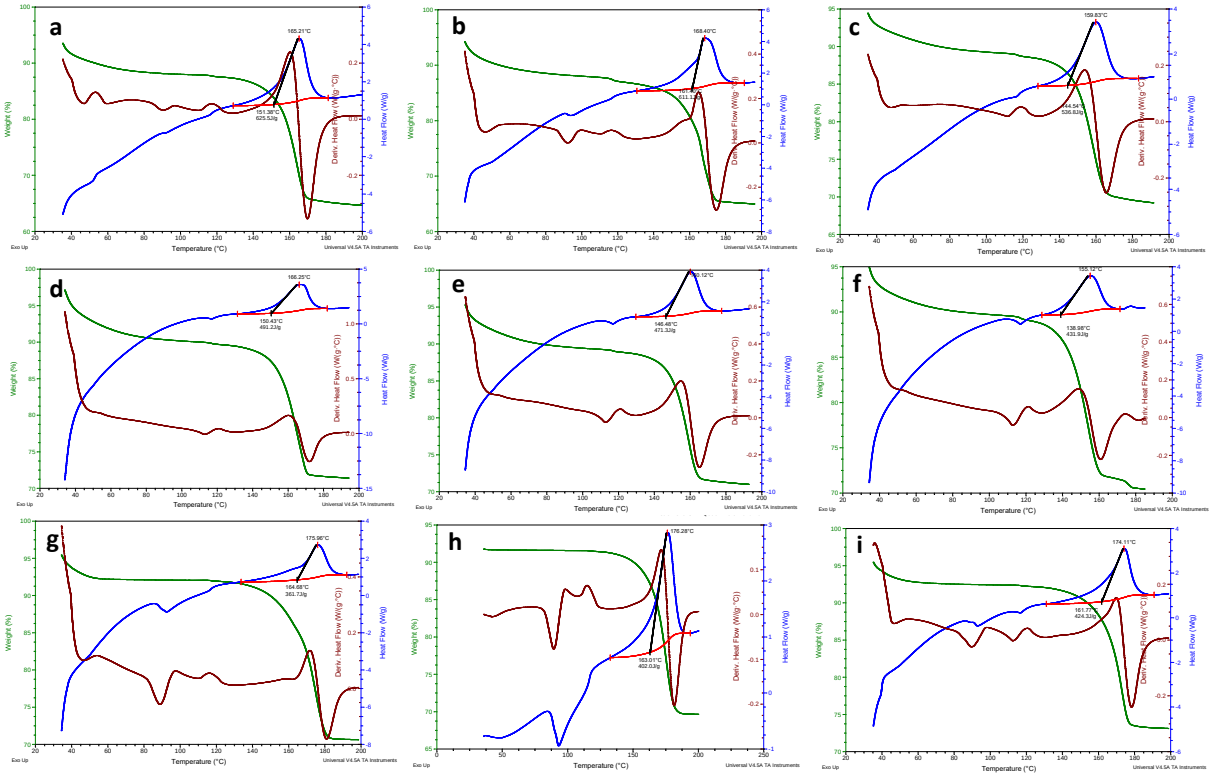

***Appendix A28.*** *Histograms showing the (a) $T_{Onset}$ and (b) ΔP values for for STY-126-9 thermal decomposition on SBa200 alumina in the custom-design micro propulsion batch reactor.*

***Appendix A29.*** *$T_{Onset}$ and ΔP values obtained from all measurements with STY-126-9.*

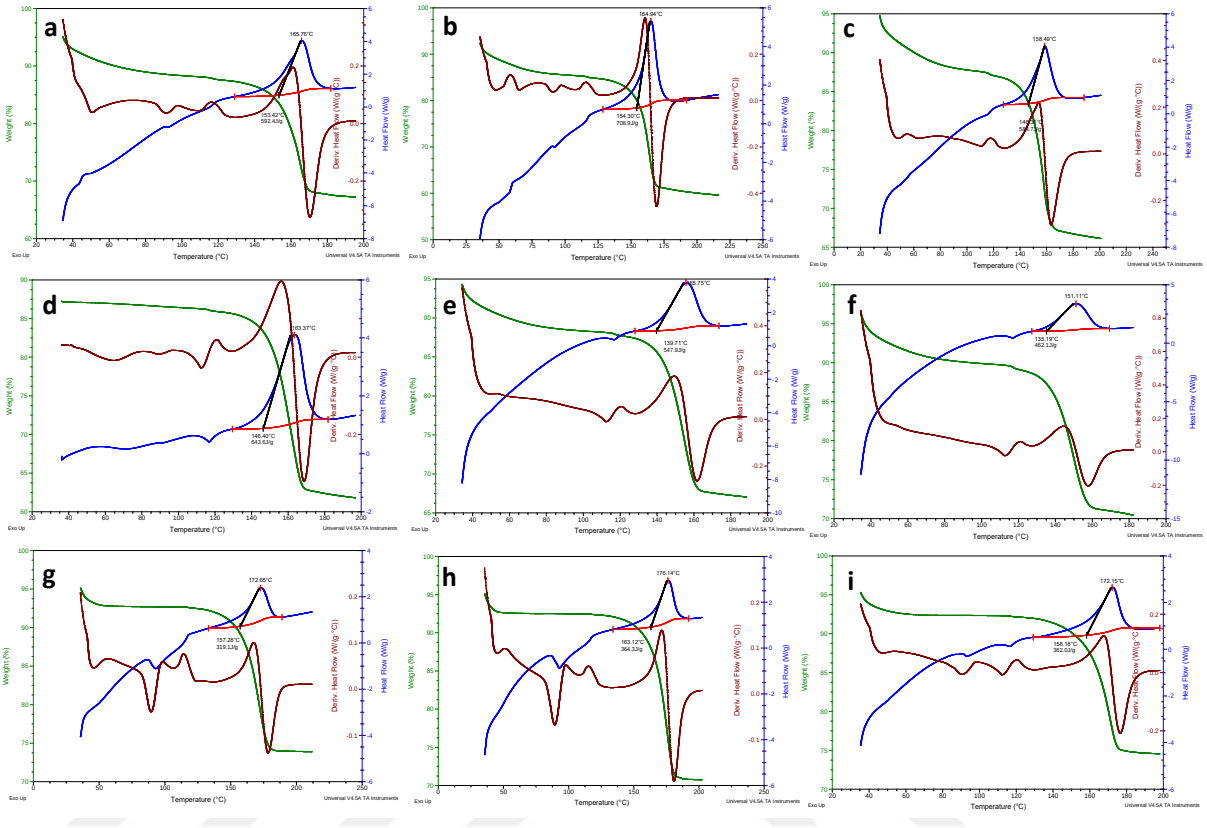
| | 1 | 2 | 3 | 4 | 5 | 6 | 7 | 8 | 9 | Average | Standard Deviation |
|---|---|---|---|---|---|---|---|---|---|---|---|
| $T_{onset}$ (°C) | 193.2 | 193.5 | 194.8 | 194.3 | 194 | 195.1 | 192.4 | 192.8 | 192 | 193.6 | 1.07 |
| ΔP (mbar) | 170 | 201.6 | 199.3 | 164 | 206.7 | 203.4 | 209.1 | 167.7 | 167.7 | 187.7 | 19.6 |

# Appendix B

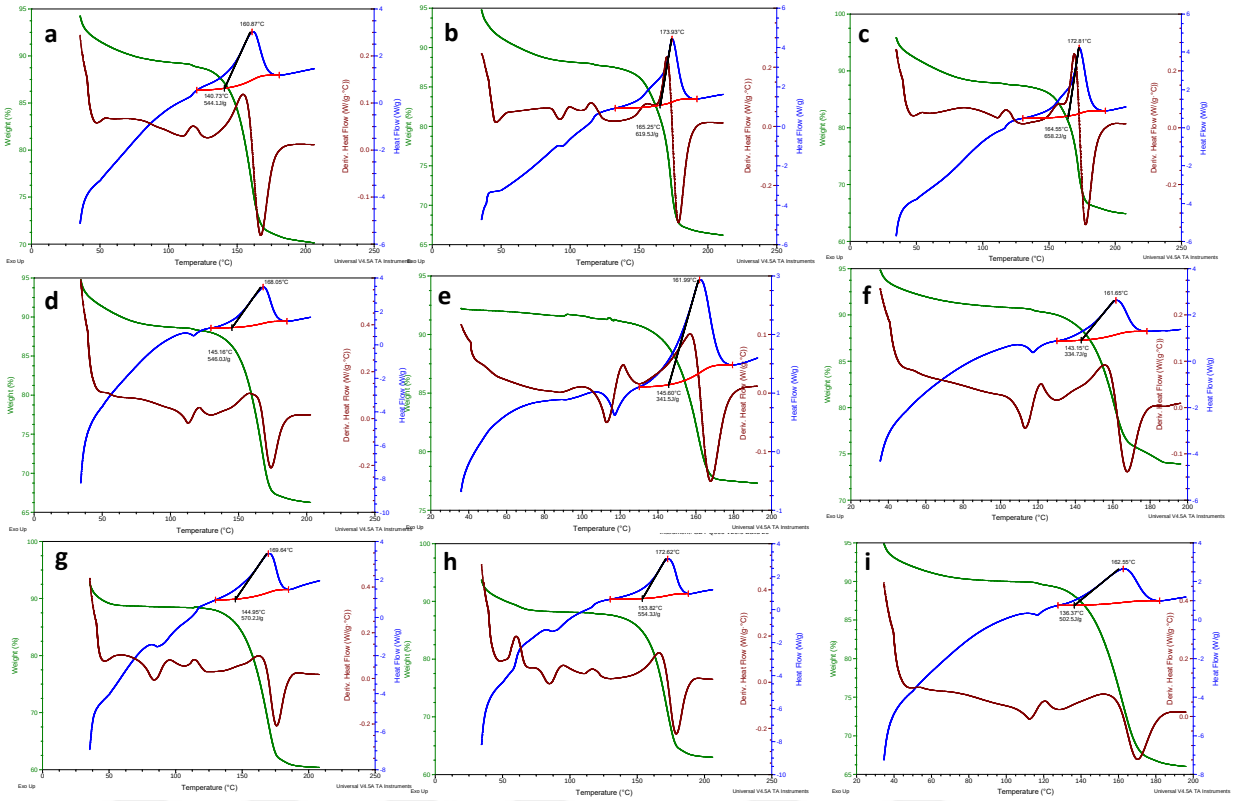
## Additional data for the catalysts synthesized via WI



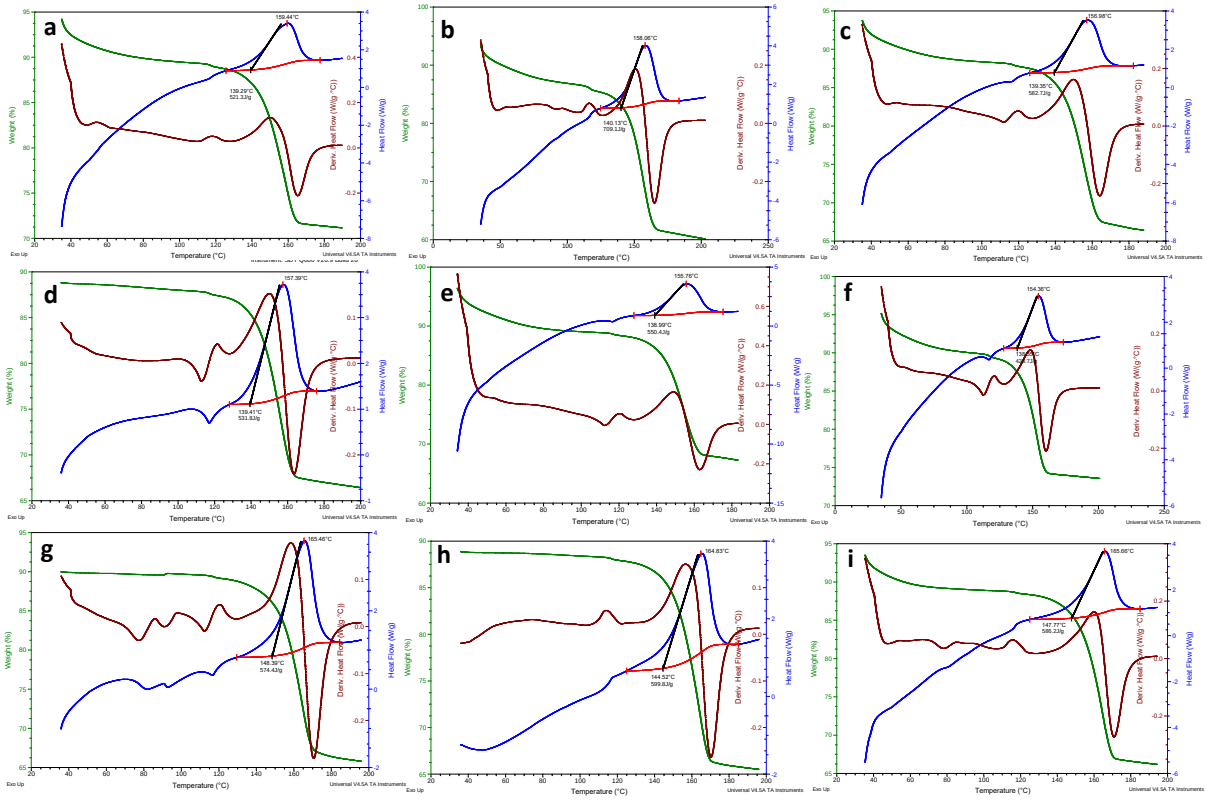

***Appendix B1.*** *DSC/TGA measurements for catalytic ADN decomposition over (a-c) 5Ir/SCFa-550C, (d-f) 5Ir/SCFa-900C, and (g-i) 5Ir/SCFa-1100C.*



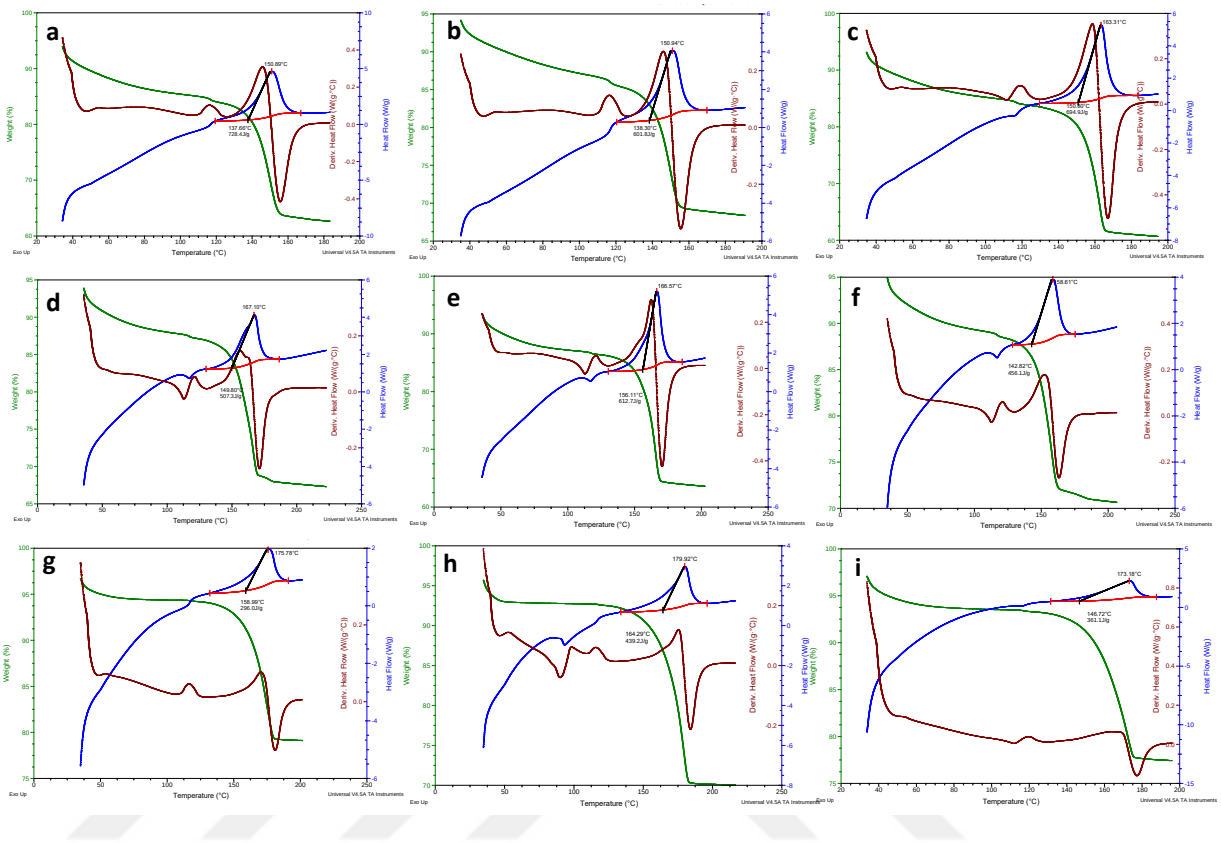

***Appendix B2.*** *DSC/TGA measurements for catalytic ADN decomposition over (a-c) 5Ir/SBa200-550C, (d-f) 5Ir/SBa200-900C, and (g-i) 5Ir/SBa200-1100C.*



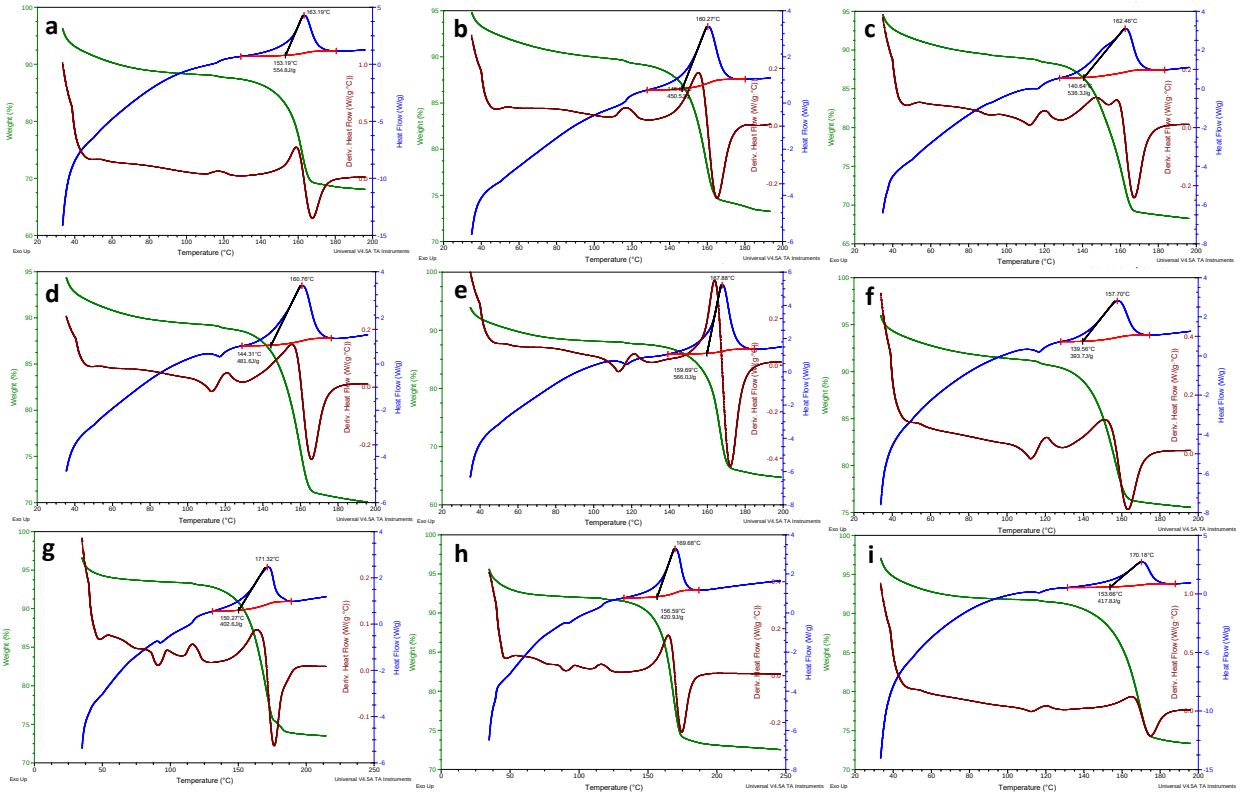

***Appendix B3.*** *DSC/TGA measurements for catalytic ADN decomposition over (a-c) 5Ir/TH100-550C, (d-f) 5Ir/TH100-900C, and (g-i) 5Ir/TH100-1100C.*




***Appendix B4.*** *DSC/TGA measurements for catalytic ADN decomposition over (a-c) 5Ir/L3-550C, (d-f) 5Ir/L3-900C, and (g-i) 5Ir/L3-1100C.*




***Appendix B5.*** *DSC/TGA measurements for catalytic ADN decomposition over (a-c) 5Ir/Mg5-550C, (d-f) 5Ir/Mg5-900C, and (g-i) 5Ir/Mg5-1100C.*




***Appendix B6.*** *DSC/TGA measurements for catalytic ADN decomposition over (a-c) 5Ir/Ce20-550C, (d-f) 5Ir/Ce20-900C, and (g-i) 5Ir/Ce20-1100C.*

***Appendix B7.*** *DSC/TGA results for the Ir-containing catalysts prepared via WI method and calcined at 550 °C.*

| | **5Ir/L3 550C** | | **5Ir/SCFa 550C** | | **5Ir/TH100 550C** | |
|---|---|---|---|---|---|---|
| | $T_{onset}$ (°C) | Energy (J/g.IL) | $T_{onset}$ (°C) | Energy (J/g.IL) | $T_{onset}$ (°C) | Energy (J/g.IL) |
| Trial 1 | 150 | 2051 | 160 | 1959 | 154 | 1670 |
| Trial 2 | 150 | 2180 | 165 | 1827 | 155 | 1926 |
| Trial 3 | 150 | 1850 | 154 | 1793 | 156 | 1855 |
| **Average** | **150** | **2027** | **159.7** | **1859.7** | **155** | **1817** |
| **Standard Deviation** | 0 | 166.3 | 5.5 | 87.7 | 1 | 132.1 |

| | **5Ir/SBa200 550C** | | **5Ir/MG5 550C** | | **5Ir/Ce20 550C** | |
|---|---|---|---|---|---|---|
| | $T_{onset}$ (°C) | Energy (J/g.IL) | $T_{onset}$ (°C) | Energy (J/g.IL) | $T_{onset}$ (°C) | Energy (J/g.IL) |
| Trial 1 | 157 | 1943 | 145 | 2212 | 160 | 1903 |
| Trial 2 | 160 | 1875 | 146 | 2347 | 155 | 1831 |
| Trial 3 | 154 | 1898 | 159 | 1865 | 147 | 2002 |
| **Avarage** | **157** | **1905.3** | **150** | **2141.3** | **157.7** | **1912** |
| **Standard Deviation** | 3 | 34.6 | 7.8 | 248.6 | 2.5 | 85.8 |

***Appendix B8.*** *DSC/TGA results for the Ir-containing catalysts prepared via WI method and calcined at 900 °C.*

| | **5Ir/L3 900C** | | **5Ir/SCFa 900C** | | **5Ir/TH100 900C** | |
|---|---|---|---|---|---|---|
| | $T_{onset}$ (°C) | Energy (J/g.IL) | $T_{onset}$ (°C) | Energy (J/g.IL) | $T_{onset}$ (°C) | Energy (J/g.IL) |
| Trial 1 | 150 | 1447 | 155 | 1766 | 158 | 1566 |
| Trial 2 | 149 | 1787 | 160 | 1779 | 157 | 1764 |
| Trial 3 | 148 | 1641 | 149 | 1476 | 155 | 1287 |
| **Average** | **149** | **1625** | **154.7** | **1673.7** | **156.7** | **1539** |
| **Standard Deviation** | 1 | 170.6 | 5.5 | 171.3 | 1.5 | 239.6 |

| | **5Ir/SBa200 900C** | | **5Ir/MG5 900C** | | **5Ir/Ce20 900C** | |
|---|---|---|---|---|---|---|
| | $T_{onset}$ (°C) | Energy (J/g.IL) | $T_{onset}$ (°C) | Energy (J/g.IL) | $T_{onset}$ (°C) | Energy (J/g.IL) |
| Trial 1 | 156 | 1769 | 156 | 1675 | 155 | 1726 |
| Trial 2 | 149 | 1703 | 156 (166) | 1707 | 164 | 1559 |
| Trial 3 | 144 | 1628 | 152 | 1686 | 151 | 2008 |
| **Avarage** | **149.7** | **1700** | **154.7** | **1689.3** | **156.7** | **1764.3** |
| **Standard Deviation** | 6.0 | 70.5 | 2.3 | 16.2 | 6.6 | 226.9 |

***Appendix B9.*** *DSC/TGA results for the Ir-containing catalysts prepared via WI method and calcined at 1100 °C.*

| | **5Ir/L3 1100C** | | **5Ir/SCFa 1100C** | | **5Ir/TH100 1100C** | |
|---|---|---|---|---|---|---|
| | $T_{onset}$ (°C) | Energy (J/g.IL) | $T_{onset}$ (°C) | Energy (J/g.IL) | $T_{onset}$ (°C) | Energy (J/g.IL) |
| Trial 1 | 156 | 1783 | 176 | 1767 | 162 | 1676 |
| Trial 2 | 160 | 1709 | 171 | 1472 | 171 | 1631 |
| Trial 3 | 160 | 1763 | 172 | 1216 | 166 | 1536 |
| **Average** | **158.7** | **1751.7** | **173** | **1485** | **166.3** | **1614** |
| **Standard Deviation** | 2.3 | 38.2 | 2.6 | 275.7 | 4.5 | 71.5 |

| | **5Ir/SBa200 1100C** | | **5Ir/MG5 1100C** | | **5Ir/Ce20 1100C** | |
|---|---|---|---|---|---|---|
| | $T_{onset}$ (°C) | Energy (J/g.IL) | $T_{onset}$ (°C) | Energy (J/g.IL) | $T_{onset}$ (°C) | Energy (J/g.IL) |
| Trial 1 | 167 | 1262 | 170 | 1396 | 167 | 1482 |
| Trial 2 | 171 | 1233 | 175 | 1490 | 167 | 1572 |
| Trial 3 | 174 | 1460 | 175 | 1415 | 165 | 1668 |
| **Avarage** | **170.7** | **1318** | **173.3** | **1433.7** | **166.3** | **1574** |
| **Standard Deviation** | 3.5 | 123.5 | 2.8 | 49.7 | 1.1 | 93 |

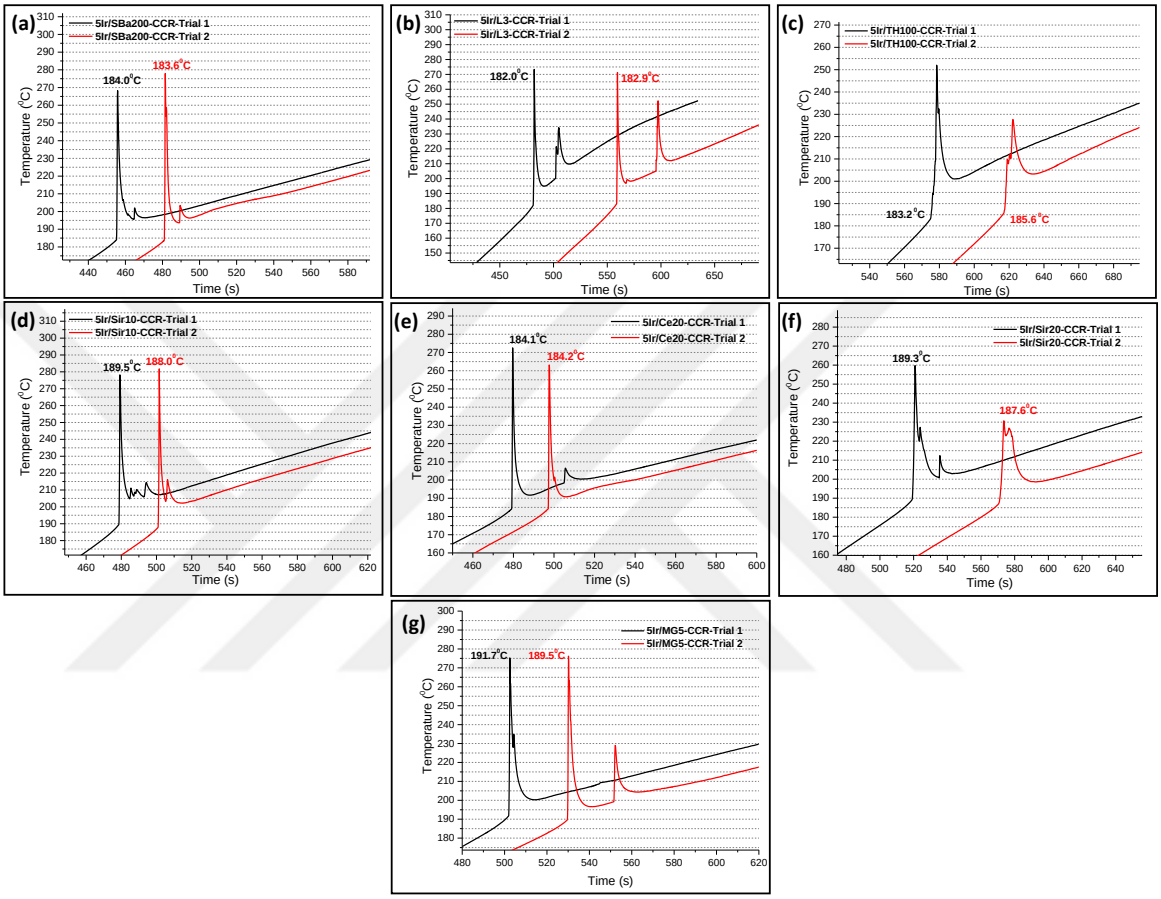
# Appendix C

**Additional data for the catalysts synthesized via IWI**

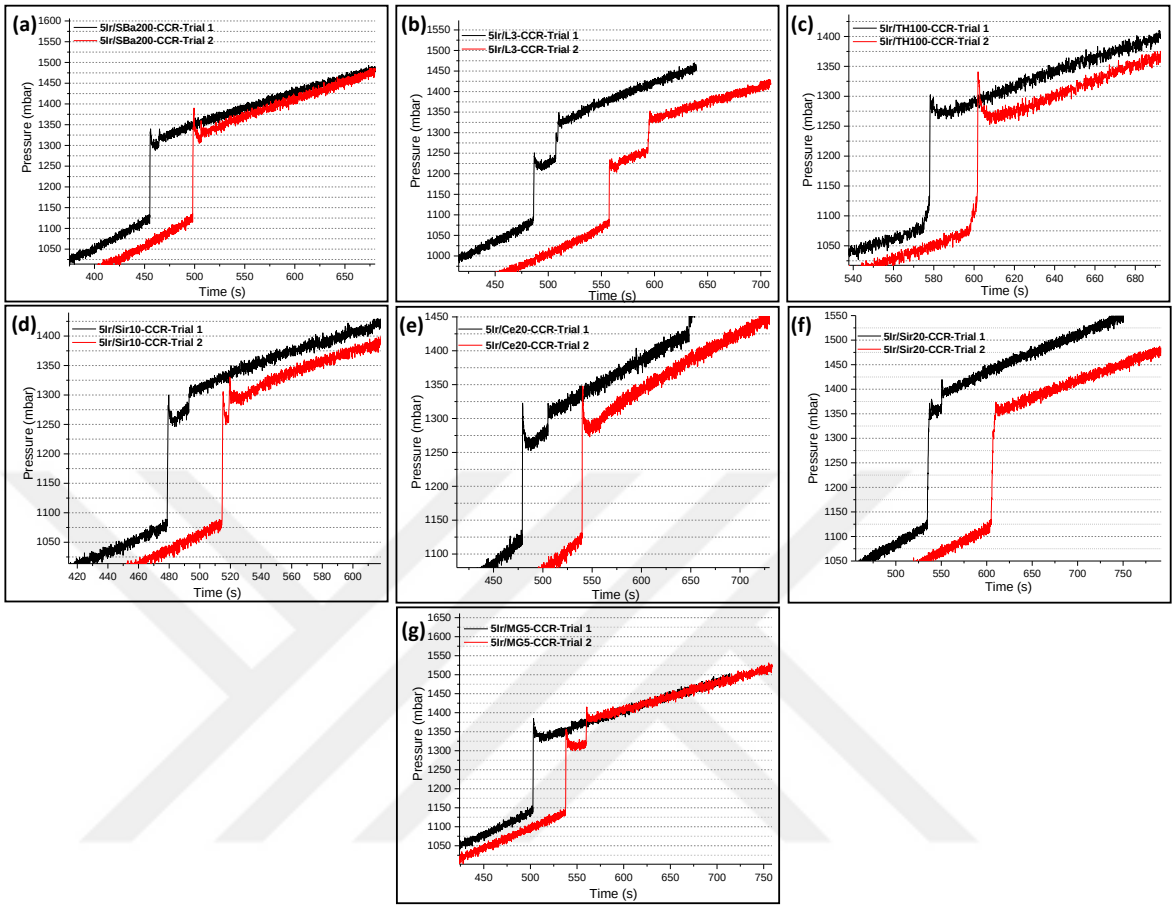
**Investigation Of the Performance of the IWI Catalysts on the Catalytic Decomposition of Different ADN Fuels using Custom-Design Micro Propulsion Batch Reactor**

In this set of experiments, catalytic decomposition of various ADN fuel formulations were investigated in the custom-design micro propulsion batch reactor using 130 μl ADN fuel mixture (i.e., STY-126-4, STY-126-3 or STY-126-8) and 100 mg powder (i.e., either SBa200 for analyzing thermal decomposition of ADN, or the relevant IWI catalyst powder for the catalytic decomposition of ADN).

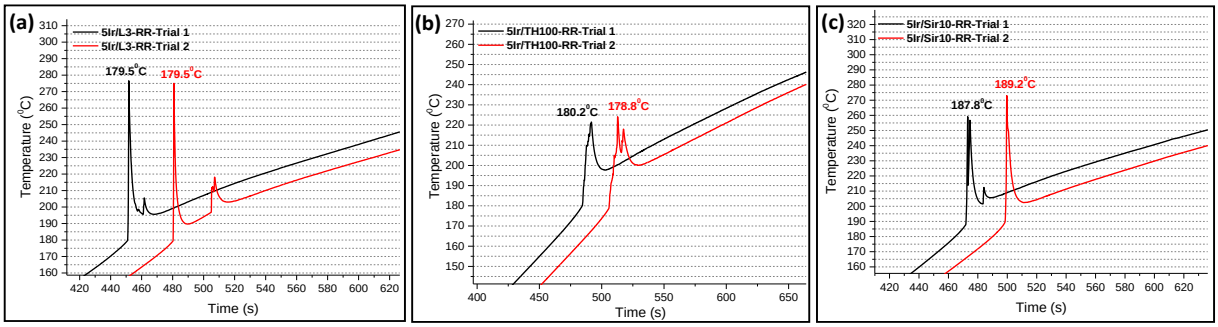
**Catalytic Decomposition of STY-126-4 with IWI catalysts in the Custom-Design Micro Propulsion Batch Reactor**



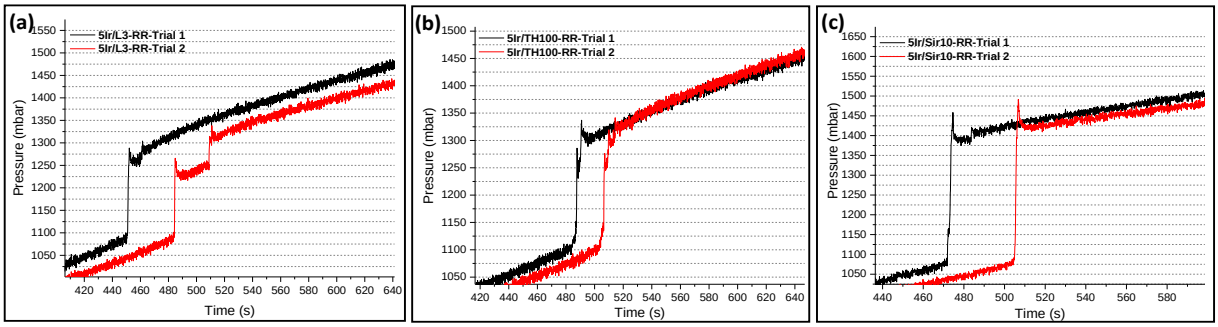

***Appendix C1.*** *Temperature vs. time curve for (a) 5Ir/SBa200-CCR, (b) 5Ir/L3-CCR, (c) 5Ir/TH100-CCR, (d) 5Ir/Sir10-CCR, (e) 5Ir/Ce20-CCR, (f) 5Ir/Sir20-CCR, (g) 5Ir/Mg5-CCR obtained from the custom-design micro propulsion batch reactor during the catalytic STY-126-4 decomposition.*




***Appendix C2.*** *Pressure vs. time curve for (a) 5Ir/SBa200-CCR, (b) 5Ir/L3-CCR, (c) 5Ir/TH100-CCR, (d) 5Ir/Sir10-CCR, (e) 5Ir/Ce20-CCR, (f) 5Ir/Sir20-CCR, (g) 5Ir/Mg5-CCR obtained from the custom-design micro propulsion batch reactor during the catalytic STY-126-4 decomposition.*




***Appendix C3.*** *Temperature vs. time curve for (a) 5Ir/L3-RR, (b) 5Ir/TH100-RR, (c) 5Ir/Sir10-RR obtained from the custom-design micro propulsion batch reactor during the catalytic STY-126-4 decomposition.*



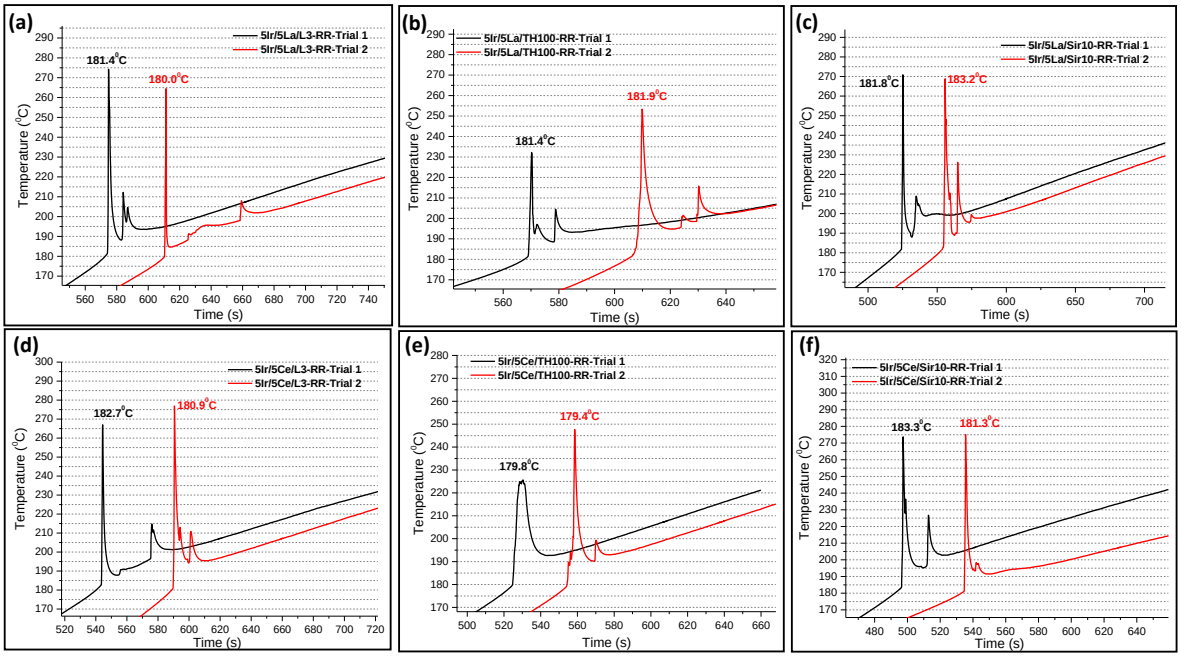

***Appendix C4.*** *Pressure vs. time curve for (a) 5Ir/L3-RR, (b) 5Ir/TH100-RR, (c) 5Ir/Sir10-RR obtained from the custom-design micro propulsion batch reactor during the catalytic STY-126-4 decomposition.*

***Appendix C5.*** *$T_{Onset}$ and ΔP values obtained from thermal and catalytic decomposition of STY-126-4.*

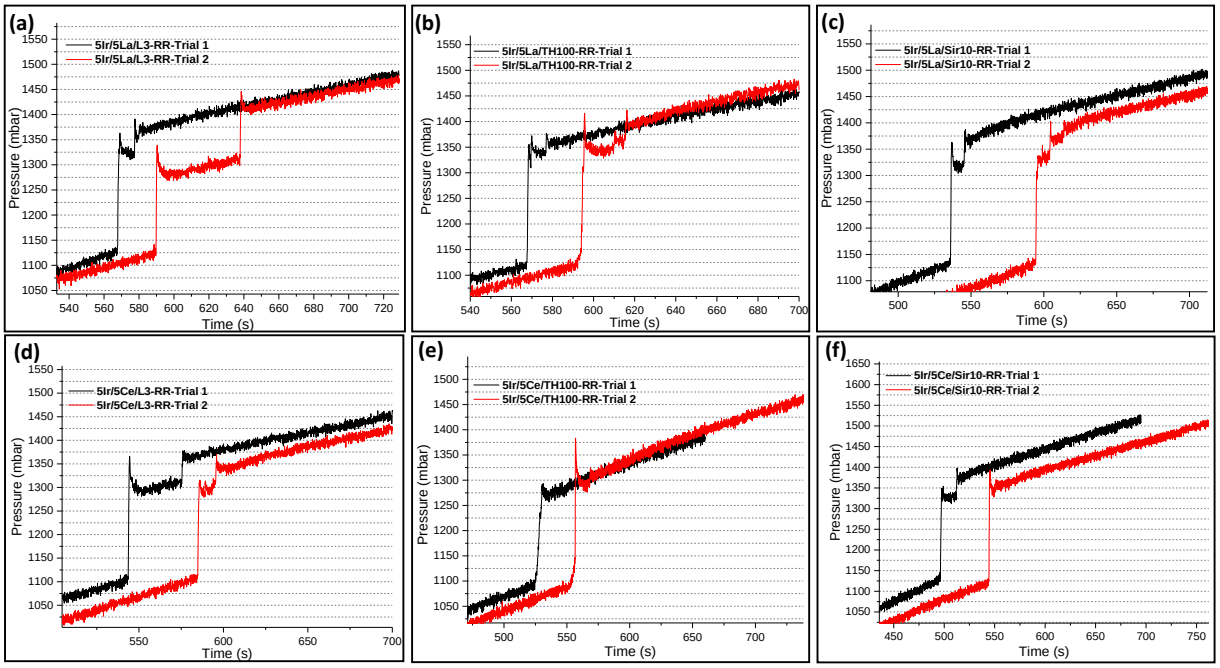
| | Onset Temperature (˚C) | | | |
|---|---|---|---|---|
| Sample Name | Trial 1 | Trial 2 | Avarage | Standard Deviation |
| Thermal | 190.1 | x | 190.1 | 0.00 |
| | | | | |
| 5Ir/L3-CCR | 182 | 182.9 | 182.45 | 0.64 |
| 5Ir/L3-RR | 179.5 | 179.5 | 179.5 | 0.00 |
| | | | | |
| 5Ir/TH100-CCR | 183.2 | 185 | 184.1 | 1.27 |
| 5Ir/TH100-RR | 180.2 | 178.8 | 179.5 | 0.99 |
| | | | | |
| 5Ir/Sir10-CCR | 189.5 | 188 | 188.75 | 1.06 |
| 5Ir/Sir10-RR | 187.8 | 189.2 | 188.5 | 0.99 |
| | | | | |
| 5Ir/Sir20-CCR | 189.3 | 187.6 | 188.45 | 1.20 |
| | | | | |
| 5Ir/MG5-CCR | 191.7 | 189.5 | 190.6 | 1.56 |
| | | | | |
| 5Ir/Ce20-CCR | 184.1 | 184.2 | 184.15 | 0.07 |
| | | | | |
| 5Ir/SBa200-CCR | 184 | 183.6 | 183.8 | 0.28 |

| | ΔP (mbar) | | | |
|---|---|---|---|---|
| Sample Name | Trial 1 | Trial 2 | Avarage | Standard Deviation |
| Thermal | 221 | x | 221 | 0.00 |
| | | | | |
| 5Ir/L3-CCR | 266 | 273 | 269.5 | 4.95 |
| 5Ir/L3-RR | 218 | 248 | 233 | 21.21 |
| | | | | |
| 5Ir/TH100-CCR | 223 | 265 | 244 | 29.70 |
| 5Ir/TH100-RR | 237 | 239 | 238 | 1.41 |
| | | | | |
| 5Ir/Sir10-CCR | 238 | 252 | 245 | 9.90 |
| 5Ir/Sir10-RR | 380 | 409 | 394.5 | 20.51 |
| | | | | |
| 5Ir/Sir20-CCR | 297 | 260 | 278.5 | 26.16 |
| | | | | |
| 5Ir/MG5-CCR | 241 | 278 | 259.5 | 26.16 |
| | | | | |
| 5Ir/Ce20-CCR | 204 | 223 | 213.5 | 13.44 |
| | | | | |
| 5Ir/SBa200-CCR | 220 | 267 | 243.5 | 33.23 |

**Catalytic Decomposition of STY-126-3 and STY-126-8 with IWI catalysts in the Custom-Design Micro Propulsion Batch Reactor**




***Appendix C6.*** *Temperature vs. time curve for (a) 5Ir/5La/L3-RR, (b) 5Ir/5La/TH100-RR, (c) 5Ir/5La/Sir10-RR, (d) 5Ir/5Ce/L3-RR, (e) 5Ir/5Ce/TH100-RR and (f) 5Ir/5Ce/Sir10-RR obtained from the custom-design micro propulsion batch reactor during the catalytic ADN decomposition*




***Appendix C7.*** *Pressure vs. time curve for (a) 5Ir/5La/L3-RR, (b) 5Ir/5La/TH100-RR, (c) 5Ir/5La/Sir10-RR, (d) 5Ir/5Ce/L3-RR, (e) 5Ir/5Ce/TH100-RR and (f) 5Ir/5Ce/Sir10-RR obtained from the custom-design micro propulsion batch reactor during the catalytic ADN decomposition.*

***Appendix C8.*** *$T_{Onset}$ and ΔP values obtained from thermal and catalytic decomposition of STY-126-8/STY-126-3.*

| | Onset Temperature (°C) | | | |
|---|---|---|---|---|
| | Trial 1 | Trial 2 | Average | Standard deviation |
| 5Ir/5La/L3-RR | 183 | 184.2 | 183.6 | 0.85 |
| 5Ir/5Ce/L3-RR | 178.4 | 179.9 | 179.15 | 1.06 |
| | | | | |
| 5Ir/5La/TH100-RR | 181.4 | 181.9 | 181.65 | 0.35 |
| 5Ir/5Ce/TH100-RR | 179.8 | 179.4 | 179.6 | 0.28 |
| | | | | |
| 5Ir/5La/Sir10-RR | 181.8 | 183.2 | 182.5 | 0.99 |
| 5Ir/5Ce/Sir10-RR | 183.3 | 181.3 | 182.3 | 1.41 |

| | ΔP (mbar) | | | |
|---|---|---|---|---|
| | Trial 1 | Trial 2 | Average | Standard deviation |
| 5Ir/5La/L3-RR | 266 | 319 | 292.5 | 37.48 |
| 5Ir/5Ce/L3-RR | 266 | 275 | 270.5 | 6.36 |
| | | | | |
| 5Ir/5La/TH100-RR | 259 | 289 | 274 | 21.21 |
| 5Ir/5Ce/TH100-RR | 204 | 287 | 245.5 | 58.69 |
| | | | | |
| 5Ir/5La/Sir10-RR | 255 | 268 | 261.5 | 9.19 |
| 5Ir/5Ce/Sir10-RR | 270 | 275 | 272.5 | 3.54 |

# Appendix D

**List of Publications of Merve Kurt**

1. M. Kurt, Z. Say, K. E. Ercan, E. I. Vovk, C. H. Kim, and E. Ozensoy, "Sulfur Poisoning and Regeneration Behavior of Perovskite-Based NO Oxidation Catalysts," *Topics in Catalysis*, 60, 40–51, 2017.
2. Z. Say, M. Dogac, E.I.Vovk, Y.E. Kalay, C, H. Kim, W. Li, E. Ozensoy, "Palladium doped Perovskite-Based NO oxidation Catalysts: The Role of Pd and B-sites for $NO_x$ Adsorption Behavior via in-situ Spectroscopy", *Applied Catalysis B: Environmental*, 51-61, 154-155, 2014.
3. Z. Say, O. Mihai, M. Kurt, L. Olsson, E. Ozensoy, "Trade-off between NOx Storage Capacity and Sulfur Tolerance on Al2O3/ZrO2/TiO2–Based DeNOx Catalysts", *Catal. Today*, 320, 152–164, 2019**.**
4. M. Kurt, Z. Kap, S. Senol, K. E. Ercan, A. T. Sika-Nartey, Y. Kocak, A. Koc, H. Esiyok, B. S. Caglayan, A. E. Aksoylu, E. Ozensoy, "Influence of La and Si Promoters on the Anaerobic Heterogeneous Catalytic Decomposition of Ammonium Dinitramide (ADN) via Alumina Supported Ir Active Sites", *Applied Catalysis A: General*, 2022, 118500, (Accepted).
5. K. E. Ercan, Z. Say, M. Kurt, M. Karatok, A. T. Sika-Nartey, E. Ozensoy, "Remarkable CO/NO Oxidation Performance of Precious Metal-Free Perovskites at Severe Reaction Conditions.", (Submitted).